UNIVERSITY OF CALIFORNIA SAN DIEGO

Data-driven systems engineering for bioinspired integrative design

A dissertation submitted in partial satisfaction of the
requirements for the degree
Doctor of Philosophy

in

Structural Engineering

by

Luca Gabriele De Vivo Nicoloso

Committee in charge:

Professor Falko Kuester, Chair
Professor Tara C. Hutchinson
Professor Petr Krysl
Professor Vlado Lubarda
Professor Marc Meyers

2021

The dissertation of Luca Gabriele De Vivo Nicoloso is approved, and it is acceptable in quality and form for publication on microfilm and electronically.

University of California San Diego

2021

DEDICATION

This dissertation is dedicated to my parents, Gabriela Nicoloso and Luca De Vivo, my sister Alessandra De Vivo Nicoloso, and my brother Gabriel Nicoloso, who provided the guidance, support, and encouragement since day one. I am where I am thanks to them and all my other mentors, professors, and coaches who have helped me succeed and grow as a professional, family, community member, and world citizen. Thank you, Falko Kuester, Denny Harper, Jefi Harper, Matt Ustaszewski, Scott Taylor, William Jewell, Gilberto Caseres, and Dominique Rissolo. I would also like to thank all my amazing friends who have accompanied me on this journey as an international student from Venezuela in California. Thank you, Reyanne Mustafa, Cameron Ravanback, Cliff Kapono, Sierra Robbins, Kevin Oliveira, July Powell, Paul Miernicki, Pedro Caldas, and many more.

I would also like to dedicate this work to my mentor and friend, Falko Kuester, who believed in me and gave me a chance to explore my imagination and engineering skills at UCSD. Thanks for providing me a fantastic work and lab space that served me as a catalyst for personal growth and professional innovation.

EPIGRAPH

nature as model, nature as measure, and nature as mentor.

—Janine Benyus

TABLE OF CONTENTS

LIST OF FIGURES

LIST OF TABLES

ACKNOWLEDGEMENTS

Thank you, Falko Kuester, for being such a great and inspiring mentor and coach. Thanks for the push and support and for providing the outstanding laboratory and equipment that formed my home on campus during my studies. More importantly, thank you for constructing the unique interdisciplinary environment that has introduced me to so many unique minds and helps every student under your supervision grow as an academic and as a person.

I must note that one of the most valuable skills I have acquired through my time as a grad student, the ability to teach, explain, and coherently convey ideas to any audience, is a direct result of the dozens of hours of classroom time that Falko Kuester handed over to me to lead. Spending time at the front of a classroom is as much a learning experience as sitting in the audience. It is an opportunity very few are privileged with, and for that, I am eternally grateful.

Thank you to my committee members and professors for providing guidance when I request it, answering questions when I have them, and for doing so without hesitation or complaint at often ridiculous hours of the day. I could not ask for a better faculty, and because of this, UCSD will always be a significant part of who I am.

Finally, I would like to recognize and extend my gratitude to all my coauthors: Albert Matsushita, Joshua Pelz, Herb Barrack, Xiang Want, Danny Tran, Eric Lo, Vlado Lubarda, Marc Meyer, Joanna McKittrick, Tara Hutchison, Petr Krysl, and Falko Kuester. They helped me conduct much of the research and construct much of the content herein and deserve my sincerest gratitude.

Chapter 1, in part, is a reprint of the materials as they appear, titled "Design and Manufacture of Optimized Continuous Composite Fiber Filament Using Additive Manufacturing Systems." in Journal of Material Science and Engineering. And title "Optimization of Varying Orientation of Continuous Fiber Direction and Its Applications to New Methods of Additive Manufacturing." in Research and Development in Material Science. De Vivo, Luca, the dissertation author was the primary investigator and author of this material.

Chapter 2, 3 and 4, in part, is a reprint of the material as it appears, titled "Towards Design of a 3D Printable Prandtl Box-Wing Unmanned Aerial Vehicle" IEEE Aerospace 2019. De Vivo, Luca; Tran, Danny; Kuester, Falko. The dissertation author was the primary investigator and author of this material.

Chapter 5, in part, is a reprint of the material as it appears, titled "Cholla Cactus: Engineering Materials and Structures Guided by Nature" Apta Biomateriala 2020. De Vivo,Luca; Matsushita, Albert K.; Kupor, Daniel; Luna, Josue; Tierra, Beatrice; Sah Robert; Krysl,Peter; Lubarda, Vlado; McKittrick, Joanna M.; Kuester, Falko Kuester. The dissertation author was the primary investigator and author of this material.

Chapter 6, and 7 in part, is in part a reprint of the material as it appears, title "Towards a 3D Printing of a Monocoque Transtibial Prosthesis using a Bio-inspired Design Workflow". as it appears in Rapid Prototyping Journal 2021. De Vivo, Luca; Pelz, Joshua; Kuester, Falko. The dissertation author was the primary investigator and author of this material.

VITA

2016	B. S. in Structural Engineering, University of California San Diego
2020	M. S. in Structural Engineering, University of California San Diego
2021	Ph. D. in Structural Engineering, University of California San Diego

[1] De Vivo Nicoloso, L. G. (2017). Design and Manufacture of Optimized Continuous Composite Fiber Filament Using Additive Manufacturing Systems. Journal of Material Science & Engineering, 06(04). doi:10.4172/2169-0022.10003363

[2] De Vivo Nicoloso, L. G. (2018). Optimization of Varying Orientation of Continuous Fiber Direction and Its Applications to New Methods of Additive Manufacturing. Research& Development in Material Science, 3(2). doi:10.31031/rdms.2018.03.000559

[3] De Vivo Nicoloso, L. G., Tran, D., Kuester, F. (2019). Towards Design of a 3D Printable Prandtl Box-Wing Unmanned Aerial Vehicle. 2019 IEEE Aerospace Conference. doi:10.1109/aero.2019.8741628

[4] De Vivo Nicoloso, L.G., A. K. Matsushita, D. Kupor, J. Luna, B. A. Tierra, R. L. Sah, V. A. Lubarda, M. A. Meyers, J. M. McKittrick, P. Krysl, and F. Kuester. (2020) Cholla cactus frames as lightweight and torsionally tough biological materials, Acta Biomaterialia, vol. 112, pp. 213–224, 2020, doi: 10.1016/j.actbio.2020.04.054.

[5] De Vivo Nicoloso, L. G., Pelz, J., Kuester, F. (2021). Towards a 3D Printing of a Monocoque Transtibial Prosthesis using a Bio-inspired Design Workflow. Rapid Prototyping Journal;Emerald Publishing, . doi: 10.1108/rjp-06-2021-0136.

[6] De Vivo Nicoloso, L. G., Pelz, J., Kuester, F. (2021). Project LIMBER: Structural Test of a Custom 3D Printed Unibody Below the Knee Prosthetic Leg. Rapid Prototyping Journal;Emerald Publishing, . doi: TBD.

ABSTRACT OF THE DISSERTATION

Data-driven systems engineering for bioinspired integrative design

by

Luca Gabriele De Vivo Nicoloso

Doctor of Philosophy in Structural Engineering

University of California San Diego, 2021

Professor Falko Kuester, Chair

Engineering design problems can be discussed under the framework of decision making, namely, engineering design decisions. Inherently, accounting for uncertainty factors is an indispensable part of these decision processes. The goal of design decisions is to control or reduce the variational effect in decision consequences induced by many uncertainty factors. If we look at current technological trends, specifically the industry 4.0 movement, we can quickly appreciate the big push in science and technology for the digitalization of design, manufacturing, and management processes to reduce the amount of uncertainty present during innovation attempts. This work explores the value of data-driven integrated design and digital fabrication and how it allowed us to drive innovation in more than one domain. From examples in biomimicry discoveries to prostheses and unmanned aerial vehicle designs to the use of drones

for emergency response, the key ideas of the proposed data-driven design paradigm are demonstrated.

Earlier works on data-driven design and digital manufacturing have demonstrated its potential to disrupt the way we think about engineering design processes. However, constant modernization in these fields keeps pushing the boundaries on what is possible, and these territories remain relatively uncharted. This research aims to explore how a combination of spatial data sets can serve as a point of entry for data-driven innovative designs. The process starts with a different range of data acquisition tools and processing techniques, followed by computational analysis and optimization designs, all the way to digital manufacturing by means of 3D printing and validation via mechanical and functional testing. These data sets enabled the synthesis of digital twin models, which allowed us to begin a reverse engineering process for a series of multiple purposes.

To begin our study, we focused on new methods of additive manufacturing with a special focus on composite 3D printing. We explored the current state of knowledge in the field of composite additive manufacturing. We investigated all different methods of 3D printing and the current broad range of materials available. We also gained a deep understanding of the different optimization opportunities that can be gained by incorporating fibers, chopped or continuous, into polymer filament additive manufacturing.

Now that we know we can design and manufacture almost anything we can imagine we asked ourselves what would that be? At this point we explored new trends in the field of digital modeling, simulation, and optimization techniques. Starting in the cyber context we can create a digital twin that satisfies the objective functions of an engineering system such as lightweight, strong, controllable, manufacturable, and then use these objective functions as an opportunity to optimize over the design space. To prove this concept, we selected an engineering system design challenge: The design and optimization of a novel box wing vertical takeoff and landing aircraft

intended to serve in long endurance environmental and archeological recognition missions as well as serving as the starting point for the development of the next generation of urban air mobility platforms.

During the design of the Prandtl Box wing aircraft system we found that if we wanted to design better aeronautical systems, we needed to find a way to design lighter and stronger structures. This is the point when we decided to look into nature's library. We dived deep into biomimicry and proved how data and visualization driven research together with traditional mechanical testing, allows us to grasp a better insight on evolutionary optimization and its applications on structural design and material science.

The ability to optimize and build stronger performing structures that follow form to function allowed us to add an extra level of complexity to our engineering system design. We added a human in the loop. This presented us with a unique set of functional requirements. We were faced with the challenge on how to translate these functional requirements into new objective functions. Using this new set of objective functions and the engineering system design methodology developed in previous studies we designed and tested a bioinspired transtibial prosthesis, which can be entirely 3D printed in a single piece allowing us to solve a global accessibility challenge.

Additional work was done where we focused on the use of drones for emergency response after natural events and its applications on data-driven structural damage assessment during and after earthquakes. This work is not presented in this dissertation, but published material can be found online and the vita section of my thesis.

Chapter 1

Industry 4.0: Next Generation Manufacturing

1.1 Additive Manufacturing Systems

1.1.1 Design and Manufacture of Optimized Continuous Composite Fiber Filament Using Additive Manufacturing Systems

Additive manufacturing (AM) is a process where machines automatically fabricate arbitrary shaped parts, pixel by pixel, layer by layer, from almost any material as opposed to subtractive manufacturing techniques. AM has many strategic advantages over traditional manufacturing processes: the production of complex internal and external part geometries that cannot be made in any other way, rapid iteration through design permutations, and the ability to build customized functional parts in small lot sizes to meet end-user specifications [Lip11]. The technology first emerged in 1987 with stereo lithography (SL) [WG11], and since then has evolved from a limited number of expensive prototypes to widely available, small-scale commodity production

tools. AM is expected to transform every aspects of our lives, and some people are calling it "the second industrial revolution". There are many different additive manufacturing processes all with their specific benefits, drawbacks, and application areas. Currently the available AM processes are divided into 7 groups. Material Extrusion, Material Jetting, Binder Jetting, Sheet Lamination, V at Photo-polymerization, Powder Bed Fusion, and Direct Energy Deposition (Figure: 1.1.

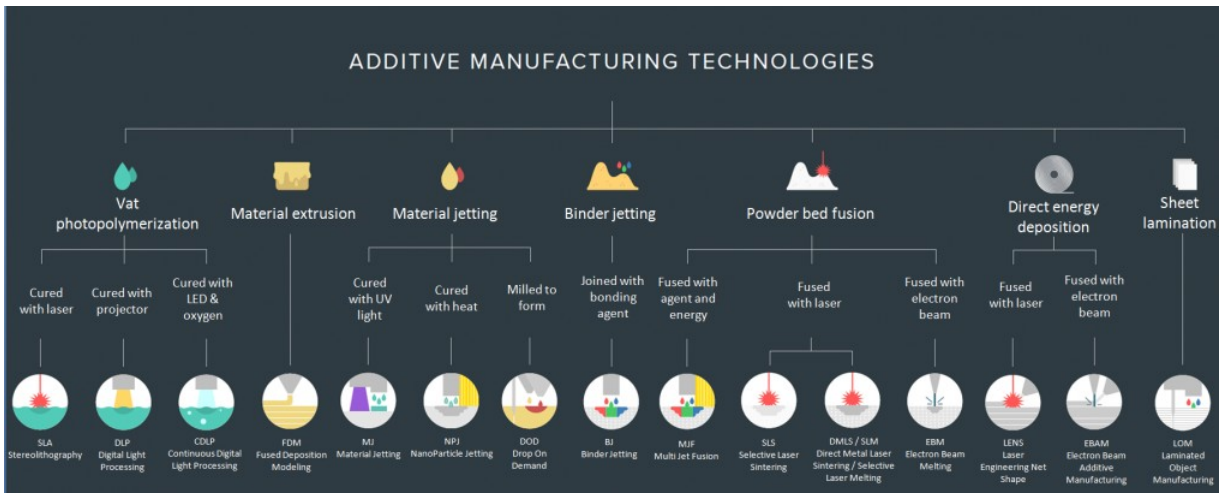

Figure 1.1: Different AM Technology Families.

The materials required for the final product will determine what AM process is used. Polymers (Thermoplastic filament or powder and Photocurable resins) , and metals (filaments and powders) are the most common types of materials used in AM and can be used to produce molds, prototypes and functioning components. Typical polymers used for 3D printing are; ABS, PLA, PC, PETG, Nylon, PEI and PEEK as can be seen in (Figure: 1.2). On the other side we find among the metals that are available for AM; Aluminum, Copper, Bronze, Cobalt, Nickel, Steel, Stainless Steel, and Titanium plus their respective alloys (Figure: 1.3). There are however possibilities for other materials to be used in AM, such as medical and biomedical graded materials, glass, ceramics, advanced fibers, living cells and food. These materials come in different shape and sizes, among them we found powders, liquids and filaments. Additive

manufacturing has distinct advantages and disadvantages, and it is up to the designer or engineer to decide if additive manufacturing is the best fit for the project. Some of the main advantages of AM are: variety is free, reduced lead time, variety if free, little lead time, and little skill manufacturing, few constraints, and less waste. On the other hand major disadvantages related to AM are: slow build rates, higher production costs, requires post processing, and poor mechanical properties in certain directions.

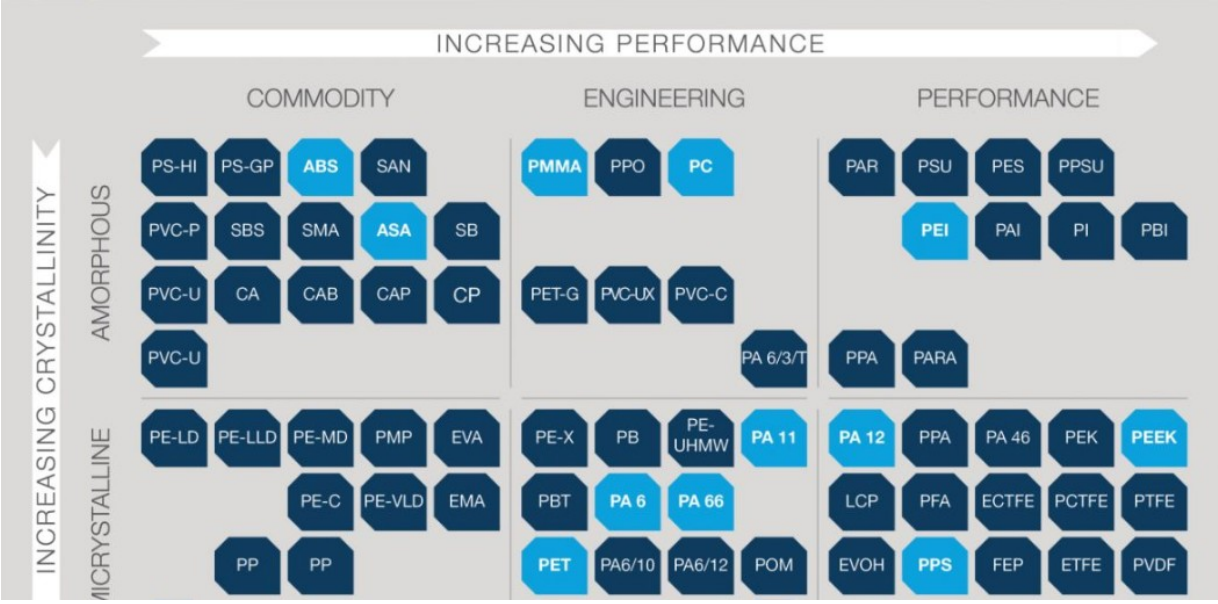

Figure 1.2: Stratasys periodic table of 3D printable thermoplastic polymers.

Even though AM has greatly evolved over the past three decades it still has a lot of room for improvements. One of the areas that have not yet been deeply investigated is the combination of composite techniques with additive manufacturing. In recent years the use of composite laminated plates has been widely adopted by the engineering community especiallyin practices such as aerospace, marine, civil and medical engineering. Composite materials are made by combining two or more materials, which often have different properties, in order to create a material with unique properties. One of the most widely used composite materialsis fiber-reinforced composite (FRC), where fibers and a matrix are used to create structures with an exceptional strength to weight ratio. The fiber provides strength in the longitudinal

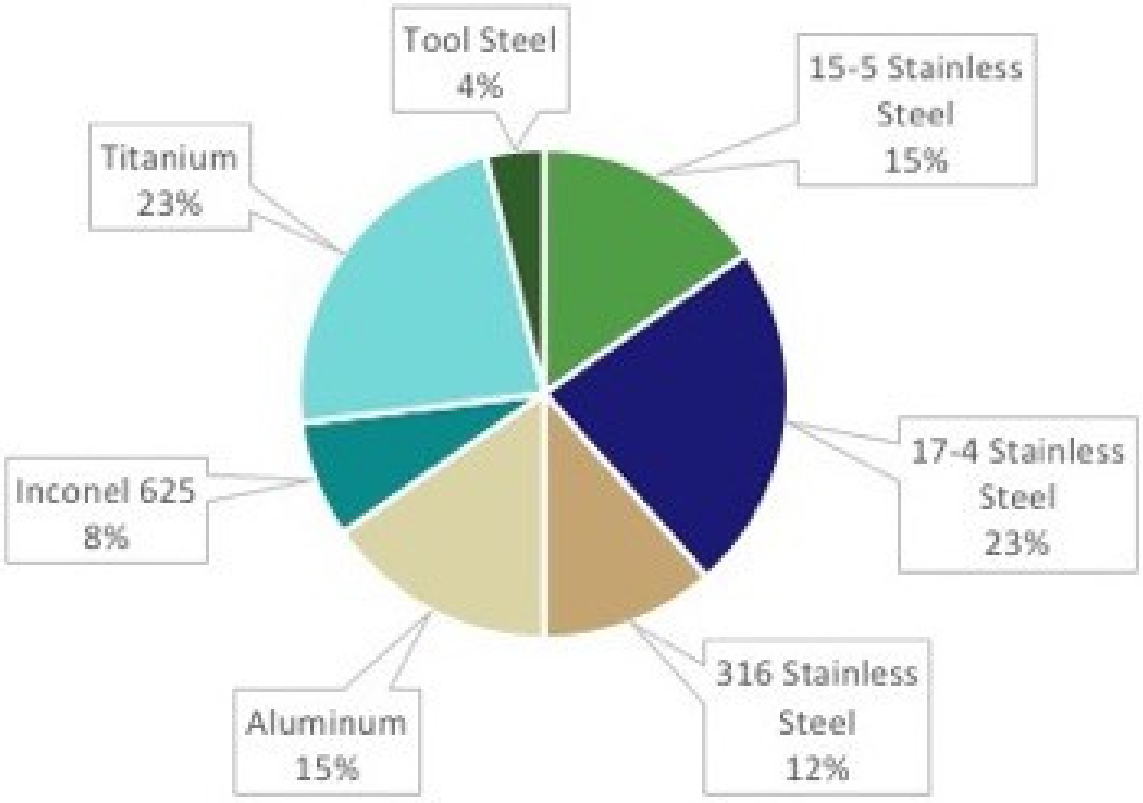

Figure 1.3: Percentage breakout by type of metal chosen for industrial 3D printing projects in 2017.

direction while the matrix, often a resin, provides stiffness and bonding of the fibers. A special characteristic of FRC is that multiple plies with different fiber orientations can be stacked in order to provide strength in multiple directions, which allows composite structures to be tailor for specific applications or load cases (Figure: 1.4).

As mentioned earlier polymers constitute one of the most popular AM materials, yielding lightweight but inherently weak components that cannot hold up against high tension and bending stresses, unless high graded plastics like PEI and PEEK are used but these can be expensive, hard to print, and require special extruders and confinements for success. A need for improved tensile strength has driven a recent interest in AM of fiber reinforced polymers (FRPs). AM-FRPs are

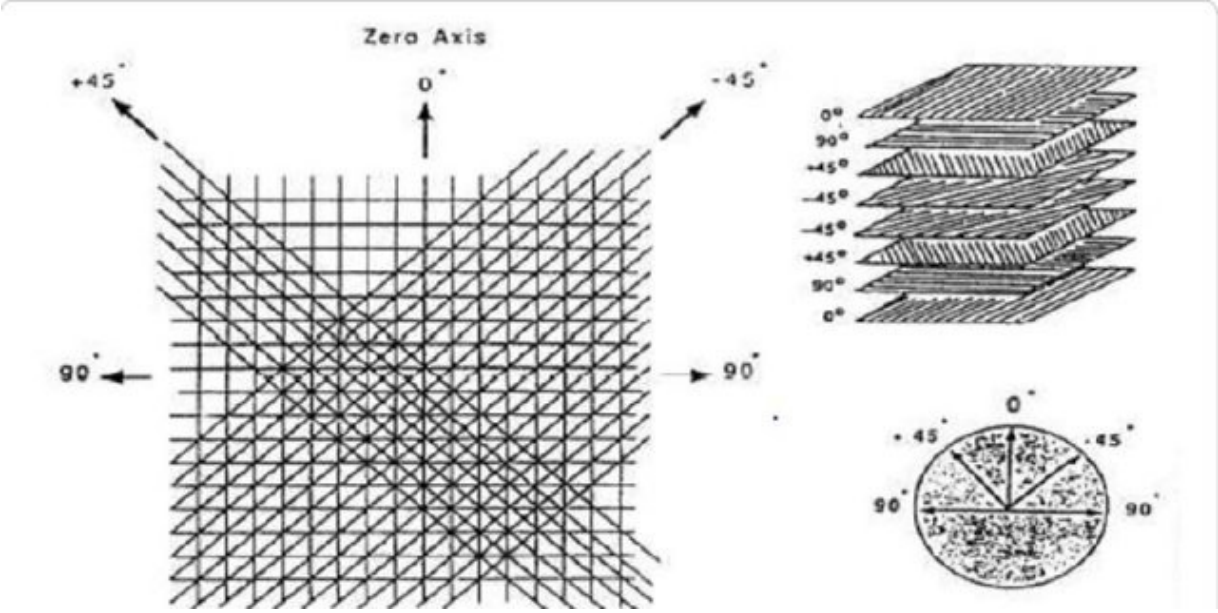

Figure 1.4: Standard composite ply orientation.

separated into two different families; short fiber reinforcement [TKVG+14], and continuous long fiber reinforcement [7-13]. AM-FRPs reinforced with short fibers have demonstrated increased mechanical strength, but with limited design and structural flexibility. AM-FRPs reinforced with continuous fibers provide structural reinforcement within plane.

Recent improvements in the area of additive manufacturing allows the production of complex arrangement of fibers using a technique known as Fused Deposition Modeling (FDM) of continuous fiber reinforced plastics. Automated fiber placement of thermoset composites were invented over 40 years ago and is now widely accepted for the manufacture of advanced composite structures. However, expensive tooling and post process such as autoclaves are required. In-situ inexpensive tooling, eliminates these post process, and can be considered an additive manufacturing process for advanced composite structures.

Griffini, Invernizzi and Natale developed a UV-Assisted 3D printing of glass (GFR) and carbon fiber reinforced (CFR) dual-core polymer composite [INL+16]. In this work a sequential interpenetrating polymer network (IPN) obtained by formulating a photocurable acrylic resin with

a thermo-curable epoxy resin was presented and proposed as matrix for the fabrication of GFR and CFR composite structures by means of 3D printing technology. The resin material combines an acrylic based photocurable resin with a low temperature (140 C) thermally curable resin system based on bisphenol and diglycidyl ether as base component, it uses aliphatic anhydride as hardener and (2,4,6,-tris(dimethylaminomethyl)phenol) as catalyst. Photoinitiated polymers played a key role in the development of this experimental work. Photopolymers belong to the family of materials that change their properties when exposed to ultraviolet radiation. In order to successfully print with this new material a new 3D printer had to be developed (Figure: 1.5). The apparatus consists of a system of rollers that feed the fiber inside the impregnation station;a head of power, which comprises a polymerization device (eg. a UV LED or laser light or a thermal emission source), positioned at the nozzle; a cutting tool for the composite material, configured to interrupt the supply of the material in the nozzle exit, and a numerical control machine of at least 3 axes that has the task of moving the head of the material supply. UV-3D printed macrostructures were successfully demonstrated giving a clear indication of their potential use in real life structural applications. The 3D printed structures were characterized by good thermal stability and mechanical properties.

Another company using a similar composite UV curing technique is Functional 3D Printing [Tyl17]. They invented a machine capable of 3D printing continuous composite structures using a new positioning system utilizing hollow tubular printing techniques and multiple print heads working together in tandem to continuously manufacture large advanced structures. Their technology harness UV light to instantly cure a combination of continuous fiber and thermoset matrix material giving them the ability to print into free space. Rapid initiation of free radical polymerization is promoted by a precise control of high intensity irradiation to quickly promote cross linking of the thermoset matrix among the continuous fibers. They are capable of printing with 8 and 16 channel nozzles utilizing different material combinations (Figure: 1.6). The printer is capable of printing 4 different material families; Hollow Core Multi-Functional (Hollow core

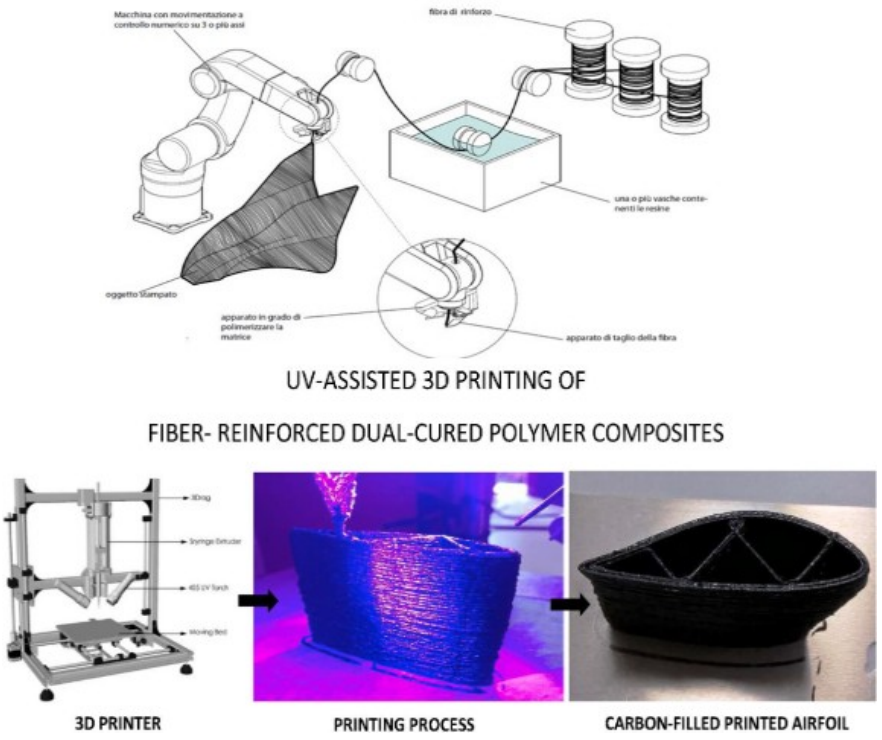

Figure 1.5: UV-assisted 3D printer of GFR and CFR.

with fiber optics, carbon fiber and polymer encasement), Multi-Strand Fiber Optic Core (Fiber optic core is encapsulated by continuous metal wire, carbon fiber, and polymer encasement), Basic CC3D Material (combination of thermoset acrylate and carbon fiber), and Carbon Fiber with Metal Core.

Matsuzaki and Ueda et al. developed a method for three-dimensional (3D) printing of continuous fiber-reinforced thermoplastics by in nozzle impregnation based on FDM [MUN+16]. A thermoplastic filament and continuous fibers are separately supplied to the 3D printer and the fibers were impregnated with the filament within the heated nozzle of the printer immediately before printing ((Figure: 1.7)). The reinforcing fibers are heated using a nichrome wire before entering the nozzle, to enhance the permeation of the fiber bundles with thermoplastic resin; the heat diffuses to the resin and decreasing the viscosity of the PLA. The reinforced filament is heated to a temperature greater than a melting temperature of the matrix material (210 C)

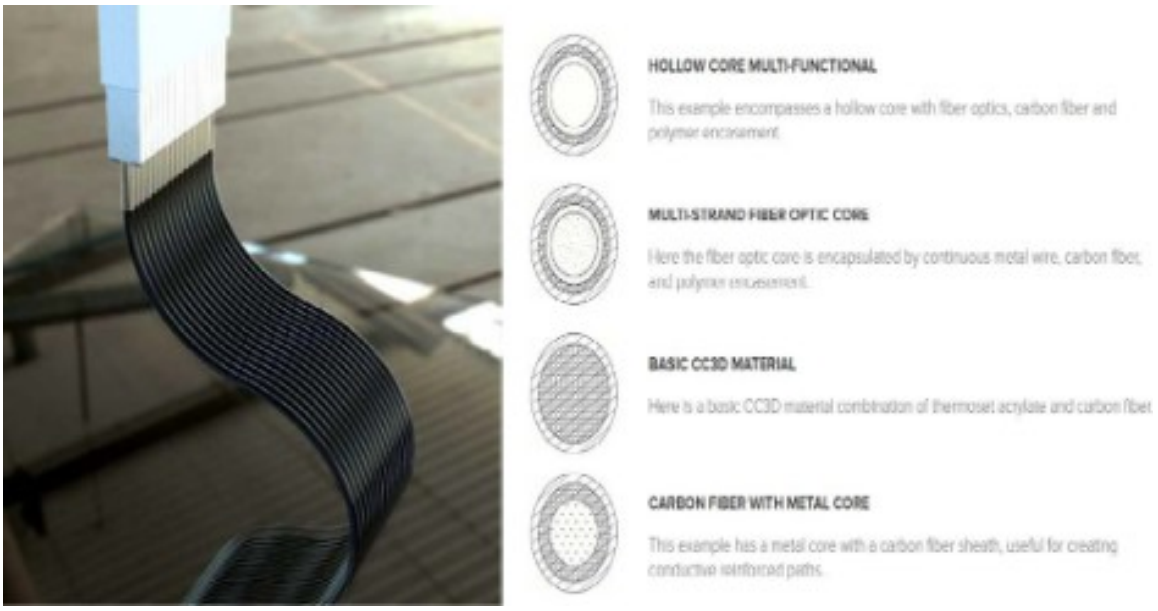

Figure 1.6: Functional 3D printing with 16 channel nozzles and materials.

and less than a melting temperature of the core fiber prior to extruding the filament from the extrusion nozzle. Polylactic acid (PLA) was used as the matrix while carbon or glass fibers were used as the reinforcement. The 3D printer for obtaining continuous fiber composites was developed by modifying the print head of a commercially available FDM 3D printer. The technique enables direct 3D fabrication without the use of molds and may become a standard next-generation composite fabrication methodology using FDM printing. Continuous fiber reinforcement improved the tensile strength of the printed composites relative to the values shown by conventional 3D-printed polymer-based composites.

Another technique proposed by MarkForged is to alternate in-plane layers of thermoplastic and fiber materials. The system has two print heads, one for plastic and one for fibers. During the printing process a layer of thermoplastic, in this case a combination of tough nylon with micro-carbon reinforcement is placed as the matrix and confinement for the continuous fibers, (Fiber, Carbon and Kevlar) which are then placed on the second layer within the plastic confinement (Figure: 1.8a). This process is repeated until the final layer is printed, and the piece is ready to be

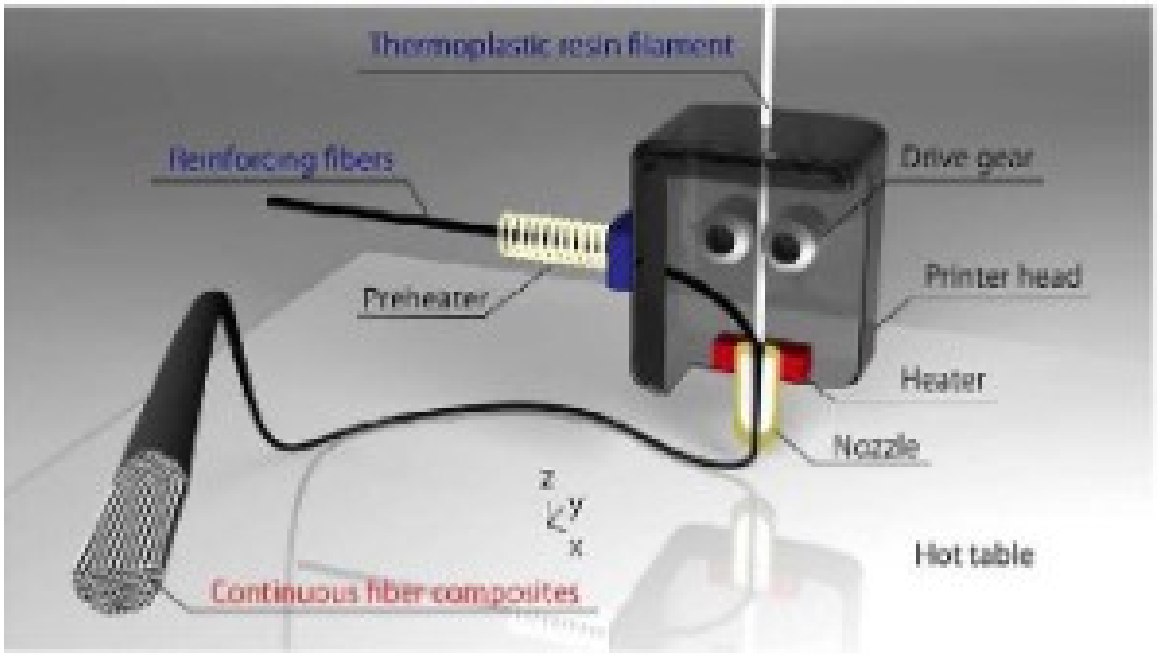

Figure 1.7: 3D printer heads used to produce Continuous Fiber Reinforced Thermoplastic Structures.

removed. Markforged printers are capable of producing parts that are 5-10 times stronger than conventional thermoplastic 3D printed parts (Figure: 1.8b).

Turk, Triebe, and Meboldt et al. proposed to use FDM together with a multi-axis robot to place continuous fiber in three dimensions and build structures from the inside out [Tyl17]. This was achieved by combining additive manufacturing tooling with in-situ automated fiber placement of thermoplastic composite rapid prototyping software with Automated Fiber Placement.

Another company utilizing the mobility and versatility of multi-axis robot for AM is Arevo Labs with its Robotic Additive Manufacturing Platform (RAMP) for 3D printing Complex Composite Parts [Lip11]. RAMP consists of a robotic AM cell (Figure 6), ultra strong composite material and a comprehensive CAM software suite. The robotic AM cell employs a standard commercially available six-axis robotic arm and a composite deposition end-effector with advanced thermal management technology for processing high-performance carbon fiber reinforced thermoplastic. The Ultra Strong continuous carbon fiber reinforcement thermoplastic

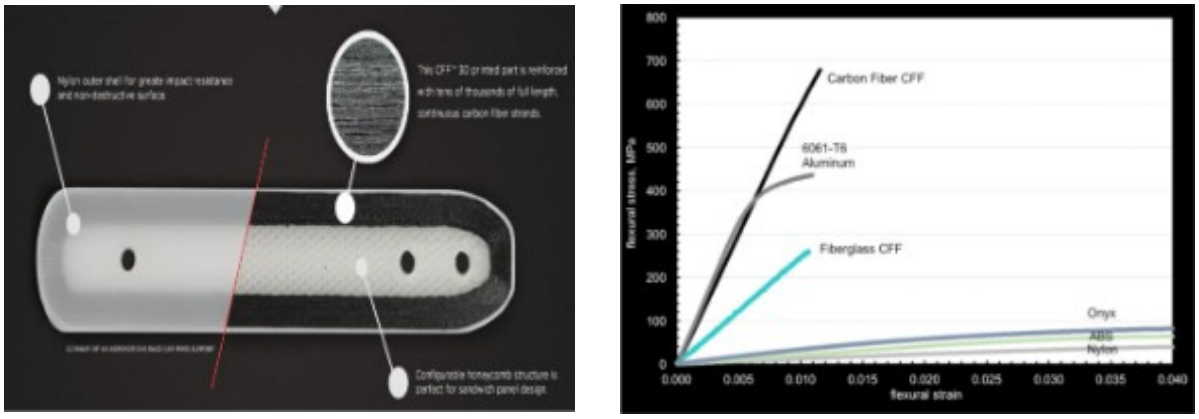

(a) MarkForged Carbon Fiber 3D printed part (b) Comparing Material Properties

Figure 1.8: MarkForged Continuous Fiber 3D Printer

composite is more than five times stronger than titanium, tolerates extreme temperatures and is highly chemical resistant. And the software converts CAD models to six degrees of freedom additive manufacturing G-Code, which combined with a precise kinematics simulator interprets deposition instructions to validate and optimize part construction.

1.1.2 Optimization of Varying Orientation of Continuous Fiber Direction and Its Applications to New Methods of Additive Manufacturing

In recent years the use of composite laminated plates have been widely adopted by the engineering community especially in practices such as aerospace, marine, civil and medical engineering. Composite materials are made by combining two or more materials, which often have different properties, in order to create a material with unique properties. One of the most widely used composite materials is fiber-reinforced composite (FRC), where fibers and a matrix are used to create structures with an exceptional strength to weight ratio. The fiber provides strength in the longitudinal direction while the matrix, often a resin, provides stiffness and bonding of the fibers. A special characteristic of FRC is that multiple plys with different fiber orientations can be stacked in order to provide strength in multiple directions, which makes composite plates

Figure 1.9: Arevo RAMP 3D Printer.

a material that can be tailored for specific applications or load cases.

Extensive literature can be found in which researchers have study several ways of optimizing composite structures with respect to multiple fiber variables such as; fibers materials [CZ13], volume fraction [[KSK09], [DII16]], size [ESSAJ13] and mesostructured. In fiber-matrix composite material mechanics the orientation of the fibers plays an essential role in dictating the performance of the composite material. This implies that there is an opportunity to optimize the orientation of the fibers to obtain composite structures that outperform unidirectional fiber lay-ups. Studies have shown that in-plane optimal fiber orientation can increase structural stiffness [[SAG06], [BWK15], [SGW06]], failure loading [[HH05], [RMT70]], and buck-

ling stress [IAG10], [KS09], [KL13]], and improve the fundamental frequency of the laminate [[SB12], [WZX15], [FSS94], [ASG07]] over the traditional quasi-isotropic fiber construction without increasing the weight.

Early studies to describe the behavior of composite plates with variable fiber spacing, and fiber orientation were conducted [[ML89], [KTC88], [HL91], [DL89], [GO93]]. Marting AF & Leissa AW [ML89] studied the buckling of a rectangular composite sheet composed of variably spaced straight and parallel fibers (variable fiber volume fr action), and achieved improvement in the buckling performance. Kuo CM et al. [KTC88] modeled elastomer composite sheets having fibers in the form of sinusoidal waves. Hyer MW & Lee HH [HL91] developed finite element models of panels with curvilinear fiber format to improve strength and buckling performance [KTC88]. Dinardo MT & Lagace PA [DL89] found that for panels with dropped internal plies the buckling performance is driven by the changes in stiffness along the panel. Gurdal Z & Olmedo R [GO93] carried out studies of rectangular panels with steered fiber path and was able to obtain solutions to the plane elasticity problem, and create the necessary equations to generate the linear variation of fiber orientation angles.

Further improvements on the understanding of the behavior and benefits o f varying curvilinear fibers in composite structures were performed at the Karlsruhe Institute of Technology in Germany. Mattheck C and Kubler et al. [MK97] studied the biomechanics of wood and bone structures. They found that trees optimize their external shape such that stress concentrations are avoided. Their studies on natural load carriers have demonstrated that shear stresses, which are extremely dangerous for fiber composite materials, are nearly eliminated by a force flow-tailored orientation of the fibers. Thus, the risk of splitting a and formation of the cracks, which may lead to failure of fiber composites, is a verted. After these findings Reuschel, D et al. [RMT70] developed the CAIO-Method which uses Finite Element Method (FEM) analyses and copies biological fiber orientation in order to minimize shear stresses within orthotropic or multi-layer composite material structures. The idea behind CAIO Method is to lay the fibers in

the direction of the principal stresses. The optimum fiber arrangement is calculated by an iterative process of alternating FE-run and CAIO-calculation. The method is characterized by an excellent convergence. Most of the times three or four iterations are enough to reduce the shear stresses by more than 90%.

As mentioned earlier spacial variation of stiffness can be induced by steering composite fibers in curvilinear paths. Fiber angles and predefined fiber angle variations are used in most of the research on fiber steered composites [VCKG12]. However, it has been proposed to design such variable stiffness structures in terms of lamination parameters. The use of lamination parameters efficiently defines stiffness variation over a structural domain with the minimum number of variables. Van Campen et al. proposed a two step design approach, where first a Variable Stiffness composite is designed in terms of Lamination Parameters, followed by a conversion of the lamination parameters into fiber angle distribution for each layer in the laminate.

A common objective function in structural optimization is the minimization of compliance, which is also referred to as the strain energy. The compliance of a structure is essentially the inverse of stiffness, and by minimizing compliance, one can maximize the stiffness. Hammer, Bendsoe, Lipton and Pedersen et al. considered the maximal stiffness design of constant stiffness laminated plates subjected to single and multiple loads, where the stiffness of the laminates were parametrized in terms of the lamination parameters. Setoodeh et al. [SAG06] used lamination parameters to investigate the optimal design of fiber reinforced rectangular composite plates for minimum compliance. They considered two types of designs: constant-stiffness and variable-stiffness and used a sequential quadratic programming to solve the optimization problem. It was shown that significant improvements in stiffness can be gained by using variable-stiffness design. Brampton J et al. [BWK15] proposed a new optimization method to minimize the compliance of a structure by optimizing the continuously varying fiber paths using a level set method. They derived the sensitivity of the structural compliance to a change of fiber direction and use the sensitivities to optimize the level set defined fiber paths. Setoodeh et al. [SGW06] investigated the

design optimization of variable-stiffness composite layers using cellular automata. The analysis is based on the equilibrium of local cells and the design process uses the compliance minimization as the objective function. They were able to show that substantial gains in compliance can be achieved through placement of fibers in their optimal spatial configuration.

Another important optimization problem is the maximization of strength, or the maximization of failure load. The strength characteristics of a composite lamina are generally just asimportant as the material stiffness of compliance characteristics. The challenge behind it is that strength properties vary as a function of load direction (compression or tension) and load type (longitudinal, transverse normal, or shear) relatively to the material orientation. The strength of alamina material can be determined through micro-mechanics equations and are defined in the material principal direction. Failure theories have been developed for lamina assuming biaxial stress state, where the strength properties are defined in the material principal directions, and thus the stresses must be transformed not to the principal stress axes but to the material axes. The maximum failure criterion can be adopted to predict failure load and the failure type (fiber failure, matrix failure, or shear failure) of a single ply. In addition to the simple strength of material approaches, other methods have been developed based upon the energy distorted within the specimen at failure. These methods allow the use of a single simple equation that can be used during preliminary design and analysis to predict the failure load of the lamina. Some of the most common energy distortion methods are Tsai-Hill, Hoffman, and Tsai-Wu failure crite-rion. We found that Tsai-Wu is a preferred failure criterion used by the composite optimization community. Huang et al. [HH05] proposed a procedure for optimizing the fiber orientation near a hole in a single layer of multilayer composite laminates for increased strength. The Tsai-Wu failure criterion was used and an optimization of the fiber direction near the hole was obtained by alternating between a gradient based search and a genetic algorithm. As mentioned earlier Reushcel et al. [RMT70] created the CAIO method which copies biological fiber orientation in order to minimize shear stresses within composite layers, thus increasing the strength of the

lamina. Temmen H et al. presented selected results of four research projects, carried by the DLR Institute of Composite Structures and Adaptive Systems, which aimed to improve the design of composites using Tailored Fiber Placement by aligning the fiber to the direction of principal stresses for a given load case. They were able to achieve improvements of about 60% for tension and 79% for compression.

Because composite material specimens tend to be relatively thin, buckling prior to the desired failure mode is a concern when specimens are loaded in compression or bending. Known as Euler buckling, the test specimen carries the applied load as it increases with no indication of incipient failure until it suddenly collapses when the load reaches a critical value. Karakaya et al. [KS09] studied the optimization of stacking sequence of laminated composite plates for maximum buckling capacity using genetic algorithm and generalized pattern search algorithm. Ho-Huu et al. [HHDTDT+16] proposed a novel numerical optimization method to maximize the buckling load of a constant stiffness laminated composite plates using improved differential evolution and smoothed finite element method. The design variables used were fiber orientation angles and thickness of layers. Van Den Brink et al. proposed a two-step variable stiffness design approach for buckling optimization of a composite fuselage window section. First the optimal fiber orientation is determined based on spline interpolation and then the physical composite fiber tows are derived. An improvement of 12% in buckling performance was found when compared to constant stiffness laminate. Abdalla et al. [IAG10] worked on the optimization of variable stiffness panels for maximum buckling load using lamination parameters. Numerical results demonstrated improvements in excess of 100% in buckling loads of variable stiffness panels compared to the optimum constant stiffness designs.

The fundamental frequency of composite laminated plates has been considered as an important factor in vibration problems. Aeronautic structures generally require that the fundamental frequency to be higher than those of the excitation. If this requirement is practically unattainable, then the fundamental frequency is required to lie between two excitation frequencies.

Koide R & Luersen M [KL13] proposed the use of an ant colony algorithm to maximize the fundamental frequency of laminated composite cylindrical shells. It Sadr et al. [SB12] presented a new method to optimize constant-stiffness composite plates for maximum fundamental frequency using a combination of Elitist Genetic algorithm and finite strip method. Wang F et al. [WZX15] worked on the fiber orientation angles optimization for maximum fundamental frequency of a constant stiffness laminated composite plates using a Generic Algorithm and a Meshless Method. Fukunaga et al. [FSS94] studied optimal design of constant stiffness laminates for natural frequency using 4 lamination parameters based on a CLPT (Classical Lamination Plate Theory) deformation analysis. Abdalla et al. [ASG07] considered the maximization of the natural frequency of variable stiffness composite panels using lamination parameters by adopting a new structural approximation scheme, the so called generalized reciprocal approximation, which leads to a robust stable convergence of the design iteration. They were able to prove that significant increase in the optimal fundamental frequency can be achieved using variable stiffness panels.

Recent improvements in the area of additive manufacturing allows the production of complex arrangement of fibers using a technique known as Fused Deposition Modeling (FDM) of continuous carbon fiber reinforced thermoplastic (CCFT). Automated fiber placement of thermoset composites was invented over 40 years ago and is now widely accepted for the manufacture of advanced composite structures. However, expensive tooling and post process such as autoclaves are required. In-situ inexpensive tooling eliminates these post process, and can be considered an additive manufacturing process for advanced composite structures. Matsuzaki R & Ueda M [MUN+16] developed a method for three-dimensional (3D) printing of continuous fiber-reinforced thermoplastics by in-nozzle impregnation [TTM16]. A thermoplastic filament and continuous fibers are separately supplied to the 3D printer and the fibers were impregnated with the filament within the heated nozzle of the printer immediately before printing. Another technique proposed by MarkForged is to alternate in-plane layers of thermoplastic and fiber materials. A limitation of these methods is that the strength of the Z axis is restricted to the

interlayer bonding strength. Turk DA et al. [HH05] proposed to use FDM together with a multi-axis robot to place continuous fiber in three

dimensions, and build structures from the inside out. This can be achieved by combining additive manufacturing tooling with in-situ automated fiber placement of thermoplastic composite rapid prototyping software with Automated Fiber Placement. Yamanaka et al. [YTU+16] worked on the fiber line optimization in single ply for 3D printed composites. They optimization of thein-plane curved carbon fiber placement in a planar ply with an open hole. The project dealt withthe in-plane strength maximization of a curved carbon fiber alignment of a ply with an open holeusing genetic algorithm.

1.1.3 Advanced Polymers in Additive Manufacturing

So far, we have explored some of the newest techniques available for the additive manufacturing of composite materials, but for this technology to make it to the upper atmosphere or space many things will have to be tailor. Of supreme importance is that the materials used in thismanufacturing method need to withstand the harsh environment of space. Polymers are widely used in space vehicles and systems as structural materials, thermal blankets, thermal control coat-ings, adhesives, lubricants, etc. The space environment includes hazards such as atomic oxygen, UV radiation, ionizing radiation (electrons, protons), high vacuum, plasma, micrometeoroids and debris, as well as severe temperature cycles. Exposure of polymers and composites to the space environment may result in different detrimental effects via modification of their chemical, electrical, thermal, optical, and mechanical properties as well as surface erosion.

Polymers are extensively used as construction materials in space systems due to their high strength-to-weight ratio and a variety of mechanical, thermal, electrical and thermo-optical prop erties. Typical polymers are polysiloxanes (silicones), epoxies, polyurethanes, polyesters, acetals, acrylics, polyamides, fluorocarbons, polymides, etc. The influence of individual constituents of the space environment, as well as their synergistic effects, should be understood for proper

selection of polymers for specific projects.

Arevo Inc has developed a technique for 3d printing composites that could poten-tially make it to space (Figure: 1.9). It uses a multi-axis, continuous fiber technology whicheliminates the need for tooling, matches strength of titanium at 1/3 the weight, and cuts part cost when compared to hand layup/autoclave cure by a factor of 5. The company is using a combination of continuous carbon fiber reinforcement and high-performance thermoplastics like Ultem polyetherimide (PEI) and polyether ether ketone (PEEK). NASA and Boeing are designing a cry tank for out-of-autoclave (OOA) manufacturing. The team is using Hex Tow IM7 carbon fibers and Cytec CYCOM 5320-1 epoxy prepreg resin. Another company, ATK Aerospace Structures, is designing and manufacturing a composite backplane for a space telescope (JWST). ATK is using Toray M55J carbon fiber and cyanate ester resin. It is important to notice that the last two projects do not aim to manufacture these structures using AM but we will use the materials they are using as a starting point for our research on materials suited for the space environment.

We will first take a look at thermoplastics and then we will explore the world of thermoset resins. A thermoplastic is a polymer that becomes pliable or moldable above the glass transition temperature and solidifies upon cooling. Most thermoplastics have high molecular weight. The polymer chains associated through intermolecular forces, which weaken rapidly with increase temperature and over time. Thermoplastics can be reshaped by heating and are typically used to produces parts by various processing techniques as injection molding, compression molding, and extrusion. Above its glass transition temperature and below its melting point, the physical properties of thermoplastic change drastically without an associated phase change. Some thermo-plastics do not fully crystallize below the glass transition temperature, retaining some or all of their amorphous characteristics. Brittleness can be decreased with the addition of plasticizers, which increase the mobility of amorphous chain segments to effectively lowers the glass transition temperature. Modification of the polymer through copolymerization of through the addition of

non-reactive side chains to monomers before polymerization can also lower it.

In the last decade attention has been paid to evaluate the possibility of using thermo- plastic matrices in place of the thermoset ones. The former has many advantages compared to thermosets: high tenacity, recyclability, no necessity of refrigerated transport and almost notempera limits of storage. In most cases thermoplastics cannot be used due to excessive relaxation phenomena caused by a wet-Tg too close to the maximum working temperatures. For this reason, only amorphous polymers with a very high Tg can be possibly used for aerospace and aeronautical applications. Examples are PEI and PES, or semi-crystalline polymers with a very high melting temperature, like PPS, PEEK and PEKK. Currently the used of PEEK and PEKK matrices is limited due to the high cost of both the raw materials and manufacturing process. The materialshigh melting temperature and viscosity make fibers impregnation very difficult. A good way toreduce each cost consists of blending a semi-crystalline thermoplastic, like PEEK, with a less expensive amorphous one, as PEI, with the aim of reducing viscosity of the fuse and increasingits Tg. Rosa, Grassiand D Amore tested the tensile response of PEEK-PEI blends at differentratio compositions ranging from PEI concentrations of 10% to 90%.

Poly ether ether ketone (PEEK) is a semi crystalline, high temperature (up to 260 C) engineering thermoplastic that is excellent for applications where thermal, chemical, and combustion properties are critical top performance. This material is though, strong, and rigid and has superior creep resistance. It is also resist radiation and a wide range of solvents. has attractive properties like good abrasion resistance, low flammability and highly resistant to thermal degradation. The glass temperature is 143 C and a melting point of 343 C with density of 1320 Kg/m3, a Young module (E) of 3.6 GPa and a tensile strength of 100 MPa. PEEK polymers are synthetized by a step-growth polymerization by the dialkylation of bisphenol ate salts. Typical reactions of 4,4 - difluoribenzophenone with the disodium alt of hydroquinone, which generated in situ by deprotonation with sodium carbonate. The reaction is conducted around 300r in polar solvents such as diphenyl sulphone.

Lockwood presented the viscoelastic behavior of PEEK composite in an attempt to bridge the gap between the mechanical properties and the viscoelastic characteristics of PEEK matrix fiber reinforced composites. He developed a simple flexure model with viscoelastic parameters substituted for elastic material constants under assumed quasi-static conditions. Theexperimental frequency-temperature shift factors were obtained under low strain in a dynastat dynamic viscoelastic analyzer and compared to shift factors predicted from the Williams-Landel-Ferry equation. Damore, Pompo and Netti also studied the viscoelastic properties of amorphousand recrystallize PEEK and of a PEEK-based composite (APC2) as a function of the aging timeand related free volume relaxation at temperatures close to the glass transition region.

We have explore the use of thermoplastics as the composite matrix and its possible use in AM for space applications. There are two major advantages of thermoplastic composites. The first is that many thermoplastic resins have an increased impact resistance of comparable thermoset composites. In some instances, the difference is as high as 10 times the impact resistance, making it ideal for outer surfaces subjected to micro debris and small meteorites impacts. Secondly is their ability to reform. This allows thermoplastic composites to be reformed, reshaped and recycle at the end of its useful life. However, there are disadvantages and challenges with the use of thermoplastics as matrix material. Because thermoplastic resin is naturally in a solid-state, it is much more difficult to impersonate reinforcing fiber. The resin must be heated to the melting point, and pressure is required to impregnate fibers, and the composite must then be cooled under this pressure. This is complex and far different from traditional thermoset composite manufacturing.

Thermoset polymers are polymers that are cured into a solid form and cannot be returned to their original uncured form. In its uncured form, the material has very small, unlinked molecules (known as monomers). The addition of a second material (catalyst) and/or heat or some other activating influence will initiate the chemical reaction. During this reaction, the molecules cross-link and form significantly longer molecular chains, causing the material to solidify. This

change is permanent and irreversible. Composites made with thermoset matrices are strong and have very good fatigue strength. They are extremely brittle and have low impact-toughness. They are commonly used for high-heat applications because the thermoset matric does not melt like thermoplastics. Thermoset composites are generally cheaper and easier to produce because the liquid resin is very easy to work with. Thermoset composites are very difficult to recycle because the thermoset cannot be remolded or reshaped.

Modified B-staged epoxy resin has been recently used for space applications. B-staged epoxy resin is a descriptive term used to define a one component epoxy system, using a latent (low reactivity) curing agent. This unique product can be partially cured (sometimes referred to as pre-dried), as an initial stage after being applied onto one substrate/surface It can be later be completely cured under heat and pressure. They can be cured at temperatures ranging from 250-350 C and higher. Some salient properties of these systems are; excellent toughness coupled with great resilience properties. Excellent resistance to high temperature and thermal cycling/shock, and good electrical insulation properties with high dielectric strength.

Chapter 1, in part, is a reprint of the materials as they appear, titled "Design and Manufacture of Optimized Continuous Composite Fiber Filament Using Additive Manufacturing Systems." in Journal of Material Science and Engineering. And title "Optimization of Varying Orientation of Continuous Fiber Direction and Its Applications to New Methods of Additive Manufacturing." in Research and Development in Material Science. De Vivo, Luca, the dissertation author was the primary investigator and author of this material.

Chapter 2

Introduction: Towards Design of a 3D Printable Prandtl Box-Wing Unmanned Aerial Vehicle

2.1 Abstract

This paper explores the design of a 3D printable Prandtl Box-Wing UAV suitable for long-endurance solar powered flight. Long-endurance UAVs, enabling extended imaging campaigns and beyond-horizon communication in support of remote exploration, environmental assessment, disaster and post-disaster reconnaissance and assistance, hold great promise for data-driven decision making. Yet, they also create a range of unique challenges for the vehicle design, propulsion system and power source, navigation and guidance, and payload package. The presented UAV design is a joined box-wing monocoque, a biplane with oppositely swept wings, with wing tips interconnected by winglets, offering a range of structural and aerodynamic design optimization opportunities, aimed at providing a balance between, flight performance, efficiency, flutter resistance, and adequate surface area for solar power generation, with a wingspan

allowing for easy field deployment. The wing and its payload-oriented fuselage are the result of aerodynamic, topology, and structural optimization, focused on enhancing structural resilience and weight, hand-in-hand with efficiency and sustainability of the resulting airframe. The aerodynamics of the wing were analyzed using high fidelity Computer Fluid Dynamic (CFD) with the goal of optimizing the Lift/Drag ratio of the wing, winglet and fuselage. In addition, we performed high fidelity Finite Element Method (FEM) analysis on spars, ribs, skins, the box wing and the assembly of all the structural components. This allowed us to optimize material allocation in order to reduce weight and maximize the flight time of the vehicle. Mechanical and electrical components were chosen to optimize vehicle autonomy and automatically placedby an optimization algorithm aimed at properly placing all components inside the fuselage envelope, while maintaining the center of gravity target where desired, allowing for tasks specific optimization functions for the overall system. Using a combination of additive and composite manufacturing, the UAV can be entirely built using thermoplastics and fiber reinforced polymer.

2.1.1 Designing next-gen UAVs

Improvements in the field of structural & fluid analysis together with new micro electro-mechanical systems, materials, and manufacturing processes are providing aerospace engineers the necessary tools to design lightweight unmanned aerial systems (UASs) with greater endurance and versatility. The main focus of this project is to design, model, simulate, optimize, 3D print and assemble a solar powered UAV with the following characteristics:

1. Develop box winged glider for increased glide ratio and overall efficiency (Figure 2.1).
2. Achieve high glide ratio by optimizing structure and aerodynamics using a virtual wind tunnel.
3. Achieve long range missions by storing electrical energy produced by high efficiency solar photovoltaic cells.

4. Implement state of the art electronics and control algorithms for robust missions.

5. Optimize structure and mechanical components using topology optimization methods.

6. Modular, portable, and accessible as a virtual shipment through 3D printing.

Our work mainly focused on the design, development, and manufacture of a new type of Aerial Unmanned Vehicle (AUV). We proposed a fixed wing device with long-range and vertical take-off and landing (VTOL) characteristics using a sustainable and efficient Prandtl Box-Wing design. This wing design in combination with improvements in the field of structural and aerodynamic analysis together with advances in microelectromechanical systems have allowed us to optimize and improve the range of the AUV by increasing the aerodynamic efficiency, structural weight, and power capabilities.

Figure 2.1: Prandtl Box Wing Glider.

A glider plane is a type of vehicle for which one can stay aloft for long periods of time with minimal need of a propulsive force. These airplanes count with a highly optimized aerodynamic design which allows them to obtain incredible lift to drag ratios. These airplanes are built with high aspect ratio wings allowing them to achieve better fuel economy, climb performance, and

glide ratio. One of the major design goals for our platform was to achieve the maximum lift to drag ratio of a box wing configuration using parametric design and computational fluid dynamics (CFD), where the goal was to iterate the design space and search for the parameters that lead to the maximum L/D ratio. Subsequently the structural members had to be optimized in order to reduce the total weight of the platform and further increase its performance. To achieve this, we analyzed the structural members, such as ribs and spars, using Finite Element Analysis (FEA) and the results were used to topology optimize them. The idea behind topology optimization is to allocate material only where is needed and remove it where is not. The topology optimization results were then further analyzed and used as a base for the development of the final structure taking into consideration safety factors and load uncertainties.

After determining the final shape, structure, and avionics of the AUV, we then calculated the solar power requirements and batteries needed to sustain perpetual flight. The algorithm takes as parameters the payload, size of the plane, and electronic component efficiencies to calculate the total power consumption, thus allowing us to select the solar cells area and batteries needed. Finally, using aerodynamic and parametric design tools, the position of payloads was optimized to allocate the center of gravity in an advantageous position for the box wing stability.

Once our platform skirt was finalized, the next step was to design the systems architecture and flight control algorithms for a VTOL fixed wing aircraft. We picked Beagle Bone Blue as an all-in-one Linux-based robotics computer. This fully open-source and actively supported platform allowed the easy design and implementation of a VTOL and efficient horizontal flight algorithm. The aircraft does not use any mechanical system to switch modes from VTOL to horizontal flight, rather it uses a combination of thrust forces to rotate the platform around its own center of gravity. Simplifying the mechanical design allowed for smooth transition and a more versatile UAV, while contributing to the overall goal of decreasing weight and components in order to increase performance.

The final step was to fabricate and assemble the UAV using additive manufacturing (AM)

and composite materials. The first prototype was fully 3D printed using a Fused Deposition Modeling (FMD) 3D Platform 400 series workbench. The material used for the plane model was PLA. Carbon fiber rods were used as for the main spars and thanks to the complex geometric capabilities of AM we were able to build a wing without using the conventional rib/spar method.

2.2 Background

2.2.1 The Dream of Flying forever:

For much of recorded history humans have been fascinated with various soaring birds and their ability to sustain flight for long periods of time with apparently minimal effort. Many land-based birds, including common crows, hawks, and buzzards exploit soaring through convective thermals. Other birds utilize ridges and other terrain features in conjunction with horizontal wind flow to extract energy as they transit through local steady-state updrafts in orographic lift. These so-called static soaring techniques require the birds to maintain nearly constant bank and pitch angles, where the rate of energy increase is based primarily on position and orientation within the flow field.

In contrast, dynamic soaring techniques exploit spatial and temporal variations in the flow field, where the participating birds fly a more complicated trajectory across the flow gradient in such a manner that total energy, comprised of altitude-based potential energy and airspeed-based kinetic energy, is increased. John Strutt (Lord Baron Rayleigh) was one of the earliest scientists to speculate on the possibility of there being sufficient energy harvesting potential in an atmospheric boundary layer shear gradient to allow perpetual flight through dynamic soaring cycles.

Birds and aircrafts can sustain long endurance flights using static and dynamic soaring techniques. However, there is a limitation with these approaches as they required the plane to be constantly adjusting its flight path so it can maximize the amount of energy harvested. In contrast, advances in the field of photovoltaic cells are allowing, if designed properly, solar powered UAVs

to achieve multiple day-night flight circles. [Koe18]

2.2.2 Defying Gravity: Perpetual Flight of the Future

Solar-electrically powered fixed-wing UAVs promise significant increased flight endurance over purely-electrically or even gas-powered aerial vehicles. A solar powered UAV uses excess solar energy gathered during the day to recharge its batteries. Given an appropriate design and suitable environmental conditions, the stored energy may even be enough to continuously keep the UAV airborne during the night and potentially subsequent day-night cycles. This so-called perpetual flight capabilities makes solar-powered UAVs great candidate for applications in which data needs to be collected or distributed either continuously or on a large scale. Large-scale disaster relief support missions, meteorological surveys in remote areas and continuous border or maritime patrol would benefit in particular from this multi-day continuous flight capability. [OMM+16]

Solar-powered flight is not a new concept, but dates back to the 1970s. A comprehensive historical overview is provided by [Bou84], [Not08], [NSE06]. One important facet of solar-powered flight is solar-powered High-Altitude Long-Endurance (HALE) operations. The groundwork in this area was laid by NASA ERAST program [CW96]. Recently, interest in employing similar large-scale (wingspan above 20m) solar-powered HALE UAVs as atmospheric satellites for telecommunications relay has peaked. Notable examples of this trend are Titan's Solara and Airbus's Zephyr, which have already demonstrated a continuous flight for 14 days, and are the first solar-powered HALE UAV to enter commercial operations.

In contrast, smaller scale solar-powered UAVs are mostly designed for Low-Altitude Long-Endurance (LALE) applications. Though faced with the more challenging meteorological phenomena of the lower atmosphere (clouds, rain, wind gust, thermals and especially low solar intensity), low altitude UAVs provide the advantages of higher resolution imaging with reduced cloud obstruction, lower complexity, cost and simplified handling. As a result, solar- powered LALE UAVs aiming to reach flight times up to 14 hours have been studied in academia

[MRGM+15] and industry (AeroVironment, 2013; Bye Aerospace, 2015). However, research targeting perpetual endurance in these small-scale robotic aircraft has been relatively sparse. Most research focuses on conceptual design studies without extensive flight experience e.g. [MSP13] and [MDP15]. Projects that have demonstrated perpetual flight are SoLong [Run19], which performed a continuous 48-hour flight using solar power while actively seeking out thermal updrafts, and SkySailor [Not08], which demonstrated a 27-hour solar powered continuous flight without the use of thermals. However, these UAVs were mainly developed to demonstrate the feasibility of perpetual flight for the first time and do neither provide sufficient robustness against deteriorated meteorological conditions nor the capability to fly perpetually with common sensing payloads. The current leader in solar powered UAV perpetual flight is a team of ETH Zurich Autonomous Systems Lab called Atlantik Solar who in 2015 achieved a new endurance world record of 81.5 hours (4 days and 3 nights) continuous flight with a platform weighing 6.8 kg and covering a range of 2338 km. [OMM+17]

2.2.3 The war on drag never ends:

In cruising flight, engine thrust is exactly equal and opposite to the drag, the combination of all aerodynamic forces that oppose its forward motion. The drag on an aircraft results from several phenomena creating resistance to the forward motion: the effect of the wing shape and of the lift distribution (induced drag), viscosity effects (friction, pressure, etc.), compressibility effects (for speeds close to that of sound). The goal is to reduce this drag allowing designs with lower fuel or energy consumption, increasing aircrafts functionality and becoming more economical for the operator. Drag reduction has motivated generations of researchers at many institutions globally (NASA, ONERA,). The simplest and most effective aircraft in the world are the best reward for their success. After the work carried out on the shape (elongation, winglets) and then on the surface condition (riblets, shark skin) that carried out today on the flow control (to prevent the flow from becoming turbulent, to deflect it, to prevent it from separating from the

wall, etc.) offers the most attractive perspectives.

2.2.4 Box wing and increased flying efficiency:

NASA's ERA Project Could Save Airlines Billions with new technologies that have the potential to cut costs, noise and emissions. NASA researchers, at its Environmentally Responsible Aviation (ERA) project, have produced technologies that could be a major game changer for the airlines and other heavy jet operators. The agency claims the new technologies could cut airline fuel consumption in half, reduce pollution by 75 percent and drop noise pollution to nearly one-eighth of today's levels. The ERA researchers came up with eight technology demonstrations, some of which were tested on Boeing's ecoDemonstrator 757 flying laboratories. These included modifications that would allow significant weight reductions in the construction of heavy airframes, a morphing wing technology to reduce drag, several changes to improve engine efficiency, modifications in flap and landing gear deployment, and new wing and engine mounting techniques. NASA invested $400 million into the six-year-long project in addition to $250 million worth of resources invested into the project by industry partners.

As seen above, new wing designs, are one of the main technologies that are driving improvements in aviation efficiencies. NASA and partners such as defense giant Lockheed Martin have been revisiting a wing model that dates back to the early 1900s. The Boxed Wing system which they claim reduces drag and improve efficiency at subsonic flights. Lets take a look first at the evolution of the box wing design.

1906: Bleriot III - First Box Wing ever built

In a 1924 NACA report, Ludwig Prandtl reasoned that a biplane joined by end plates corresponds to a solution of minimum induced drag for a fixed lift, span, and vertical extent. He called this solution the Best Wing System. In the same report, Prandtl also gave an approximate procedure with which to estimate the span efficiency of such box wing systems. For example, for a height-to-span ratio of 0.3, an optimally-loaded box wing should only generate 60% of the

Figure 2.2: Different Non-planar Wing Designs. Box-Wings are a Member of the Closed Non-Planar Wing Family.

induced drag of a monoplane of the same span and lift. [Pra24]

One of the first attempts to adapt the box-wing design to a transonic transport was initiated at Lockheed in the early 1970s, first by Mirand [Mir72], then by Lange [LCB+74]. While Miranda successfully retrieved the expected induced drag savings predicted by linear theory, the ensuing feasibility study of Lange on a Mach 0.95 boxplane uncovered a series of unforeseen problems. Among these was the appearance of both symmetric and asymmetric instabilities well below the target flutter speed and concluded that no ramp weight reduction over a conventional baseline could be achieved and that the boxplane might only be advantageous at lower Mach numbers (for which case the flutter speed requirement would not be as stringent). [GZ16].

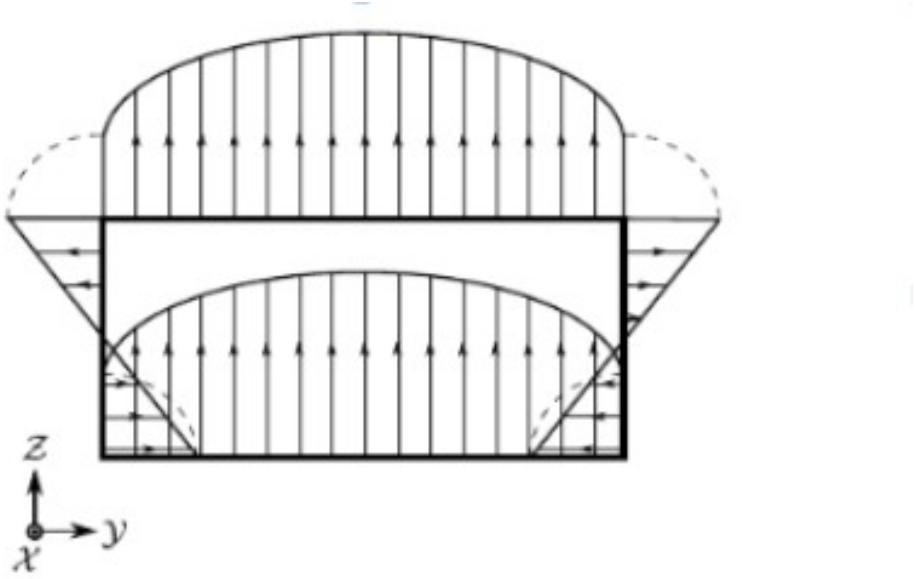

Figure 2.3: Prandlt Span-Wise Optimal Lift Distribution for a Box Wing.

NASA's ERA Project Could Save Airlines Billions with new technologies that have the potential to cut costs, noise and emissions. NASA researchers, at its Environmentally Responsible Aviation (ERA) project, have produced technologies that could be a major game changer for the airlines and other heavy jet operators. The agency claims the new technologies could cut airline fuel consumption in half, reduce pollution by 75 percent and drop noise pollution to nearly one-eighth of today's levels. The ERA researchers came up with eight technology demonstrations, some of which were tested on Boeing's ecoDemonstrator 757 flying laboratory. These included modifications that would allow significant weight reductions in the construction of heavy airframes, a morphing wing technology to reduce drag, several changes to improve engine efficiency, modifications in flap and landing gear deployment, and new wing and engine mounting techniques. NASA invested $400 million into the six-year-long project in addition to $250 million worth of resources invested into the project by industry partners.

2013: IDINTOS - First Personal BoxWing Prototype

2016 - NASA - VTOL AEROSPACE First VTOL Capable Box Wing

2018: Project PARSIFAL - Prandtl plane Architecture

Many attempts have been made to optimize the aerodynamic efficiency of the box wing configuration. [GZ16], [Cav14]. However there has been no attempts to design, optimize, and prototype a box wing for a LALE UAV platform. In this work, we focus on the design optimization rather than numerical optimization but paying close attention to what literature advises such as optimal height to span ratio, lift distribution, and wing twist.

(a) 1906: Bleriot III - First Box Wing ever built.

(b) 2012: Lockheed Martin and NASA - 2025 PSC UltraFan.

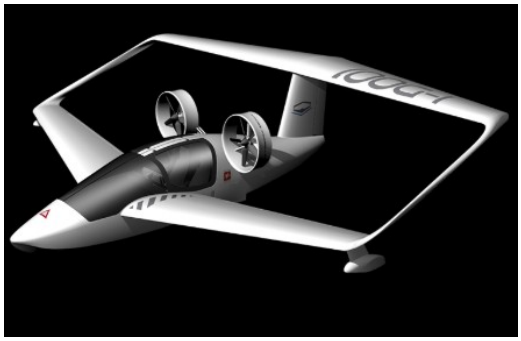

(c) 2013: IDINTOS - First Personal BoxWing Prototype.

(d) 2016: NASA - VTOL AEROSPACE First VTOL Capable Box Wing.

Figure 2.4: Historical Evolution of Box Wing Designs

2.3 Platform Design

2.3.1 Design Evolution

The Prandtl Box wing platform presented us with an opportunity to redesign every aspect of a flying vehicle. The design process took into account the overall platform specifications, aerodynamics, structural, mechanical, electrical, controls, and system integration. Over the life of the project, we developed multiple aircraft designs, see (Figure: 2.5) and (Figure: 2.6), that made use of the box wing aerodynamic, structural, and functional benefits. Three potentially working prototypes were fully designed: a single engine box wing glider (Figure: 2.1), a VTOL multi engine flying box wing, and a monocoque multi engine VTOL aircraft (Figure: 2.7). We focused on the latest, because it proved to be the most functional while maintaining excellent flight efficiency. in Chapter 2, where we discuss digital Structural and Aerodynamic simulation techniques, we will dive deeper into the analytical results that guided us through the decision making process and lead us to our final design.

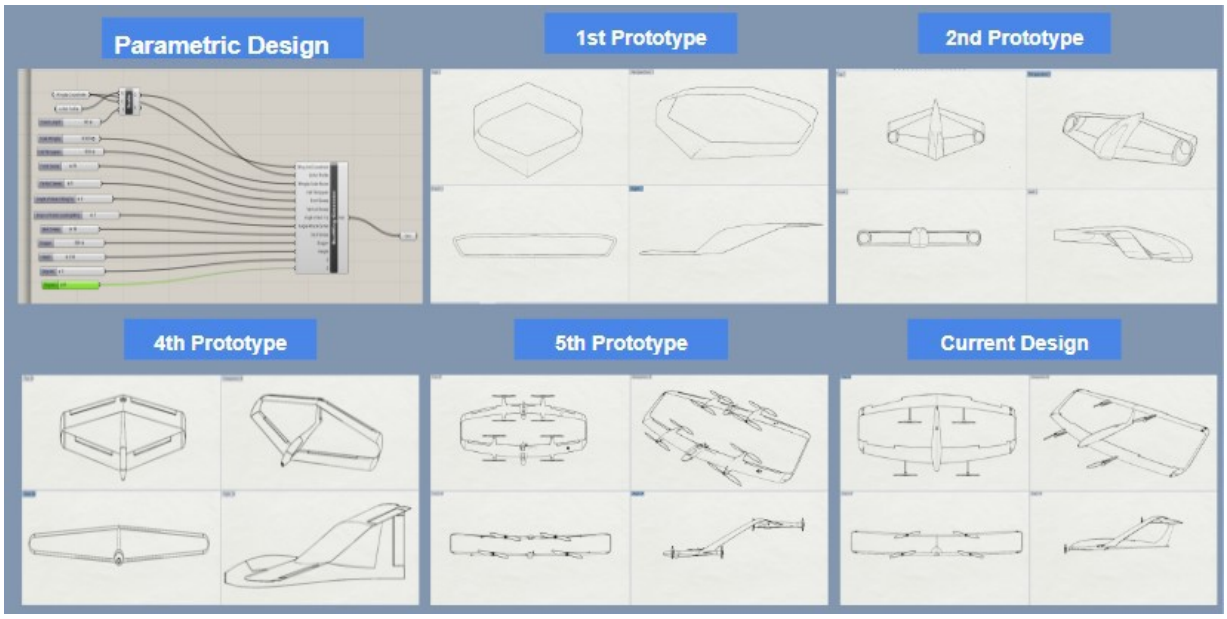

Figure 2.5: Design Evolution of the Prandtl Box Wing UAV.

(a) Box Wing Paper Model

(b) Box Wing Balsa Wood Model

(c) Box Wing 3D Printed Model

(d) Box Wing 3D Printed Full Scale

Figure 2.6: Models of Box Wing Designs.

2.3.2 Final Design

The LALE UAV was designed for extended imaging campaigns and beyond-horizon communication in support of remote exploration, environmental assessment, disaster, post-disaster reconnaissance, and assistance. The aircraft has a Canard Prandtl Box Wing design, with each wing having a two-meter wingspan and a total lifting area of (0.36 m^2). It was designed for a maximum takeoff weight (MTOW) of 6 kg, to cruise at 24 m/s and with the capability of vertical takeoff and landing (VTOL). The current version uses 4 U5 KV400 brushless DC electric motors, a 4-in-1 ESC module built into the control stack, and 16 X 5.4 carbon fiber propellers for its propulsion system. The motors are distributed evenly and symmetrically over

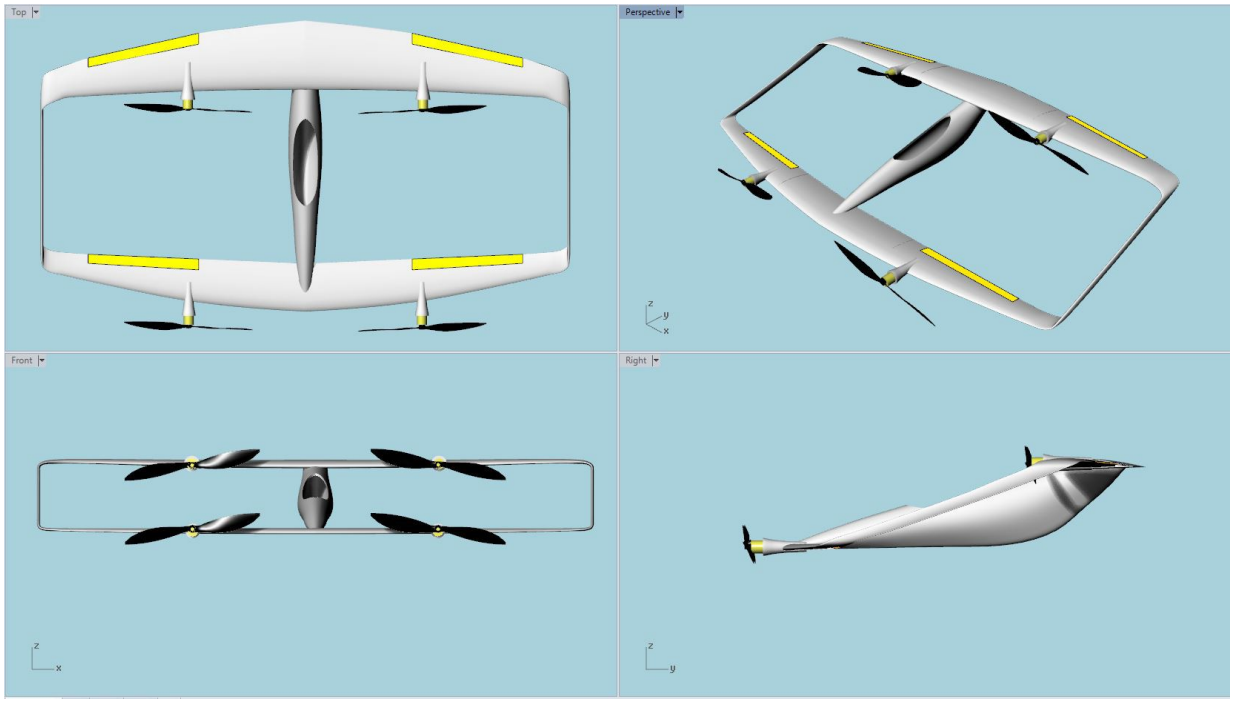

Figure 2.7: VTOL Enabled Prandtl Box Wing UAV (Views)

the two wings. Placing two on the front and two on the back allows for the design of an efficient VTOL capability. If a greater carrying capacity and added robustness was desired we could add 4 extra motors and distribute these in the same manner. As a UAV designed for long surveys we wanted it to fly multiple sensors simultaneously. We designed the fuselage so it confined all the avionics, communication, electronics, and mechanical systems together with two different bays for payloads, one aft, and one stern both facing downward and mounted on gimbals. We are also considering adding an extra camera on top of the fuselage facing forward and slightly upward. This will allow the aircraft and the remote pilot to visualize what is in front during Beyong Visual Line of Sight (BVLOS) deployments. Having the ability of VTOL, or hover, will also enable the platform to complete surveys of complex environments and targets such as bridges, dams, and other large-complex structures. We recognize we are not the optimal design for such missions, as this aircraft was intended for long raster surveys rather than precision infrastructure surveys. The endurance of the non solar aircraft was designed to be 1 hr at cruise flight at 20 min hover time.

Table 2.1: UAV Prandtl Box Wing General Info Table

Parameter	**Fore Wing**	**Aft Wing**
Type of Aircraft	Prandtl Best Wing Solar UAV	
Purpose	Long Endurance Survey	
Wingspan	1.3 m	1.3 m
Half Wing Area	0.13 m^2 (40%)	0.19 m^2 (60%)
Aspect Ratio	13.0	9.0
Root Chord Length	0.12 m	0.18 m
Tip Chord Length	0.06 m	0.09 m
Sweep Angle	3◦ backward	3◦ forward
Dihedral Angle	2◦ up	2◦ down
Stagger	Stagger, X: 0.60 m & Height, Z: 0.18 m	
Total Wing Area	0.32 m^2	
Maximum Takeoff Weight	6.0 kg	
Cruise Speed	24.5 m/s	
Cruise Altitude	120 meters	
Number of Motors	4 motors	
Max Thrust Required for VTOL (per motor)	2850 grams	
Thrust Required for HFly (per motor)	150 grams	
Payload Bays	2	
Endurance	Experimental Need	

We expect improvements in batteries and propulsion systems in the next few years which will allow us to increase the endurance without changing the dimensions of the platform.

We are still working on the the solar design, but we aim to design a multi-day fliying platform. Its endurance will vary greatly with weather, specially with sun irradiance conditions,

2.3.3 Theory and Conceptual Design of a Canard Box Wing UAV

1. Stall: Canard wing (front) stalls first. Back wing never approaches critical angle of attack.

2. Stability: Canard wing has higher wing loading than back wing. Canard wing generates

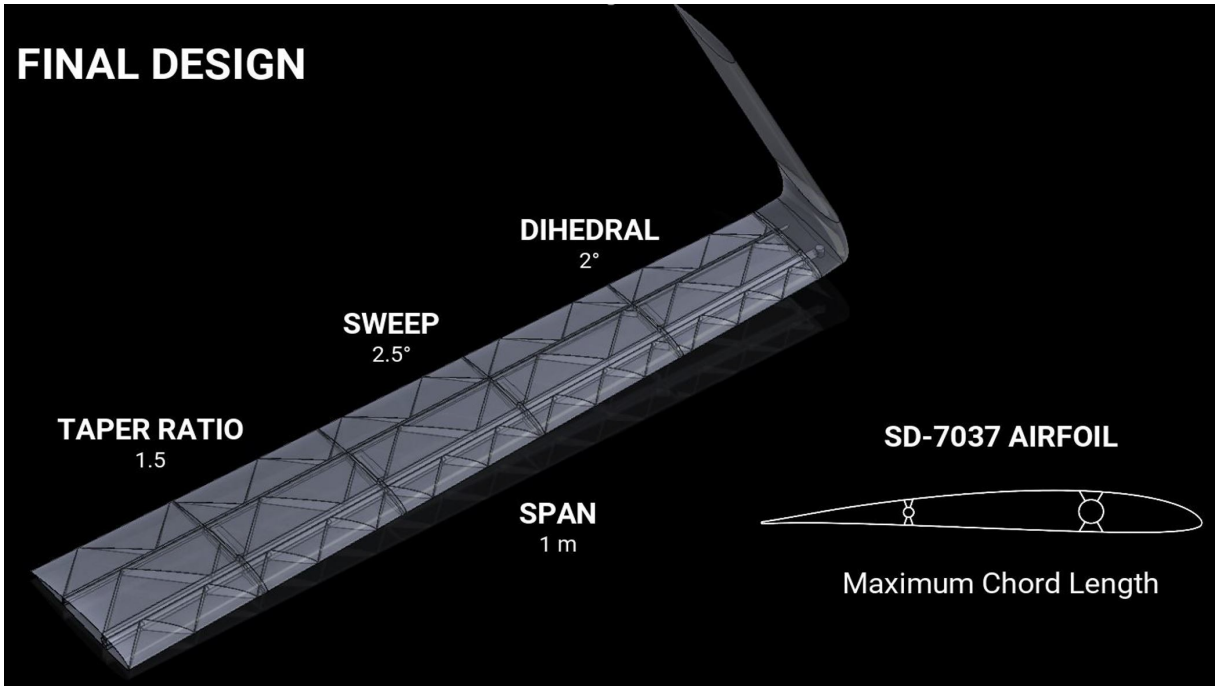

Figure 2.8: Box Wing Specs (Views)

more lift per meter square. Need a vertical stabilizer which was to be set back from center of gravity of plane. For the box wing to fly stable it is also important to place the X_{cg} ahead of neutral point X_{np}.

3. Performance: High aspect ratio canard.

4. Box Wing Optimization Opportunities: Goal is to design a box wing with maximum (L/D) ratio, Prandtl Equation: Height-to-Span Ratio Optimization.

$$1/e = (1 + 0.45 * (\frac{h}{b})/(1.04 + 2.81 * (\frac{h}{b})$$

Where:

e = Wing Efficiency

h = Vertical Wings Separation

b = Wingspan

5. Optimal Lift Distribution: Elliptical lift distribution is equal in both wings (L1 = L2) and butterfly-shaped side force on the winglets.

Chapter 2, in part, is a reprint of the material as it appears, titled "Towards Design of a 3D Printable Prandtl Box-Wing Unmanned Aerial Vehicle" IEEE Aerospace 2019. De Vivo, Luca; Tran, Danny; Kuester, Falko. The dissertation author was the primary investigator and author of this material.

Chapter 3

Digital Design and Analytic Tools for UAV Optimization

3.1 Digital Design and Analytic Tools for UAV Optimization

3.1.1 The Iterative Design Approach

The final design was achieved thanks to a combination of design principles and analytical feedback tools. We iterated over the design space using the following strategy: team brainstorming, preliminary sketches, computer aided design (CAD), Computer Fluid Dynamic (CFD) and Finite Element Analysis (FEA). It is important to notice that this should not be consider a close loop system as we can jump from step to step in a non-order manner like the one shown in (Figure: 3.1.). At the same time is is worth noticing that in order to achieve a final successful design each step should be satisfied. Parametric CAD tools were implemented to speed the design process with the capability of generating hundreds of different designs (Wings, Winglets and Fuselages) in seconds. The analytical tools were used to optimized, guide and aid the designer to make experimental and numerical driven decisions. Additive Manufacturing tools allowed us to generate scaled down and full-size prototypes and molds directly from the computer with

minimum prior manufacturing experience, man labor and at a relatively accessible cost. The final step was to design, select and assemble the robotic architecture (control board, communications, navigation, propulsion and power systems, and payload instruments), followed by the design of the control algorithm to give our fix wing aircraft the Vertical Take Off and Landing capabilities utilizing a thrust differential approach.

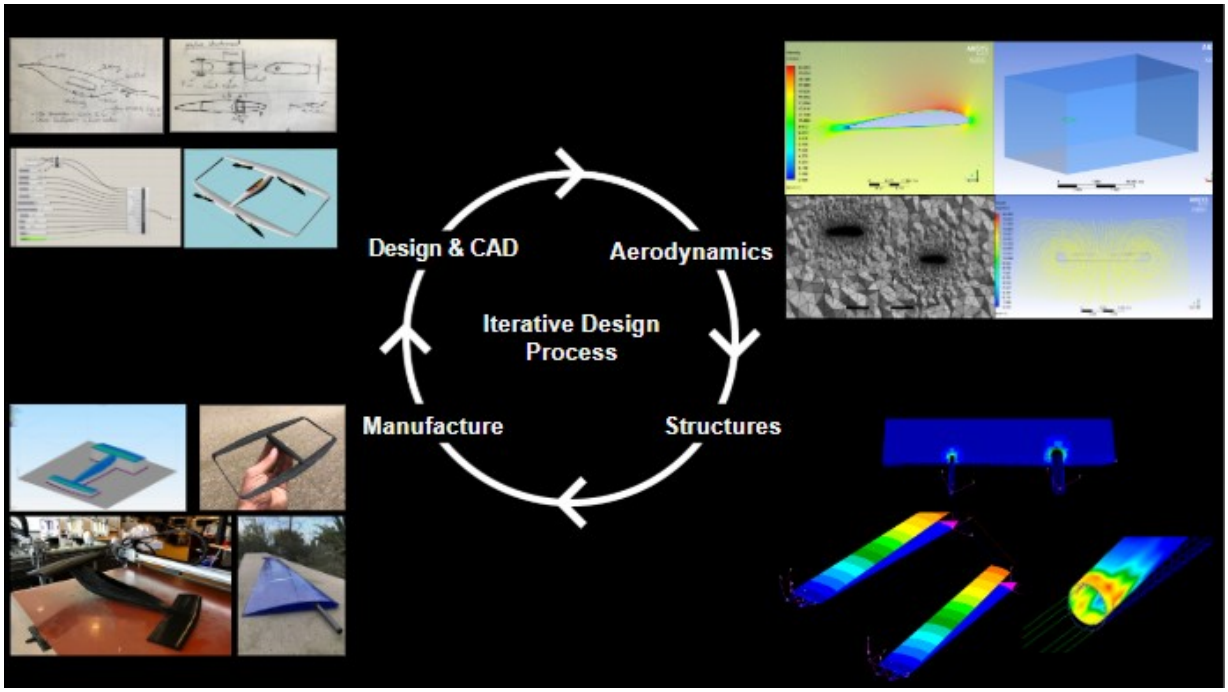

Figure 3.1: Iterative Computer Analysis Aided Design.

3.1.2 Computer Aided Design

60 years ago, the Father of CAD, Dr. Patrick Hanratty created the first numerical control system, which would later become Computer Aided Design or CAD. The precision, versatility, and edit-ability of CAD designs revolutionized the engineering, architecture and manufacturing landscape. The importance of CAD cannot be understated. A detailed infographic of the history of CAD can be seen in figure 3.2.

While the History of CAD closely parallels the history of the computer, there have been

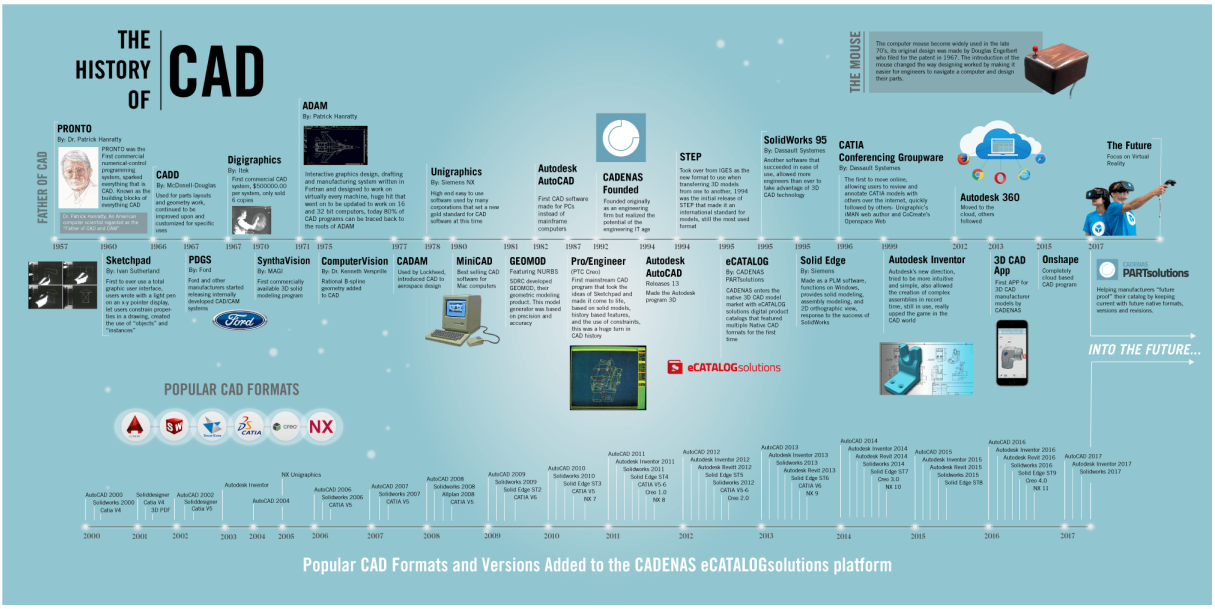

Figure 3.2: The History of CAD.

many innovations and iterations along the way. With its introduction in 1957, it was still decades ahead of small and affordable computers which could run the software. Pencil and paper would remain the primary way draftsman would create designs for another 30 years. But the groundwork was laid for things to come, CAD software would a fundamental tool for nearly every industry.

The idea of CAD has grown from simple 2D designs into complex, multi-layered 3D structures with kinematic-movement and detailed meta-data. 3D wireframe features were developed in the beginning of the sixties, and in 1969 MAGI released Syntha Vision, the first commercially available solid modeler program. Solid modeling further enhanced the 3D capabilities of CAD systems. NURBS, mathematical representation of freeform surfaces, appeared in 1989, first on Silicon Graphics workstations. In 1993 CAS Berlin developed an interactive NURBS modeler for PCs, called NoRBS.

In 1989 T-FLEX and later Pro/ENGINEER introduced CADs based on parametric engines. Parametric modeling means that the model is defined by parameters. A change of dimension values in one place also changes other dimensions to preserve relation of all elements in the

design. MCAD systems introduced the concept of constraints that enable you to define relations between parts in assembly. Designers started to use a bottom-up approach when parts are created first and then assembled together. Modeling is more intuitive, precise and later analysis, especially kinematics easier.

CAD/CAE/CAM systems are now widely accepted and used throughout the industry. These systems moved from costly workstations based mainly on UNIX to off-the-shelf PCs. 3D modeling has become a norm, and it can be found even in applications for the wider public, like 3D buildings modeling, or mechanical and structural design. Advanced analysis methods like FEM (Finite Element Method as for structural analysis), flow simulations like CFD (Computer Fluid Dynamics) are a ubiquitous part of the design process. CAM systems are used for simulation and optimization of manufacturing, and NC code is created and loaded to NC machines.

The past of CAD has been full of unmet expectations; this continues. Some anticipate 3D modelling without flat screens or mouse pointers, a fully immersing 3D environment where modelling tools include special gloves and goggles. In the future, designing will be closer to sculpting than painting.

3.1.3 Finite Element Model:

An analysis of complex structures and other systems in a matrix formulation is now unthinkable without the finite element method. Our personal belief is that the origins of such a rich and applicable method cannot be attributed solely to one person or school of thought but rather to a synergy of various scientific developments at various research establishments. The notion of geometrical division can be traced back to the Greek natural philosopher Archimedes who in order to compute the area of a complex shape divided it into triangles and quadrilaterals whose area could be easily computed; the assembly of the individual areas provided the total area of the complex shape. More recently, Courant used variational and minimization arguments for the solution of physical problems. Courant [5], and Prager and Synge [6] had both proposed the

concept of regional discretization which is essentially equivalent to the assumption of constant strain fields within the elements. The adaptation, however, and development of these concepts for structural analysis and other physical and technical problems was not conceptually achieved until during and shortly after World War II.

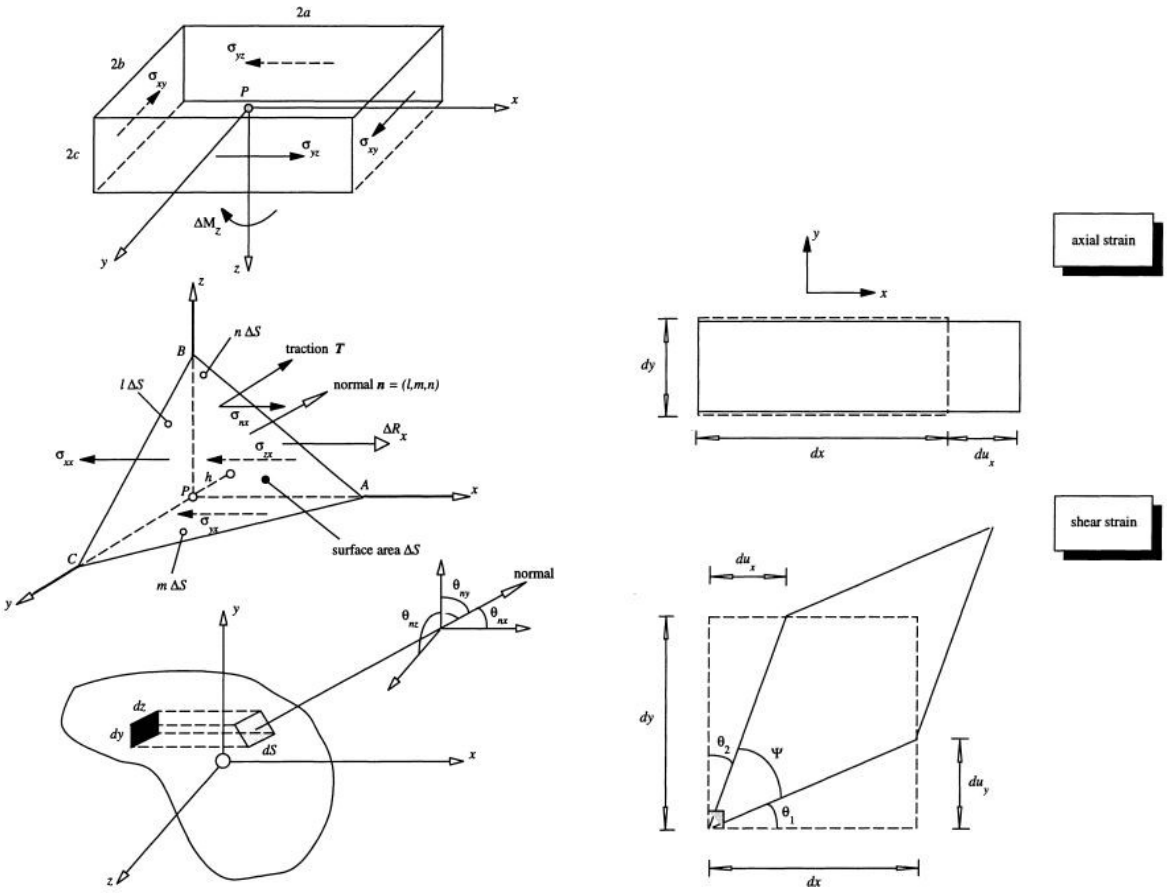

(a) Formulation of Surface and Volume Forces on rectangular and tetrahedrons elements for the calculation of resultant stresses

(b) Axial and Shearing Strain Formulation

Figure 3.3: Basics of FEA stress and strain formulations

The FEM has been in existence for more than 50 years. One of the authors, John Argyris, invented this technique in World War II in the course of the check on the analysis of the swept back wing of the twin engine Meteor Jet Fighter. In this work, he also consistently applied matrix calculus and introduced triangular membrane elements in conjunction with two new definitions of

triangular stresses and strains which are now known as the component and total measures. In fact, he was responsible for the original formulation of the matrix force and displacement methods, the forerunners of the FEM 3.3.

In 1962 a new approach in the context of the matrix displacement method was initiated by Argyris and Scharpf [14], [15]. Experimentation with problems involving large displacements, strains and inelastic behavior led to the basic concepts of geometrical stiffness and the idea of natural modes. These natural modes essentially represented invariant fields, including both rigid body and pure straining measures, that were used to describe the elemental kinematics. Since then this fundamental idea has evolved significantly, and has facilitated the computer simulation of large and complex structures in the linear and nonlinear regimes. In addition, it has provided an insight into the fundamental behavior of structures undergoing small and large displacements. It is now possible to create finite elements based on rigid body and straining modes of deformation. The technique is particularly suited to the creation of simple truss, beam, plate and shell triangular elements, and tetrahedron volume elements for large scale and fast engineering computations.

3.1.4 Computer Fluid Dynamics:

Engineers are increasingly reliant on computational fluid dynamics (CFD) for the design, analysis, and optimization of aerospace vehicles. Confidence in industry has been gradually building in the ability of the Reynolds-averaged Navier Stokes (RANS) equations as well as simpler coupled Integral Boundary Layer (IBL) methods to adequately predict the design trends and flow fields of aerospace vehicles with attached flow. Much of this confidence comes asa result of increased computer power and the consequent ability to more faithfully model the complex geometries used in the experiments or flight tests.

On the other hand, both numerical errors and lack of geometric fidelity may result in inadequate or inconsistent CFD results. It is difficult to ensure adequate grid resolution for 3-D complex geometries, and it is easy to overlook or ignore potential geometric inconsistencies and

aeroelastic effects. Also, it is rarely cost-effective to fully resolve all aspects of a flow field in a computation. For example, side-wall boundary layers and slotted wall effects in wind tunnels are usually modeled approximately in some way, and undoubtedly introduce some errors. These errors may manifest themselves for any flow field but become particularly important when the dynamics of the flow are very sensitive to small changes in flow field properties or geometry. Some possible reasons for inconsistent CFD predictions of complex aerodynamic lifting surfaces are: (1) unsteady effects, (2) inadequacy of turbulence models, and (3) numerical errors and lack of geometric or modeling fidelity. Based on the results of the past reviews, it appears that number (3) probably plays the most dominant role at this point in time.

3.2 Parametric Design

For the rapid evaluation and optimization of the box wing system we developed a series of parametric design tools in the CAD environment using Rhinoceros 3D and Grasshopper. An overview of the design evolution that was achieved thanks to this rapid parametric CAD tool was seen in (Figure 2.5). We developed a parametric design tool showed in (Figure: 3.4) that allowed us to produce hundreds of wing configuration by varying values of: wing span, chord lengthsat different sections, dihedral and sweep angles, stagger, and height of wings relative to each other. The tool was built using a combination of geometric translation equations that allowed us to allocate the wing section coordinates points and produce preliminary line based design of the box wing. An example of the the wing model generated in this CAD environment, (Figure: 3.5. These points and lines were then used to generate structured surfaces and solids that were exported into Computer Fluid Dynamic (CFD) and Finite Element Analysis (FEA) solvers. The ability to develop and design with parametric tools speeds up the design process dramatically and allows for aerodynamic, structural, architectural design optimization of complex shape systems such as wings, winglets, fuselages, and entire systems.

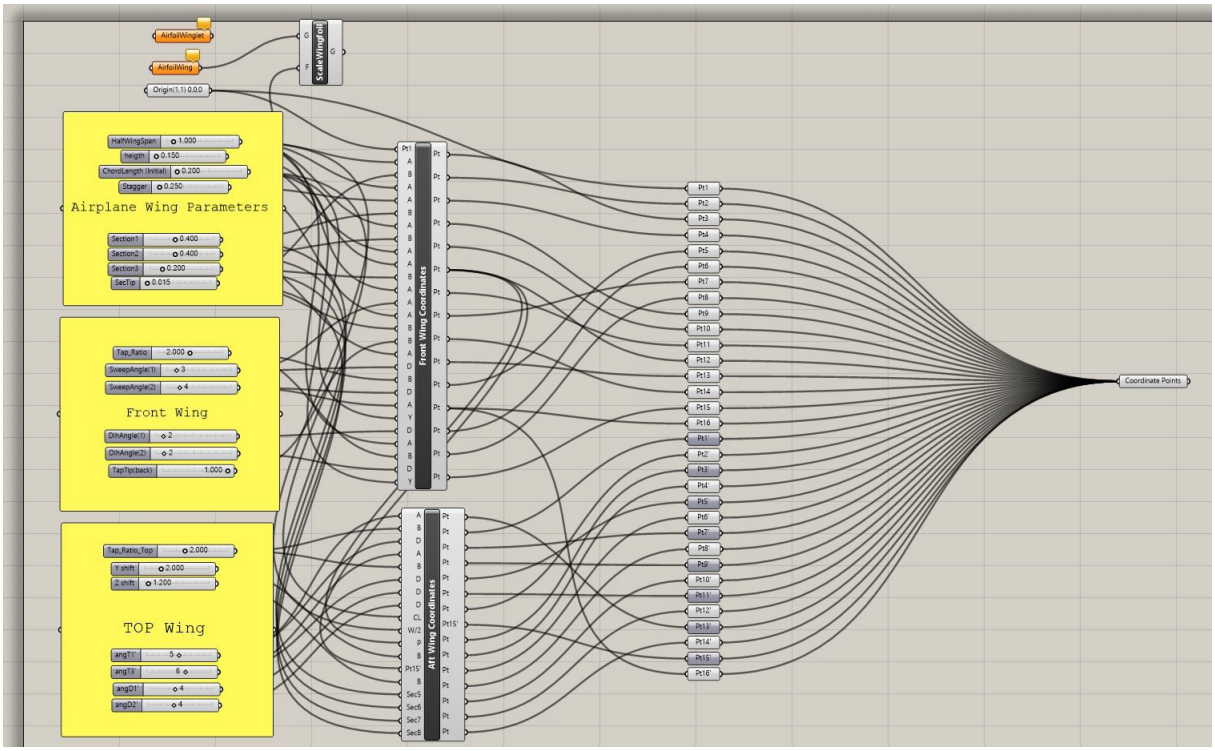

Figure 3.4: Grasshopper: Wing Parametric Design

The final wing geometry values can be seen in (Figures 2.7, 2.8, and Table 2.1), and are the following;

Front Wing: 1.3 meter wingspan, 120mm chord length at the root and 60mm at the tip, 2.5◦ backward sweep angle and 2◦ positive dihedral angle.

Back Wing: 1.3 meter wingspan, 180mm chord length at the root and 90mm at the tip, 2.◦ forward sweep angle and 2◦ negative dihedral angle.

Both wings used a Clark Y airfoil for its good performance flying at low speeds and low Reynolds Number (RE). In order to satisfy Optimal Box wing and Canard wing design a positive twist of 1 deg was added at the root of the front wing, and a negative twist of 1 deg was added at the root of the rear wing. This twisting of the wings guarantees that the critical angle of attack will always be reach first at the from wing causing it to stall first and pitch the nose of the airplane down avoiding instability and lost of control. In addition, the fore wing has a higher

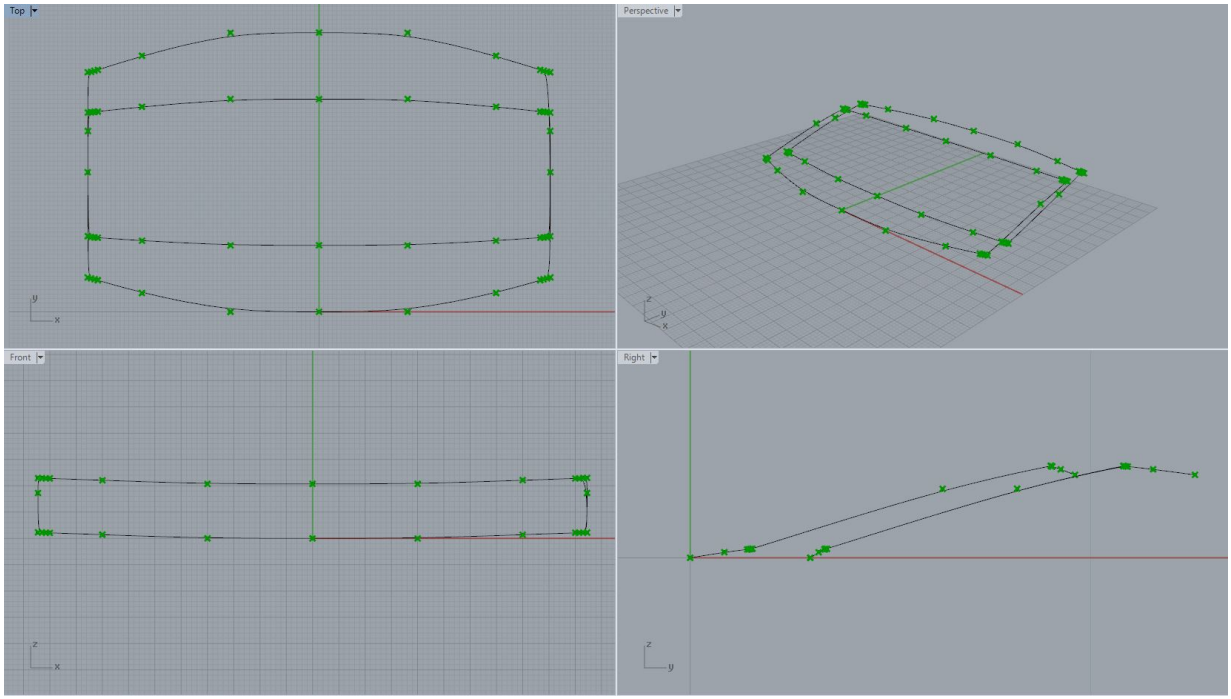

Figure 3.5: Rhinoceros 3D: CAD View of Wing

aspect ratio when compared to the aft wing. This is to also satisfy the condition of the canard wing having higher wing loading for stability and performance purposes. In order to ensure a stable wing design, numerical stability analysis were performed using an open source software called XFLR5, v6.35. We built a simplified version of the bi-wing system using the dimensions described above and checked for satisfactory curves on the eighth stability modes of a flying plane. This allowed us to understand and determine the center of gravity necessary for stable, efficient, and robust flight. This information was then used in conjunction to a simple algorithm to place all components of the airplane in an advantageous location, so the overall CG location matched the one obtained in our numerical analysis. The balanced aircraft will fly at 4 AoA at a speed of 24 m/s, thus achieving this maximum L/D ratio. We finally proved the efficiency of the wing system by running a high-fidelity Computer Fluid Dynamic analysis (CFD) using Fluent by ANSYS. In future work we plan to use the calculated pressure distribution on a Fluid-Structure Interaction (FSI) analysis carried also in ANSYS.

Mechanical and electrical components were chosen to optimize vehicle autonomy and automatically placed by an parametric optimization algorithm (Figure 3.6) aimed at properly placing all components inside the fuselage envelope, while maintaining the center of gravity target where desired, allowing for tasks specific optimization functions for the overall system. An example of the graphical interface and the result of the CG calculation and placement can be seen in (Figure: 3.6), where the Center of Gravity is displayed as a yellow sphere. This tool proved to be essential for fixing the location and the design of the internal fixtures for all the avionics and other components.

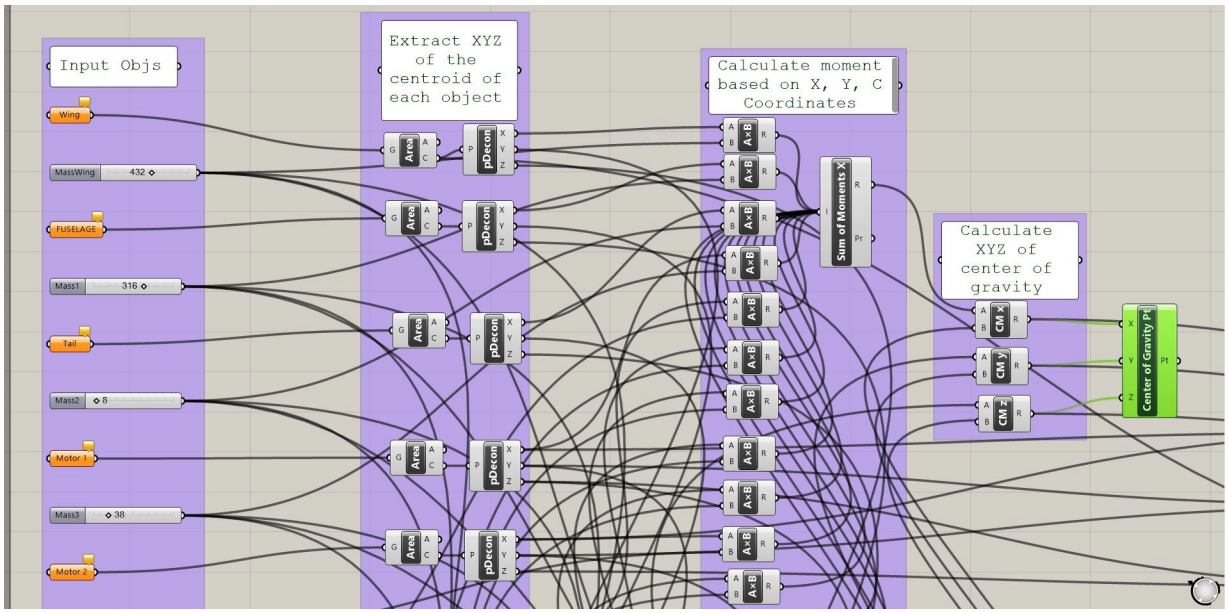

Figure 3.6: Grasshopper: Parametric Center of Gravity Optimization

3.3 Structural Analysis

3.3.1 Wing Load Calculations

Preliminary analysis was performed on MATLAB in order to quickly iterate through designs and quickly change variables. MATLAB codes were written to plot the operational

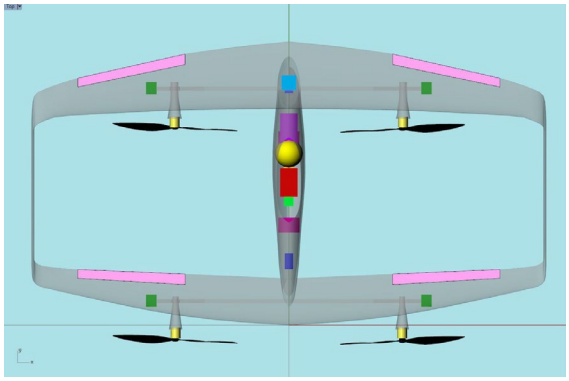

(a) Final Design Top View

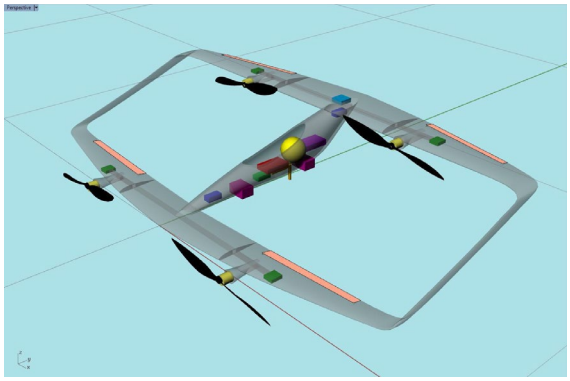

(b) Final Design Isometric View

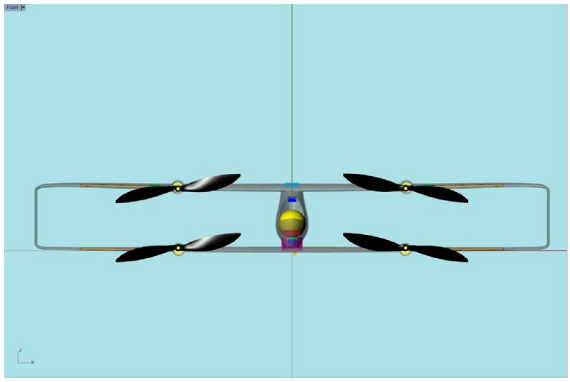

(c) Final Design Front View

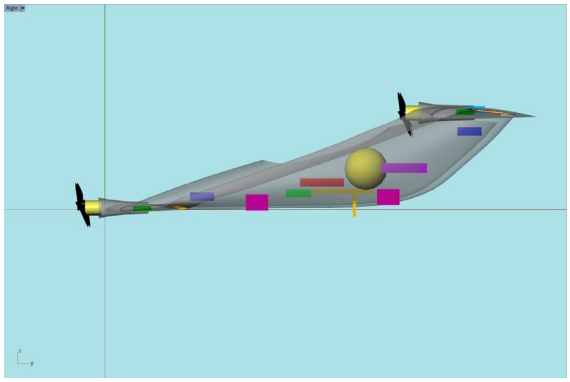

(d) Final Design Side View

Figure 3.7: Final Design and Component Placement for CG Stability

envelope (V-n diagram, Figure 3.8), calculate the angle of attack required at each load case to maintain lift-weight equilibrium, approximate the operational loads.

The V-n diagram is a plot of the aircraft's operational domain; velocities are along the x-axis and load factor (n) is along the y-axis. The load factor is a multiplicative factor applied to the weight of the aircraft and is a consequence of certain maneuvers (such as pull-up or pull-down) which causes additional acceleration. The V-n diagram defines important velocities such as the maximum speed, take-off speed, as well as the types of maneuvers the aircraft is capable of doing. The target air speeds (take-off speed, cruise speed, dive speed) were chosen by looking at a similarly sized UAV - the Decode 1. The load factors, which define the type of maneuvers the aircraft is capable of doing, were chosen based upon recommendations inside the Federal

Aviation Regulations (FAR), Part 23. These critical air speeds and load factors are summarized in (Figure 3.8) as well as in (Figure 3.9).

Table 3.1: Critical Air Speeds

Variable	Value
Take-Off Speed (with Flaps)	11.2 m/s
Take-Off Speed (without Flaps)	13.4 m/s
Cruise Speed	24.5 m/s
Dive Speed	29.1 m/s
Positive Load Factor	3.80
Negative Load Factor	-1.52

The critical load cases were identified by looking at the lift equation and the corners of the V-n diagram. The lift function used can be seen below:

$$L = n * W = \frac{1}{2} * \rho * V^2 * S * \frac{dC}{d} * (a - a0)$$

Where:

L = Total Lift

W = AUV Weight

V = UAV Speed

A = Wing Area

dC = Airfoil Drag Coefficient

dL = Airfoil Lift Coefficient

a = Angle of Attack

$a0$ = Zero Lift Angle of Attack

Drag is also present but is significantly lower in magnitude than lift. With that being said, the top right corner of the V-n diagram was identified to be the critical load case since it has the highest velocity and highest load factor. These two combined will create the largest lift

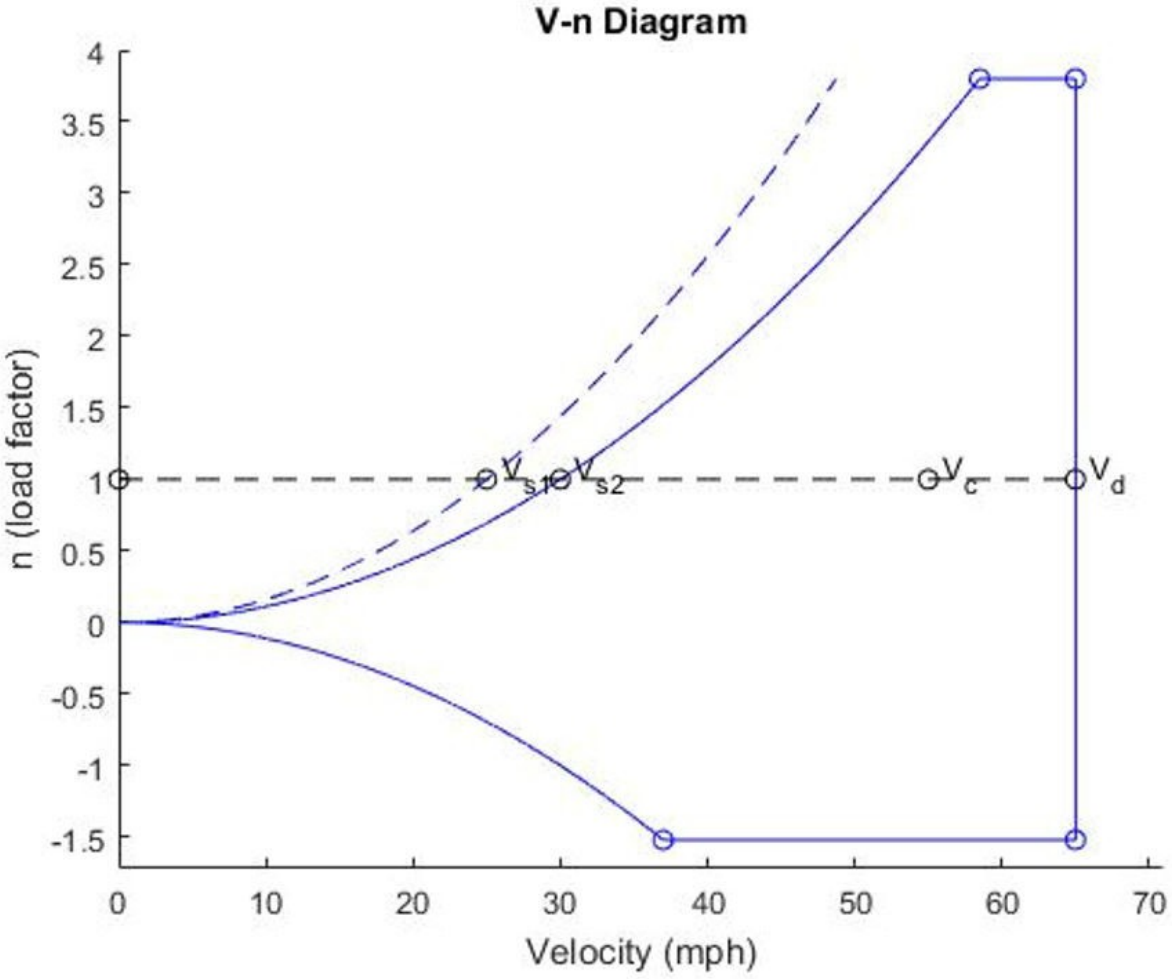

Figure 3.8: V-N Diagram (mph).

distribution of all the load cases. This corner is commonly called Positive Low Angle of Attack (PLAA) in aerospace applications.

The operational loads were approximated using a theory developed at NASA by O. Schrenk. It takes into account taper ratio and sweep angles but not winglets. For preliminary purposes, the team deemed this inaccuracy to be acceptable. The lift, drag, and aerodynamic moment distribution calculated per Schrenk's approximation are given in Figure 3.9.

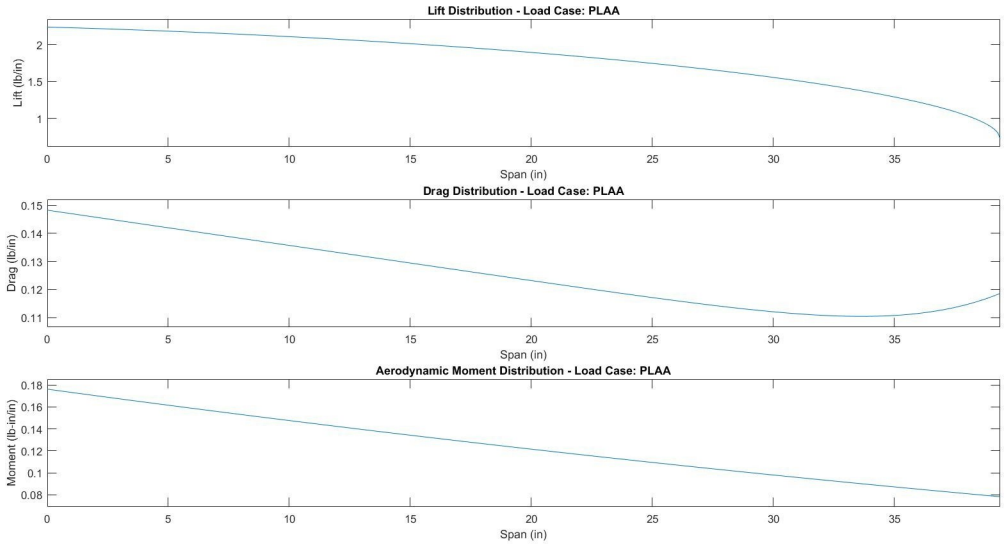

Figure 3.9: Preliminary Wing Load Distribution

3.3.2 Airfoil Aerodynamic Load Calculations

XFOIL has been well established to be accurate for a variety of flight conditions, particularly low Reynold's Number flow, such as the flow conditions the drone is designed for and is expected to experience. XFOIL shows excellent agreement with both experimental data and computational fluid dynamics simulations. Using the critical load condition, the airfoil was run through XFOIL in order to find the pressure coefficients across the airfoil. Because it is not possible to easily map the discrete data points from XFOIL to Patran, a pressure distribution function was approximated in Patran using a curve fitting toolbox to create a polynomial function with the shape and magnitude of the pressure distribution (Figure 3.10).

Assumptions:

1. Viscous (dynamic viscosity (μ = 1.8e-5 kg/(m*s))
2. Compressible (minor)
3. Isothermal

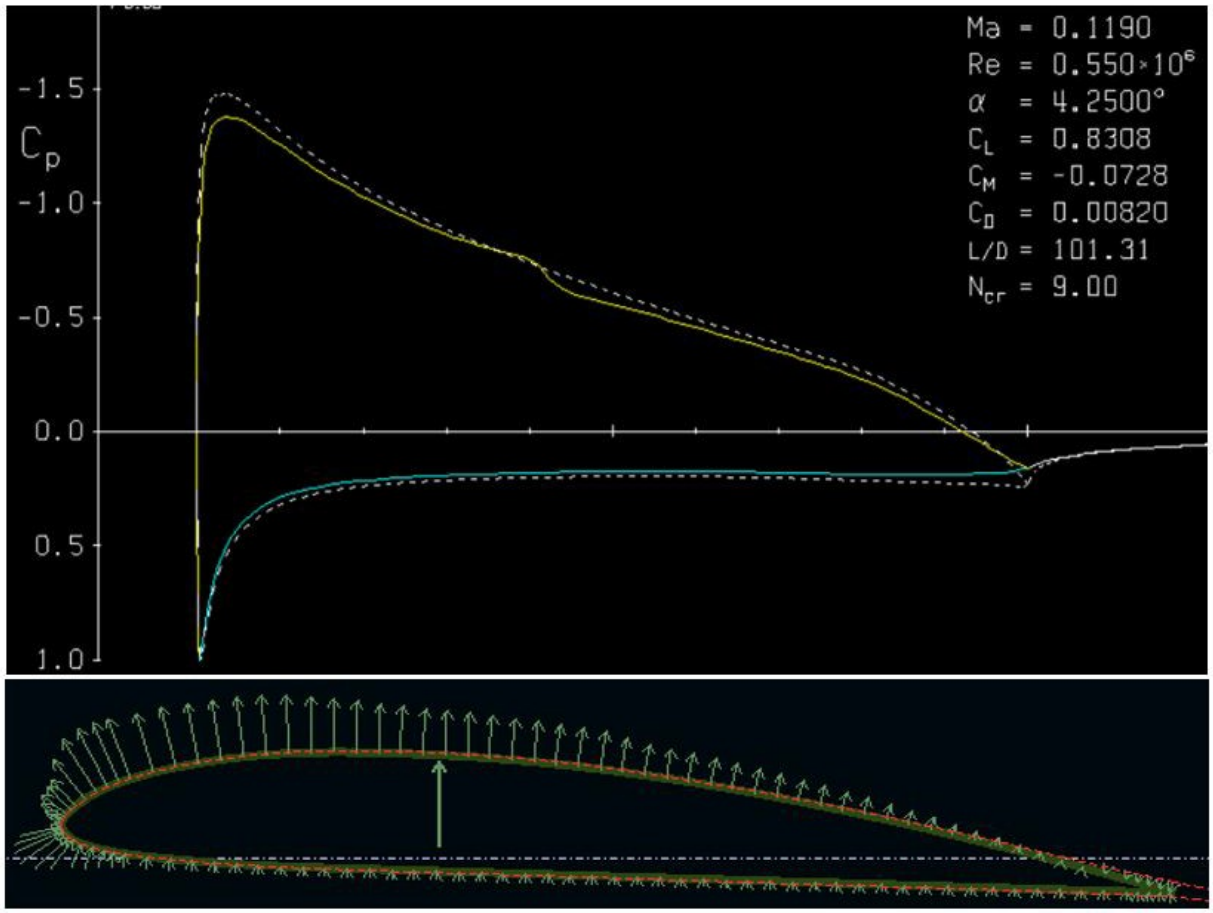

Figure 3.10: Pressure Coefficient Distribution over the Clark Y Airfoil

4. 2D (infinite length) airfoil (with corrections for 3D effects)
5. Standard atmospheric conditions (air density = 1.225 kg/m3, dynamic viscosity = 1.8e-5 kg/(m*s), pressure = 101,300 Pa, Temperature = 15°, speed of sound = 343 m/s)
6. Isotropic material for the wing
7. Nominal material properties

Nominal material properties given in (Tables 3.2 and 3.3) were used for preliminary structural analysis in place of material testing due to the constant changes to the print settings. The team deemed it inefficient to constantly test material coupons for all of the changes to the

print settings. PLA was selected as the material of choice for its good specific strength and ease of print.

3.3.3 Low Fidelity Structural Analysis

A preliminary MATLAB code was written to assess the deflections of the wing. It is a simple finite element code which takes in the material/geometrical properties and formulates a user-defined number of structural beam elements to model the wing. The lift distribution from Schrenk approximation was discretized and applied onto the beam model. The wing tip displacement was calculated to be around 1.6 inches or 40.1 mm with a nominal main spar layup of [04] and a nominal rear spar layup of [45/-45]s.

Table 3.2: Nominal Material Properties of (PLA)

	PLA
Elastic Modulus (GPa)	3.31
Flexural Modulus (GPa)	4.00
Shear Modulus (GPa)	1.29
Poisson's Ratio	0.36
Tensile Strength (MPa)	110
Density (g/cm3)	1.24

3.3.4 High Fidelity Structural Analysis

In order to more accurately assess the structural performance of the box-wing, a finite element model created in MSC Nastran/Patran was used to extract loads for failure analysis. The model included both the forward wing and the aft wing.

The finite element model consisted of mainly of CQUAD4 (4-noded quadrilateral) and some TRIA3 (3-noded triangle) shell elements. Shell elements were chosen due to their updatability (i.e. the thickness can easily be changed) as well as their computational efficiency.

Table 3.3: Nominal Material Properties of (Woven AGP370/3501-6S)

	AGP
Longitudinal Modulus (GPa)	77
Transverse, In-Plane Modulus (GPa)	75
Transverse, Out-of-Plane Modulus (GPa)	13.8
In-Plane Shear Modulus (GPa)	6.5
Out-of-Plane (2-3) Shear Modulus (GPa)	4.1
Out-of-Plane (1-3) Shear Modulus (GPa)	5.1
Major Poisson's Ratio	0.06
Out-of-Plane (2-3) Poisson's Ratio	0.37
Out-of-Plane (1-3) Poisson's Ratio	0.50
Longitudinal Tensile Strength (MPa)	963
Transverse Tensile Strength (MPa)	856
Longitudinal Compressive Strength (MPa)	900
Transverse Compressive Strength (MPa)	900
In-Plane Shear Strength (MPa)	71
Density (g/cm3)	1.60

The mesh of the forward wing is shown in Figure 3.11a. The mesh of the aft wing is similar. The mesh was created using a combination of mesh seeds, strategically placed partitions, and Patran point/curve/surface association tool. These tools assisted in cleaning up the geometry from SolidWorks, which initially imported in as broken and intersecting surfaces.

Table 3.4: Laminate Analysis Results

Element	**Nx (N/m)**	**Ny (N/m)**	**Nxy (N/m)**	**MS**
600,002	84,807	65,813	-3,981	+1.08
700,283	-85,257	-61,610	3,664	+0.75

The ribs, wing skins, and spars all have coincident nodes at their interfaces. By meshing the model in this fashion, there will be no need for permanently glued contact constraints which can increase computational time and over predict stiffness. Due to the taper of the wing, the mesh

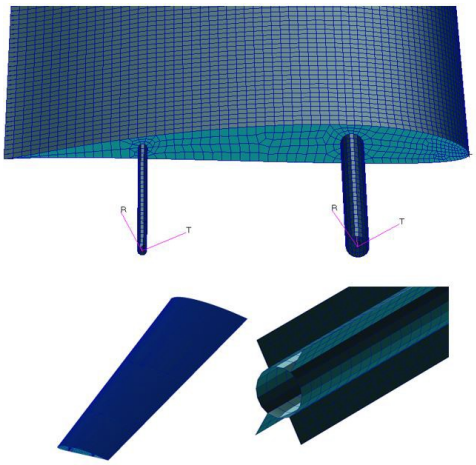

(a) Forward Wing FEA Mesh

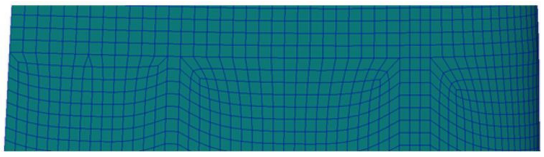

(b) Mesh Transition

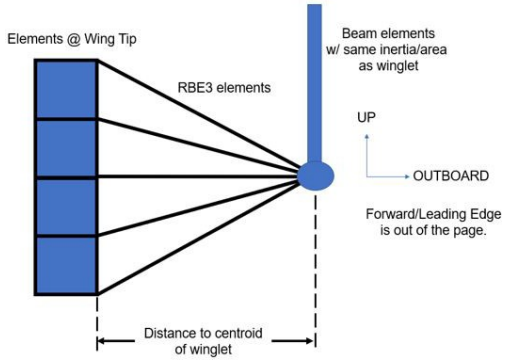

(c) Winglet Model

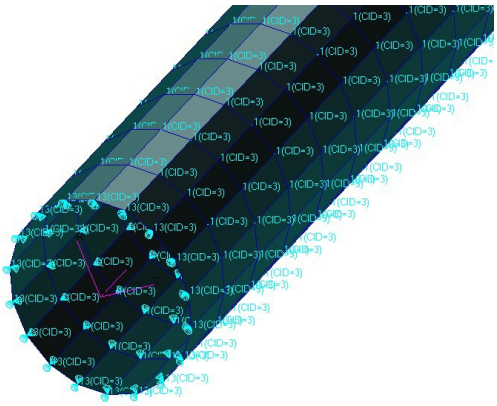

(d) Main Spar Boundary Conditions (others similar

Figure 3.11: Finite Element Analysis Model Preparation

was also transitioned into a smaller number of elements toward the tip of the wing. To ensure the elements do not become skewed, mesh seeds were placed to create a mesh transition. This is shown in (Figure 3.11b).

Additionally, to model the coupling effect between the forward and af3t wings, the winglet will have to be modeled. Due to the decreased loads at the wing tip, modeling the explicit geometry of the winglet is not something of interest. In order to estimate the effect of the winglet, 10 beam elements are used to connect the forward and aft wings. To model the load transfer between the wing and the winglets beam elements, rigid bar elements (RBE3) are used. The

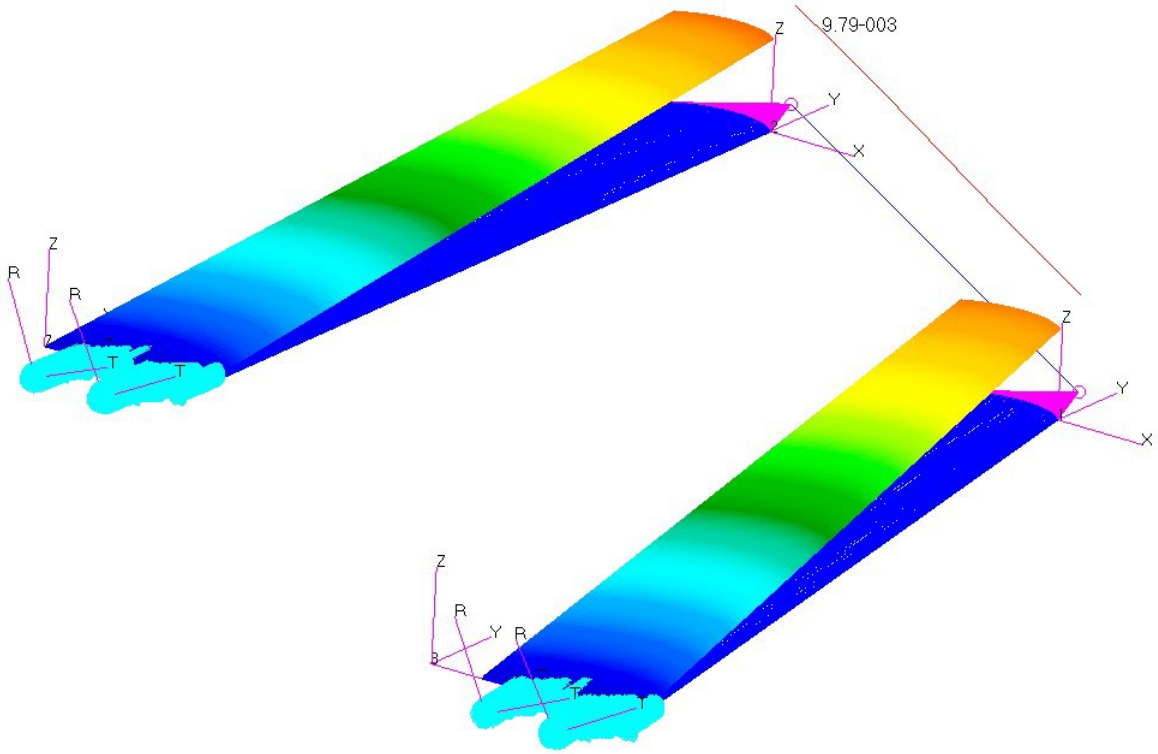

Figure 3.12: Displacement Field, Solution Sequence 101

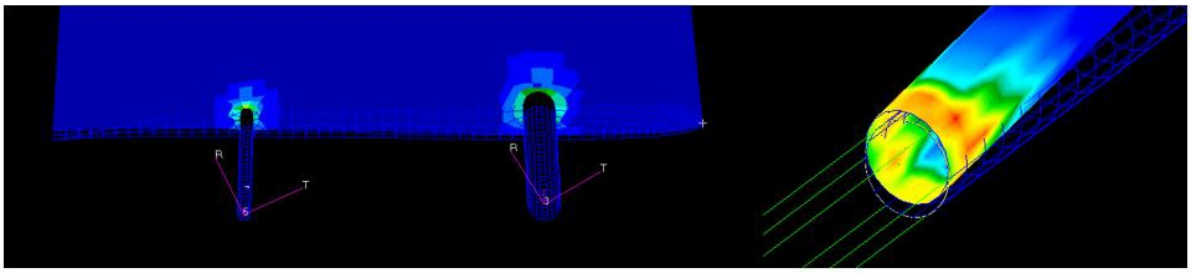

Figure 3.13: Von Mises Stress Plot of the Forward Wing, Main Spar Housing

elements at the wingtip were selected as the independent nodes with all translational degrees of freedom transferred. The dependent node was selected to be the node on the winglet side, with all degrees of freedom transferred. This is shown in Figure 3.11c.

To model the contact between the main spar and the main spar housing, linear, zero-length CGAP elements were used. This is to avoid the use of contact constraints, which slow down

the model. A closing stiffness was calculated using an elementary axial stiffness equation, k = EA/L, where E is the modulus of PLA, A is the contact surface area, and L is the wall thickness of the housing. The sliding stiffness was selected to be 10 percent of the closing stiffness to avoid numerical issues.

The team assumed a linear distribution with no edge effects (no drop in loads toward the tip) for the three-dimensional aerodynamic load distribution. This assumption was based upon the XFOIL analysis done. The pressure distribution over the airfoil was converted into a polynomial equation using MATLAB curve fitting toolbox. This equation allowed us to apply the pressure load over the entire wing FE model in order to simulate total deflection and obtain critical loads acting on the structure. A pictorial depiction of the distributed pressure load was shown in Figure 3.10.

The load resultant was checked after running the analysis to ensure the total load applied in the lift-direction was equal to the load factor multiplied by the maximum take-off weight.

It was assumed that there would be four housings in which the four spars of both wings would slot into. For boundary conditions, a cylindrical coordinate system was created in each of the spars. The nodes of the spar that protruded from the wing was constrained in the radial direction. This is equivalent to modeling a rigid housing in the fuselage. To prevent sliding and rigid body motion, the outermost nodes were also constrained in the longitudinal direction (z-direction) of the cylindrical coordinate system. This is shown in Figure 3.11d.

A linear static analysis was run (Solution Sequence 101 in MSC Nastran) and yielded a maximum tip displacement of 9.83 mm or 0.39 inches at the leading edge of the tip cross section in the aft wing. The displacement field can be seen in Figure 3.12. This is a significantly smaller tip displacement than what the MATLAB code predicted which was calculated to be around 1.6 inches or 40.1 mm, or 4 times greater. The team attributed this to the addition of the winglet in the finite element model. The MATLAB code did not model the additional stiffness of the winglet, and thus, resulted in a higher tip displacement. This results validate our hypothesis that the box

wing system, or frame system, would have beneficial structural characteristics. Less deflection at the wingtips signifies also less stresses at the root and thus a wing that uses less or lighter material and components can be designed and manufacture.

The finite element model is only used to calculate loads, stresses, and displacements. The loads and stresses are then used to calculate margins of safety by comparing them to the material allowable.

For isotropic materials (i.e. PLA), the Von Mises or octahedral stress will be extracted from the finite element model and compared to the tensile ultimate strength to calculate the margin of safety. The team chose this failure criterion because it is an accurate failure criterion for isotropic and ductile materials. It is easy to implement in MATLAB because it is not dependent on the coordinate system of the material; the Von Mises stress is a scalar energy-based value.

The largest Von Mises stress of 65.1 MPa was found to be in the root cross-section of the Forward Wing within the main spar housing (Element 203,593). A plot of the Von Mises stress is shown in Figure 3.13.

The tensile strength of PLA is nominally 110 MPa. However, based upon experience, the team assumed a knockdown factor of 30 percent. This is to account for uncertainties and variation in the material from print to print. This results in an allowable yield stress of 77 MPa. The margin of safety then is calculated to be +0.18 (meaning an 18 percent excess in strength).

A MATLAB code to perform laminate failure analysis was also written. The MATLAB code takes in the material properties, laminate layup, and loads in the form of stress resultants. The output is a margin of safety. Inside the code, it calculates the ABD matrix (stiffness matrix for composite materials) and uses it to calculate the effective laminate strains due to the loads. The strains are converted into local ply coordinates to calculate local ply stresses. The ply stress components are then combined into a scalar energy equation and first ply failure is evaluated using the Tsai-Wu criterion.

The maximum tensile stress resultants from the finite element model was from Element

600,002. The maximum compressive stress resultants from the finite element model was from Element 700,283. Element 600,002 is in the forward wing, aft spar, and Element 700,283 is in the aft wing, main spar. To be conservative, the team assumed a knockdown of 50 percent. This is to account for material uncertainties and also manufacturing defects associated with manufacturinga spar this small (10 mm diameter).

Both sets of loads were inputted into the MATLAB code and laminate analysis was performed. Both PCOMP elements show positive margins. The results are summarized in Table 3.4.

It is important to know that the finite element model does not model the composite skin. This finite element model analyzes a baseline design with only a composite spar. The assumption is a 17 kg payload, which yielded a critical margin of safety of +0.18. In practical applications, the payload will be much greater than 17 kg, which is why we decided to pursue a composite skin as well in the final design. In order to model a composite skin, the elements comprising the wing skin would need to be duplicated and then assigned a PCOMP property card. The nodes between the PLA skin and the composite skin would be guaranteed to be coincident, thus they can be easily equivalent as to modeling a rigid inter-laminar bond.

3.3.5 Topology Optimization

In order to further optimized the weight function of the aircraft we decided to explore the capabilities of the novel topology optimization technique. Topology Optimization (TO) is a mathematical method that optimizes material layout within a given design space, for a given set of loads, boundary conditions and constrains with the goal of maximizing the performance of the system. Most TO formulations used today make use of finite element methods (FEM) to evaluate the design performance. The design is optimized using either gradient based mathematical programming algorithms such as the optimally criteria algorithm and the method of moving asymptotes or non-gradient based algorithms such as genetic algorithms.

Topology optimization has a wide range of applications in aerospace, mechanical, bio-chemical, and civil engineering. Currently, engineers mostly use TO at the concept level of a design process. Due to the free forms that naturally occur the result is often difficult to manufacture. For that reason the result emerging from TO is often fine-tuned for manufacturability. Adding constrains to the formulation in order to increase the manufacturability is an active field of research. In some cases result from TO can be directly manufactured using Additive Manufacturing techniques, which makes TO a key part of the design for additive manufacturing.

In this experiment we made use of TO algorithms developed by Solid Thinking Inspire 2018 by Altair. The optimization workflow is at follows:

1. Design Model in CAD environment (Rhinoceros 3D or SolidWorks).
2. Export as STL or STEP.
3. Import into Topology Optimization Software
4. Define Boundary Conditions and Loads (Lift Pressure Force over Wings)
5. Define Optimization Type (Topology)
6. Define Objective Function (Minimize Mass or Maximize Stiffness)
7. Define Mass Target (% of Total Design Space Volume or Total Mass)
8. Define Frequency and Thickness Constrains.
9. Run Topology Optimization.
10. Refine Resulting Mesh.
11. Export as STL or STEP and Import in Meshmixer for Mesh smooth and cleanup.
12. Export as STL or STEP and Import into CAD Software for Final Assembly.

13. Send to Slicer software as STL in order to generate G Code for 3D printing.

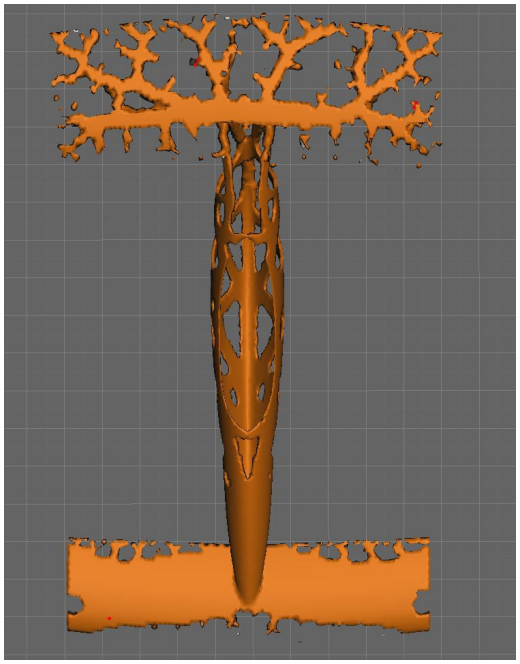

(a) Topology Optimization Results: Top

(b) Topology Optimization Results: Front

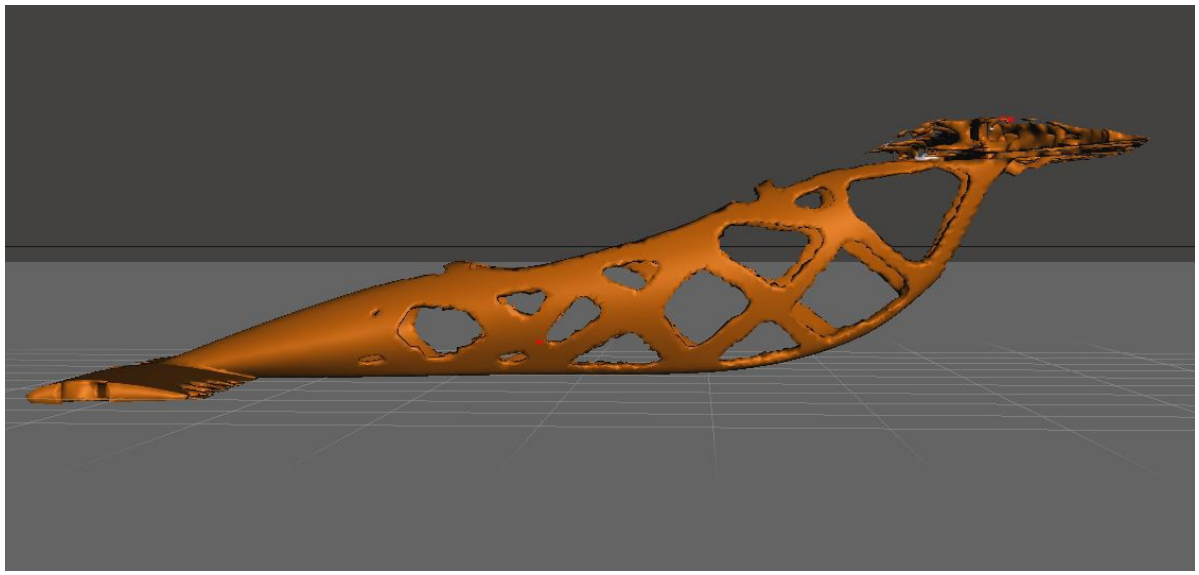

(c) Topology Optimization of Results: Side

Figure 3.14: Topology Optimization of Fuselage

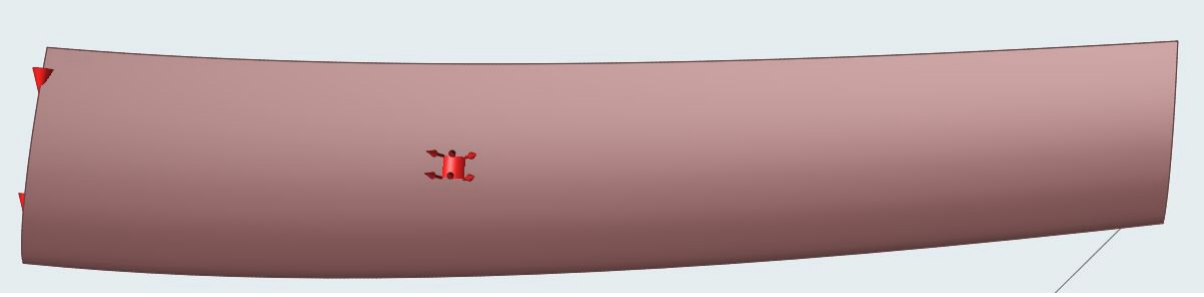

(a) Topology Optimization of Wing Model

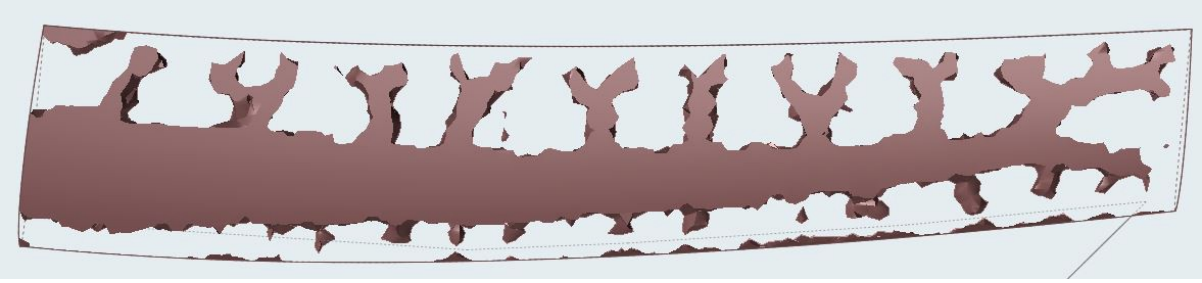

(b) Topology Optimization of Wing Results

Figure 3.15: Topology Optimization of Wing

3.4 Aerodynamic Analysis

3.4.1 Low Speed Airfoil Selection

For the selection of the airfoil, an extensive literature review was carried out. We looked at previous work on the design of airfoils for LALE UAVs [**?**]. We targeted our search on airfoils that exhibit good performance when flying at low Reynolds Numbers. For our study, we boundthe RE search space from 100,000 to 500,000 and virtually tested a series of Airfoil designs suggested by the literature. Airfoils like Clark Y, S7075, S1223, E387, RG14, S1223, S7012, S7075, SD7080, SD7037, SD7043 showed great stability results as well as generating high Cl vs Cd values over a range of angle of attack values as seen in (Figure: 3.16). Of special interest was to find an airfoil with an extraordinary Cl/Cd ratio and even though airfoils like S7075 and SD7043 showed the highest values of Cl/Cd peaking at 110, we selected airfoil Clark Y because it performed extremely well over the range of Reynolds numbers. ClarkY airfoil yielded Cl/CD

values near the 100s at a large range of AOA for good stability and controllability. The airfoil also has advantageous shape for manufacturability which allowed to satisfy our thickness requirement for the placement of the main spar. The aerodynamic properties and plots of the Clark Y airfoilcan be found in (Figure: 3.17) and (Table 3.5).

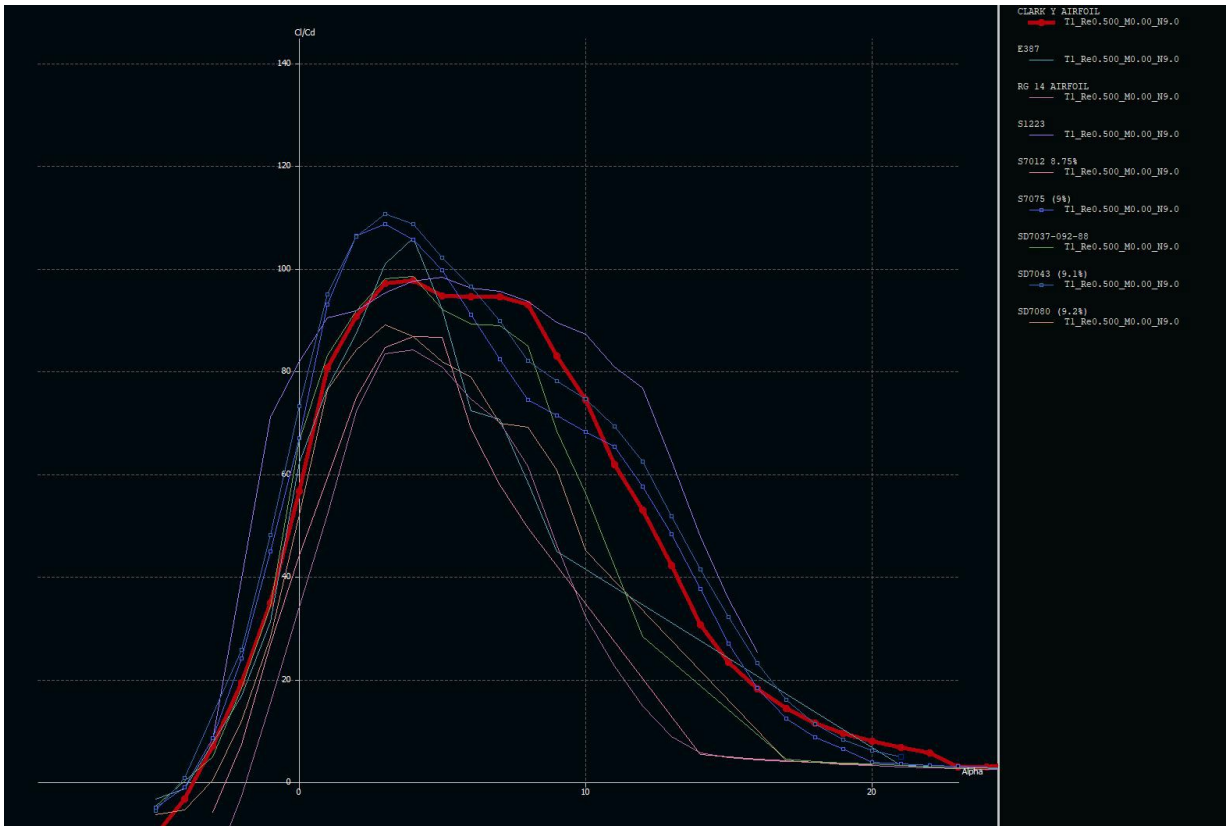

Figure 3.16: Airfoils Analysis and Selection: Cl/Cd vs alpha

3.4.2 Stability Analysis

After having defined a base wing model the next step in the design process was to understand the aerodynamic behavior of our biplane wing system. We ran low fidelity analysis of different airfoils and a biplane wing to get preliminary lift and drag plots which were used to select a proper airfoil and validate the size of our wing system. Further this code was also used to derive the eighth stability modes and plots (Figure 3.18); 4 longitudinal (2 symmetric Phugoid,

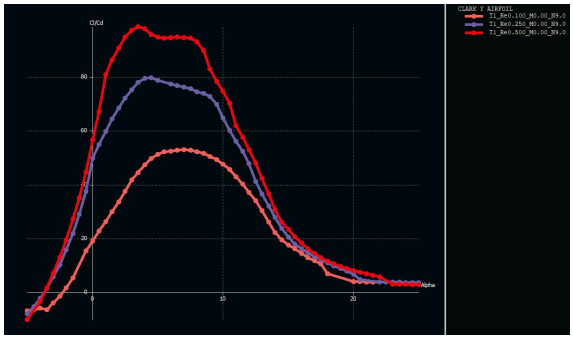

(a) ClarkY: Cl/Cd vs alpha

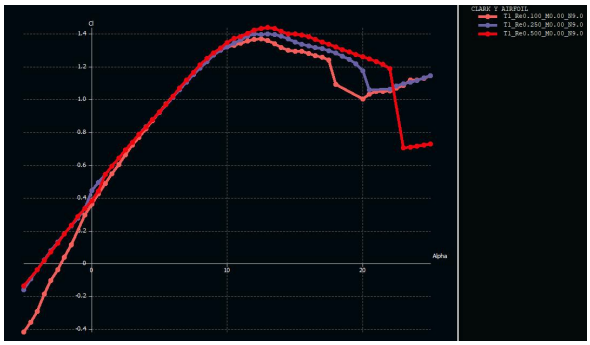

(b) ClarkY: Cl vs alpha

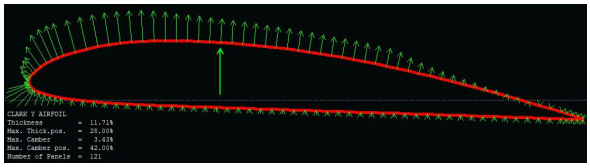

(c) ClarkY: Pressure Distribution at alpha 4

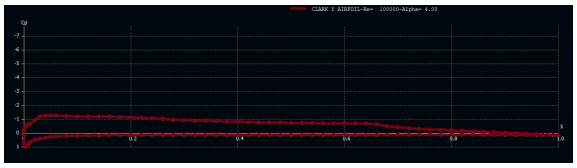

(d) ClarkY: Cp Distribution at alpha 4

Figure 3.17: ClarkY Aerodynamic Plots at 100e3,250e3 and 500e3 Reynolds Number

Table 3.5: Clark Y Airfoil Aerodynamic Properties

Clark Y Airfoil		
Thickness	11.71	%
Max. Thick Pos	28.28	%
Max. Camber	3.43	%
Max Camber Pos	42.42	%
Zero Lift Incidence	-3.68	deg
Zero Incidence Lift	0.41	-
Section Pitching moment Coefficient	-0.086	-
Constant Parasitic Drag	0.007	-
Maximum Section Lift Coefficient	1.43	-
Max Cl/Cd	95.0	-
Optimal AoA @ Max Cl/Cd	3.6	deg
Cl @ Optimal AoA	0.8	-
Cd @ Optimal AoA	0.008	-

2 symmetric short period), 4 Natural (1 spiral, 1 roll damping, 2 dutch roll) which allowed us not only to validate the behavior of the wing but also the location of the center of gravity for

stable and robust flight performance. This location of the center of gravity will force the aircraft to cruise at an AOA of 3.6 which is optimal for the airfoil and wing system selected. At this AOA the L/D ratio of the airfoil and Wing is near maximum, providing us a good start for our high fidelity fluid analysis.

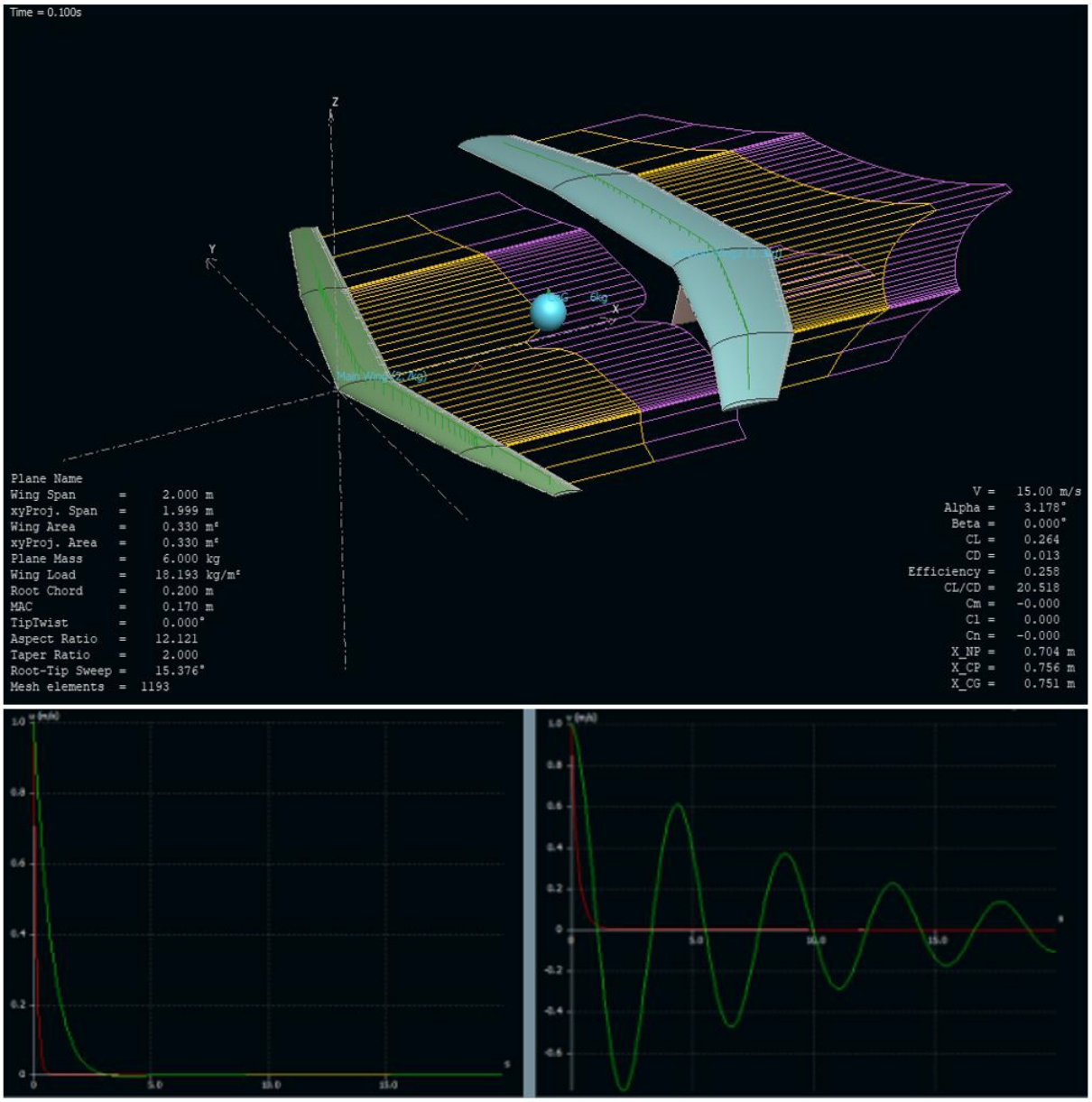

Figure 3.18: Low Fidelity Fluid Dynamics and Stability Plots, XFLR5)

3.4.3 Lift-to-Drag Ratio Optimization

In order to fully understand the aerodynamic behavior and performance of the Prandtl Box Wing a high fidelity steady CFD analysis were performed using ANSYS Fluent. ANSYS Fluent allowed us to calculate with high accuracy the L/D resultants, derive velocity, pressure contour, as well as vorticity plots. The main goal of this analysis was to confirm that the total Lift generated by the wing system flying at the targeted speed and AOA was enough as to counteract the MTOW of the platform. We also wanted to detect any regions of excessive drag and use this information to iterate over the design of the wing, specially near the tip/winglet sections to find the best L/D wing system.

The CFD setup follows this workflow:

1. Export CAD geometry in the proper field type, from .3dm to STEP or IGES, and import into solver (Rhino3D to ANSYS)

2. The wing was set to fly at an AOA of 4°. Using the distance between the root of the trailing edge of the back wing to the root of the leading edge of the front wing as the characteristic length, we constructed a fluid domain large enough to avoid fluid-boundary disturbances/interactions. We had to have at least 15 times the characteristic length from trailing edge of aft wing to end of the fluid domain and 5 times from all other extremes to end of the domain in each respective direction. Only half of the wing was analyzed to save on computation time. (Figure 3.19).

3. We then meshed the fluid domain using unstructured tetrahedrons near the UAV and structured hexahedrons everywhere else for the volume. The regions near each wing was refined enough to obtain a y^+ value < 1 to capture the viscous sublayer as determining drag effects on the UAV was imperative in confirming our box wing's design parameters (Figure 3.20). Our final mesh model comprised of about 8.2 million elements.

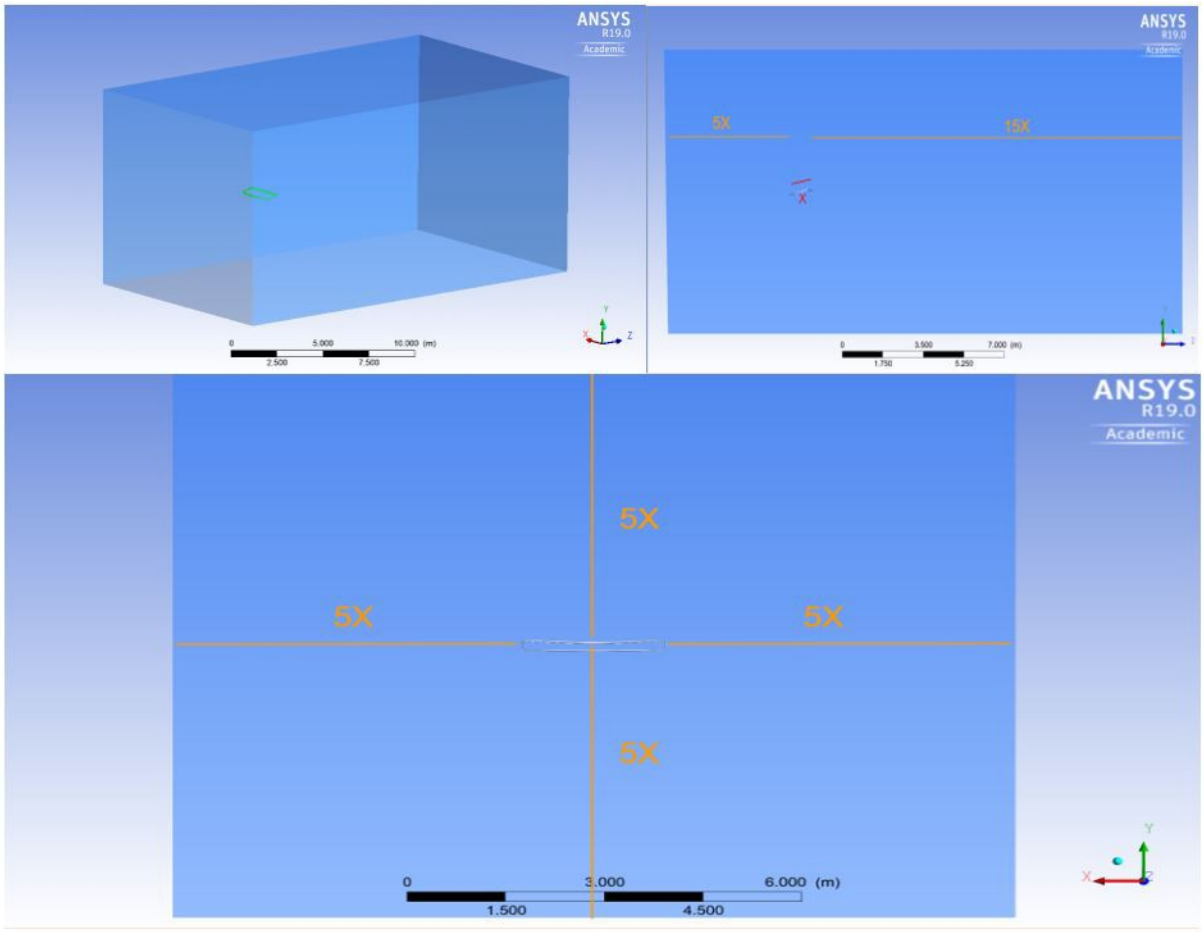

Figure 3.19: Fluid Domain of Virtual Wind Tunnel and Dimensions

4. We set up the Fluent solver to use the SST k-omega viscous model to calculate a 2nd order accurate steady-state solution using the Semi-Implicit Method for Pressure Linked Equations (SIMPLE) pressure scheme algorithm. We wanted to predict the aerodynamic forces acting on our wing flying at 200 ft. The face in front of the wing and lateral faces of our fluid domain surrounding the wing were set as an inlet velocity of 24 m/s. At the fuselage line, a symmetry boundary condition was implemented. The face behind the aft wing which was a pressure outlet set to 0-gauge pressure. A temperature of 15°C was set at the inlets and outlet. The air flow doesn't slip over the wing. At 200 ft, the atmospheric pressure was calculated to be 100,595.43Pa using the barometric formula shown below.

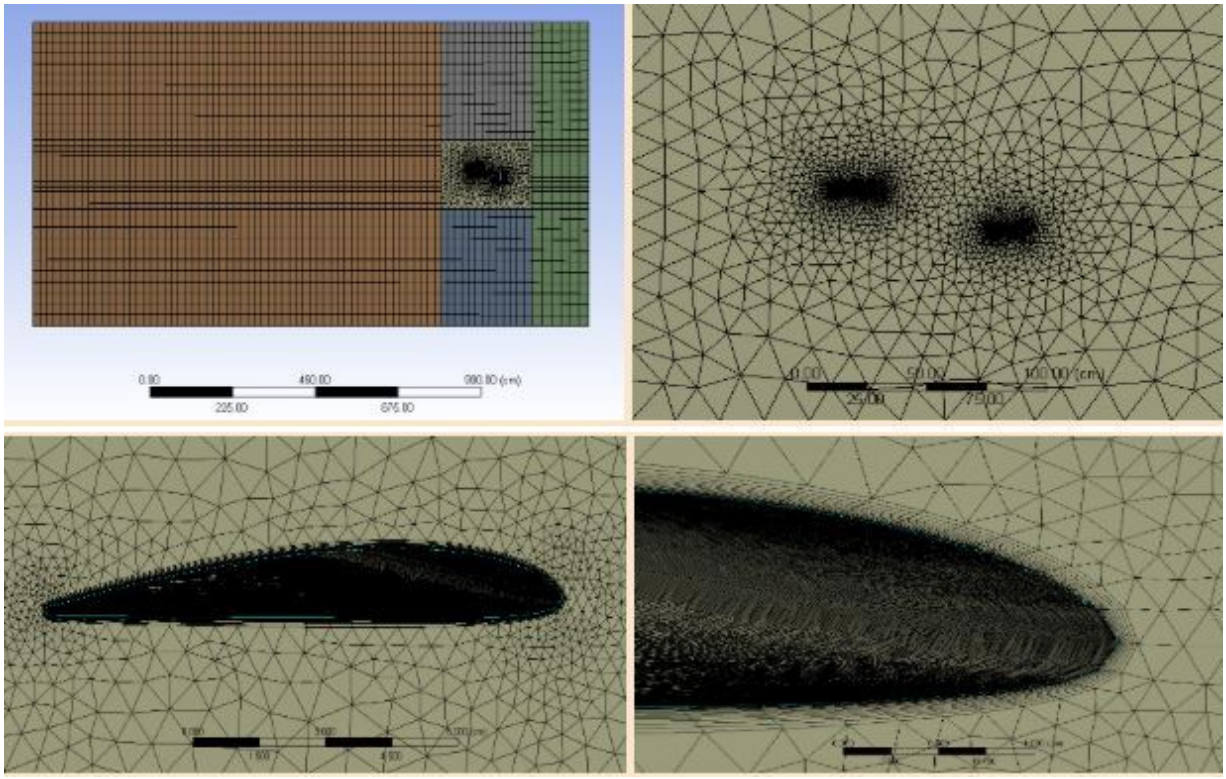

Figure 3.20: CFD Mesh Domain Perspectives

$$P = P_0 * exp[-g * M * (h - h_0)/(R * T)]$$

Where:

P = Pressure at Target Altitude

g = Earth's Gravitational Acceleration

M = Molar Mass of Air

h = Target Altitude

h_0 = Reference Altitude

R = Universal Gas Constant

5. The achieved steady flow solution produced a series of 3D contour plots (Figure 3.21). The analysis took 3.5 hours to converge with a total number of 750 iterations and yielded the following results.

- Total Lift: 62.72 N = 6.4 kilograms
- Total Drag: 3.84 N = .392 kg
- L/D Ratio: 16.31

The results obtained allowed us to confirm: First, that the wing system flying at the target velocity and AOA was capable of lifting the aircraft and payloads. Secondly, that the Prandtl Box Wing configuration designed outperformed the biplanar wing without connecting winglets. This proves the theory that a box wing, if designed properly, is capable of delivering an efficient wing system without compromising performance or safety.

We continued our aerodynamic work by now analyzing the performance of our designed fuselage as well as the performance of the combined wing/fuselage model (Figure 3.22). We achieved minimally drag design by constructing a fuselage which took use of two different airfoils, on the vertical axis the fuselage used the profile of the Clark Y airfoil used in the wing, while on the horizontal axis we used a symmetric airfoil NACA 0008. Finally, we lofted the two airfoils together and achieved a fuselage that performed well at the target velocity and AOA. Figure 3.22 shows the CFD results of the fuselage analysis as well as the combined model.

- Combined L/D ratio = 14.61.

3.4.4 AM Design

All parts throughout the design process were printed on the Ultimaker 2+ using Simplify3D slicing software. The first step was to print some small blocks with a male dovetail

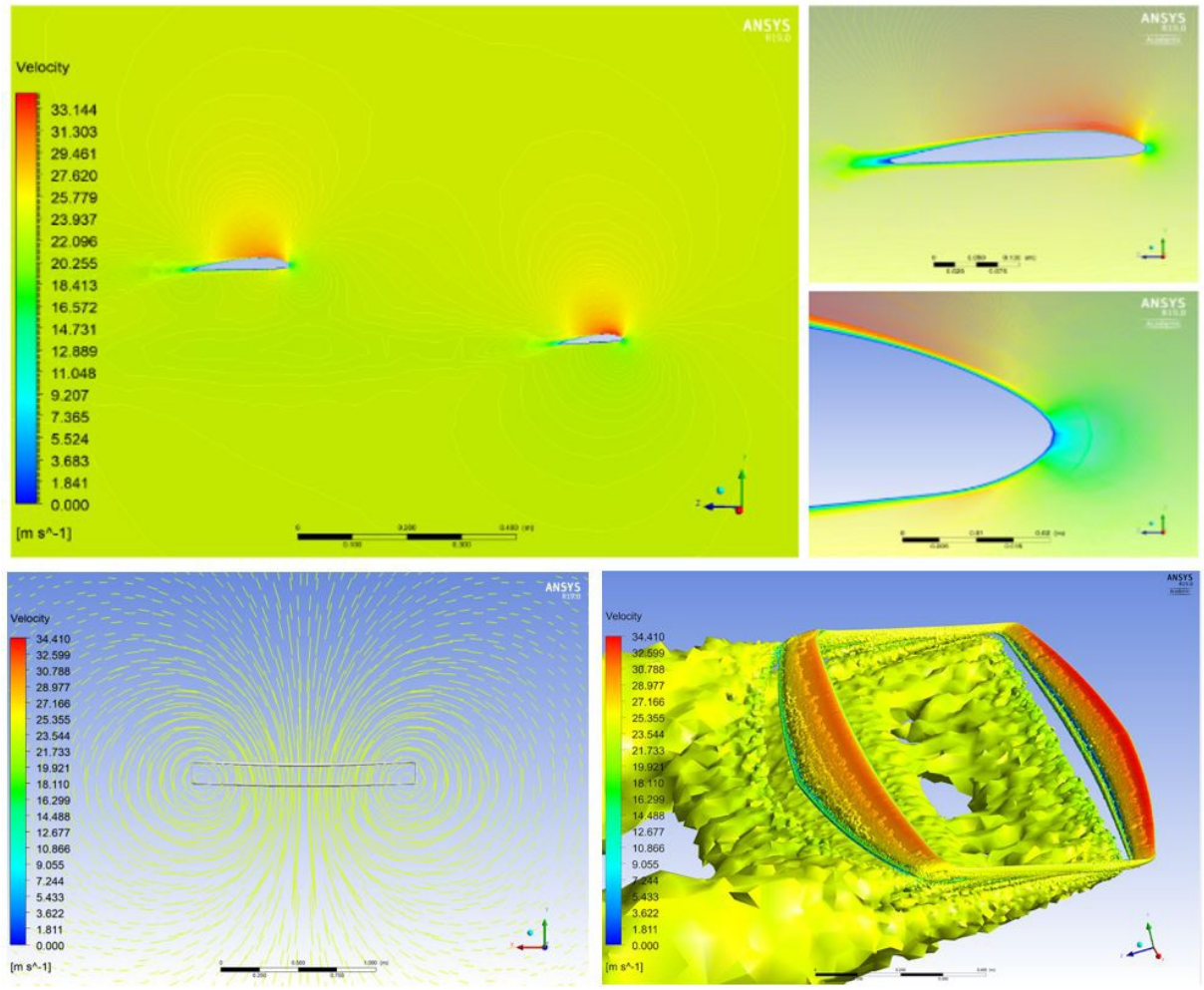

Figure 3.21: ANSYS Fluent Results, Wing Only: a-b: Pressure Contours Map, c: 2D Vorticity Field, d: 3D Voricity Field

connection and female dovetail connection at each end to gain a better understanding of both the printers and the softwares capabilities. These small parts were printed in both polylactic acid (PLA) and Polyethylene Terephthalate (PETG) to compare materials and to develop a base- line understanding of the print quality with default settings. The PETG connections appeared tobe stringier and worse quality in the bridging area of the female connection. See Figure 3.23a. PLA connections tended to be smoother and more receptive to tolerance.

After trying several female offsets on connections with sharp corners, the connections

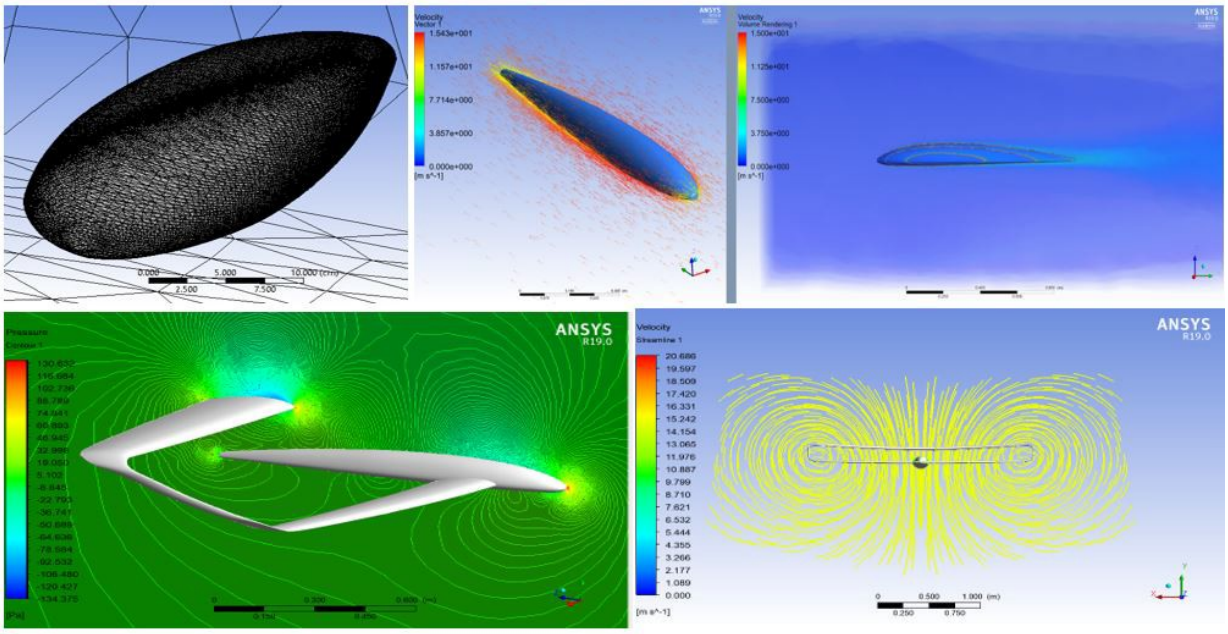

Figure 3.22: ANSYS Fluent Results, Fuselage and Combined Model: a: Fuselage Mesh, b-c: Fuselage Velocity Field, d: Pressure Contours Map, e: 2D Vorticity Field

underwent a redesign, Figure 3.24, which utilized dovetails with gently filleted corners. This would allow the male and female parts to slide together more smoothly and improve the tolerancing of the joints. Nicely printed filleted connections can be achieved using the default print settings and a 0.102 mm female offset.

Once well printed connections were achieved, the focus was shifted to the airfoils. The main concern regarding the airfoils was about printing something tall and skinny with minimal infill. It was predicted that there would be issues with warping, over extrusion, and adherence of the first layer to the bed.

In addition to printer jams, the team had to consider warping and bridging when printing the airfoil. Warping can cause gaps between male and female connections to form, Figure 3.23b. Improperly bridged areas create rough surfaces that can interfere with the connection. To reduce warping, cooling fan speeds were reduced to 25 percent after the first few layers. In addition, brims were used when necessary. To improve bridging quality, solid layer infill angles were

adjusted to create shorter bridge lengths (Figure 3.23c). Table 3.6 summarizes the total print time and weight of each airfoil section. The only post-processing required for the airfoils was removalof the support structures at the leading edge of the female connection.

Table 3.6: Wing Print Time and Weight

	Weight (g)	**Time**
Foil 1	130.87	14:00 hours
Foil 2	126.75	13:40 hours
Foil 3	116.8	12:45 hours
Foil 4	106.68	11:45 hours
Foil 5	96.91	10:45 hours
Winglet	49.89	4:40 hours

3.4.5 Large Scale AM

- Talk about printing full size and functional prototypes
- Talk about post processing

3.5 Composites

3.5.1 Augmenting AM Structures

The first step to prove the capabilities of reinforcing the 3D printed wing with a composite manufacturing approach was testing the 3D printed wing sections under vacuum pressure. To achieve the goal of wrapping the wing in fiberglass, the Wet Lay-Up method was used to wrap two 45-degree fiberglass plies around the wing. For the best air suction, compression, and optimization of the resin percentage in the fiberglass wing, vacuum bagging is normally utilized. The vacuum bagging consists of placing the wing section right after the wet lay-up method into peel-ply cloth and breather cloth, and ultimately placing it in a tacky tape-sealed vacuum bag.

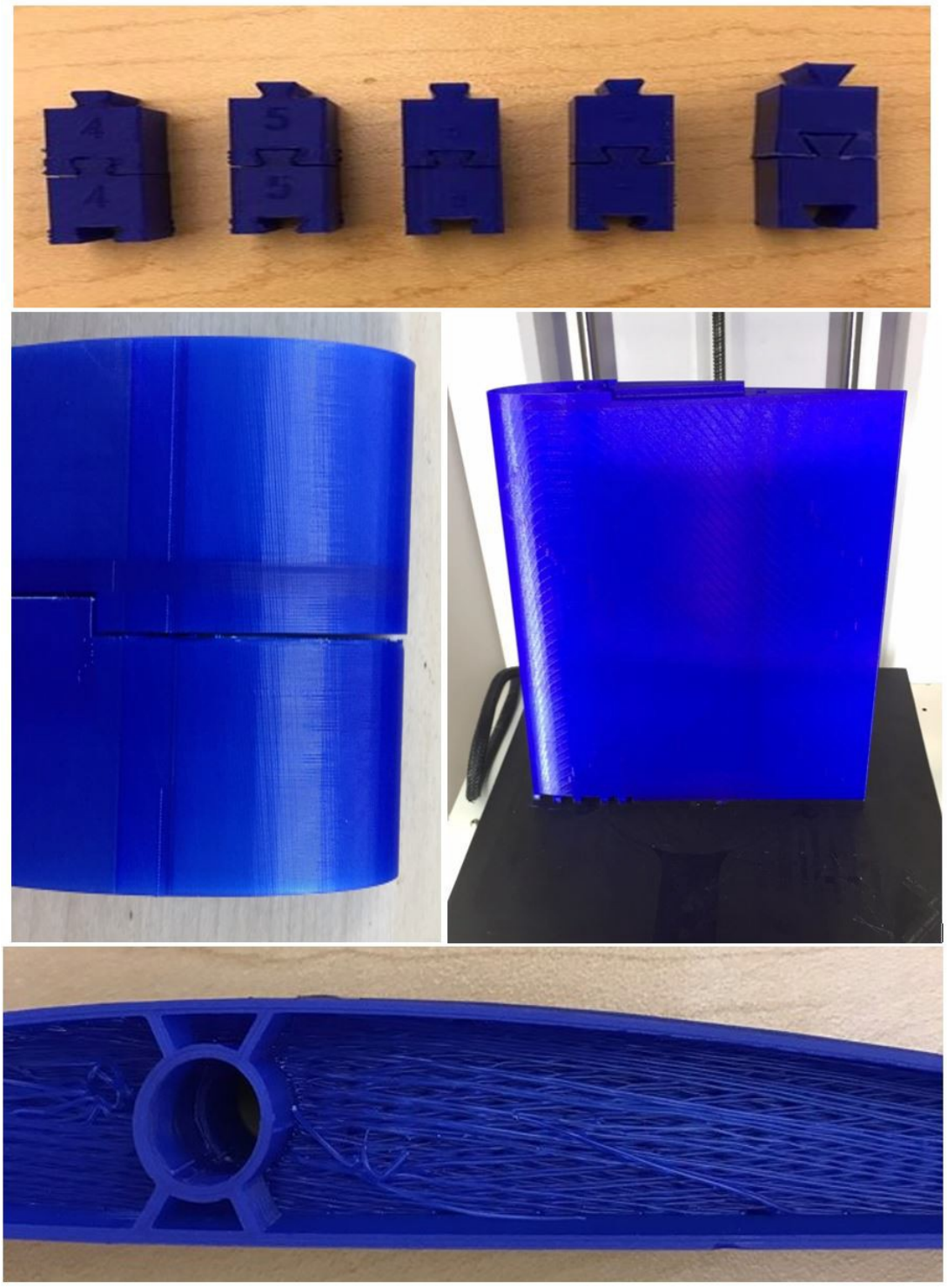

Figure 3.23: 3D Printing: a: Devenails, b: Connections, and c: Wing with spar hole

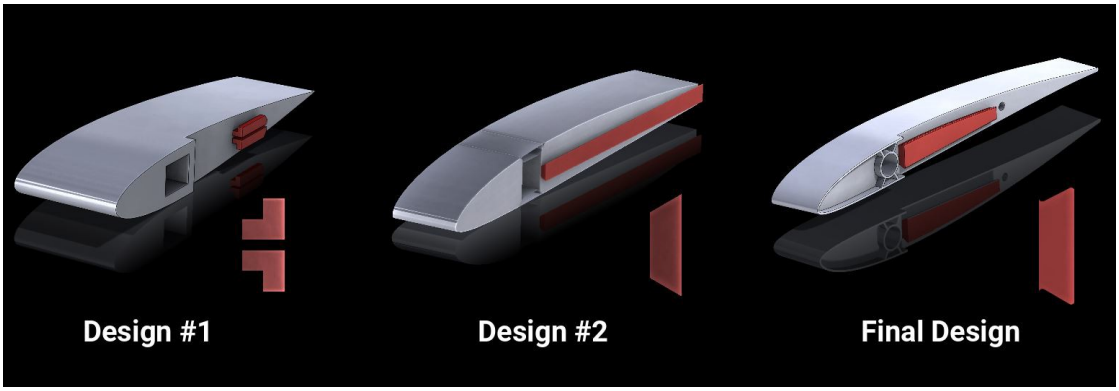

Figure 3.24: 3D Printing: Connection Design Evolution

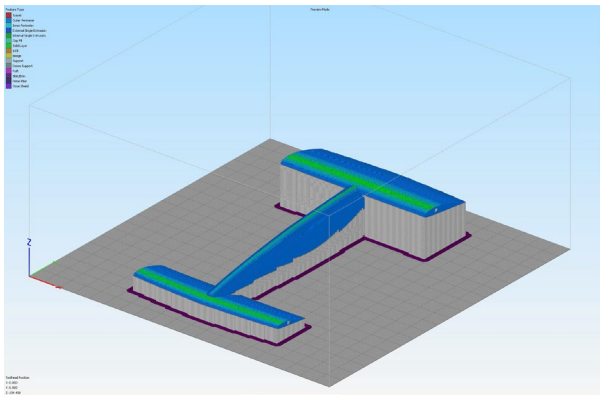

(a) Fuselage on Slicer

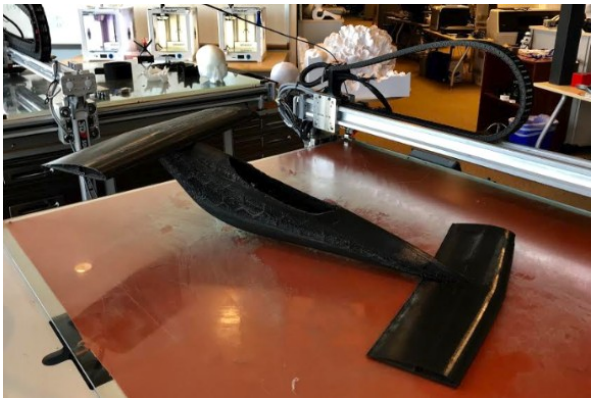

(b) Fuselage Printed

(c) Real Scale Prototype

(d) Final Prototype Assembled

Figure 3.25: Real Scale Print of UAV Prototype

Once the wet-laid part is sealed in the bag, vacuum is pulled from the bag. Standard composite parts that are manufactured with the wet lay-up method usually have to reach 100 kPa vacuum

pressure for 24 hours. With visual inspection of the wing sections that were going to be wrapped in composites, we decided to test the 3D printed wing sections under vacuum pressure to inspect if the sections would deform under a certain magnitude of applied pressure.

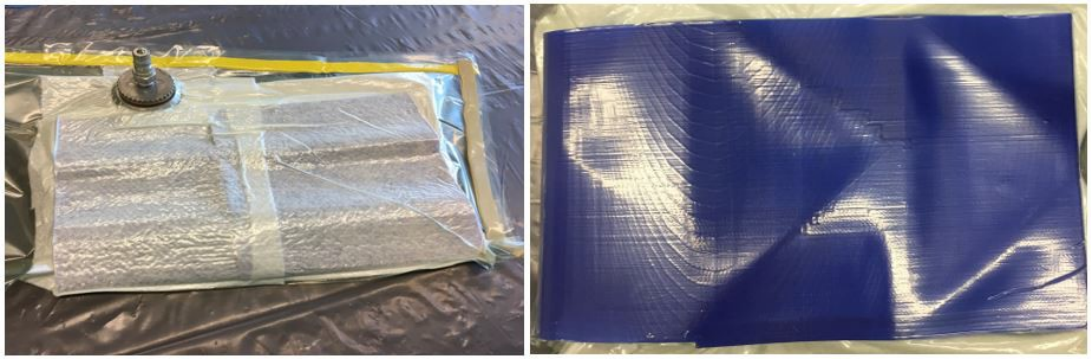

Figure 3.26: Vacuum Bag Pressure Tests on 3D printed wing sections: Left, Vacuum Back Fail of Unsupported wing section. Right: Vacuum Bag Fail of Supported Wing Section

Shown in Figure 3.26, wing sections with both no infill wall support and full infill wall support deformed under vacuum bag pressure. These deformations were undesirable because if the wing sections were to be used in an actual wet lay-up process with wrapped fiberglass, the deformation of the wing sections would cause the fiberglass to conform to the deformed state. Once the epoxy that would be used to manufacture the wrapped wing section cures, the final part would result in an airfoil with dents throughout the airfoil, which diminishes the aerodynamics and structural performance of the wing. Additionally, through vacuum bag pressure tests, it was observed that the fully infill supported wing section started deforming when the vacuum pressure was reaching around 15 kPa which is 85 percent lower than the expected vacuum pressure that a composite-wrapped part should normally undergo. With these results and observations, we ultimately decided to utilized 3D printed wing molds that fit the wing and were used to clamp the wing to provide the compaction that a vacuum bag would provide.

Despite the results of the vacuum bag pressure tests, a 1-inch wing test-section was wrapped in fiberglass using the wet lay-up method and vacuum bag pressure. Because the wing section was so small, the wing section did not undergo any buckling under pressure and therefore,

was able to be used as a manufacturing test to examine the stiffness and manufacturability of a fiberglass-wrapped wing s ection. To start this whole process, the two wing sections that were connected through a dovetail connection were sanded and cleaned thoroughly with isopropyl alcohol to prepare the surface where the fiberglass were going to be w rapped. This surface preparation allows a better bond between the fibers and the wing sections. Once the surface preparation was finished, the wing sections were wrapped with two p lies of fiberglass with mid-cure 15 min. epoxy. The mid-cure 15 min. epoxy was very hard to manufacture with dueto the fast cure time of the epoxy, and therefore, the fibers were not fully saturated with epoxy. Despite the epoxy difficulty, the wrapped part did not deform under vacuum pressure and was cured successfully. The final cured fiberglass-wrapped wing section was very stiff and light, and with this successful result, the motivation for wrapping the whole wing with fiberglass was encouraged even more.

3.5.2 3D Printed Wing Molds

The mold sections went through several iterations before arriving at the final design. The first version was designed to be robust enough in all dimensions to ignore the complex geometry of the wing and be able to be laid flat in the x, y, or z-direction. The first version was also designed to be thick enough to handle a variety of infills and perimeter layer options while being strong enough to evenly distribute the pressure from whatever compression method was used (clamps; washer, nuts, and bolts; weights placed on top; vacuum bag over the whole mold). Due to concerns that the root mold might not print properly from coming so close to the edges of the print bed, a second version was designed that was 12 mm shorter in width and 6 mm shorter in height; it also decreased the infill percent from 15 percent to 10 percent and the number of perimeters from 4 to 2. The second version did not need to be used and was never printed. Version 3 came about as a way to reduce the print time of the mold. It follows the taper, sweep, and

dihedral of the wing to maintain a thin cross-section while lying flat on a table and leaving room for clamps, alignment rods, and connections. As seen in Figure 31, version 3 cut down the print time by over 30 hours per piece, saving over 360 hours (15 days) over the course of the entire mold print.

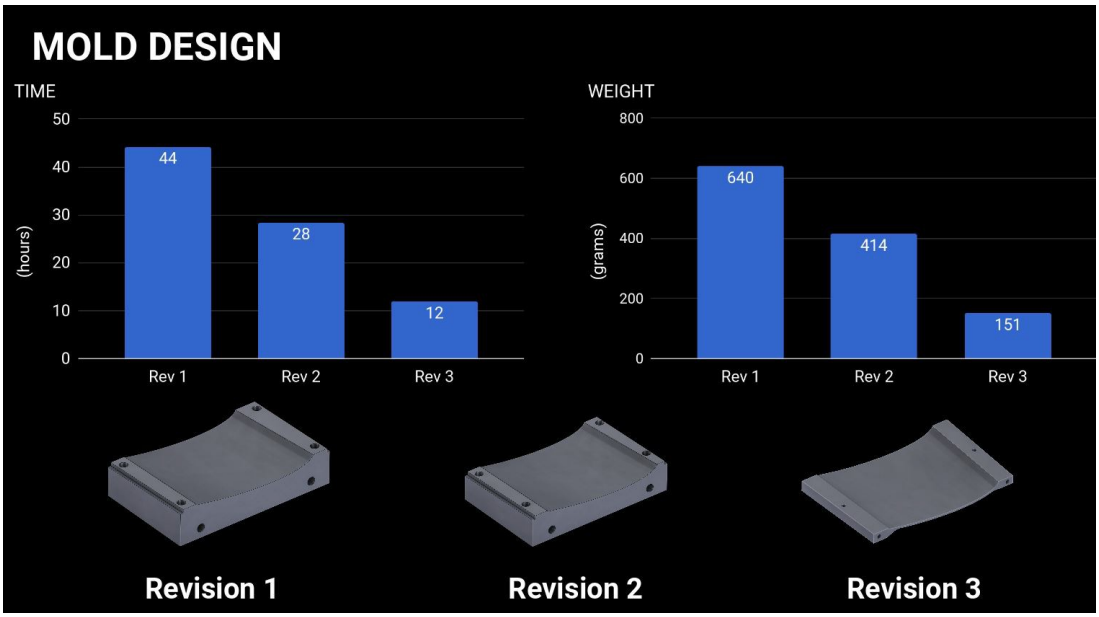

Figure 3.27: Print Time Comparison for Mold 1, Bottom Design Iterations

Figure 3.27 compares the top root mold sections. As can be seen in the images, the infill (fast honeycomb) is noticeably denser, and the amount of support is significantly higher. While this led to a very sturdy mold, time limitations forced a redesign. This is where the benefits of 3D-printing can be seen. Less than 2 days of CAD work led to the complete redesign of the mold, and the first section was done printing by the next day. We achieved a 70 percent reduction of time and a 75 percent reduction of weight and material usage without compromising the final quality of the wing.

Figure 3.28 above shows the full assembled female mold surrounding the wing assembly. The mold sections were connected using 1/8-inch diameter wood horizontal alignment dowels and 1/4 inch diameter wood vertical alignment dowels.

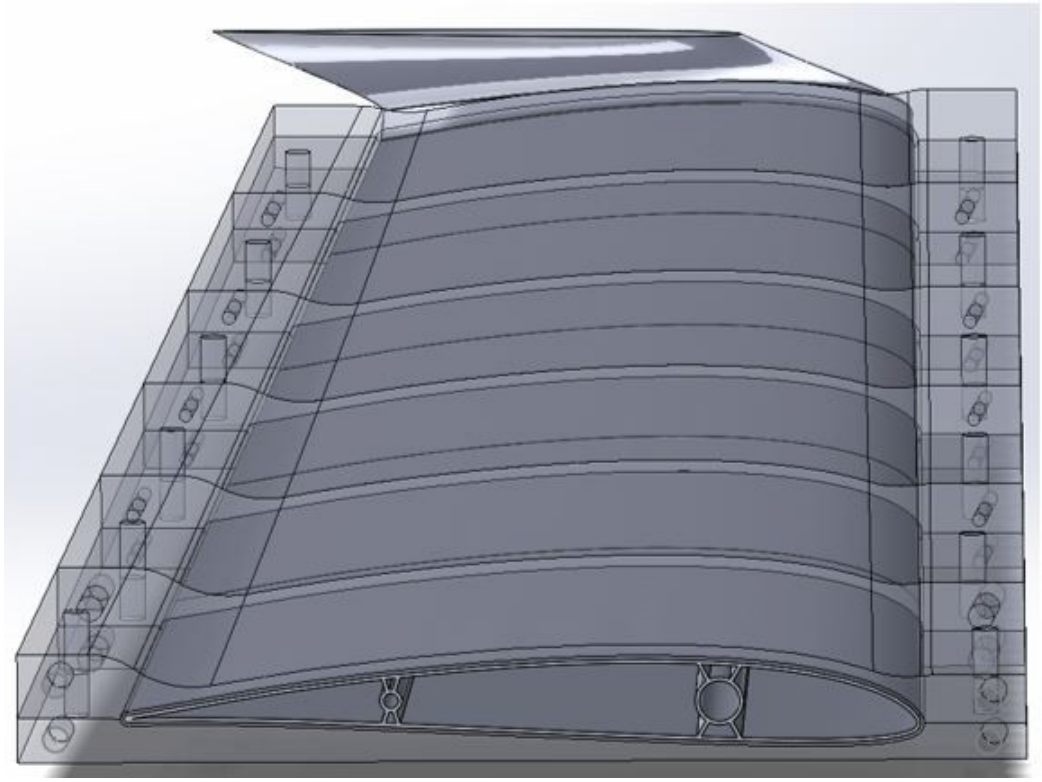

Figure 3.28: CAD Image of Wing in Final Mold

Molds were printed in silver PLA on an Ultimaker 2+. Print settings were nearly identical to the airfoils except 7 percent honeycomb infill was used to provide some support to dissipate the pressure generated during the layup of the wing. Rafts were added to all of the mold sections to prevent warping and ensure that the prints stick to the bed. The only post-processing required for the molds was removal of the rafts and minor reaming of the holes to account for inconsistencies in the wood alignment dowels.

The layup of the fiberglass wrap around the wing male mold included the following materials listed in Table 3.7.

The layup procedure includes the following steps:

1. Clean surfaces and cut the material according to ply cut map.

2. Cut and oversize disposables. Note plies cover total surface area of wing, and the overlap

Table 3.7: Composite List of Materials

Material	List
Tools	• Wing Male Mold • Wing Female Mold
Disposables	• Vacuum bag • Breather film • Perforated release film
Composite	• [45] Fiberglass • Epoxy Resin
Misc	• Clamps • Weights

Figure 3.29: Layup (Left), and Wing in Mold (Right)

seam is on the trailing edge.

3. Lay disposables on bottom female mold according to layup map: vacuum bag, breather film, perforated film, and fiberglass.

4. Position dry fibers over mold and disposables and wet out the first ply. It is important to wet the fibers for the bottom skin and some past the leading edge to the top skin. Repeat with 2nd layer of glass.

5. Position male wing mold the fibers, disposables, and mold. Wrap the dry fibers onto the top skin. Wet out the first layer on the top skin around the leading edge to ensure no wrinkles (Figure 3.29 (Left)). Continue wetting and working to the trailing edge.
6. Do a wet trim of the fibers and wrap over with the disposables.
7. Place over top female mold and insert alignment dowels (Figure 3.29 (Right)).
8. Ensure everything is aligned and that there are no wrinkles.
9. Clamp and apply weights to evenly distribute pressure onto mold to wing.

Figure 3.31 shows the final weight breakdown of half of the leading wing. It can be noticed that the majority almost 70 percent of the weight comes from the 3D printed PLA plastic. For future iterations we are working with a 3D printable material with a much lower density. We believe that doing so will allow us to further bring down the final weight of the wing without compromising the structural integrity. A different alternative would be to use 3D printed molds to do conventional composite layups. Doing so will allow us to build wings that are entirely made out of CFRP, thus yielding the most optimal wing solution in terms of weight and structural performance.

3.5.3 3D Printed Fuselage Molds

Abstract

The following section presents the design, modeling, and manufacturing of a 3D printed composite part tooling. Our focus was to come up with a proof of concept to highlight the benefits 3D printing could have for the aerospace industry where there is a widespread use of composite materials which currently require costly metallic tooling to produce components. The chosen route for our design was focused on creating a 3D printed tool that could be used to

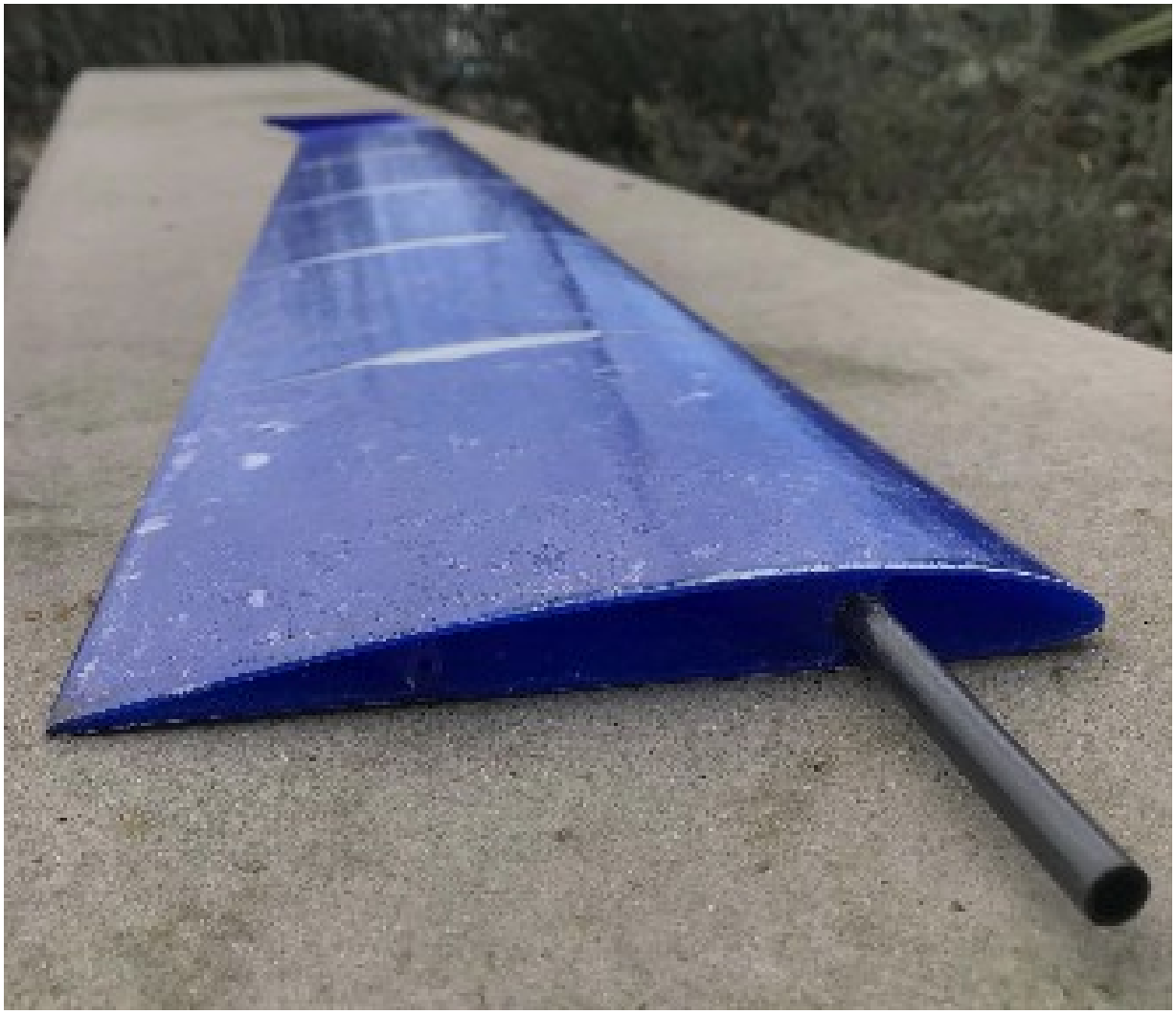

Figure 3.30: Final Fiber Reinforced 3D Printed Wing

fabricate the Box Wing UAV fuselage. Aircraft fuselages normally have complex geometries that can be difficult to machine with traditional methods. By leveraging the advantages of 3D printing we can create a tool that can be quickly produced at a low cost while still conforming to complex geometries. To implement this our team created a tool that would conform to the existing box-wing UAV fuselage. This tool was made from materials that could be dissolved in water which would allow for the fuselage to have reduced weight while also maintaining requirements for an internal payload compartment. Overall, we showed that not only could complex composite

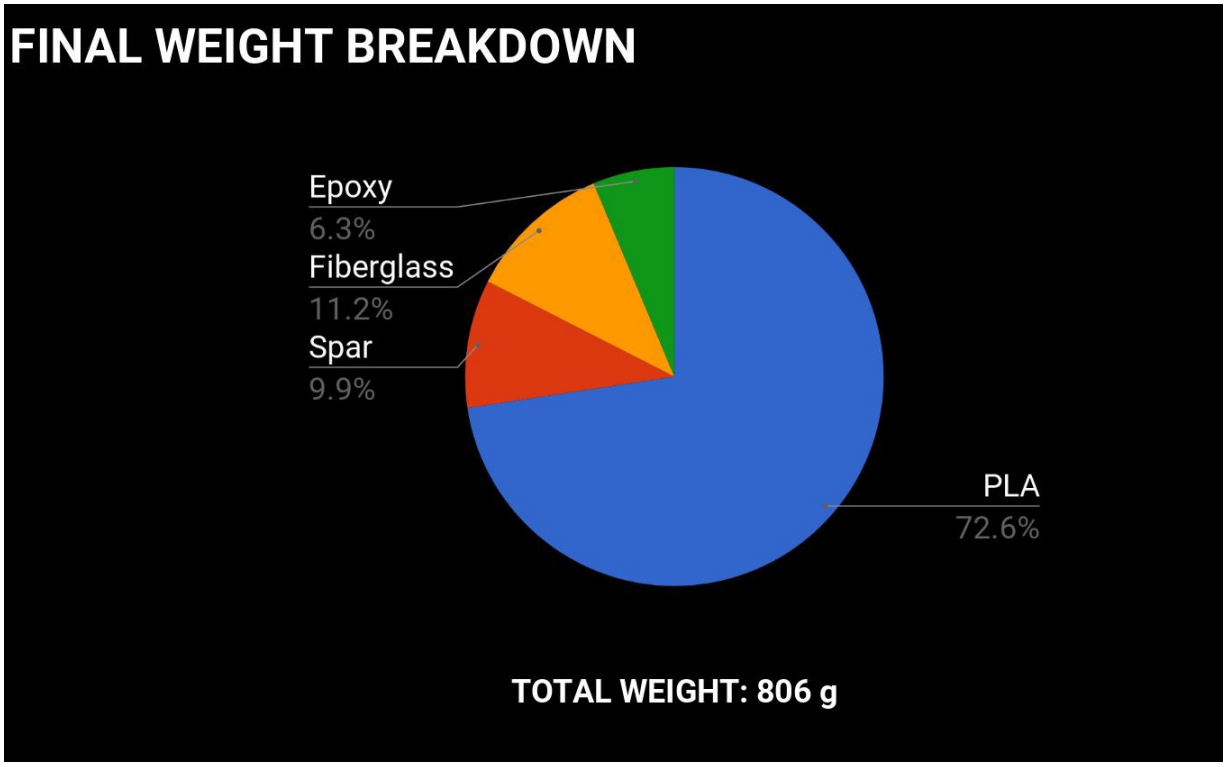

Figure 3.31: Weight Breakdown of Half Wing

components be made using 3D printed tools, they could be made with significant benefits over metallic tooling as outlined in the following sections.

Related Work

There has been a considerable amount of interest into the viability of 3D printed composite part tooling in both academia as well as the aerospace industry. Industry application for 3D printing are significant in that it can provide a cost effective alternative to traditional prototyping as well as potentially for rapid production of final components.

Currently Stratasys Ltd. is the main industry provider of 3D printed tooling surfaces for composite fabrication in both the aerospace and automotive industry. Several case studies have been presented by Stratasys regarding its work with 3D printing. These include providing 3D printed composite tooling solutions for industry leaders such as SSL, Dassault, and Boeing

subsidiary Aurora Flight Sciences [1] [2].

Dassault made use of 3D printed tooling in order to construct interior components for its Falcon 2000LX series of business aircraft. These were parts made of fiberglass as well as traditional carbon fiber sandwich structures and made use of Fused Deposition Modeling (FDM) 3D printing methods. Images of one of these parts can be seen in figure 3.32 below. The results of making the switch to 3D printed tooling showed that there was a significant cost savings while still being able to hold the types of tolerances needed by Dassault Âs´ 2.5mm. Similarly both SSL and Aurora Flight Sciences were able to create multiple prototypes due to design changes quickly and at a low cost due to the benefits of 3D printed tooling.

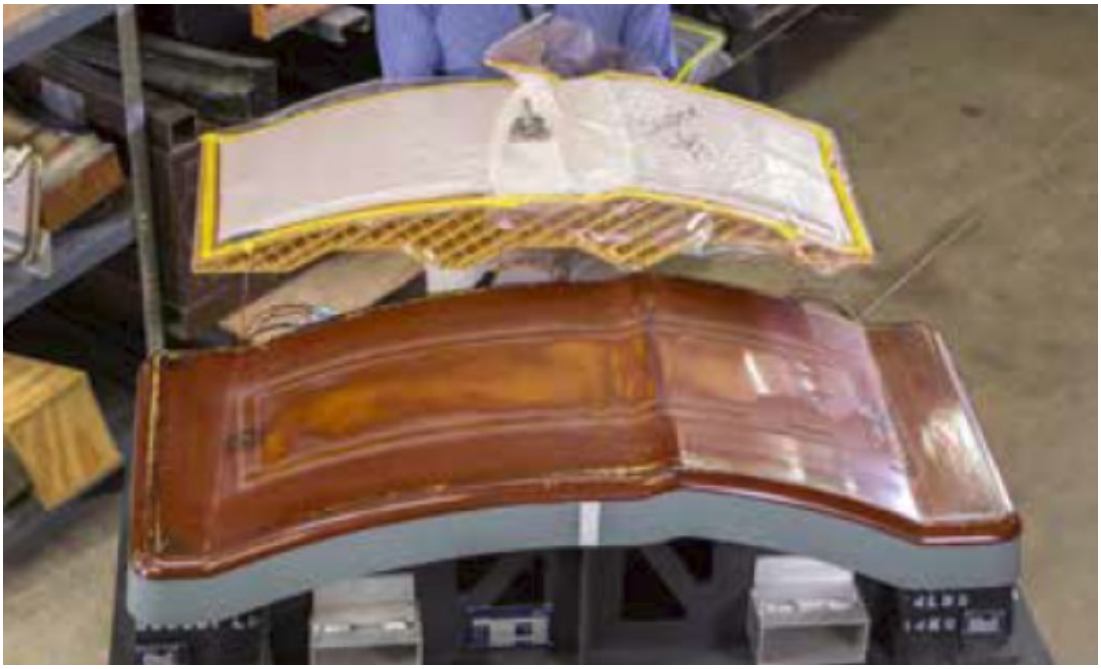

Figure 3.32: Dassault Interior part lay-up molds. 3D printed (top). Traditional (bottom)

In academia there has been a good amount of research supporting industry 3D printed composite tooling. In a paper published by Virginia Polytechnic and State University [4] a design guide was made for developing composite tooling using additive manufacturing specifically regarding the FDM method. The paper outlined testing as well as the material characterization for FDM molds which would be used in high temperature (350F). Finally in another paper

published in the International Journal of Advanced Manufacturing Technology by Stellenbosch University highlighted the use of 3D printed molds for composite part fabrication using the vacuum-assisted resin transfer molding (VARTM) process. This paper showed that several methods could be used in order to increase the life of the 3D printed tools and overall highlighted that 3D printed molds for VARTM components is suitable as well as cost effective as shown by the papers own cost models compared to industry results [3].

Intro and Motivation

The overall objective of this project was to create a 3D printed tool which could be used to manufacture composite parts while showing the benefits that 3D printing can bring when compared to traditional manufacturing methods. Specifically, the tool would be used to manufacture a composite fuselage for the existing box-wing UAV.

Composite materials have been rapidly expanding in the aerospace industry and it is currently common to see a large majority of aerospace structures made of composites due to its high stiffness to weight ratio. Composites are composed of layers of fibers which are combined with matrix material such as epoxy resin. This mixture of materials then undergoes a curing process involving vacuum pressure to form the final part. In order to achieve the desired geometry specific tooling must be made to lay the fiber plies into prior to the curing process. These tools have traditionally been made of aluminum, steel, or invar which must be machined from stock material. An example of these traditional tools can be seen in figure 3.33 below.

When working with complex geometries that have many closed sections with curves on them the machining process for metallic tooling can be prohibitively expensive and will require a significant investment to construct a prototype. These drawbacks limit the amount of design changes that can be made and limits testing of potential components for research and development.

The above mentioned drawbacks can be addressed by switching to 3D printed tooling.

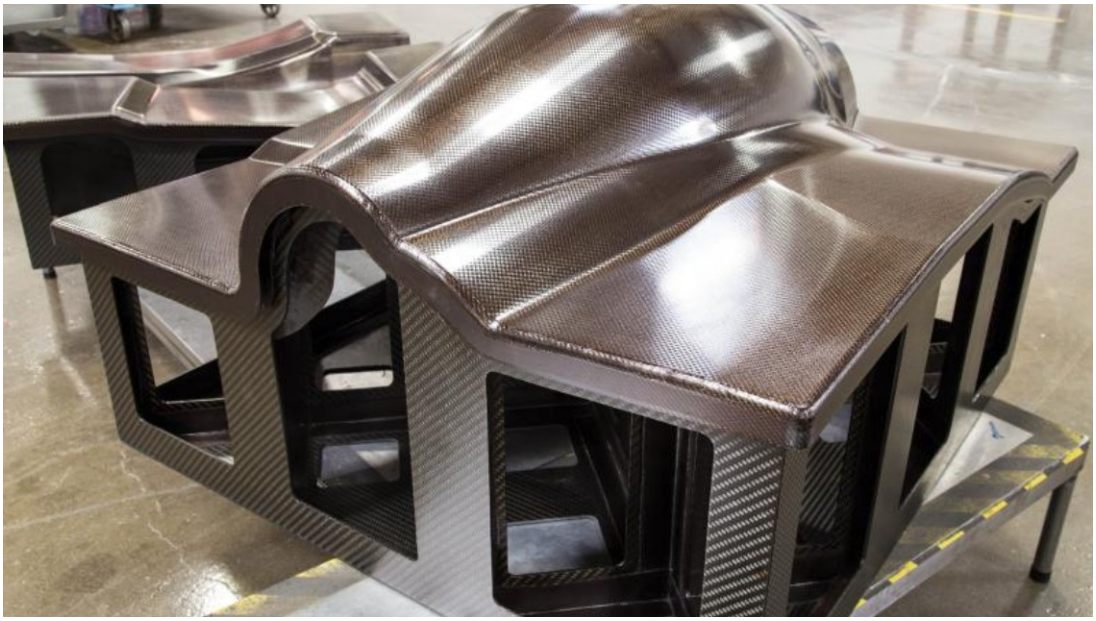

Figure 3.33: Metallic tooling with cured composite

Additive manufacturing methods like 3D printing have the ability to easily create complex geometries, reduce cost of fabrication, and increase turnaround time from concept to prototype (Risk Mitigation). Furthermore, 3D printing can take advantage of a number of different materials such as PVA (polyvinyl alcohol) which can be dissolved in water after the composite part is made. This opens up the ability to make hollow composite components in a timely and cost effective manner.

The use of dissolvable tooling leads into our proposed design. This will be a mold of the fuselage of the box wing UAV which will be printed using PVA as shown in figure 3.34. This mold will have composites laid around it. The composites will be made using resin that can be cured at room temperature so that the PVA will not be exposed to temperatures outside of its operating range. Once the composite is cured it will be placed into a water bath to dissolve the PVA printed tooling.

Because the proposed tool will only include the fuselage and not the wing segments that protruded from the original design the wings will be able to connect to our mold through

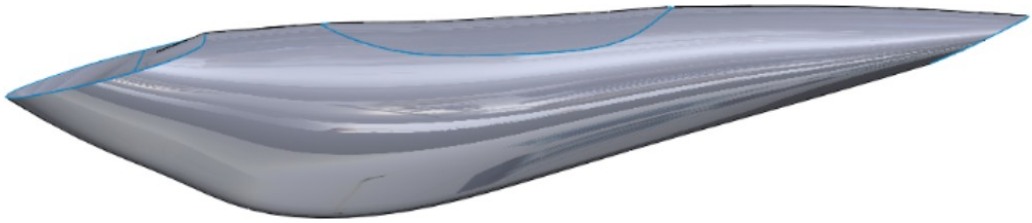

Figure 3.34: CAD of initial design of fuselage tooling.

a 3D printed clip system as shown in figure 3.35. These clips will be bonded to the composite structure after the PVA mold has been dissolved using structural adhesive. Overall, this design provides a solution that addresses the disadvantages of traditional metallic tooling. It is low cost, comparatively quick to fabricate, and adaptable to complex geometries.

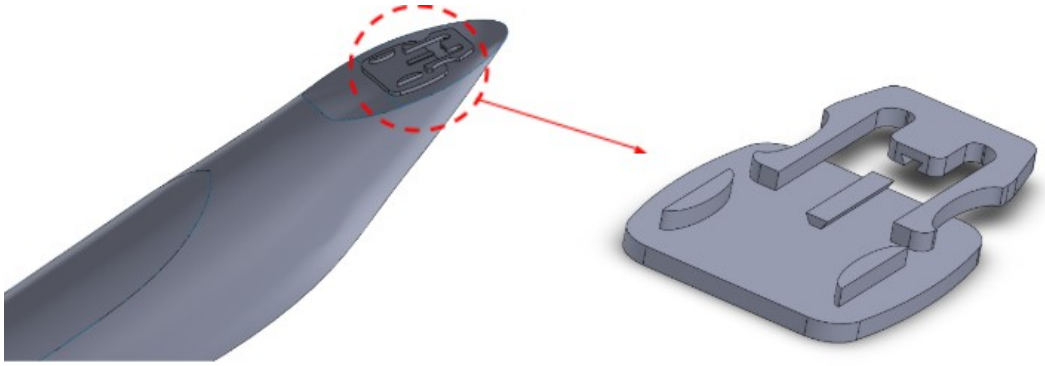

Figure 3.35: CAD of initial design of fuselage tooling.

Tooling Design

The final design for this project was obtained after a few trials of prototyping and design changes. The first design objective was to take the hollow fuselage CAD and invert it to obtain a solid interior CAD that could be 3-D printed and used as a mold. The first iteration of this solid mold CAD was shown in figure 3.34f. This initial design was printed on a small scale and atrial layup was performed to see if any design changes were required. The trial layup revealed

a glaring weakness, it was very difficult to layup on this mold without any aids showing the boundaries of the central opening in the fuselage. To remedy this, the design was altered to have a small extrusion extending out of the central portion of the mold, this would provide a barrier to prevent any composite being laid up over the central portion of the fuselage: figure 3.36 After this design change was implemented and a small scale was printed, it was determined that no other changes were necessary - so this became the final design.

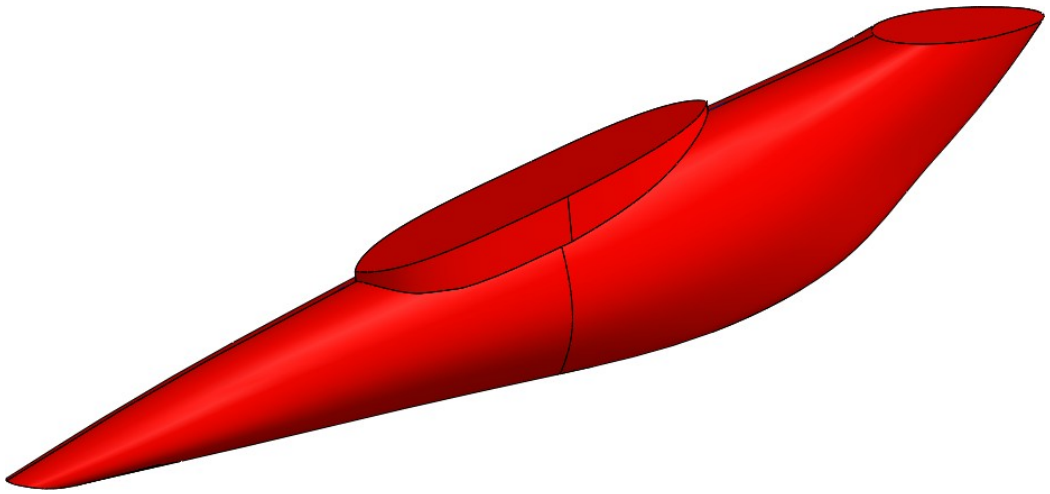

Figure 3.36: Final Design over First Design Prototype.

Simulation and Analysis

Our modelling approach was to create a male tooling for a given aircraft fuselage geometry. The tooling was the main structural component of our print, consisting of the surface on which the composite was to be laid out on and the inner infill of the structure. In an ideal case, the surface of the structure would be non-porous and airtight, but in reality, this is not a valid assumption. Sincethe material has some inherent porosity, we must include that into our simulation assumptions.

We knew that the entirety of the final structure would be subjected to a compressive load of 1 atm, during the vacuuming portion of the composite lay-up process. To test for the amount

of infill needed to sustain the outer geometry, we conducted a small-scale testing and later scaled up the model to finalize the amount of infill needed for our full scale model.

In our CAD, we did account for the inner support geometry, and did a preliminary Solid works FEM to test if the material could withstand 1 atm of pressure. We assumed the surface of the tool would be subject to the vacuum, which would be a pressure load over the entire surface of the tooling. After the FEM, the weakest point in our tool was evaluated to be the skin, with a material yielding mode of failure. This mode of failure is directly influenced by the internal supports, which support the external skin. The pressure load across this stretch of skin is the predicted failure load, with the external layer of the tool being 0.125. Our CAD model was able to handle 1 atm of pressure without yielding with 20% support infill. From the model, we were able to start prototyping with 20% infill as our baseline and continued to improve the model experimentally.

Fabrication

For printing the actual component, there were a few printers available to us. Of these printers, the Ultimaker 2+ and the 3DP 300 Series were the two printers utilized in this project. The Ultimaker was used for the small-scale prototype and the 3DP 300 series was used for the full-scale print. The slicer program used for both printers was Simplify 3D. Due to the shape of the fuselage, printing it was a challenge for two reasons.

Firstly, there is no area on the entire fuselage itself that is flat except for the protrusion we made to act as boundaries for the opening. This means that there will be a significant amount of supports needed throughout the entire fuselage footprint. More supports mean more material, and this was a problem since the PVA sourced only came in spools of 500 grams and the full-scale print was going to take a predicted 1300 grams of material. This would mean the spool of material would need to be replaced twice within the same print. This is two points in time where human error could be introduced into the print process and possibly cause the print to

fail, especially if the material was not changed out in time. To best mitigate this, the amount of material needed for the print was reduced to 800 grams. This came at the cost of reducing the internal infill and the shell thickness (Infill reduced from 30% on the small scale to 10% on the full scale and shell thickness was reduced from 3 layers to 2).

Secondly, the Ultimaker 2+ (used for the small-scale print) does not natively support PVA as a printing material. This meant a custom profile was needed for the print and a few jams occurred in the beginning until the settings were tuned to be just right.

Table 3.8: Print Settings for PVA (water dissolvable material).

Print Setting	Ultimaker 2+	3DP 300 Series
Infill	30%	10%
Infill Type	Hexagonal	Hexagonal
Shell Layers	3	2
Layer Height	0.25 mm	0.25 mm
Nozzle Temperature	220 C	220 C
Bed Temperature	60 C	60 C

Testing

With the CAD finished and understanding of the 3D printers and slicers, a small-scale test will be used for a proof of concept on the sacrificial 3D printed model as well as the composite manufacturing on the complex curvature of the fuselage. The small-scale was decided to be 35% of the actual size so that there would be enough room to layup the carbon fiber around it for the fabrication tests, while also being small enough to barely fit inside the Ultimaker 2+. One thing to note also, was that the part was printed using a 30% infill so that the mold was strong enough to survive under the vacuum pressure needed to cure the composite. After the small-scale part was created, the layup procedure was then applied onto it. Using the scrap dry AS4 carbon fibers and epoxy, the part was then wrapped with long sheets around to contour the airplane fuselage and when that was completed, the whole part was then put under vacuum to cure the composite.

There were many challenges with laying up on the part, but there was a lot that was learned from this small-scale test. One main difficulty was that the carbon fiber sheets that were used to wrap around the 3D part were too long that the fibers wrinkled in a lot of places. To fix this issue, implementing the use of small patches so that the composite wrinkles will be minimized and with the bigger geometry of the full-scale print will make the patches will be even easier to contour to the fuselage. Another challenge was that the opening of the fuselage was not controlled with manufacturing, so the opening of the small-scale was from trying to avoid that general area of the opening based off idealized pictures. This was solved with an elliptical extrusion to provide an area so that the fibers can be easily cut off to provide. A clean fuselage opening. But everything that came out of the small-scale testing was not all bad. One positive that came out well from the test, was that the infill for the mold was more than enough for the vacuum pressure and because of the availability for the PVA material, being able to lower the infill will be a huge benefit when moving toward the full-scale model.

The last time to prove the concept of the sacrificial mold is to see how well the PVA will dissolve with the composite. When putting the part in a bucket of water, the mold did fully dissolve after 24hrs without warming the composite. But from how the part was orientated, the fuselage opening was upright, keeping the vicious solution of the PVA inside the now hollow composite fuselage. This can be easily fixed for the full-scale part with orientating the fuselage opening to allow it to become an egress for the vicious PVA solution.

Results

The tool was printed successfully (Figure: 3.37, but was a more compliant and porous than anticipated due to a smaller shell thickness then was modelled. However, the final structure was still successful in its application as a mold, withstanding the vacuum pressure it was designed for while still holding its outer geometry. It provided an excellent tool to lay up the composite on.

The composite laminate was cured in a way to protect the outer layer with a coat of resin,

Figure 3.37: Final 3D printed Fuselage Mold.

preventing moisture absorption during the mold dissolving process (Figure: 3.38). The overall quality of the mold was up to expectations. The outer layer of the tool can be further finished through sanding or other processes.

Figure 3.38: Final Carbon Fiber Reinforced Polymer Fuselage, mold has not been dissolved yet.

Our manufacturing procedure was followed effectively, with the cutting plan reducing wrinkling in our final product. The upper extrusion provided a clean surface for trimming the excess carbon fiber, allowing for the implementation of the fuselage payload hole. Any additional geometrical defects were removed through trimming.

With the success of the small-scale test of the sacrificial mold provides a proof of concept for this unorthodox composite tool. This will help streamline fabrication processes, reducing time and resources spent towards prototyping in industrial applications. Due to the fact that the moldwas 3D printed, any modifications can be easily made to the mold to accommodate as opposed to

the metal tooling that is commonly used

3.6 Assembly

3.6.1 Wing and fuselage Joint Connection

A challenge of the project was to design the attachment clips for the wings. The inspiration for these attachment clips was taken from the attachments for go-pro camera mounts. Based on this inspiration, the design shown in figure 3.39 was created. This initial design was 3-d printed to see if any design changes were required. For the most part, everything about the design was functional except it was a little flimsy. To make sure it could handle any loads from attachment, the design was changed to make the clips a little bit thicker. After this design change was implemented and printed, it was determined that no other design change was required.

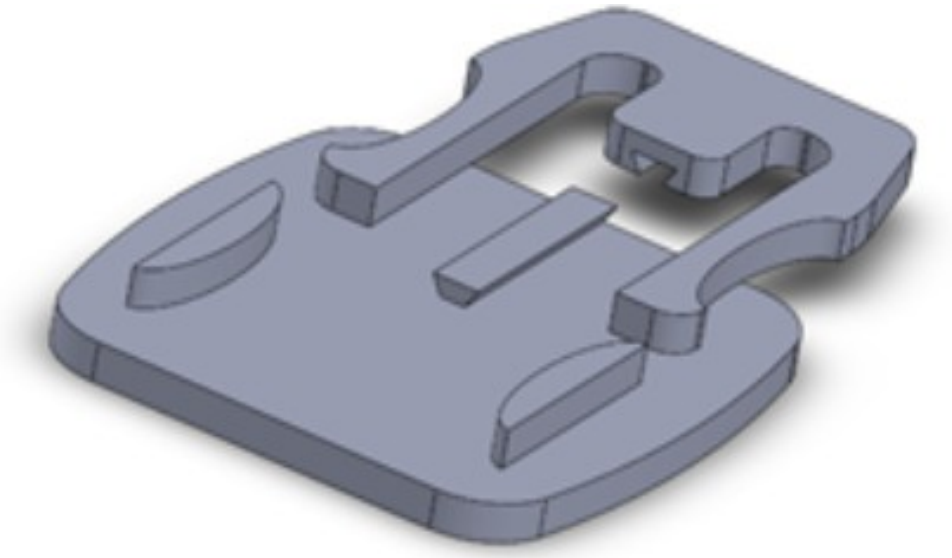

Figure 3.39: Final Design of Wing-Fuselage Attachment Clips.

3.6.2 Wing and winglet Joint Connection

A challenge of the project was to design the attachment clips for the wings. The inspiration for these attachment clips was taken from the attachments for go-pro camera mounts. Based on this inspiration, the design shown in figure 3.39 was created. This initial design was 3-d printed to see if any design changes were required. For the most part, everything about the design was functional except it was a little flimsy. To make sure it could handle any loads from attachment, the design was changed to make the clips a little bit thicker. After this design change was implemented and printed, it was determined that no other design change was required.

The winglet connection, Figure 3.40, consists of a cam lock fitting that restrains the spar from translating out spanwise. This cam lock integration works by having the head of a cam dowel fitting into the cam lock. Then the cam lock is rotated between 90àěř to 180àěř to cause the two prongs as seen in Figure 28 to catch the head of the dowel. The Cam lock has a decreasing radius to restrain the head of the dowel at full rotation. A carbon spar with an inner diameter of greater than or equal to 6 mm was selected to fit a cam dowel in. The cam dowel fits into pultruded carbon spar with 0.4 mm (0.016 in) left for adhesive bond. Typical bonds require 0.005 - 0.030 in for optimal bond strength - anything beyond that the material shear strength becomes unknown as testing was done for that range. After the cam dowel is bonded to the spar, it is inserted into the winglet and the camlock is inserted over the head of the dowl. The camlock has an arrow that should be aligned that it points to the dowel for the acceptance of the head direction. Lastly, the camlock is rotate clockwise to lock the dowel and spar from translating spanwise out of the wing sections.

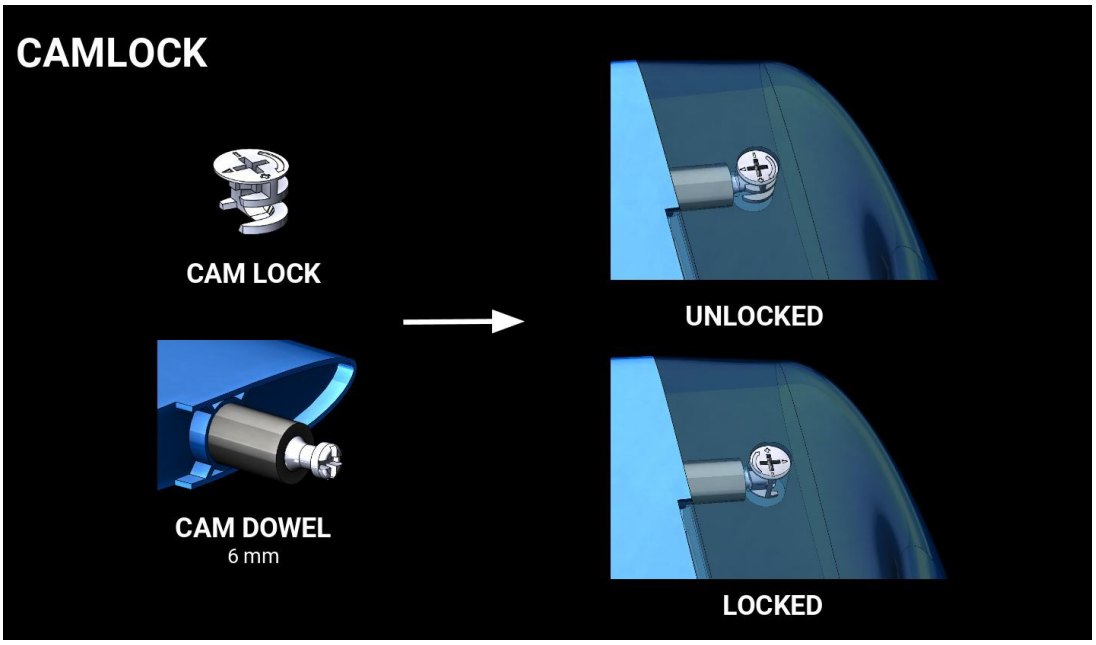

Figure 3.40: Camlock and M6 Cam Dowel Assembly.

Chapter 3, in part, is a reprint of the material as it appears, titled "Towards Design of a 3D Printable Prandtl Box-Wing Unmanned Aerial Vehicle" IEEE Aerospace 2019. De Vivo, Luca; Tran, Danny; Kuester, Falko. The dissertation author was the primary investigator and author of this material.

Chapter 4

Robotic Systems and Control Design

4.1 Robotic Systems and Control Design

4.1.1 Quad copters vs Fix Wings

The advent and evolution of Unmanned Aerial Vehicles (UAVs) and photogrammetry techniques has provided the possibility for on-demand high-resolution environmental mapping. Ortho-images and three-dimensional products such as Digital Surface Models (DSMs) are derived from the UAV imagery which is amongst the most important spatial information tools for environmental planning. The two main types of UAVs in the commercial market are fixed-wing and multi-rotor. Both have their advantages and disadvantages including their suitability for certain applications. Fixed-wing UAVs normally have longer flight endurance capabilities while multi-rotors can provide for stable image capturing and easy vertical take-off and landing.

If you want to get a small camera in the air for a short period of time, then it is hard to argue with a multi-rotor, figure 4.1. They are the easiest and cheapest option for getting an eye in the sky, and because they give you such great control over position and framing they are perfect for aerial photography work.

The downside of multi-rotors is their limited endurance and speed, making them unsuitable

Figure 4.1: Multi-Rotor: DJI Matrice 210.

for large scale aerial mapping, long endurance monitoring and long-distance inspection such as pipelines, roads and power lines.

Although the technology is improving all the time, multi-rotors are fundamentally very inefficient and require a lot of energy just to fight gravity and keep them in the air. With current battery technology they are limited to around 20-30 minutes when carrying a lightweight camera payload. Heavy-lift multi-rotors are capable of carrying more weight, but in exchange for much shorter flight times.

Fixed-wing drones, Figure 4.2 use a wing, like a normal airplane, to provide the lift rather than vertical lifting rotors. Because of this they only need to use energy to generate forward speed, not hold themselves up in the air, so are much more efficient.

For this reason they are able to cover longer distances, map much larger areas, and loiter for long times monitoring their point of interest. In addition to the greater efficiency, it is also possible to use gas engines or fuel cells as their power source, and with the greater energy density

Figure 4.2: Fix Wing: AeroVironment RQ-20B Puma.

of fuel many fixed-wing UAVs can stay aloft for 16 hours or more.

The main downside of a fixed-wing aircraft is obviously their inability to hover in one spot, which rules them out for any general aerial photography work. This also makes launching and landing them a lot trickier, as depending on their size you can need a runway or catapult launcher to get them into the air, and either a runway, parachute or net to recover them safely again at the end. Only the smallest fixed-wing drones are suitable for hand launch and belly landing in an open field. Other downsides are their higher cost, and that it is much more difficult to learn the ropes with fixed-wing drones.

4.1.2 Vertical Take Off and Landing Fix Wings

Merging the benefits of fixed-wing UAVs with the ability to hover is a new category of hybrids which can also take off and land vertically.

There are various types under development, some of which are basically just existing fixed-wing designs with vertical lift motors bolted on. Others are tail sitters aircraft which

look like a regular plane but rest on their tails on the ground, pointing straight up for take off before pitching over to fly normally, or Tilt rotor plane types where the rotors or even the whole wing with propellers attached can swivel from pointing upwards for takeoff to pointing horizontally for forward flight.

Many of these configurations were tried in the 1950s and 60s for manned aircraft, but they proved too complex and difficult to fly, with some disastrous results. With the arrival of modern autopilots, gyros and accelerometers, suddenly these wacky types are feasible because the autopilot can do all the hard work of keeping them stable, leaving the human pilot the easier task of guiding them around the sky.

There are only a handful of hybrid fixed-wing aircraft currently on the market, but you can expect this to be a much more popular option in the coming years as the technology is perfected, demand and public acceptance for urban air mobility grows as well as governmental institutions allocate the necessary funding, build the infrastructure, and create legal framework for a massive adoption of on demand and private flying vehicles as well as a broad range of drone services such as package delivery, emergency response and monitoring among others.

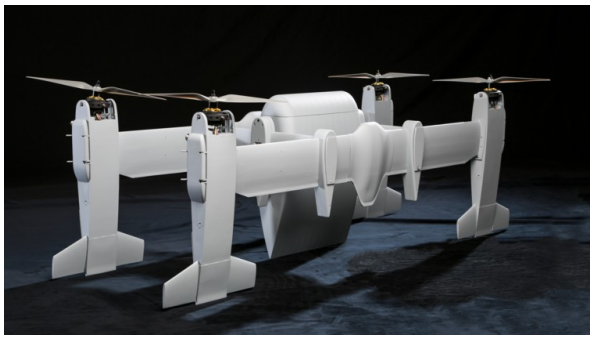

(a) Bell Autonomous Pod Transport (APT)

(b) BlackFly: The latest attempt at flying car

Figure 4.3: State of the Art: Vertical Take Off and Landing Fix Wing

4.2 Prandtl Box Wing VTOL Enabled

One of the main goals of the design of the platform was the capability of Vertical Take Off and Landing (VTOL). As seen on the previous section there has been many attempts to provide fix wing aircraft the capability of taking off and landing like a helicopter, in a small confined area. We have designed our aircraft with four propulsion systems (Motor, Propeller and ESC) placed at a strategic location along the wings in order to allow us to articulate the platform into different headings using thrust differential to create moment forces around the center of gravity of the aircraft. All this without the need of tilt rotors that use extra servo motors and without compromising flight efficiency. The aircraft will achieve VTOL and cruise flight by following these four different flight phases as seen in (Figure: 4.9):

1. Take off & Landing Rotations.
2. Vertical Climb & Descend.
3. Mid Air Rotation.
4. Cruise Flight.

Controlling an Aircraft by Thrust Differential

Story of DC-10 using it for emergency landing

In the history of aviation there have not been many attempts to design a fix wing aircraft which controls depended on the thrust generated by the propulsion system. Usually this thrust force is used for carrying the aircraft forward so Lift can be generated by the wings. A primary reason that prevents airplanes from using thrust forces to control roll, pitch or yaw is the time of response and reaction of motors to abruptly change these forces.

The goal was to find a pair of motor propeller that allowed for rapid changes of lift forces so quick changes of attitude are achieved.

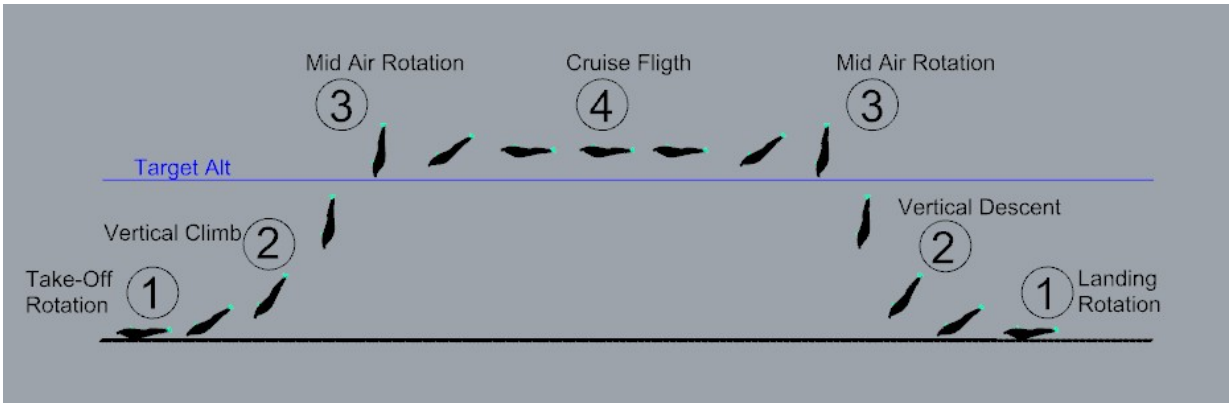

Figure 4.4: Mission Plan of Prandtl Box Wing VTOL.

4.3 Kinematic and Dynamic Models

The main four forces present on a flying aircraft are Lift, Drag, Weight, and Thrust. All the forces acting on the Prandtl Box Wing UAV are represented in (Figure: 4.5) where it can observe the lift contribution, shown in blue, of each wing as well as the drag contribution, shown in red, mainly from the wings, fuselage, landing gear and propulsion systems. The weight forcesacts towards the center of the earth, usually pointing downwards at the center of gravity of an object, and is a resultant of all the individual weights: payload, batteries, avionics, airframe, and propulsion. The final force is thrust, and it is provided by each of the four propulsion systems. These forces act at the leading edge of the wings pointing forward. We can think of lift and thrust as positive forces and drag and weight as negative forces. All these forces need to be in balance and the variation of these, specially thrust differentials and deflected control surfaces, allow us to articulate the aircraft in multiple positions and headings with the final goal of being able to VTOL and cruise flight without the need of multiple tilt rotor mechanisms or extra motors. We have derived the kinematic, dynamic and momentum equations that are needed to generate a control algorithm capable of allowing four different flight faces (Figure: 4.9) and these will be described in the following subsections.

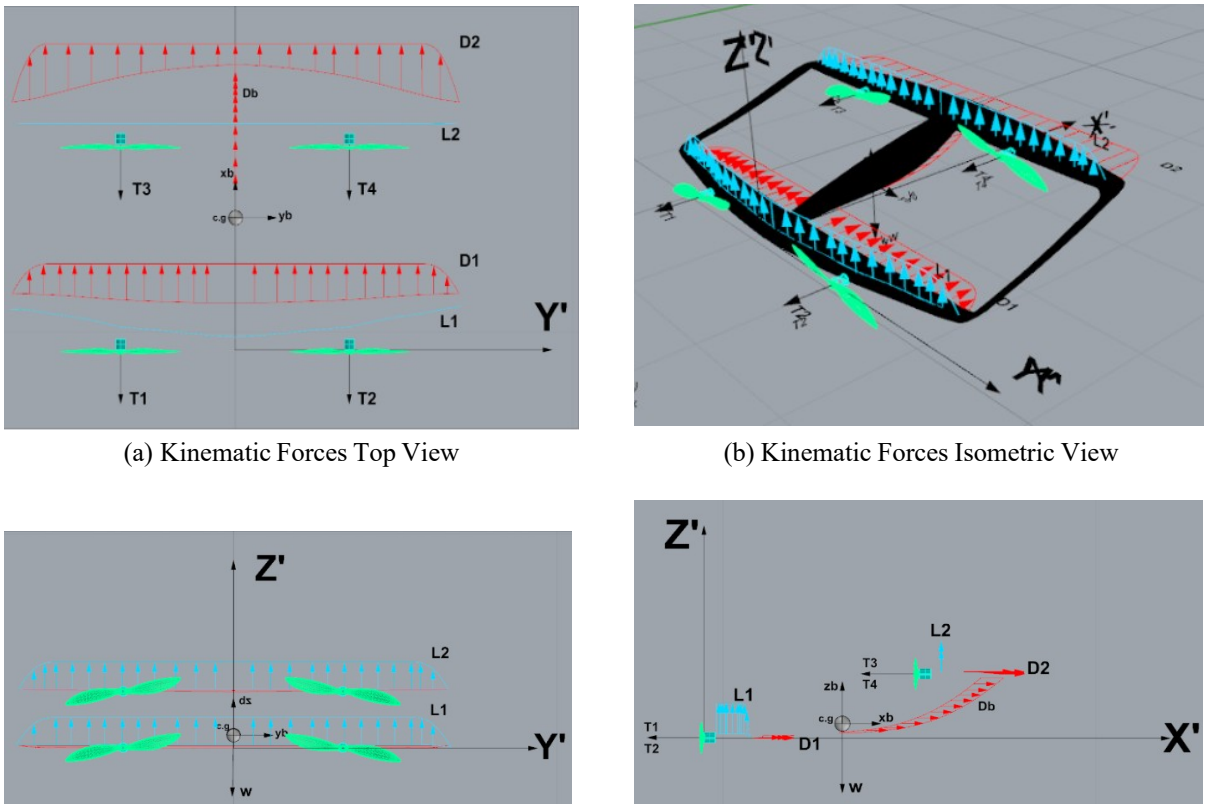

(a) Kinematic Forces Top View

(b) Kinematic Forces Isometric View

(c) Kinematic Forces Front View

(d) Kinematic Forces Side View

Figure 4.5: Kinematic Forces Acting on UAV at Cruise Flight

4.3.1 Phase 1: Take off & Landing Rotations.

The first phase of the flight is the take off. As can be seen in (Figure: 4.6) the aircraft will have an initial positive angle of attack (AOA) of around 30 deg that will be provided by thedesign of the fuselage and landing gear. Using the initial positive AOA the motor forces, whereF1 is the resultant force if the two front motors and F2 is the resultant of the two back motors. These forces will provide the necessary vertical force to get the aircraft airborne. Then a thrust differential between the F1 and F2 forces will generate a moment force around the CG (Mcg < 0)that will cause the airplane to rotate counterclockwise for a nose pointing up movement. At thispoint the aircraft will enter the second flight phase, vertical climb.

The rotation for landing will come after the vertical descend and will have similar dynamics as phase 1. Once the airplane reaches a low altitude the phase one rotation will kick in

and one more time thrust differential will be employed to rotate the airframe around its center of gravity. The difference between taking off and landing rotations is that in taking off (F1 > F2) and during landing (F1 < F2), meaning that during the landing rotation phase the aircraft will see a clockwise rotation (Mcg > 0) which will cause the nose to rotate downwards. The following equations express the kinematic, dynamic and momentum equation of phase one.

Static Equilibrium for phase 1:

$$F_{x_1} = F_1 \times cos(\alpha)$$

$$F_{y_1} = F_1 \times sin(\alpha)$$

$$where: F_1 = F_{T_1} + F_{T_2}$$

$$and: 30deg \leq \alpha \leq 90deg$$

Dynamic Balance for phase 1:

$$X: F_{x_1} + F_{x_2} - F_f = 0$$

$$Y: F_{y_1} + F_{y_2} + N - G = 0$$

$$Z: 0$$

$$Where: G = mgand, F_f = \mu N$$

Theorem of moment of momentum for phase 1:

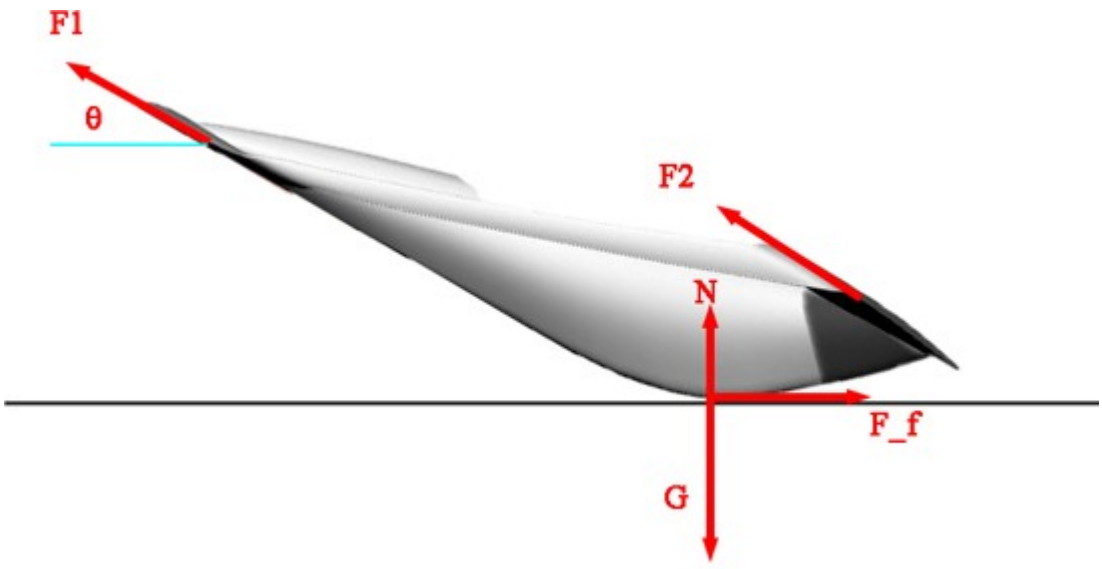

Figure 4.6: Forces Diagram of Phase 1: Take off & Landing Rotations.

4.3.2 Phase 2: Vertical Climb & Descend.

Once phase 1 is completed and the aircraft nose is completely pointing up to the sky phase 2 will take place. The primary goal of this phase is to stabilize vertical flight using all four motors to create equilibrium and propel the aircraft upwards using only thrust from the propulsion systems. It is of primary importance that the four motors achieve equilibrium (F1 = F2 and Mcg = 0) and bring the aircraft upwards in a control and stable manner. Phase 2 will originate close to the ground and it will end once the airplane reaches a predefined altitude. Once this altitude is reached phase 3 will kick in where the airplane will be brought to horizontal position for the cruise flight configuration. The following equations express the kinematic, dynamic and momentum equation of phase two.

Dynamic Balance for phase 2:

$$X : F_{x_1} + F_{x_2} - F_f = 0$$

$$Y : F_{y_1} + F_{y_2} + N - G = 0$$

$$Z : 0$$

$$Where : G = mgand, F_f = \mu N$$

Theorem of moment of momentum for phase 2:

Figure 4.7: Forces Diagram of Phase 2: Vertical Climb & Descend.

4.3.3 Phase 3: Mid Air Rotation.

As stated above the goal of phase 3 is to bring the aircraft to its cruise flight position or phase 4. Phase 3 will kick in right after the airplane have reached a desired altitude for cruise flight. At this point the propulsion system will generate a thrust differential between the front

and back systems once again. At the beginning the rotation will be clockwise meaning the forces will need to be (F2 > F1 and Mcg > 0), while at the end of the cruise phase the forces required to bring the aircraft back into vertical position will have to be (F1 > F2 and Mcg < 0) to create a counter clockwise that will cause the nose of the plane to point upwards. The main different between the initial step and ending step of phase 3 is that there will be a breaking step during the last moments of phase 4 (cruise flight) to kill much of the horizontal velocity and momentum so the aircraft can easily rotate.

4.3.4 Phase 4: Cruise Flight.

The last phase to be described is phase 4 where the airplane will enter the cruise flight configuration. This will come right after initial phase 3 have concluded and the wings are in their horizontal position. The aircraft here will be required to provide forwards thrust to generateairflow over the wings which will create the necessary lift forces to maintain the airplane aloft. At this point the global forces will be in equilibrium (Lift = Weight and Thrust = Drag). The next step is to control the 3 motions of a regular fix wing airplane (Roll, Pitch and Yaw). We will achieve this by combining the forces generated by four control surfaces located on each wing section which will be actuated by servo motors as well as thrust differential provided by thepropulsion systems. Roll and Pitch will be mainly controlled using surfaces and its respective servo motors while yaw will be controlled using thrust differential of the propulsion system.

4.3.5 Control Model and Algorithm

4.4 System Architecture

The system integration relied on having inputs from the pilot and base station, while outputs to the control arms and motor all went through the flight computer. The system architecture, provided by James Strawson, the developer of the robotic cape and software, can be seen in Figure 4.10. We used the BeagleBone Black is an all-in-one Linux-based computer for robotics, integrating onto a single small (3.5" x 2.15") board the Octavo OSD3358 microprocessor together with wifi/bluetooth, IMU/barometer, power regulation and state-of-charge LEDs for a 2-cell LiPo, H-Bridges, and discrete connectors for 4 DC motors + encoders, 8 servos, and all of the commonly-needed buses for additional peripherals in embedded applications. The user Pulse Width Modulated (PWM) inputs are transmitted wirelessly via the Digital Signal Modulation (DSM) radio to the flight control unit, which sends a signal to actuate the motor and servo arms. The data acquisition sensors consisted of an Inertial Measurement Unit (IMU), barometer, speed sensor, compass, GPS, laser rangefinder, and voltage meter. This data is transmitted wirelessly to the ground station via a two-way long range telemetry unit (RFD900). The user can view the visualized data in an easy User Interface (UI). Once autonomous control features are fully implemented, the user will also be able to specify a flight path by setting GPS way-points that can be uploaded to the UAV via the RFD900 telemetry before or during flight.

4.4.1 Navigation and Communication

- ADD GPS information - ADD Radio and Telemetry Communication

The communication between the sensors, inputs, and outputs are summarized in Figure 4.10. The telemetry communication to the ground station was achieved through the integration of a communication module to the BeagleBone Black Robotics Cape. The device tree overlay, a

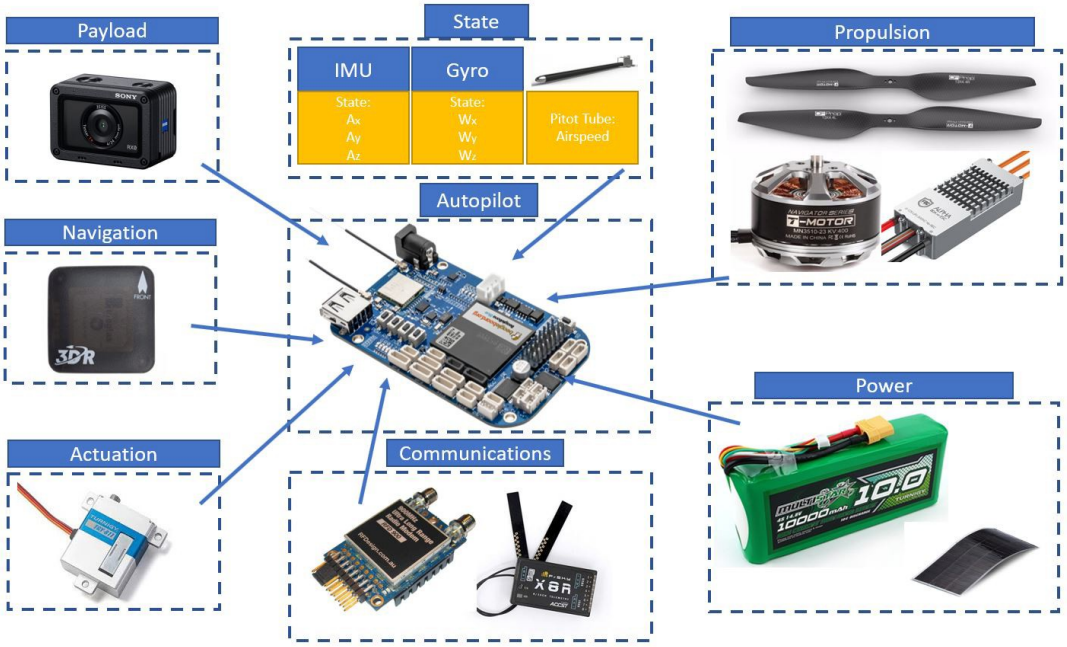

Figure 4.8: Aircraft Robotic Architecture.

file that specifies a set of rules that will govern which hardware modules will be assigned to a header pin, was modified to allow the BeagleBone Black Robotics Cape to communicate with the communication module over Universal Asynchronous Receiver/Transmitter (UART). UART is a communication protocol allowing for asynchronous digital communication between devices. The firmware to initialize the communication module was then written, and a header file that hosts UART initialization and text strings transmission functions was created. The UART pins are connected to the RFD900 an easy-to-use, high-range wireless modem, which receives UART data such as roll, pitch, yaw angles, altitude, and speed from the Beaglebone Black and transmits it to the ground station.

4.4.2 Propulsion System

The selection of the propulsion system was a result of a detailed performance-and-efficiency analysis performed over a large database of commercially available brushless DC

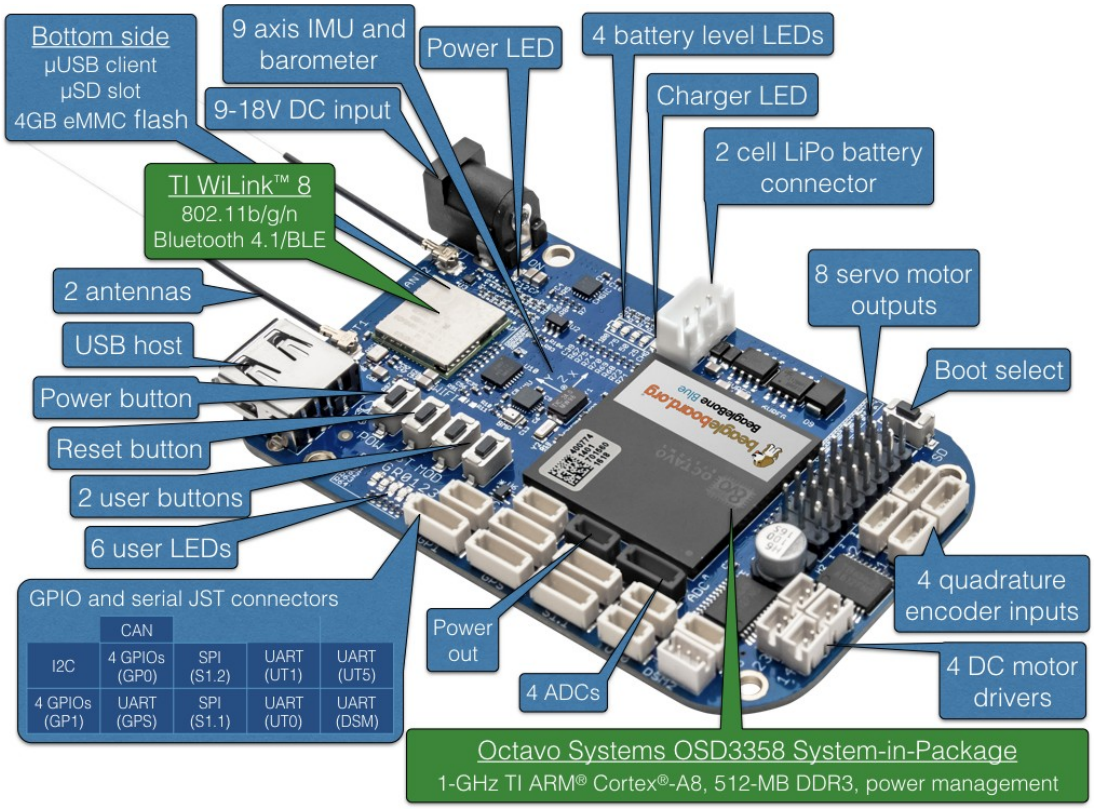

Figure 4.9: Schematics of BeagleBone Blue Computer.

motors and propellers. We analyzed each motor-propeller pair and evaluated their ability to cope with the functional requirements. First, the propulsion system had to be able to produceat least twice the thrust for VTOL procedures, and second it had to deliver the necessary thrust for horizontal flight while maximizing efficiency. We based our decisions by combining simple calculations with efficiency plots provided by the manufacturers. Once a champion was identified, we ran an in-house efficiency test to derive our own propulsion thrust and efficiency plots. This information was then used to build the control algorithm feedback loop since it required specific information on the performance of the propulsion system at different throttle percentages.

We selected a set of motor/propeller based on a 4 motor configuration, which satisfied both the VTOL 2800 grams and horizontal flight 150 grams requirements. The motors are the the U5 KV400 with 16x5.4 carbon fiber propellers both manufactured by T-Motor. This pair

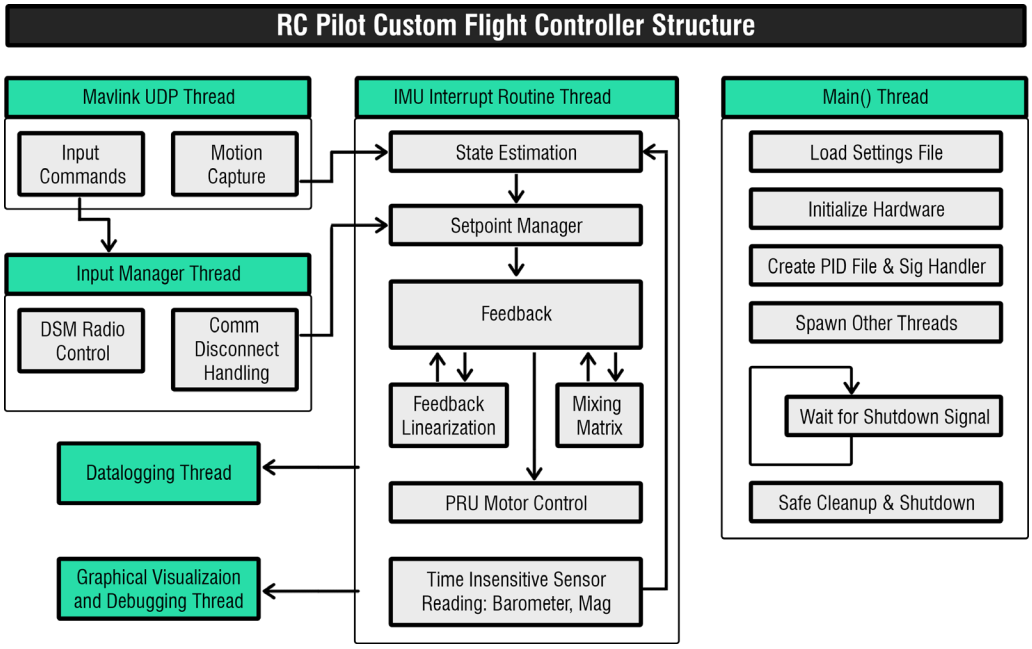

Figure 4.10: RC Pilot Custom Flight Controller Architecture.

configuration provides a maximum thrust of 2850 gram-force each which is just enough to provide vertical take off and landing capabilities while maintaining good performance during horizontal flight.

4.4.3 Payloads

Visual, Thermal, and Multispectral cameras are the three main payloads intended to be used while flying this platform. The visual camera will provide RGB data while thermal and multispectral will provide bands of data in the Near-Infrared (NIRS). In the future we would like to incorporate other sensors such as small Lidars, compact hyperspectral cameras, and laser-based gas sensors. Doing so will expand the capabilities of this UAV making it a perfectly suited vehicle for large scale infrastructure inspection, mineral exploration, and environmental monitoring.

Chapter 4, in part, is a reprint of the material as it appears, titled "Towards Design of a 3D Printable Prandtl Box-Wing Unmanned Aerial Vehicle" IEEE Aerospace 2019. De Vivo, Luca; Tran, Danny; Kuester, Falko. The dissertation author was the primary investigator and author of this material.

Chapter 5

Cholla Cactus: Engineering Materials and Structures Guided by Nature

5.1 Biomimicry

— Into to Biomimicry and the design process

"We must draw our standards from the natural world. We must honor with the humility of the wise the bounds of that natural world and the mystery which lies beyond them, admitting that there is something in the order of being which evidently exceeds all our competence."

Vaclav Havel, president of the Czech Republic

Over the past few years, it has become more and more common to find researchers and scientists looking into natural species for insights that lead to discoveries or new ways of doing things. We have seen numerous examples of men and women who are exploring nature masterpieces - photosynthesis, self-assembly, natural selection, self-sustaining ecosystems, eyes and ears and skin and shells and fins, talking neurons, natural medicines, and more-and then copying these designs and manufacturing processes to solve our problems. This is what Janine Benyus called their quest biomimicry, the conscious emulation of life's genius. Innovation

inspired by nature

— Years of evolution stored in the biggest library on earth

"We Luckily for us, our planet mates the fantastic meshwork of plants, animals, and microbes have been patiently perfecting their wares since March, an incredible 3.8 billion years since the first bacteria. In that time, life has learned to fly, circumnavigate the globe, live in the depths of the ocean and atop the highest peaks, craft miracle materials, light up the night, lasso the sun energy, and build a self-reflective b rain. Collectively, organisms have managed to turn rock and sea into a life-friendly home, with steady temperatures and smoothly percolating cycles. In short, living things have done everything we want to do, without guzzling fossil fuel, polluting the planet, or mortgaging their future. What better models could there be?" [Ben09] How much we still do not understand?

Furthermore, why are we not putting more effort into preserving these species and their environments so we can continue reading the biggest library on earth? According to the UN Environment Programme, Scientists estimate that 150-200 species of plant, insect, fish, bird, and mammal become extinct every 24 hours. This is nearly 1,000 times the natural or background rate and, say many biologists, is higher than anything the world has experienced since the vanishing of the dinosaurs nearly 65 million years go. [uni19] With this rate of extinction also goes extinct the vast amount of information that nature could provide us, I like to think as if this big library with millions of books is slowly burning and there are no enough firefighters to fight the fire.

5.1.1 The Biomimicry Design Spiral

Even tho the information is out there; this does not imply that it would be easy to translate nature knowledge into viable technology and products. It is the quest and mission of a biomimicry practitioner to unveil nature knowledge and learn how to apply these patterns into its design. The Biomimicry Institute have been training scientist and designers on how to learn best and emulate nature principles and designs. One of the tools they use to guide designers over the design process

is what it is called The Biomimicry Design Spiral.

The spiral geometry can be found at all scales of nature, and apparently across the universe. Though we call them cycles, natural processes are also spirals, because, over time, the endpoint of any cycle is never the same as the starting point. Spirals are everywhere in nature because they perform so many functions. It is no wonder, then, that when Carl Hastrich set out to create adesign process for biomimicry, he turned to the spiral. That is very fortunate for all of us, becausethe spiral design process not only allows us to tap into the power of nature, it allows us to tap into the power of our creativity and imagination, exactly what we need to tackle the tremendouschallenges that we face today.

The Biomimicry Design Spiral is a step-by-step process for turning nature strategies into innovative and sustainable design solutions. The Biomimicry Design Spiral was developed in 2005 by Carl Hastrich, an industrial designer. He was one of a cluster of devoted individuals that we can thank for building the foundations for biomimicry as we know it today. Hastrich took a standard design process, added the different steps needed for biomimicry, and then, emulating one of nature pervasive patterns, he turned the process into a spiral.

The Biomimicry Design Spiral is shown in figure 5.1 is used when you know what problem you are trying to solve. To use this method, you start with the Identify step, where the objective is to identify the functions that your design needs to perform what you want your design to be able to do. Once you have created a list of functions, you Translate those functions into words or terms that make sense in the biological world. Next, you Discover strategies that nature uses to accomplish these functions. (This is the step most unique to biomimicry.) In the Abstract step, you reverse engineer the strategies you have discovered and describe how they work in terms that make sense to your design profession. The Emulate step is where you use your professional skills to create a design solution based on emulating one or more of the strategies that you have discovered and abstracted. In the Evaluate step, you do three things. One is to evaluate your design solution against your original design brief. Another is to evaluate your design against

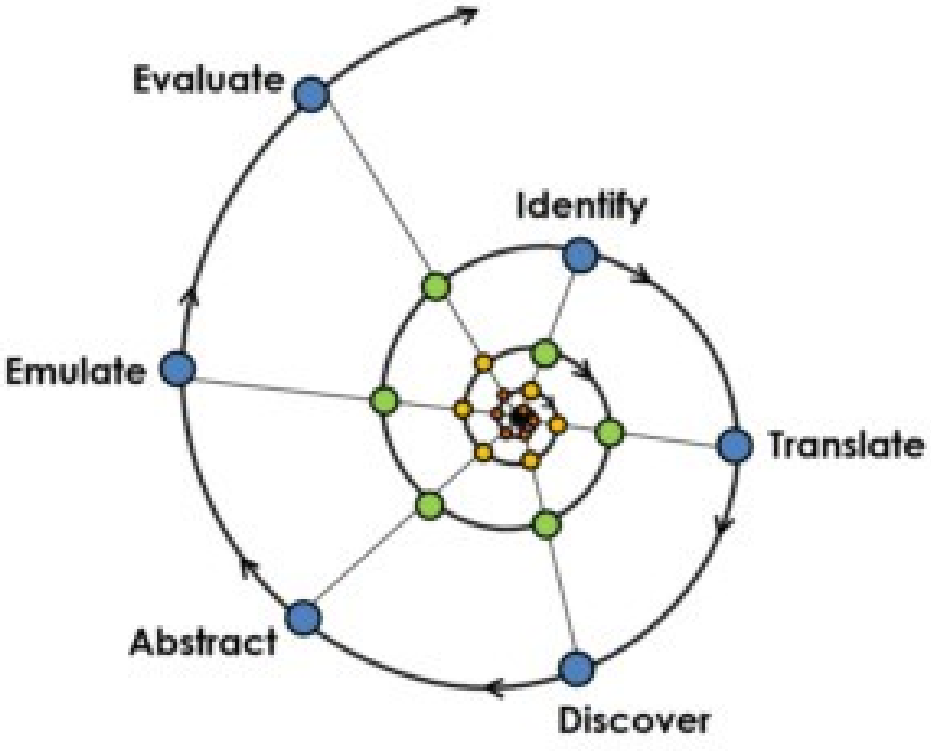

Figure 5.1: The Power of the Biomimicry Design Spiral, adopted from Carl Hastrich (2005) via The Biomimicry Institute.

Nature Unifying Patterns (or Life Principles), nature rules for sustainability. The third is to reflect on the many ideas and lessons that emerged in the previous steps and strategize how you want touse the next lap or laps around the spiral and you will likely take many laps! [DeL16]

So in one lap around the Biomimicry Design Spiral you will:

1. Identify one or more functions that you want your design to perform,
2. Translate those functions into biological terms,
3. Discover strategies that nature uses to perform those functions,
4. Abstract those strategies back into technical terms,

5. Emulate those strategies in your design solution,
6. Evaluate your design against your design brief and Life's Principles, and then decide how you want to use your next lap.

Another method to consider when using biomimicry to guide us through the design process is to look at Nature Unifying Patterns. The idea focused on identifying persistent patterns in how organisms function and interactions that contribute to resilient ecosystems. These patterns are worth paying attention to because they can have profound implications for human design. Ifwe aim to build a sustainable world (i.e., compatible with life on Earth over the long haul), we need to consider nature lessons in a system's context.

Nature unifying patterns is the Biomimicry Institute's attempt to identify the ten most essential lessons from the natural world that should be considered as part of a design process. They called them, nature unifying patterns because examples of the patterns can be found broadly across the majority of life on Earth. We should Consider these patterns at the start of any design process and return to them throughout the process as an evaluation tool [bio]. The ten nature unifying patterns defined by the Biomimicry Institute are:

1. Nature uses only the energy it needs and relies on freely available energy.
2. Nature recycles all materials.
3. Nature is resilient to disturbances.
4. Nature tends to optimize rather than maximize.
5. Nature provides mutual benefits.
6. Nature runs on information.
7. Nature uses chemistry and materials that are safe for living beings.

8. Nature builds using abundant resources, incorporating rare resources only sparingly.
9. Nature is locally attuned and responsive.
10. Nature uses shape to determine functionality.

In my work, I try to use as many of these patterns as possible. I have found that the most common principles used during my studies and designs were; Nature tends to optimize rather than maximize: Through the chapters of this work, we utilized a series of software to optimize various aspects of our design. We optimized the structure and shape of the human leg for our work on 3D printable prosthetics. Also, we optimized the structural and aerodynamic performance of wings and fuselage of our Prandtl Box Wing UAV.

Nature runs on information. in a similar matter on how we used optimization software we used a broad range of data acquisition tools to gather information from the real world. Which then allowed us to analyze natural materials, the human body, and a broad range of structural systems.

Nature builds using abundant resources: Here, our abundant resource was Polymers thanks to their affordability, durability, and mechanical performance plastics have become part of our everyday life. Plastics are also the most common material used in the 3D printing industry, and it can be found in many forms. Plastics are ideal for additive manufacturing thanks to their thermal properties that allow them to become moldable at higher temperatures but hold shape, form, and structural integrity once the temperature is cooled down.

Nature uses shape to determine functionality. During our design journey, we were faced with many challenges and opportunities to innovate and push the boundaries. In or work of the Cholla Cactus, we were amazed by nature's way of designing and building long-lasting resilient structures using a combination of topology optimization and fiver orientation optimization. We found that the plant is not only capable of resisting the harsh desert environment, but it is also able to cope with all its biological functions like water and nutrient transfer and defense mechanisms.

During or work on the prosthesis, we utilized the human body morphology to design structural components capable of withstanding ISO standard loads as well as providing the necessary flexibility for functional mobility. Here the shape of the individual components determined the functionality of the overall system. Lastly, for the design of the Prandtl wing, we were faced with the challenge of designing a wing system that was aerodynamically efficient as well as structurally sound, the shape of the box wing proved to be extraordinary at providing benefits on both fields. In addition to the wing system, the shape of the fuselage was designed having aerodynamic performance in mind while hosting all the avionics and robotic architecture. At the same time, it was also designed to provide the aircraft with the ability to smoothly rotate for vertical take-off and landing.

I want to point out that Biomimicry has served me as a scientist, engineer, and designer through my research endeavors, and I would not have accomplished the results presented in this work without nature knowledge and mentorship. A clear example of my attempts to use Biomimicry as a mentor is the work we realized on the structural properties of the Cholla Cactus, as it will be described in the following sections. During this study, we worked alongside the Biomimicry Spiral to define a species, extract information, understand this information, and apply it to engineering design. The process in which we achieved this is described in the list below:

Biomimicry method used for understanding the structure of biological materials and its applications:

1. Select Species of Interest → Cholla Cactus
2. Imaging Data Acquisition → *Photography, Laser, CT and EM.*
3. Imaging Data Process → *Agisoft, Scan Studio and Amira.*
4. Imaging Data Analysis → *Formulate nature algorithm.*
5. Mechanical Test → *Compression, Tension, Torsion.*

6. Material Characterization → *Young & Shear Modulus and Poisson ratio.*

7. Bioinspired Design → *CAD, MATLAB, Visual Programming.*

8.. Validation → *FEA, CFD, and Optimization methods.*

9. Manufacture and Testing → 3*D printing and Structural Test.*

10. Design Applications → *Prosthesis, Aircraft Fuselage and Wings.*

5.2 Cholla Cactus Frames as Lightweight and Torsionally Tough Biological Materials

Biological materials tested in compression, tension, and impact inspire designs for strong and tough materials, but torsion is a relatively neglected loading mode. The wood skeletons of cholla cacti, subject to spartan desert conditions and hurricane force winds, provide a new template for torsionally resilient biological materials. Mesostructural characterization methods of laser-scanning and photogrammetry are used alongside traditional optical microscopy, scanning electron microscopy, and micro-computed tomography to identify mechanisms responsible for torsional resistance. These methods, in combination with finite element analysis reveal how cholla meso and macro-porosity and fibril orientation contribute to highly density-efficient mechanical behavior. Selective lignification and macroscopic tubercle pore geometry contribute to density-efficient shear stiffness, while mesoscopic wood fiber straightening, delamination, pore collapse, and fiber pullout provide extrinsic toughening mechanisms. These energy absorbing mechanisms are enabled by the hydrated material level properties. Together, these hierarchical behaviors allow the cholla to far exceed bamboo and trabecular bone in its ability to combine specific torsional stiffness, strength, and toughness.

5.3 Introduction

Researchers have been studying biological materials for their superbly efficient mechanical properties, discovering a variety of hierarchical architectures responsible for them. For example, Bouligand structures found in mantis shrimp dactyl clubs provide extrinsic toughening (i.e., crack driving suppression as opposed to crack initiation suppression) via crack deflection under impact. The combination of dense and cellular structures found in cortical and trabecular bone respectively provide weight-efficient stiffness and strength [1], [2]. Nacre comprises interdigitating ceramic plates in a protein matrix that combine crack deflection, pull-out and frictional resistance, and sacrificial bonds to greatly increase toughness and strength [3],[5]. Most of these investigations for sources of bio-inspiration, however, have focused on compressive or tensile modes of loading [6], [7]. Studies of how natural materials bear torsional loads may unlock new bio-inspired structural design elements with applications in structural and aerospace industries. To this end, we may turn to free-standing plants which bear a combination of axial loading, bending, and torsion to support their own mass against gravity, wind, or snowfall. Their adaptations to torsion broadly fit into the categories of minimizing or maximizing torsional stiffness [8]. Petioles (leaf stems) exemplify the former: their cross-sections maximize the bending moment to support leaves for proper exposure to the sun, but minimize the torsional moment to allow twisting under high winds, thereby reducing drag [9]. On the other hand, primary structural materials (i.e. tree stalks and trunks) typically exhibit torsional stiffness. We hereby focus on this latter category of adaptation as it is applicable to structures such as driveshafts.

To understand the torsional behavior of trees, we must understand the wood of which they are made. It is a closed-foam, anisotropic cellular solid with three perpendicular directions defining its orthotropy: the axial (vertical direction of growth), radial (from the plant center to the periphery), and the tangential (perpendicular to both axial and radial directions). Wood anatomy is characterized by three mesostructural features: tracheids, rays, and vessels. Tracheids describe

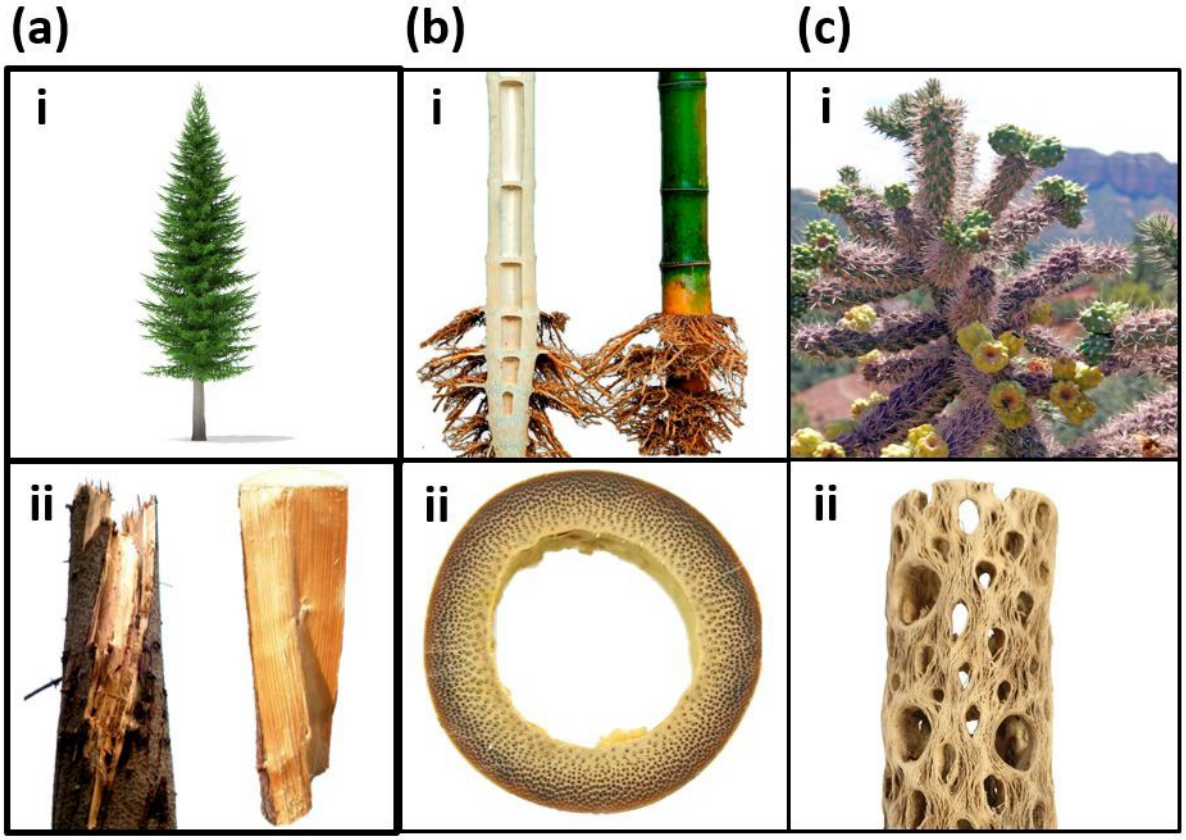

Figure 5.2: The structure of natural materials are characterized by adaptations to mechanical loading. (a) The trabecular struts within bone grow directionally in response to complex loading conditions to provide mechanical support while being light enough to allow mobility [19], [59]. (b) Norwegian spruce trees can grow spiraling grain to increase torsional strength in the direction of spirality. Spiral handedness can differ from tree to tree depending on the prevailing wind direction [22], [23]. (c) The hollow culm and radial density gradient of bamboo maximize its moment of inertia and beam-bending stiffness, allowing rapid and material-efficient growth [27], [60]. (c) Cholla cacti grow in harsh, windy deserts of the North American southwest. The fleshy, succulent tissue is supported by an internal lignified skeleton of wood with helical porosity. Previous work that examined the tubercle pores hypothesized they help optimize spine-packing density or thermal stability of the cactus [32], [36].

the long, axially growing cells comprising the bulk of trees. Rays are rectangular, radial arrays of cells responsible for the transport of nutrients and fluids from the center of a tree to the periphery, where growth occurs. Finally, vessels are enlarged, thin-walled pores that conduct fluids vertically and only found in angiosperms [10]. Wood is weaker in longitudinal shear (shear plane parallel to longitudinal axis) than in transverse shear (shear plane perpendicular to longitudinal axis);

pure torsion about the longitudinal axis results in failure along the axial direction (although shear stiffness in the radial-tangential (R-T) plane is the lowest, shear strength is lowest in the axial-radial (A-R) plane).

Evenly exposed to a uniform wind field, a radially symmetric plant would strictly bend at such a condition, however, is exceedingly rare. A non-uniform wind field, radial asymmetry in the canopy or the roots, and shielding by neighboring features of the landscape can all cause a plant to undergo additionally torsion [11]. In modeling the bending and twisting of a tree due to wind, Skatter and Kucera [12] found that isolated spruce trees were as likely to fail in either mode. This finding was supported by the observation that after a storm in Switzerland, 11% of fell spruces failed in bending and 17

Trees possess several adaptations to resist these torsional loads. At the macroscopic scale, Norwegian spruce trees (Figure 1a, i) can grow axially spiraling fibers (called spiral grain) that become visible in trunks or logs split along fibers in the A-R plane (Figure 1a, ii). The torsional strength is increased in the direction of chirality, and depending on prevailing wind direction, trees of the same species can grow spirals of different handedness and even grow branches asymmetrically to encourage twisting in the stronger direction [11], [12], [14]. More generally, a tree can grow or shed branches to act as dynamic mass dampers and mitigate harmonic and resonant swaying frequencies, minimizing the transfer of wind bending and torsion to the trunk and root system [15]. Trees also exhibit a gradient of increasing axial stiffness from the center to the periphery, with an order of magnitude difference in Young's modulus. The gradient reflects an optimization for flexibility during the tree's early life, but as the tree matures and grows a larger crown it requires greater stiffness to prevent Euler buckling [16]. The increased stiffness at the tree's periphery also enhances its torsional strength as the stresses increase linearly with distance from the neutral axis [8], [17], [18].

Bamboo has also been studied in torsion for new potential applications in construction that go beyond its traditional known strengths in axial compression and bending [17], [19].

Consisting of a hollow shaft separated by nodes into sections called culms or internodes as illustrated in Figure 1b, i, bamboo is a natural composite. At the meso-scale it comprises dense vascular bundles of heavily lignified structural cells embedded in a matrix of thin-walled living (parenchyma) cells. From the inner to the outer surface of the culm, the frequency of vascular bundles and their volume fraction increases to produce a positive radial density gradient, which leads to correspondingly increasing gradients of stiffness and strength (Figure 1b, ii). This arrangement allows the bamboo to optimize the moment of inertia to resist bending and axial compression [10], [18]. Askarinejad et al. [17] tested whole internode sections of bamboo in torsion at varying degrees of environmental humidity and found that the shear strain at failure increases with humidity (as in other plants) [20]. Samples conditioned at approximately 60% humidity had the highest average shear modulus and strength of 1.2 ± 0.35 GPa and 15 ± 8.6 MPa, respectively. Samples failed via brittle fracture consisting of a single crack propagating along the length of the internode. Their simulations revealed that the radial stiffness gradient of bamboo matches the stress gradient induced by torsion. The study did not reveal new micro or meso-structural adaptations, since the stiffness gradient documented had already been noted by several researchers [8], [17], [18], [21].

In the southwestern deserts of North America, one may find exquisite structures of hollow wooden cylinders, the walls of which are perforated by spiraling arrangements of holes (Figure 1c, i). These are the remains of cholla cacti (genus Cylindropuntia): spiny and ranging in size from shrub-like to 4.6 m tall, they are characterized by extensive cylindrical branches [22]. On death, the cholla leaves behind wooden skeletons of hierarchically porous hollow tubes sometimes used by artists to craft objects such walking sticks, chairs, and other furniture (Figure 1c, ii) [23]. These skeletons are formed by the vascular cambium, a growth layer which produces xylem on the interior and phloem on the exterior. The xylem comprises thick cell walls reinforced by lignin, a highly branched and compressively stiff (but brittle) polysaccharide [24], [25]. The support of lignin allows the xylem to conduct fluid and provide structural integrity for the phloem

which comprises still living parenchyma responsible for nutrient storage and transport, lacking lignified cell walls [26]. A young cholla cactus forms a net-like series of vascular bundles with soft parenchyma cells in between, and as the cactus matures, the vascular bundles and bridges between them lignify to form the wood skeleton. The parenchyma cells in between remain unlignified, maintaining centimeters wide holes in the wood skeleton to maintain the succulence of tubercles (i.e. the fleshy projections tipped with spines). As the cactus grows taller, a new tubercle will grow roughly 137 degrees away about the vertical axis at a slightly higher position eventually resulting in a dense, spiral arrangement of tubercle pores shown in Figure 1c, ii [23]. In some species such as Cylindropuntia leptocaulis, the holes are long and narrow, but in species with wide tubercles the holes are more circular [23]. Botanists have considered the positioning of these holes in context of the function of the tubercles: some hypothesize that they maximize packing efficiency of spines to protect the plant while minimizing interference [27], while others that they confer thermal stability against the extreme temperatures of the day and night of the desert [23]. Here, we explore the hypothesis that the positioning of the tubercle pores in the wood skeleton is an adaptation that confers density-efficient torsional integrity in a resource-sparse desert environment. As highly branched and squat plants, cholla are subjected to significant torsional loading compared to bending according to the geometric criteria developed by Skatter and Kucera [11], [12]. The skeleton must conferenough torsional integrity to not only bear the weight of the cactus but also desert wind speeds of up to 28 m/s [28].

This work characterizes the macro-structure, meso-structure, and mechanical properties of the wooden cholla cactus skeleton from Cylindropuntia acanthocarpa (common names: staghornor buckhorn stick cholla) via experimental techniques, and finite element analysis. The meso-structure of the wooden skeleton of Cylindropuntia ramosissima (common name: pencil cholla) was also characterized to investigate the level of detail captured by laser scanning. This different, smaller species of cholla was selected for the laser scanning technique due to the size limitations of the scanner.

5.4 Materials and Methods

5.4.1 External mesostructure characterization:

Eight dried specimens of staghorn cholla wood were obtained from the Superstition Mountains, AZ and locally in San Diego, CA; one specimen of pencil cholla wood was obtained locally in San Diego, CA, for external mesostructural characterization as received in dry conditions. A NextEngine 3D Scanner (Santa Monica, CA) was used to obtain the 3D model of a pencil cholla (n = 1 samples) via a laser array scanning the skeleton in parallel, each scan of which was then stitched in ScanStudio software (Santa Monica, CA). To solve the accuracy and resolution challenges of laser-scanning, another technique known as close range photogrammetry [29] was implemented on specimens of staghorn cholla (n = 8 samples) using a Sony Alpha a7II Digital camera (Tokyo, Japan) with a resolution of 24.3 effective megapixel, together with a Sony FE 90mm f/2.8 Macro Lens (Tokyo, Japan). The combination of the high-resolution camera and the macro lens allowed the acquisition of several hundred zoomed, high-resolution images of small regions of interest on the staghorn cholla surface. These images were then processed using Agisoft Metashape (St. Petersburg, Russia), a software specialized in photogrammetric processing of digital images for the generation of 3D spatial data. The average angle from the R-T plane between nearest neighbor tubercle pores (ang1) was then measured by un-rolling the 3D model using CloudCompare (Paris, France) to obtain a planar surface from the 3D cylindrical point cloud. These measurements were compared to ang1 values obtained by physical measuring the cholla cactus, by which pore dimensions were also obtained. The pitch (pore center-to-pore center distance), axial pore length (LPore, A), and tangential pore width (Wpore, T) were obtainedas shown in Figure 2a. The bulk sample density (ρ^*) was measured as that of a hierarchical cellular solid using the equation:

$$\rho* = \frac{m}{L_A \pi (r_o^2 - r_i^2)} \tag{5.1}$$

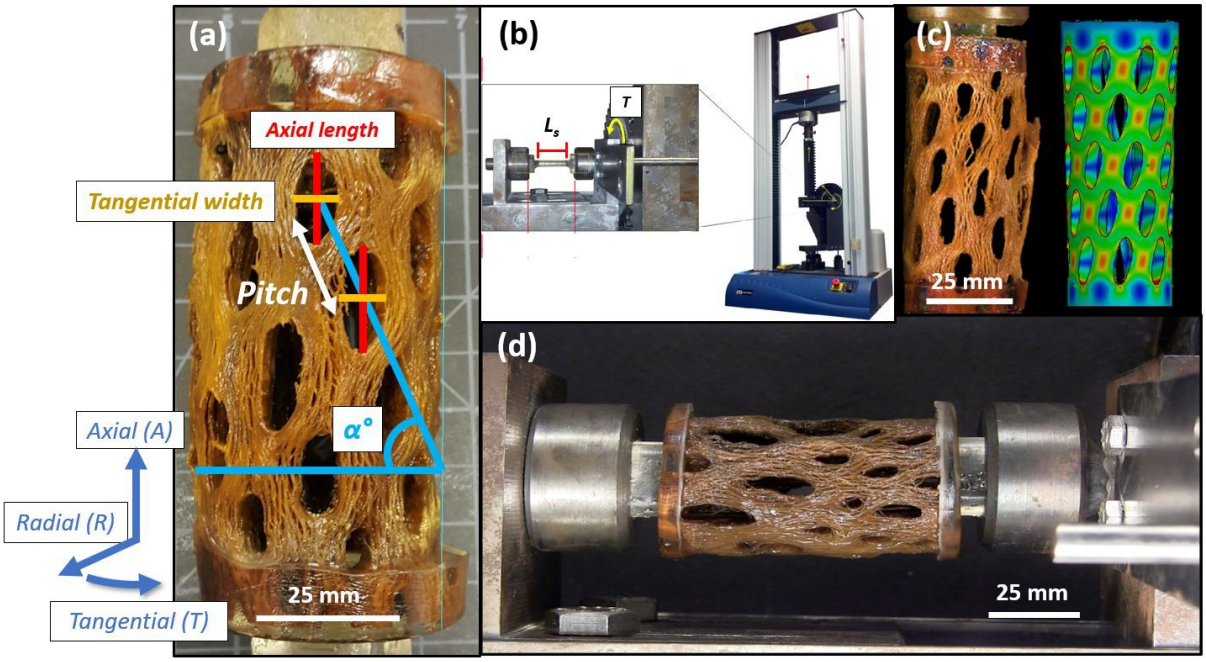

Figure 5.3: (a) Manual measurements of the tubercle dimensions, pitch, and angle of orientation with respect to the radial-tangential plane were obtained for each cholla sample. (b) Before testing, all /specimens were fully hydrated to mimic in vivo conditions. (c) A torsional adaptor from previous work [39] was fitted to the Instron 3367 Dual Column Testing Systems device (Norwood, MA). It comprises a rack and a pinion that translates the vertical displacement of the Instron crosshead to torque on the sample. (d) A hydrated cholla sample with epoxy reinforcements at each end, fitted into the torsion tester.

In which LA = the A length of the specimen, router = the outer radius of the wood, rinner = the inner radius of the wood, and m = the hydrated mass of specimens.

5.4.2 Internal mesostructure characterization:

A section of staghorn cholla wood was cut from a dry stalk used in external mesostructural characterization, and the radial-tangential plane (wood endgrain) was examined by cutting and polishing the axial face using progressively fine-grit sand paper and then imaged in a Keyence VHX1000 optical microscope (Osaka, Japan). This was followed by sputter coating with iridium at 85 mA for 10 seconds to reduce charging using an Emitech K575X Sputter Coater (West Sussex,

England). Samples were then imaged using the secondary electron detector of a Zeiss Sigma 500 field emission scanning electron microscope (SEM, Thornwood, NY) at an accelerating voltage of 2 keV and working distance of 10.4 mm. Unpolished, whole samples of cholla were also scanned in a Skyscan 1076 micro-computed tomography scanner (Kontich, Belgium) both before and after mechanical testing to examine deformation mechanisms. The imaging was performed at 35 micrometer isotropic voxel size for gross scans and 9 micro meter voxel size for finer scans.

5.4.3 Torsion testing:

From the eight large stalks of staghorn cholla received for mesostructural characterization, ten samples of staghorn cholla wood were cut into segments of varying length (13-18 cm) to maximize the number of straight-edged cylinders that could be obtained from the curved bulk material. After measuring the dry weight, length, inner radius, and outer radius of each sample, the cholla were hydrated for a week in water to mimic in vivo conditions of being surrounded by succulent cactus tissue which is typically 80-95 wt.% water [23]. Following hydration, the samples were re-measured to obtain hydrated mass and the length (L), inner radius (rinner), and outer radius (router) of each sample. The end of each cylinder was then reinforced with 25 g of epoxy in a dog-bone mold (Figure 2a) to allow samples to be secured to a custom-built torsion testing device (Figure 2b) [30] mounted to an Instron 3367 Dual Column Testing Systems device (Norwood, MA). The custom-built device translated a linear displacement rate of 0.02 mm/s to a torsion rate of 2.0 x 10-4 radians/s, and the raw load vs. displacement data were translated into torque vs. rotation data and then shear stress vs. shear strain, according to the procedures described by Porter et al. [30]. The calculation of shear stress required the sample torsional moment of inertia (Js) which quantified the cross-sectional geometric resistance to twisting. Rather than estimate sample torsional moment of inertia as that of a hollow tube, Js of each sample was obtained via generating n = 9 models in finite element analysis that approximate the range of geometries to obtain a Js surface profile, the process of which is described in section

2.4. A comparison of a typical cholla sample to the average geometry as represented in FEA is shown in Figure 2c. To compare the hydrated cholla torsional mechanical behavior to that of other biological materials, the shear strain results of whole bamboo internode culms conditioned in 100% humidity were taken from Askarinejad et al. [17]. The literature values were normalized by bulk density, which were not reported by Askarinejad et al. but could be inferred from the sample dimensions of the internode sections tested: Amada et al. [31] have previously determineda relationship between culm width and length and the culm number, which in turn determines bulk density. Literature values of physiologically hydrated bovine trabecular bone under torsionwere taken from Fatihhi et al., which provided sample dimensions and density [32]. Five samplesof balsa wood (Ochroma pyramidale) were also tested in torsion alongside the staghorn cholla samples. Balsa was chosen due to its highly hydrated physiological state, providing a similar wooden material of different macrostructure for comparison [33]. The 12 w.t.% moisture contentbalsa was obtained from National Balsa (Ware, MA) and prepared as cylindrical samples (L = 62mm, r = 16.45 mm) cored from the centers of plainsawn planks to obtain radial symmetry. The cylinder length corresponded to the axial direction. As with the cholla samples, the end of eachcylinder was reinforced with 25 g of epoxy in a dog-bone mold, after which the samples were fully hydrated to reflect physiological conditions.

$$J_s = \frac{\pi}{2} * (r_{oute}^4 - r_{inner}^4)$$

5.4.4 Finite element analysis (FEA) Simulation:

Finite element analysis (FEA) in SolidWorks was employed to (1) approximate the Js of each physically tested sample, (2) understand the stress concentrations caused by torsional loading and axial loading in isolation, and (3) investigate how the pore geometry affects the cholla cactus mechanical properties. To the first end, an initial cholla cactus-like model was developed using average relative dimensions of pore geometry and wall thickness. Then, maintaining

constant single pore area and cactus outer diameter while varying pore circularity and stalk wall thickness-to-outer diameter ratio, a total of n = 9 models were generated. The pore circularity and the wall thickness-to-outer diameter ratio were varied each had three levels of 0.98, 0.78, and 0.54 and 0.0811, 0.135, and 0.189, respectively. Pore circularity was defined as:

$$Circularity = 4\pi \frac{\pi r^2}{(2\pi}$$

In which a perfect circle has a circularity = 1. The pore circularity = 0.78 was based on the average measurements of pore pitch, Lpore, A and Wpore, T, and α° collected from several specimens. The wall thickness-to-outer diameter ratio of 0.135 was similarly based on average measurements. The bulk material for the models was simulated as isotropic steel with E = 210 GPa and ν = 0.3 and was subjected to torsion with torque (T) in the elastic regime with one fixed end. From the angular displacement (ϕ) and known shear modulus, G, an approximation of Js (which is a strictly geometric parameter) was obtained using the below equation for the torsional deflection of a circular shaft:

$$J_s = \frac{\pi}{2} * (r_{oute}^4 - r_{inner}^4)$$

From the resulting surface profile of Js values, the torsional moment of physical samples was approximated based on their pore circularity and wall-to-outer diameter ratio.

To the second aim of understanding stress concentrations caused by torsional loading and axial loading separately, it was necessary to obtain material parameters of the anisotropic cholla wood. Using the density of the dry cholla wood, an initial set of estimates for Young' s moduli (E_A, E_R,, E_T), shear moduli (G_{AR}, G_{RT}), crushing strength ($\sigma_{c,A}$, $\sigma_{c,R}$, $\sigma c_{,T}$), tensile strength ($\sigma_{t,A}$, $\sigma_{t,R}$, $\sigma_{t,T}$), mode I fracture toughness ($K^*_{IC,A}$, $K^*_{IC,RT}$), and Poisson's ratios(ν_{AR} , ν_{TR}) were obtained via Gibson-Ashby equations summarized in Table 1 [10]. These values were then adjusted for their moisture content [20] using the equation:

$$P = P12 * \left(\frac{P12}{Pg}\right)^{\frac{12-M}{Mp-}}$$

In which P = property at moisture content M, P12 = property at 12% moisture value (obtained using Gibson-Ashby equations), MP = 25 (fiber saturation point), and M = moisture content as calculated by:

$$M = \frac{massDry - massWet}{massdr} * 100\%$$

The moisture-adjusted material parameters were then input into FEA simulation. For each set of material parameters, three simulations were run with prescribed torque corresponding to three values of shear stress in the linear elastic range of an experimental curve. Simulation material properties were adjusted iteratively and in proportion to one another according to Gibson-Ashby equations until the three points produced a shear stress-strain slope matching the average experimental slope. Stress concentrations of this model were examined in torsion and in axial loading.

Finally, to the third aim of understanding how pore geometry affected the cholla mechanical properties, the material parameters obtained in the second aim were applied to all n = 9 models described in the first aim. All models were again prescribed axial compression and torsion separately within the elastic regime, with one fixed face. The ratios of the effective axial modulus to material axial modulus and effective shear modulus to material shear modulus were then compared.

5.5 RESULTS DISCUSSION

5.5.1 External mesostructure characterization:

Despite its high cost, the laser scanner only captured the pencil cholla's tubercle pores without the complexity of its fiber orientations (Figure 3a). On the other hand, the photogrammetry-produced model of the staghorn cholla more accurately reflecting the natural material and captured the tubercle pores and fiber protrusions and troughs (Figure 3b). The photogrammetric model clearly showed how fibers grow axially and diverted around, wove between, or split into smaller fibers at a tubercle pore seemingly at random, as illustrated in the magnified portion of Figure 3b. One growth step may not dictate the next: a fiber may weave between pores only to split into smaller fibers at the next. Analysis of the "unrolled" staghorn cholla model produced lower angle measurements (50 ±1.5 °) compared to the physical measurements (65 ± 2.1 °). The digital measurements from the photogrammetric model provided the line of best fit through several tubercle pores whereas the physical measurements were obtained only by considering nearest neighbors, and so provided more accurate information of the geometry of the cactus. Because of its low-cost and ease of use, photogrammetry presented a powerful method in 3D characterization of biological materials.

5.5.2 Internal mesostructure characterization:

Polished cross sections of the cholla endgrain (Figure 4a, b) revealed a conventional wood mesostructure that can be described using categories developed by the International Association of Wood Anatomists (IAWA) [34]. The large, thin-walled tubules are vessels responsible for axial nutrient conduction and are dispersed uniformly in a diffuse-porous arrangement. The alternating bands of light and dark wood visible in the optical microscope correspond to bands of aggregate rays and tracheids, respectively.

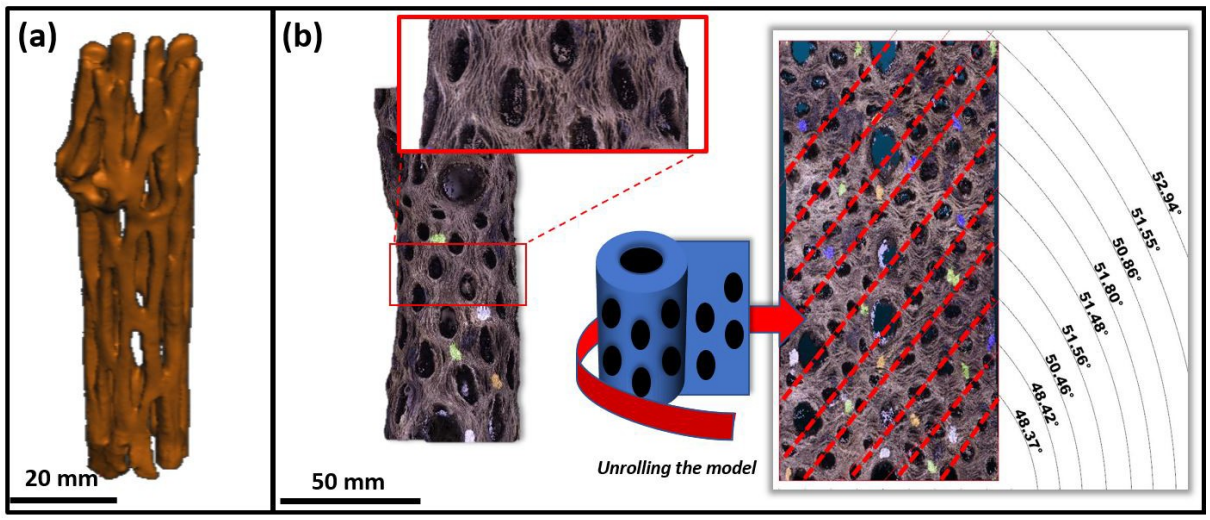

Figure 5.4: (a) Though useful for creating 3D models that capture the general shape of a biological structure, the laser scanner was unable to capture the fiber complexity of the pencil cholla skeleton imaged. (b) The photogrammetric model successfully captured the fiber complexity of the staghorn cholla. By "unrolling" the model in MATLAB, a more accurate assessment of overall tubercle arrangement could be obtained than by hand measurements: lines can be drawn (red, dashed) through the centers of tubercle pores to examine the overall growth pattern (i.e. angle of orientation with respect to the radial-tangential plane) rather than neighbor-to-neighbor comparisons as was done manually (Figure 2a).

Gross μ-CT (voxel size = 35 μm) revealed that like other woods, cholla was characterized by alternating rings of light "earlywood"(colorized in blue in Figure 5a) and denser "latewood" (colorized in green in Figure 5a) which correspond to faster growth during the spring and summer and slower growth during cool autumn and winter. As observed from photogrammetry, the fibers in the staghorn cholla diverted around, wove in between, or split intosmaller fibers at tubercle pores (Figure 5b). Compared to the photogrammetry scan however, itwas observed visually that the fibers were more densely packed in the interior with fewer voids in between than at the surface, consistent with their growth pattern discussed in the Introduction.

Slowly raising the density threshold (Figure 5c, i‑iii) exposed a network of discontinuous "islands" of heavily lignified tissue embedded in the xylem in between the tubercle pores,in the ligaments. Unlike in bamboo, which exhibits radial density gradients [18], the islands appeared to be radially continuous, indicating that points of reinforcement were consistent

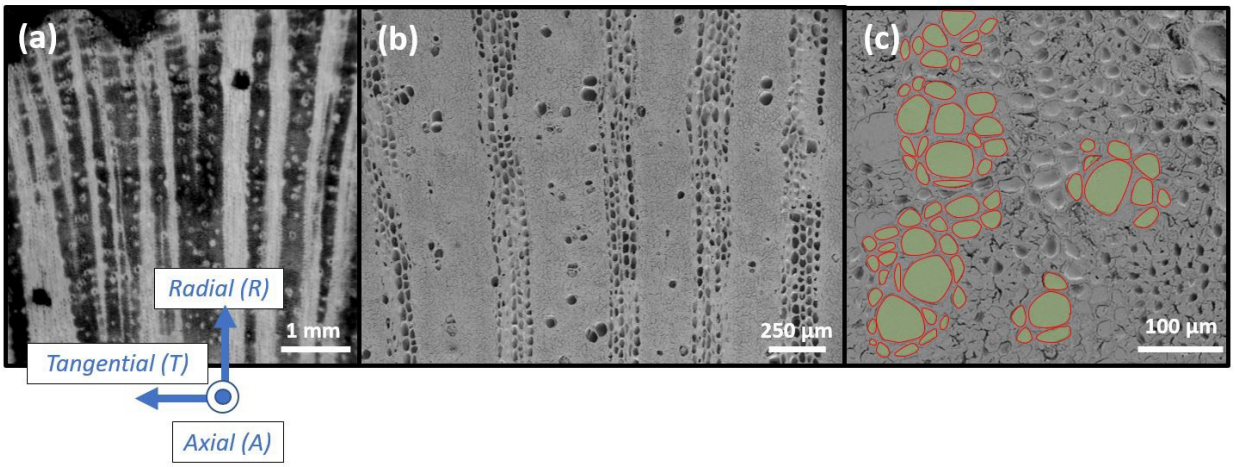

Figure 5.5: (a) The endgrain of the cholla cactus as observed in optical microscopy features aggregate rays and a diffuse-porous arrangement of vessel elements. (b) The relatively small but numerous vessels allow maximum axial conduction of water during intermittent rain while preventing cavitation during dry seasons [53]. The similar ray cells conduct water to fleshy succulent tissue for storage, and can store water themselves [54].

over time (Figure 5c, iii). The tubercle pores edges were only somewhat discernable at the highest density threshold, indicating that the ligaments were preferentially reinforced (a point that we note for discussion in the results of the finite element model of the cholla in torsion, Section 3.4).

5.5.3 Torsion testing:

Staghorn cholla shear stress-strain curves consistently exhibited a linear regime followed by a decreasing, jagged plateau under torsion. The average shear modulus and strength (n = 8) were found to substantially vary at 41 ± 7.8 MPa and 2.7 ± 1.0 MPa, respectively, butwhen normalized by hydrated bulk density showed more consistent behavior, typical of woody structures: the specific effective shear modulus, $G/\rho_c^* = 150 \pm 23$ MPa $(g/cm^3)^{-1}$ and the specific shear strength, $\sigma y / \rho_c^* = 9.3 \pm 2.5$ MPa $(g/cm^3)^{-1}$. Most notably, the toughness was strikingly high (1100 ± 430 kJ/m^3). Plotting the density-normalized behavior of cholla allowedcomparisons to balsa wood, bamboo, and trabecular bone as well as account for sample-to-sample

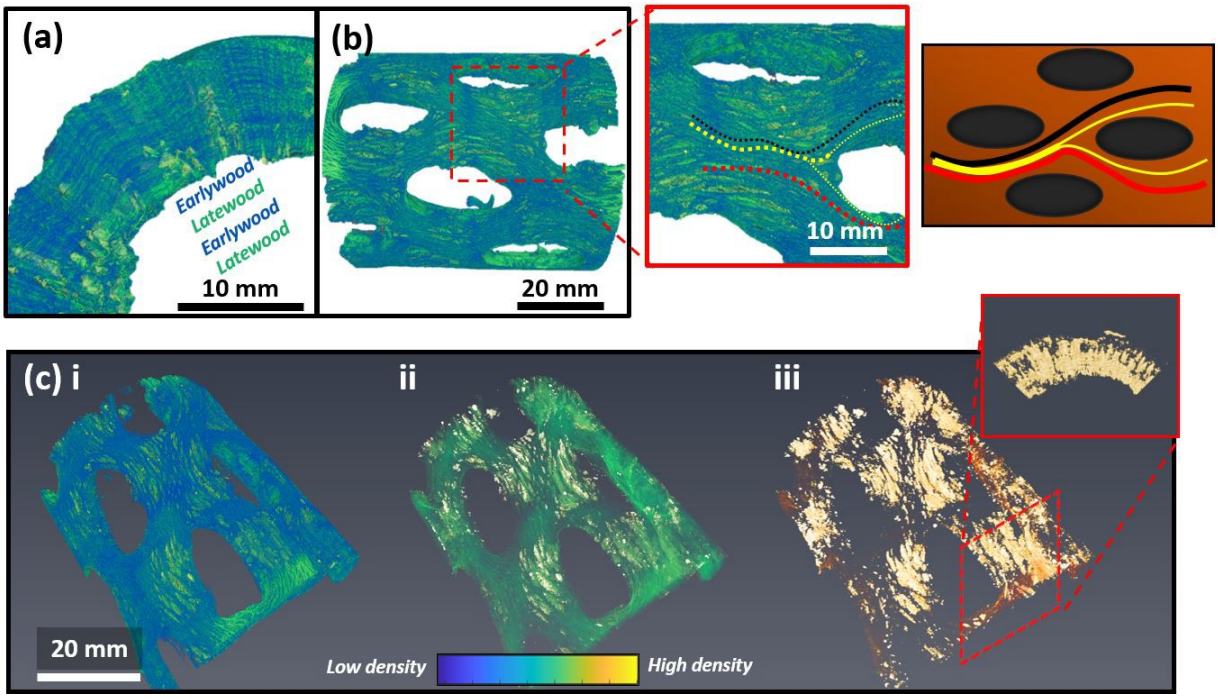

Figure 5.6: μ-CT of a specimen revealed (a) banding of latewood and earlywood in the radial-transverse plane, corresponding to slow and fast growth periods respectively. (b) Fibers were observed to weave in between, divert around, or split off into smaller fibers at tubercle pores. (c) Slowly raising the density threshold progressively from (i- iii), radially continuous regions of increased lignification were observed, mainly at the tubercle ligaments.

variation (Figure 6). Though its curve profile was similar to the cholla cactus, hydrated balsa exhibited a far lower density normalized shear stiffness, strength, and toughness indicating low mechanical efficiency. Failure occurred via a single oblique fracture plane 45° to the axial length of wood. The density normalized shear modulus of the bamboo was greater than that of the cholla ($G/\rho^* = 550$ MPa $(g/cm^3)^{-1}$), but its strength comparable (11 MPa $(g/cm^3)^{-1}$) and toughness less than half (350 kJ/m^3). Bamboo's ultimate failure strain occurred at less than 0.06, a full order of magnitude below that of cholla, and was characterized by a single axial crack propagating along the entire length of the bamboo internode culm [17]. Fatihhi etal. [32] showed trabecular bone's G/ρ^* to be comparable to that of cholla but with lower $\sigma y/\rho^*$.

Like cholla, trabecular bone exhibited torsional toughness but failed at a shear strain of 0.2-though Fatihhi et al. did not report how trabecular bone failed under pure monotonic torsion, Bruyere-Garnier et al. [35] reported that torsion induced an oblique fracture plane 45° tothe axial

length of trabecular bone. Thus, while torsion in bamboo generated shear failure (creating A-R plane cracks), in balsa and trabecular bone the tension caused by torsion resulted ina tensile failure oriented 45° to the A axis. The properties of each material were summarized inTable 2.

That cholla, like balsa and bone, decomposed torsion into tension and compression is key to its high toughness. As evidenced by the sequence of deformation in Figure 6c, initially elliptical tubercle pores were compressed tangentially and stretched axially at a coordinate offset of 45° to the A axis of the plant, prior to tensile failure in which fibers ruptured. The difference between bamboo (shearing decomposition) and balsa and cholla (tensile and compressive decomposition) was that the fibers in the l atter were highly saturated with water, reducing the stiffness and strength of the wood [36]. Water hydrated the hemicellulose matrix between fibers and facilitated inter-fiber sliding while retaining some stiffness via constant breaking and reforming of hydrogen bonds [24], [37], [38]. With less moisture in their physiological state, bamboo fibers were over-adhered to one another and unable to bend or slide past one another. Instead, they failed at their interfaces to produce clean A-R plane cracks. The balsa fibers were clearly able to bend and slide, but due to their lower density cell walls and higher state of hydration exhibited lower mechanical efficiency. Bone is a markedly different material than wood, but according to literature deforms via a similar flowing mechanism between mineralized collagen fibrils in its hydrated physiological state-the fibrils themselves and the mineral platelets experience very little deformation [37].

The unique deformation mode in cholla was due to the hierarchical arrangement of fibers which is quite different from balsa, in spite of similarities in composition and hydration. The cholla's hydrated material properties determined four mesostructural deformation mechanisms illustrated in Figure 6d: fiber straightening, fiber delamination, pore collapse and friction, and ultimately fiber rupture and pullout. As noted in Figure 5b, the cholla fibers grew in serpentine paths in the axial direction. As the wood began to plastically deform in torsion, individual fibers

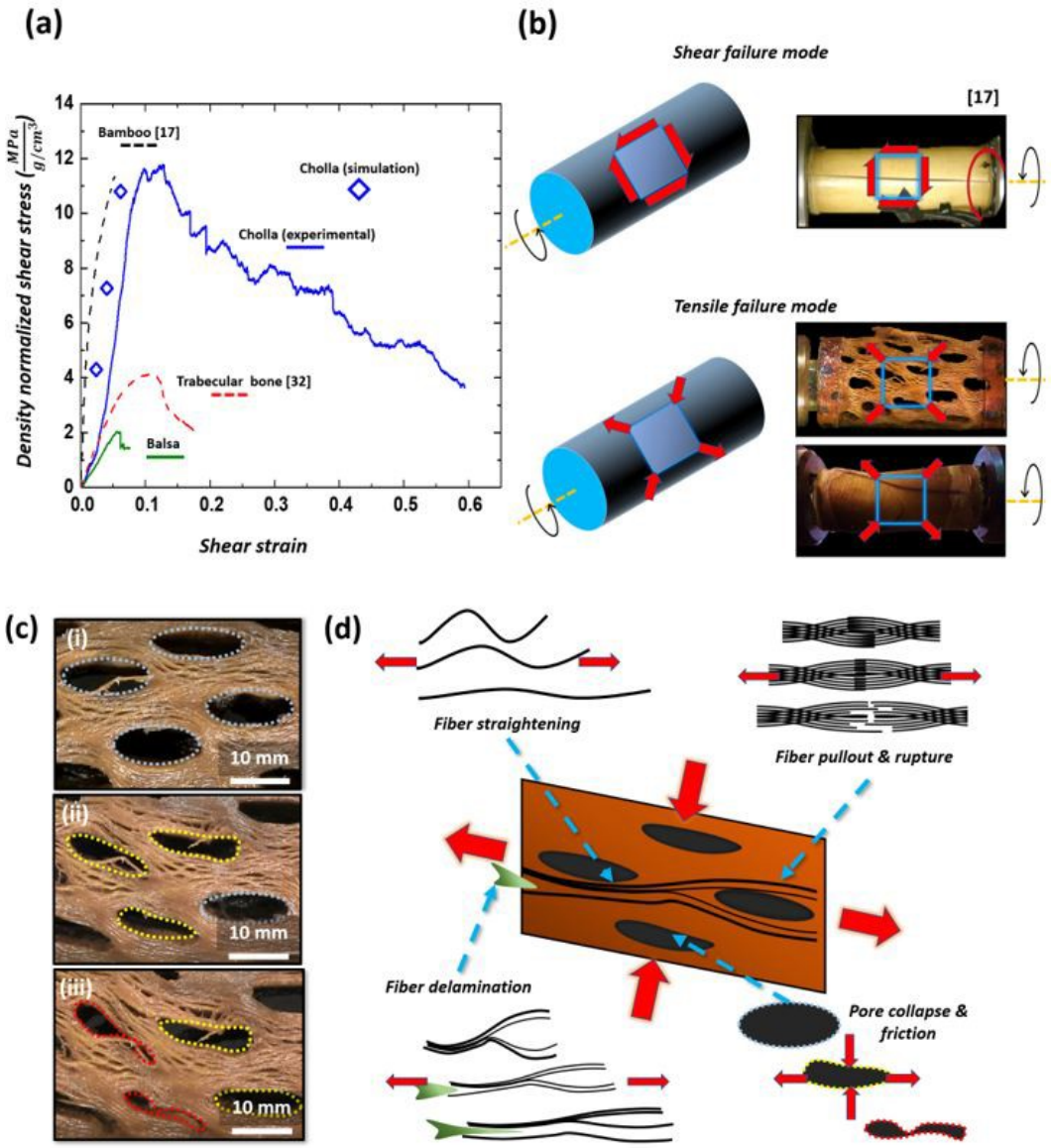

Figure 5.7: (a) Compared to the density-normalized performance of bamboo [26], balsa,and trabecular bone [13], cholla exhibited a far greater combination of stiffness, strength, and toughness. (b) Its behavior was characterized by three regimes of deformation: linear elastic deformation of the whole structure (i) from initially elliptical tubercle pores, (ii) delamination of the fibers and crack propagation in the axial direction (marked with arrows) initiated at the axial points of the tubercle pores, (iii) and ultimately, hinging of the tubercle ligaments in a spiraling band (circled in blue) and fiber rupture. These numerous and progressive failure modes contrast with the brittle behavior of hydrated bamboo and bone.

were elongated in the direction of tension and absorbed energy via straightening and then elastic stretching of the fiber itself. As the fibers straightened, however, they separated from neighboring fibers and further energy was absorbed via delamination. All the while, the macroscopic tubercle pores were flattened by the compressive force in the perpendicular direction until they collapsed. Like the densification effect of a cellular solid under compression, each collapsed tubercle pore newly offered compressive and frictional resistance under torsion. The pores did not deform simultaneously but sequentially from the loading face. Once the fibers were fully straightened in tension at an extreme shear strain (0.6), an energy-absorbing fiber failure occurred in the R-T plane. At this point the cholla lost its cylindrical shape as sections of the wall twisted inward, but even then, the wood did not catastrophically fail and still retained some stiffness. Due to the sequential nature of the post-elasticity in cholla torsional deformation, these four mechanisms (fiber straightening, fiber delamination, pore collapse and friction, and fiber rupture and pullout) happened in parallel and avoided catastrophic failure, resulting in a gradual decrease of torsional load.

Compared to other biological materials, it was this toughness that was most striking. As previously discussed, the squat and branched geometry of the cactus creates a strong evolutionary pressure to adapt accordingly for torsion. The question remains, however, on why toughness was seemingly prioritized. High stiffness and strength would require either devoting more bulk material growth to the plant or increased lignification. In a resource poor environment, these may not be feasible. Alternatively, reduced hydration stiffens and strengthens the stalk, but this may interfere with other biological functions of the plant. Additionally, a lower fiber hydration embrittles the wood as in bamboo, making catastrophic A-R failure more likely from which recovery would be near impossible [39]. It may be that the cactus primary response to torsion in anon-catastrophic, localized, and staggered failure sequences helps it to recover from damage anduses resources most sparingly. Rather than regrow entire sections of plant or heal massivecracks spread throughout the plant, it is more efficient to seal and regrow smaller, distributed delamination [39], [40].

Micro-CT images of the cholla after torsion (Figure 7a) showed further detail in the tensile fiber failure: in Figure 7b, i, fiber rupturing was shown to be caused by fiber pullout in amixture of delamination and tensile fiber failure. This mode is known as "progressive delamination" in the field of composite failure and describes optimally adhered fibers that are neither over nor under adhered to allow maximum energy absorption in failure [41]. In some cases, this delamination terminated at another tubercle pore in a process akin to crack blunting (Figure 7b, ii), while in others the delamination was diverted around a neighboring tubercle. This was determined by whether the fibers along which the crack propagated diverted around, wove between, or split into smaller fibers at a tubercle p ore. In Figure 7b i ii iv, for example, the crisscrossing of fibers deflected an incoming crack to force a more tortuous path. All these mechanisms enhanced the torsional toughness of the cholla.

5.5.4 Finite element analysis (FEA) Simulation:

FEA was implemented with three aims: (1) to capture the variation of torsional moment Js (with parameters of pore circularity and stalk wall thickness-to-diameter), from which torsional stress was calculated, (2) to understand stress concentrations caused by torsional and axial loading acting separately on cholla models with appropriate anisotropic wooden material parameters and (3) to understand the effect of pore geometry and wall thickness-to-diameter ratio on the cholla's ability to resist torsional and axial loads. Boundary conditions were validated by simulating solid-walled tubes with isotropic steel parameters and back-calculating input material parameters.

While the first aim was a means to analyze experimental data, the second and third aims provided significant insight into the material behavior of the cactus. By inputting a relative density of 0.15 into equations summarized in Table 1 and adjusting with M = 25% according to Equation4, an effective shear modulus (i.e., the slope of the three simulated shear stress-strain values)

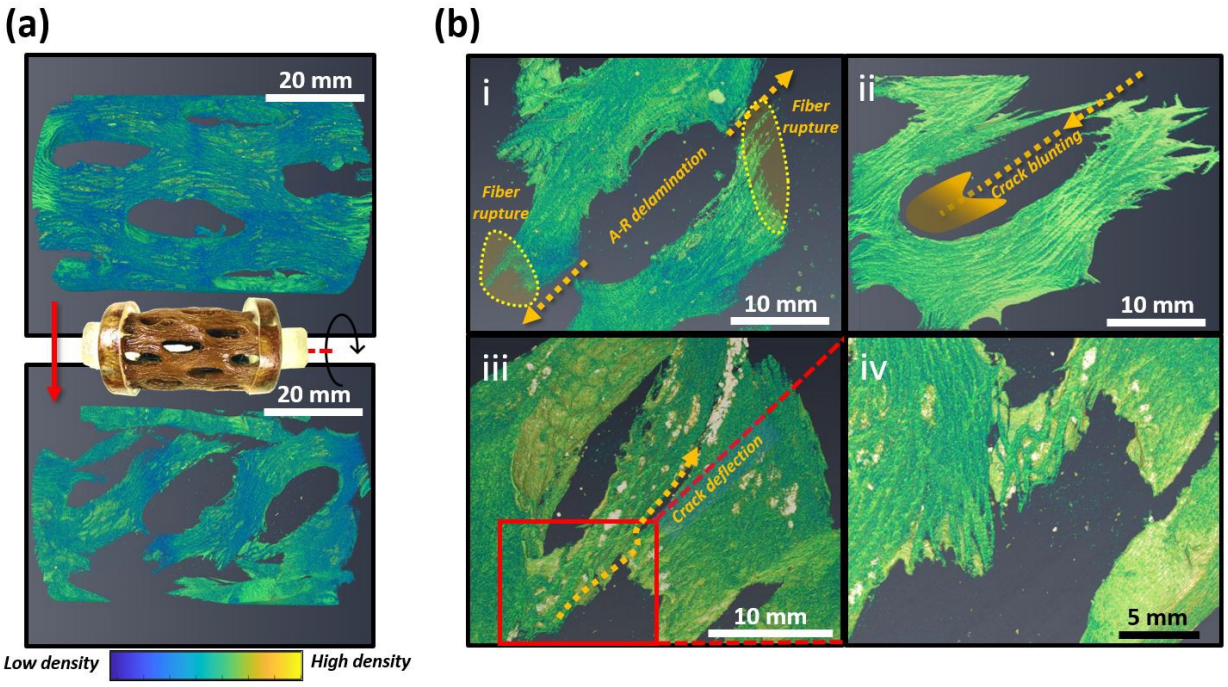

Figure 5.8: (a) Micro-computed tomography images of a specimen (i) before and (ii) after torsion revealed several extrinsic toughening mechanisms. (b) (i) Cracks typically initiated at the axial ends of tubercle pores near the center of the specimen and propagated axially. The tubercle ligaments near the center would still be loaded in tension, however, and eventually fail by rupture with extensive fiber p ullout. (ii) On encountering a neighboring tubercle pore, crack blunting would occur and slow its advance. (iii, iv) Alternatively, the weaving and criss-crossing fibers would deflect the crack on a still more tortuous path.

within 10% of the experimental shear modulus was obtained, the results of which are shown in Figure 6a. Because the Gibson-Ashby equations were not meant to calculate precise mechanical properties from relative density but rather estimates, it was not a significant discrepancy that the average cholla relative density was in fact 0.23 ± 0.017 [10]. It should be re-emphasized that the average experimental "shear modulus" calculated using Equation 3 (Geffective, experimental = 41 ± 7.8 MPa) represented the tube's resistance to torsion and not its material shear stiffness. As discussed in Section 3.3, the torsional shear can be decomposed into tensile and compressive loads acting at ± 45° to it. The cholla wood's true shear stiffness is likely GA-R, material 340 MPa which was input into the material simulation to obtain Geffective, simulation = 50 MPa shown in Figure 6a. Because all material properties were simultaneously

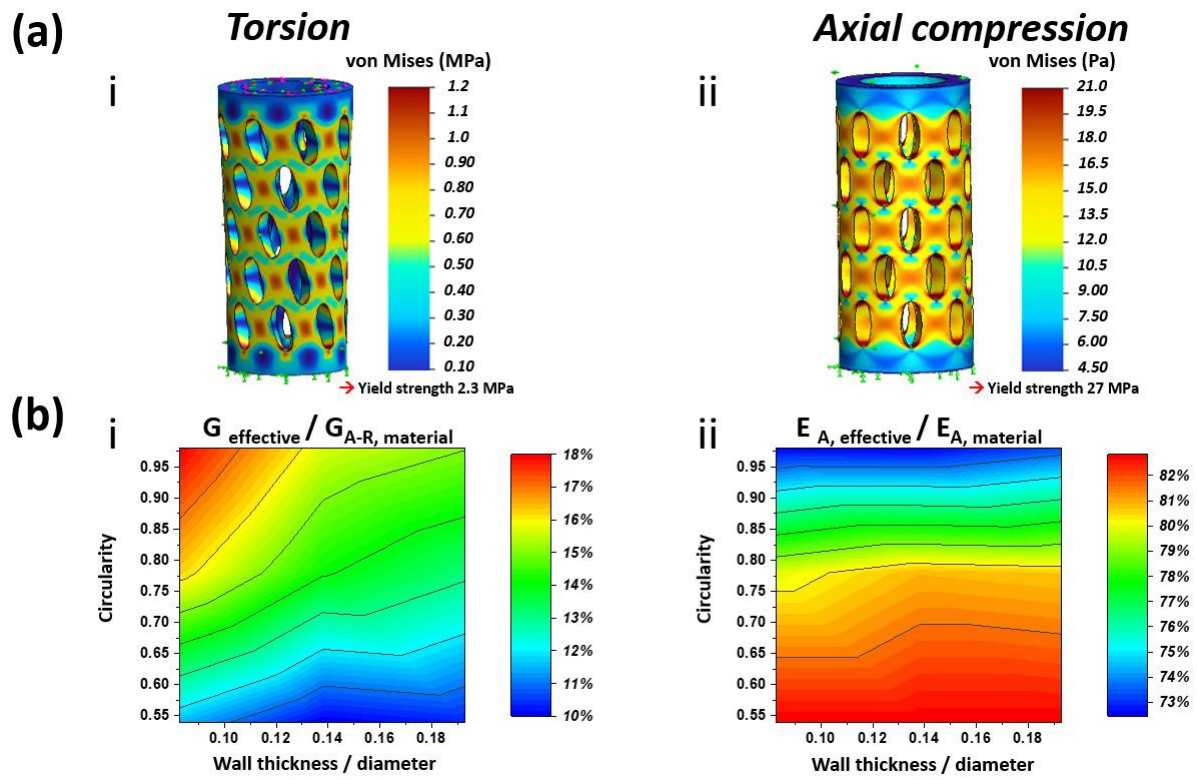

Figure 5.9: (a) Finite element analysis (FEA) was used to model a unit cell of the cholla wall using homogeneous, isotropic material parameters to isolate the geometry's contribution to mechanical behavior. By taking the density-normalized specific, effective moduli and comparingit against that of the input material, we observed that the cholla geometry was highly optimized for compression in the axial direction and shear. Observing the stress concentration in (b) axial compression and (c) pure shear indicated that the lignification of the tubercle ligaments (Figure 5c, i-iii) was primarily a plant response to shear forces.

adjusted using relative density for the simulation, it is possible that in the actual wood some properties were separately higher or lower than the relative values predicted by the Gibson-Ashby equations (i.e. the wood's shear stiffness may be lower than the Gibson-Ashby equations predict, while the wood's axial stiffness may be higher).

With anisotropic material parameters verified against experimental results, it was possible to examine stress concentrations produced by torsional and axial loading. It was clear that torsion produced stress concentrations in the middle of the ligaments between tubercle pores (Figure 8a, i), while axial compression produced stress concentrations at the axial ends of the tubercle pores

(Figure 8a, ii). The regions of heavy lignification observed in micro-CT (Figure 5c, iii) matched the points of stress concentration in torsion rather than compression. Because woody plants reinforce branch junctures [42], taproots [43], and other stem portions [8], [43]-[46] in response to mechanical stress, it is likely that cholla selectively increased lignification to create a mechanically efficient stalk of high torsional stiffness.

The models in Figure 8a represented the average geometries of the measured cholla: to investigate the effect of the pore geometry on the cactus, pore circularity and stalk wall thickness-to-diameter ratio were varied with three levels each. The centers of the heat maps of Figure 8b reflect the average cholla pore circularity and wall thickness-to-stalk diameter ratio, while the color intensity reflects the effective stiffness as a percentage of the prescribed material stiffness. It was observed that for thin-walled tubes, a higher pore circularity improved the effective shear stiffness whereas in thicker walled tubes there were diminishing returns past circularity 0.65 (Figure 8b, i). In axial loading, the wall thickness-to-diameter ratio had little effect on the effective compressive stiffness while a lower pore circularity improved the effective stiffness (Figure 8b, ii). At approximately the average geometry of the staghorn cholla there was a balanced compromise between the effective axial and shear stiffnesses, indicating that the macrostructure of the cholla is an adaptation to bear both torsional loads due to wind and axial load due to its own weight. As observed in Figure 2d, however, cholla pore geometry can vary even on a single stalk itmay be that a cholla cactus can locally adjust pore roundness as a mechanism to control its stalkstiffness. This FEA analysis was limited, however, in that staghorn cholla wood may be optimized simultaneously for several factors such as other loading modes (e.g. radial compression due to tissue swelling, bending) and biological functions. For example, plant xylem is responsible for nutrient and fluid conduction which are of particular importance in the desert, where cacti must be able to rapidly take-up liquid during rare instances of rain fall [47]. Unique adaptations to this end have been observed at all hierarchical levels of cacti: these include a shallow, spreadingroot system (ideal for transient rainfall) [23], a relatively thin living-cell layer in the roots to maximize axial conduction [47], small and numerous vessels in the stem to maximize conductionand prevent cavitation during drying [48], [49], and larger vessels at the

root-stem juncture to induce air bubbles and prevent water loss from the succulent stem into the dry soil [47]. It is possible that too oblique a mesopore distribution in the wood (i.e. too oblique a fiber angle of the wood that must wrap around them) interferes with this critical function of xylem, explainingwhy the cholla cacti mesopores are distributed at an angle greater than 45°. Another example of a biological function that our analysis did not account for is spine distribution (each tubercle pore corresponds to the placement of spines). We have already mentioned the theory that the helical geometry of the tubercles allows maximum packing density of spines while minimizing spine overlap for efficient protection against would-be water thieves [27]. Another function of thespines, however, is to collect moisture from air and transport droplets by their aligned grooves to fine, water-absorbing outgrowths at the spine base (trichomes) [50]. The mesopore distribution may optimize for spine packing efficiency not just for protection but water condensation, too.A final, major biological function unaccounted by our analysis is that of the surrounding living tissue: compared to the parenchyma of conventional plants, the parenchyma of cacti are extremelyhydrated. The elastic yet strong bark combined with this succulence confer high turgor pressure which substantially augments the cactus mechanical properties [51]-[53]. The results of our FEA show a compromise between torsional and axial loading of the cholla wooden frame, but can provide only a partial insight as to the evolutionary reasons for the cholla's mesopore distribution.

5.5.5 Topology Optimization:

Topology optimization of a hollow tube in torsion predicted a somewhat similar structure to the staghorn cholla cactus (Figure 10a), generating a perforated tube with holes positioned along a 45° orientation with respect to the axial direction (compared to the average angle of 50± 1.5° observed in staghorn cholla). The rhombohedral geometry of the holes, however, starkly

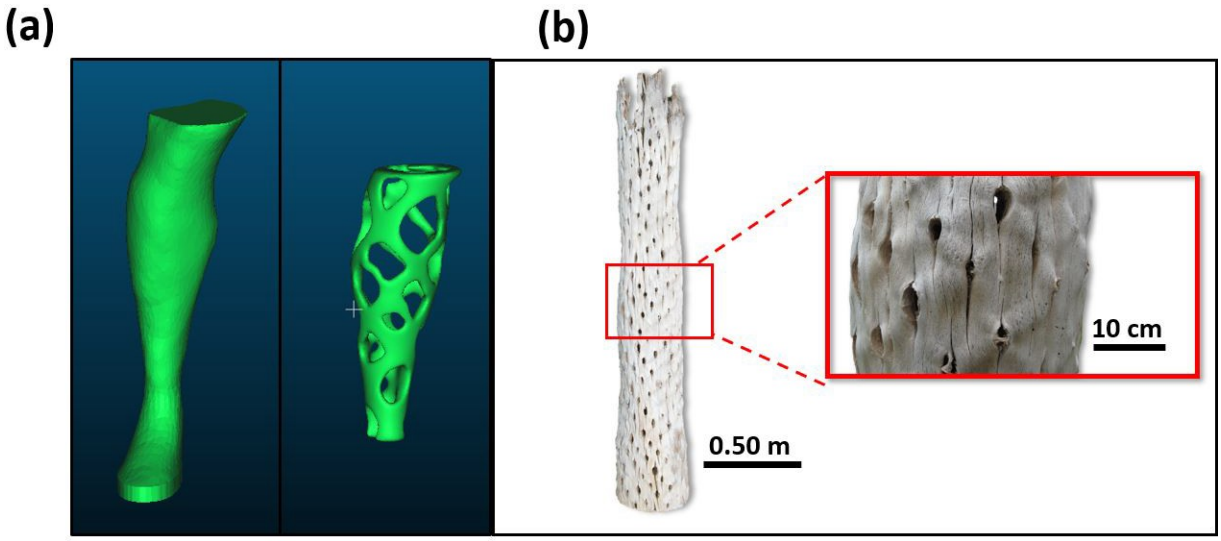

Figure 5.10: . Finite element analysis (FEA) was used to model unit cells of identical pore angles and pitch but varying roundness (left to right: 1.0, 0.98, 0.78, 0.54) to understand how the pore shape contributes to mechanical behavior. At approximately the geometry of the original staghorn cholla (roundness = 0.78), there is a triple point of high specific axial and shear stiffnesses, reinforcing the hypothesis that the cholla pore geometry is a unique adaptation to help resist torsion and axial compression.

contrasted against the smooth ellipses of the staghorn cholla even with density-threshold filter smoothing. Additionally, the size ratio of holes to ligaments in the optimized model is far greater than in the staghorn cholla structure, despite the former sharing latter's the percent volume constraint. These discrepancies may be attributed to several possible factors, the most obvious of which is the limited nature of the topology optimization specifically for torsional s tiffness. In reality, staghorn cholla wood may be optimized for several factors simultaneously such as other loading modes (e.g. compressive, bending) as well as biological functions. For example, plant xylem is responsible for nutrient and fluid conduction which are of particular importance in the desert, where cacti must be able to rapidly take-up liquid during rare instances of rain fall [52]. Unique adaptations to end have been observed at all hierarchical levels of cacti: these include a shallow, spreading root system (ideal for transient rainfall) [32], a relatively thin living-cell layer in the roots to maximize axial conduction [52], small and numerous vessels in the stem to

maximize conduction and prevent cavitation during drying [53], [54], and larger vessels at the root-stem juncture to induce air bubbles and prevent water loss from the succulent stem into the dry soil [52]. It is possible that too oblique a mesopore distribution in the wood (i.e. too oblique a fiber angle of the wood that must wrap around them) interferes with this critical function of xylem, explaining why the cholla cacti mesopores are distributed at a higher angle. Another example of a biological function that our topology optimization did not account for is spine distribution (each tubercle pore corresponds to the placement of spines). We have already mentioned the theory that the helical geometry of the tubercles allows maximum packing density of spines while minimizing spine overlap for efficient protection against would-be water thieves [36]. Another function of the spines, however, is to collect moisture from air and transport droplets by their aligned grooves to fine, water-absorbing outgrowths at the spine base (trichomes) [55]. The mesopore distribution may optimize for spine packing efficiency not just for protection but water condensation, too. A final, major biological function unaccounted by the topology optimization is that of the surrounding living tissue: compared to the parenchyma of conventional plants, the parenchyma of cacti are extremely hydrated. The elastic yet strong bark combined with this succulence confer high turgor pressure which substantially augments the cactus mechanical properties [56]-[58]. The results of the topology optimization may provide a template for the design of mechanical structures in torsion but can provide only a partial insight as to the cholla's mesopore distribution.

5.6 Conclusions and Future Work

To understand how cholla cacti withstand torsion induced by high desert winds, specimens of staghorn cholla were characterized using photogrammetry, optical microscopy, and scanning electron microscopy (SEM), and then hydrated and tested in quasi-static torsion. Photogrammetry proved to be a cost-efficient method of producing a 3D model relative to laser-scanning that

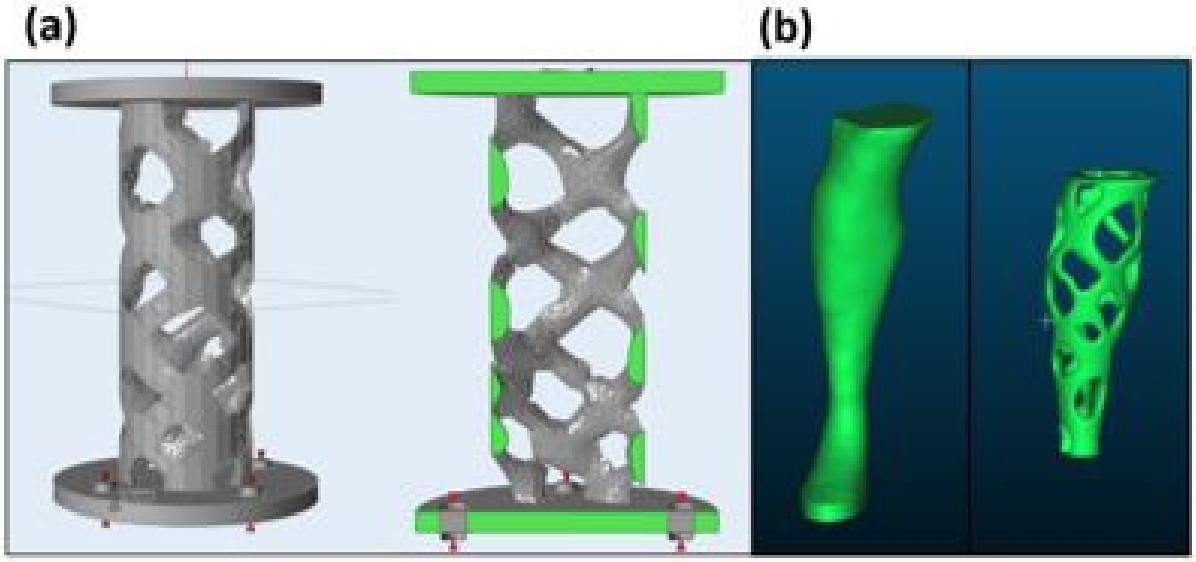

Figure 5.11: . (a) A topology optimized hollow tube in torsion yielded a somewhat similar structure to the cholla wood skeleton. The angular, rhombohedral geometry of the pores contrasted against the smooth ellipses observed in staghorn cholla (and circular pores observed in other species). Discrepancies may be attributed to the fact that the topology optimization, unlike nature, did not simultaneously account for other biological functions. (b) Even though the topology optimized result did not completely match that of the cholla, it may still be combined with other architectural features of the cholla (e.g. fiber-crossing) to inspire light and torsionally stiff composites. Applications could include prosthetics or next-generation composite driveshafts.

could still capture fine features such as fiber orientation, while SEM revealed a conventional diffuse-porous and aggregate ray wood mesostructure. Specimens tested in torsion exhibiteddensity-normalized torsional stiffness and strength comparable to that of bamboo, but theirmost remarkable property was their toughness (1100 ± 430 kJ/m^3) far exceeding that of other biological materials. The cholla's highly hydrated physiological state allowed the wood material to decompose the torsion into tension and compression rather than shear via fibril slidingand bending. These material properties were further enhanced by the mesostructural deformationmechanisms that absorbed high amounts of energy. Post-damage characterization in μ-CT revealed that fiber rupture occurred via progressive delamination, and that crack blunting by tubercle pores and winding fiber growth impeded delamination in the A-R plane.

FEA revealed how the cholla pore geometry provided a compromise of density-efficient axial compressive stiffness and torsional stiffness, while μ-CT revealed how regions of lignification matched FEA stress concentrations under torsion. These were our major findings:

- Cholla's physiological hydration reduced torsional stiffness by allowing fibril sliding and bending, but in turn improved toughness.
- These material properties were hierarchically complemented by mesostructural deformations of fiber straightening, fiber delamination, pore collapse and friction, and ultimately fiber rupture via progressive delamination.
- FEA demonstrated that pore geometry macrostructure provided a balance between torsional and axial stiffness, highlighting the need for the cholla to resist twisting forces while supporting its own mass.
  - Torsional loading stress concentrations in FEA corresponded to regions of extensive lignification in the cactus, demonstrating a feedback between local material properties and macroscopic structure.
- Topology optimization can provide inspiration for structurally efficient materials but provide limited insight into the architecture of biological materials unless they are similarly optimized for several factors simultaneously.

The mesostructural features identified in this paper may be translated into bio-inspired designs, particularly with fiber-laminate composites that could combine the cholla's use of geometry and fiber-toughening mechanisms. In drive-shafts or lower limb prostheses for example, cholla-inspired helical porosity can be implemented via topology optimization while also using winding fiber patterns to create torsionally stiff, strong, and tough columns using minimal material (Figure 9a). Furthermore, a similar approach as this study may be used to examine species such as the cirio tree (Fouquieria columnaris) shown in Figure 9b. This North American desert plant, only distantly related by clade, grows its wood with a helical porosity that hints at convergent

evolution in the Sonoran Desert. Future work should investigate how topology optimization and FEA could be used to investigate the fiber orientations of the cholla cactus and provide a more complete picture of how stresses are distributed in the material.

5.7 ACKNOWLEDGEMENTS

This publication is based on work supported by the US Army Corps of Engineers under research Cooperative Agreement W912HZ-17-2-0024, NIST Award 70NANB17H211, as well as NSF award CNS-1338192, MRI: Development of Advanced Visualization Instrumentation for the Collaborative Exploration of Big Data. This work is also supported by a Multi-University Research Initiative through the Air Force Office of Scientific Research (AFOSR- FA9550-15-1-0009) and a National Science Foundation Biomaterials Grant (1507978). This work was performed in part at the San Diego Nanotechnology Infrastructure (SDNI) of UCSD, a member of the National Nanotechnology Coordinated Infrastructure, which is supported by the National Science Foundation (Grant ECCS-1542148). Additional support was provided by the the Qualcomm Institute at UC San Diego. We thank all collaborators at Calit2, UC San Diego, as well as all other contributors to ideas, suggestions and comments of this work. Opinions, findings, and conclusions from this study are those of the authors and do notnecessarily reflect the opinions of the research sponsors.

Chapter 5, in part, is a reprint of the material as it appears, titled "Cholla Cactus: Engineering Materials and Structures Guided by Nature" Apta Biomateriala 2020. De Vivo, Luca; Matsushita, Albert K.; Kupor, Daniel; Luna, Josue; Tierra, Beatrice; Sah Robert; Krysl, Peter; Lubarda, Vlado; McKittrick, Joanna M.; Kuester, Falko Kuester. The dissertation author was the primary investigator and author of this material.

Chapter 6

Project LIMBER: Limber, Integrative Imaging, Modeling, Manufacturing for Bold Exoskeleton Research.

6.1 Abstract

There are over 40 million amputees globally with over 185,000 Americans losing their limb every year. The amputations are caused by trauma, infections, diabetes, or other medical problems. In the United States, the number of amputees is expected to rise, strongly correlated with obesity related diabetes.

For most of the world, prosthetics remain too expensive and too uncomfortable. The custom fit requirements of each prosthetic make it difficult to mass produce a low-cost solution. Access to proper health care and medical professionals can make acquiring the perfect prosthetic nearly impossible. Size, weight, fit, durability, aesthetics, cost, performance, adjustability, maintainability, and resilience are the most important metrics reported by prosthetists and patients and were the boundary conditions for the multidisciplinary optimization performed during this

study.

The work of this paper presents the design and manufacturing of a custom made, cost effective and reliable 3D printed transtibial prosthesis including socket, pylon, foot, and a monocoque design. The design of the prosthetic integrates 3D imaging, modeling and simulation techniques coupled with biomimicry to showcase the possibilities of manufacturing complex geometries with 3D printing. This report will outline advancements made by a group of students interested in advancing the restoration of human abilities through lower limb prosthetics, Figure 6.1.

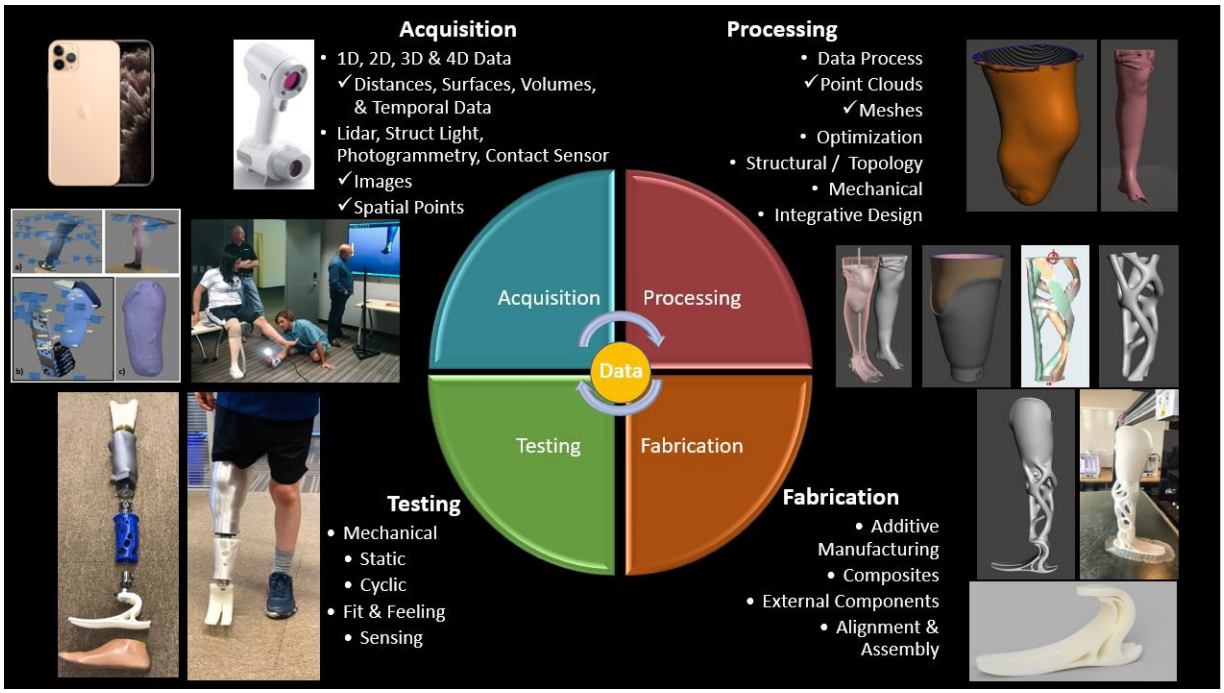

Figure 6.1: LIMBER Process developed for the Digital Design and Manufacture of Custom Transtibial Prosthesis using state of the art of 3D Imaging, Design, Analysis, Optimization and Printing technologies.

6.2 Introduction

6.2.1 Global Challenge: Access to Prosthetic Devices

The World Health Organization estimates that there are 40 million amputees throughout the developing world, but only about 5% of them have access to any form of prosthetic devices or assistance [SP94]. The result? A staggering 38 million people worldwide, two million of whom are in the United States, live painful and restrictive lives. Vascular disease (54%) often in the form of diabetes and peripheral arterial disease & trauma (45%) and cancer (less than 2%)cause more than 185,000 Americans to lose limbs every year. [ZGME+08]. Millions of amputees are left behind because prosthetics remain too expensive and too uncomfortable. Custom fit requirements make it difficult to mass produce low-cost devices and the lack of access to proper health care and medical professionals prevents adjustments needed to maintain safe, comfortable prosthetic devices. Imperfections at the prosthetic-limb interface can be the difference between an amputee wearing their prosthesis or choosing to sacrifice access to the world we take for granted. This study was profoundly motivated to develop devices that could realistically satisfy the current and future global demand. Current prosthetic sector challenges were summarized in the list below [SP94]:

- Limited funding, as prosthetic devices are frequently not included in national health and social insurance systems.
- There are not enough trained prosthetic clinicians: Currently there's a shortage of trained clinicians who can make custom-fitting prosthetic and orthopedic mobility devices. The WHO estimates 40,000 more clinicians are needed to meet demand.
- Limited availability of appropriate products in many countries.
- Fabricating devices is costly & time consuming: Traditional methods of producing custom-fitting devices is expensive and takes several days. It's a labor-intensive process that

involves making a plaster cast and hand-wrapping the materials. Even low-cost alternatives may be perceived as expensive, particularly in low- and middle-income countries.

- Patients must attend many appointments, often required to travel far to the capital or other large cities at personal expenses; It's time consuming and costly for families to attend multiple appointments. This is especially true if they need to travel long distances to reachthe nearest clinic.

- Services for the poor are usually provided by charities, some of which offer products of poor quality, while rich populations are frequently served by private clinics.

Advances in digital design software, plus democratization of 3D imaging and Additive Manufacturing (AM), have allowed for new methods for the design and analysis of prosthetics. By using these new techniques the price and comfort of these devices can be greatly enhanced.

6.2.2 History of the Prosthetic Leg Through The Ages

The history of prosthetics began before the advent of writing. Over time, advances allowed for the replacement of a simple week or iron artificial leg with more sophisticated devices that came closer to mimicking biological functions. The oldest surviving prosthetic leg was uncovered in Capua, Italy and dates back to 300 B.C. It was discovered in a tomb with the remains of its wearer and shows signs of frequent use. Ambroise Par (1510 - 1590) was an accomplished surgeon and anatomist who was the official royal surgeon of four French kings. He is regarded as many as the father of modern surgery. Along with improving amputation techniques and survival rates during his time as a war surgeon, he developed functional prosthetic limbs for all parts of the body. He was the first to develop an above knee prosthetic with an adjustable harness and a hinge-knee with lock control both of which are still used today. Pieter Verduyn was a Dutch surgeon who in 1696 invented a non locking below-knee prosthetic. This device had external hinges and a leather thigh socket, which is similar in form and function to modern corset prosthetics. The American

Civil War (1861-1865) ushered in an era of rapid growth in prosthetic leg technology with over 80 patents filed between 1861 and 1873. The World Wars necessitated new advancements in prosthetic technology. After WWI the American Prosthetics and Orthotics association was created. But major advancements will come post WWII when the U.S. government provided funding to military companies to improve the form and function of prosthetics by making use of modern materials such as plastics, aluminum and composites. [Dev19]

6.2.3 State of Knowledge

There are three basic components to a transtibial prosthesis: the socket, pylon, and ankle-foot complex (see Figure 6.2). The socket attaches the prosthesis to the wearer; this attachment can be through means of corsets, straps, lock-pins, or vacuums. Sockets are mostly made from composite materials such as Carbon Fiber Reinforced Polymer (CFRP). Pylon which are mostly made of medical graded metals and are used to adjust height, serve as load transfer elements, and connectors between socket and foot. These are usually attached with pyramid connectors which allow for proper Trochanter Hip and Ankle (TKA) line adjustment. The ankle-foot complex interface with the ground and these can be active or passive actuated to provide proper gate mobility.

The modern era for prosthetics started shortly after World War II with the introduction of the patellar tendon bearing (PTB) socket [LeM18]. The PTB socket capitalizes on the pressure-tolerant areas of the residual limb, such as the tendons and flat structures of bone, to support the forces necessary to restore ambulation. This attachment to the wearer is the primary function of the socket. In years more recent than those closely following WWII, socket science and engineering has greatly benefited from advancements in modern medical technology. To start with, modeling of the residual limb to custom fit the socket is being done via direct surface scanning and integrated with MRI data to map bone tissue depth to socket material stiffness properties [SH13a]. Osseo integrated prosthesis sockets use attachment points embedded in the residual bone, a method

recently approved by the United States Food and Drug Administration [MLL17]. Computer aided drafting (CAD) software is being used to manufacture molds of the residual limb, over which new thermoplastic materials can be shaped and formed to the user's specific needs [SS98]. These plastic sockets can even be re-molded multiple times during the early amputation healing stages as changes occur in the residual limb size.

Modern socket design often incorporates a liner to interface between the prosthetic user's skin and the material of the socket both to increase comfort and to provide energy ab-sorption. These sock-like devices, frequently made of silicon, can help prevent "pistoning" (movement of the residual limb within the socket) when used in conjunction with a vacuum check valve or Vacuum Assisted Suspension System (VASS); unfortunately, the silicon liners are also susceptible to the transmission of shear forces that can create friction-based hotspots on the residual limb [LeM16]. Numerous studies have been conducted on the designs of sockets, in-socket interface pressure measurements, and socket biomechanics, reiterating the importance of the socket in the overall design of the prosthetic device [PAOE+14]. new innovations are producing adjustable sockets, allowing the wearer to customize the fit of the socket throughout the day to account for residual limb volume loss or swelling.

Recent advances in computer imaging techniques and computed simulation driven design coupled with 3D printing technology have reshaped the way we think about when designing and building custom sockets for amputees. One clear example is the work done at the MIT media lab by PhD student David Sengeh and Professor Hough Herr. Their study focuses on variable impedance sockets designed from magnetic resonance image (MRI) data. The idea is to use a computer algorithm to assign regions of variable material stiffness on the socket walls based on the information gather from the MRI scan and then use a multi-material 3D printer to allocate different materials where designed. The authors claim to have reduced the pressure experience by the wearer by up to 17% [SH13a]. As a result of these academic efforts, companies such as ProsFit, and Mercuris, are using multi-material or layered 3D printing to manufacture custom

fit prosthetic devices. ProsFit, from Bulgaria, and Mercuris, from Germany, have teamed upto produce a low-cost transtibial prosthesis for trial in the United Arab Emirates. Although the device is still beyond the price availability of impoverished amputees, the proof-of-concept and materials testing experience it provides is invaluable [3dp].

The pylon section of the prosthesis structure, for which many advances are also being made, bears the compressive load between the socket and the foot. Typically constructed of stainless steel, titanium, or aluminum, the pylon can be extendable to accommodate for growth and may also contain a shock absorption system to facilitate ambulation. As an historical perspective on the pylon, pre-WWII prosthetics in Japan were made almost exclusively out of bamboo, a practice that was abandoned as the country became more globally integrated [LeM18]. Recently, however, bamboo is being revisited as a subject of bio-inspired design for pylon construction, due not only to its abundance and cost efficiency, but also because of its impressive ability to withstand compressive loads [Str06].

Designs of the ankle-foot complex have also benefited from advancements in material science and manufacturing technology in the decades following WWII. In general, whether the foot design is stationary or articulated, the top of the complex includes a horizontal edge to offer a connection with the pylon. The Solid Ankle Cushioned Heel (SACH) model, a jointless prosthetic foot having a resilient foot inset, is molded inside a prosthesis body. The stiff material and basic design of the SACH results in asymmetric gait characteristics and high metabolic costs with little energy return benefit [LeM18]. While basic prosthetic foot models similar to the SACH model are still in use, such as the Jaipur foot [jai] and the EB1 foot [app] that are made with locally-available materials, many other new materials and designs are emerging [Str06]. These new models include carbon fiber blade-type prosthesis attachments adapted mostly for running and the Niagara foot, a futuristic-looking solid ankle foot made from Hytel, a thermoplastic polyester elastomer which provides superior durability and energy return, and has been tested to over 3,000,000 cyclic loads to show increased durability over carbon fiber feet. [nia]. Seattle feet, which are numerous in

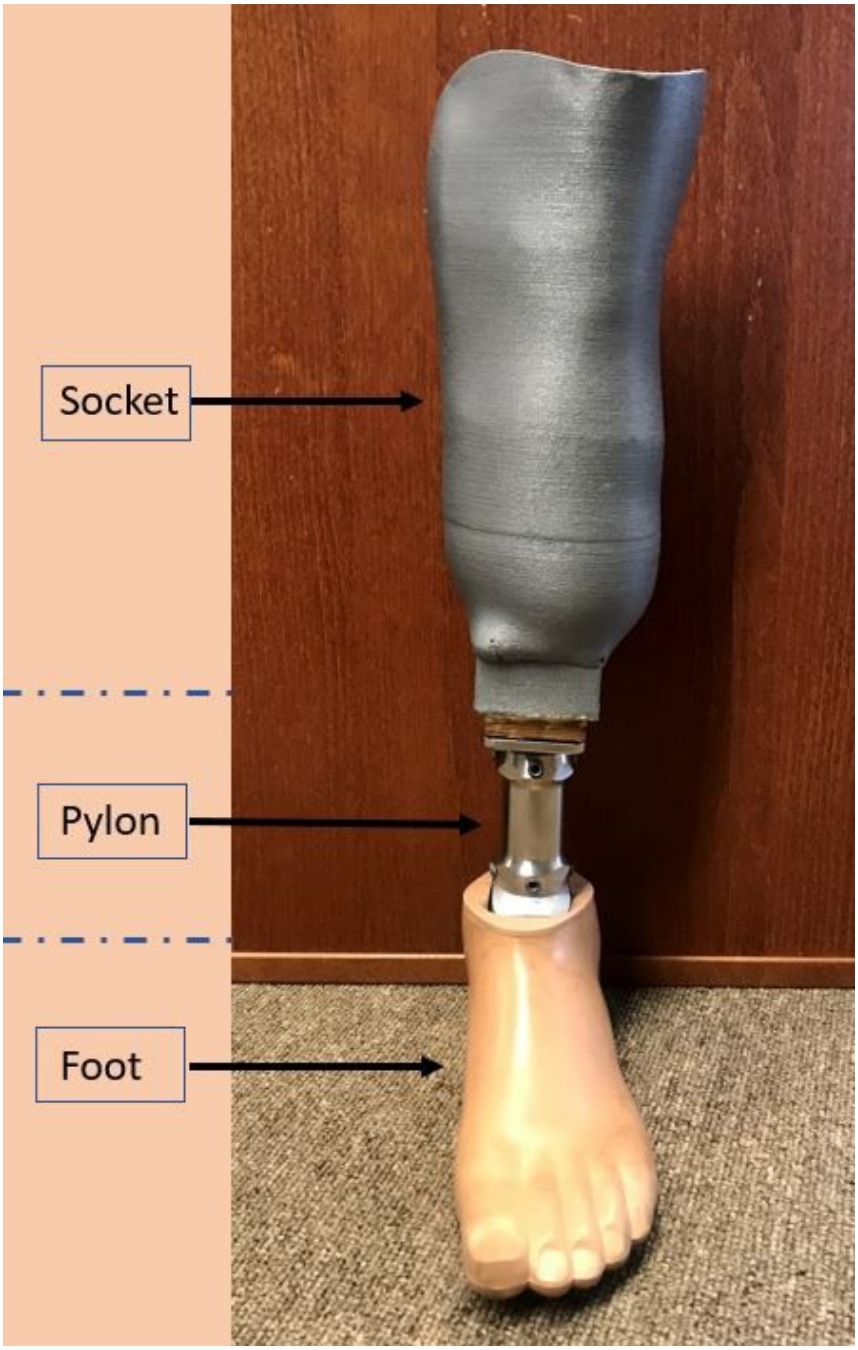

Figure 6.2: Typical pylon with socket and foot attached.

design, incorporate molded and manufactured components of various materials including carbon fiber, nylon, a metal parts for prosthetics that can be attached directly to the pylon (stationary) or with specially designed adapters to simulate ankle articulation [tru].

6.2.4 Advanced 3D Imaging, Modeling and Manufacturing

Prosthetic wearers report that they are unlikely to use the device if the fit is uncomfortable and that gaining access to professionals for repairs or adjustments is difficult [Gri16]. That is why the ideal result of this project is a 3D printed transtibial prosthetic with a custom fit socket builtfrom a digital model of the residual limb. Of great importance to the usability of the prosthesis beyond just supporting normal ambulation are its durability, comfort, and ease of integration into everyday activities [HJTA17]. To produce a device capable of achieving these objectives we focused on applying state of the art 3D imaging, modeling and simulation techniques, bio-inspired design, and additive manufacturing (AM).

3D Imaging

Over the last few years, substantial improvements in three-dimensional (3D) scanning technology have increased the popularity of this method for fast and accurate surface reconstruction. Three-dimensional scanning technology is employed in many science and technology fields for a variety of purposes, including law enforcement work, cultural heritage investigations, medicine and entertainment [LAWS18]. In the medical field, 3D scanning technology is employed for many different purposes [TW07], including body surface analysis for anatomical structure detection [mic], [GMSW10] and internal body analysis [SFSA12]. In this paper, we focus on the acquisition of comprehensive measurements of a residual limb of an amputee. Currently, the most popular full-field measurement techniques used for 3D human surface acquisition are the laser triangulation (LT), time of flight (TOF) [Mar], [SPH08], structured light (SL) [Gen11], [DKY89] and structure from motion (SfM) [[BHB], [DSTT] methods. Given the cost constraints ofthis study, and taking into consideration field deployment we selected and compared the speed, accuracy and ease of use between photogrammetry and structured light.

An ideal Imaging and Design workflow goes as following:

1. Photos or scan data are taken in the field.
2. The images/data are used to reconstruct a 3D model from the photo data using SfM techniques or with a structured light software.
3. This 3D model is used by a professional practitioner as a baseline to generate the design of the final prosthetic which can then be 3D printed.
4. The prosthetic can either be printed by a professional and delivered to the patient, or it can be sent to a 3D printer near the patient.
5. The patient tries prosthetic for fit and comfort, then makes comments to the professional.
6. If fit requirements cannot be met in the field, the prosthetic can be refined by the specialist and re-printed.
7. Repeat steps 5 and 6 as needed.
8. Patient receives a functional prosthetic without ever having to physically meet with a specialist.

Structure from Motion or Photogrammetry is the science of extracting physical reference data from photographs, particularly for the purposes of constructing a 3d model of a target. Photogrammetry relies on photo overlap to extract common features from the data. The program then calculates the position of the camera for each photo and from this spatial data constructs a 3d point cloud which can then be turned into a solid mesh. The advantages of SfM lies in its high capture frequency capacity as well as a low cost of hardware and software. On the other hand, SfM can be a time consuming process, requiring large computational power, and the final model can be low resolution in some areas as it is hard to know if the proper data is acquired before reconstruction. Photo overlap necessarily implies a certain number of photos, however, the angle of these photos is important as well. This project's plan is to create a 3D scale model of the

residual limb so that a usable prosthetic socket can be constructed from it. Ideally this process could be done with a basic smartphone camera, so as to maximize outreach potential.

Structured Light consists of active illumination of the scene with specially designed 3D spatially varying intensity patterns. The varying intensity patterns are generated by a special projector or a light source modulated by a spatial light modulator. An imaging sensor is used to acquire a 2D image of the scene under the structured light illumination. The geometric shape of the surface distorts the projected structured light pattern as seen from the camera. The principle of structured light 3D surface imaging is to extract the 3D surface shape based on the information from the distortion of the projected structured light pattern. Accurate 3D surface profiles of objects in the scene can be computed by using various structured light principles and algorithms. [geng] The main advantages of using structured light is its high capture frequency, high resolution and accuracy, as well as ease of use and speed to derive a 3D model.

3D Modeling and Design

Socket Design - In order to obtain a well-fitted socket, patients must currently undergo several rounds of appointments with licensed prosthetists. These experts take measurements of the residual limb with a fitted liner and then mark anatomical areas on the limb. After assessing the limb, the prosthesis will use plaster bandages to create a cast around the limb. The anatomical marks will transfer to the interior of the mold, such that the prosthesis can attempt to design the socket to consider regions of bone and soft tissue. The prosthesis can manipulate the plaster bandages while they are hardening to adjust its shape. This shaping requires years of experience and will only result in a successful socket if the prosthesis is highly skilled. Once the plaster hardens, the cast is removed and used to create a plastic male mold that experts can build off of to create a check socket.

the prosthesis must mark anatomical landmarks on the residual limb. Certain areas of the limb, like bony protrusions, must be avoided to prevent patient discomfort, while other areas like

flat bones and soft tissue can withstand b earing. Prosthesis must ensure proper distribution of pressure to prevent hot spots. For transtibial amputees, it is important to avoid placing pressure on the tibia (shinbone) and fibular nerves. Instead, pressure zones should be along the patellar tendon and the soft tissue along the sides of the shin bone. It is also important to design a socket that allows for the natural hinging movement of the knee. The majority of amputees do not have access to expensive specialists who can ensure that their sockets fit comfortably. As a result, it was imperative to develop a process that would output a well-fitting socket that could be modified digitally and 3D printed iteratively to find the perfect fit.

Pylon Design - As the critical component that was necessary to tie all of the trans-tibial prosthesis components together, the design of the pylon was carefully engineered to satisfy multiple constraints. Most importantly, the prosthetic pylon was designed to be strong enough to satisfy the strength requirements in ISO 10328 2006. Following this, bioinspiration from the Cholla cactus structure combined with topology optimization, and Finite Element Analysis simulations were used to iterate over the design space to create an anatomically correct, lightweight design with the required compressive, and torsional strength. Finally, the design of the pylon had to be fine-tuned in order to allow for the foot and the socket to become properly aligned and fully integrated together. Most importantly, the Pylon had to conform with ISO standard 10328 regarding the structural requirements for lower limb prosthetics. The ISO standard clearly specify proof loads, which show the forces normally encountered during regular use, and maximum stress loads which are the maximum possible force prosthetics are expected to be able to handle at multiple planes within the prosthetic.

Foot and Ankle Design - The human foot is a complicated system made up of over twenty bones and thirty joints. Our design goal is to replicate the functionality of the foot, while simplifying the structure. Specifically, this means lowering our part count and number of flexible joints. The structure of the ankle and foot offer necessary degrees of freedom. The expected range of motion changes with age, gender, body size, and flexibility. Dorsiflexion, described as

the lifting of the toes, can range from 10-20 degrees. Plantar flexion, described as the lowering of the toes, can range from 40-55 degrees. Inversion, described as curling your toes inwards, is estimated at 23 degrees. Finally, eversion is estimated at 12 degrees. It is important to replicate as much of the original expected range of motion as possible. In addition, it would be ideal to have the range of motion customized for the end user based on his or her preferences. It is easy to see this full range of motion after studying the gait cycle. Beginning with heel strike, your toes curl up, then flatten out, and finally push off prior to the swing phase. This motion is pivotal for both activities involving jumping and landing. Landing flat-footed can be extremely painful as that force is driven directly into the leg. Alternatively, landing on extended toes can be thought of as a shock absorbing event. That potential energy is converted into large displacements in a natural movement. This energy conversion is what separates high and low performing prosthetics.

Most commercially available foot prosthetics products remain too expensive. While carbon fiber offers ideal mechanical properties, it is inherently pricey. It also requires tooling and skilled technicians. In addition, these products are often outfitted with either machined stainless steel or titanium. Both metals offer ideal hardness as an interface but are expensive and can be difficult to machine. Regardless of the method of manufacturing, the design considerations for a prosthetic foot are basically the same. Most importantly, the foot must be able to support the weight of the subject without collapsing. With this requirement achieved, the secondary functions of the prosthesis can be more closely examined: design effect on gait continuity, design accommodation of shock absorption and energy return, mimicry of remaining or bio-typical model, and overall prosthesis customization capability. When aiming to use 3-D printing as the primary means of production some additional design restraints are incorporated, including material selection for durability and toughness, methods for attachment and articulation, and maintaining costs at or below current industry standards. In order to address the design basis for the 3- D printed foot, we considered several different models, materials, and techniques for construction.

Additive Manufacturing

3D Printing, also known as additive manufacturing, holds great promise and proved to us to be an essential technological enabler for the manufacturing of customized prosthetics. The ability to build physical objects one layer at a time allows for the generation of optimized complex structures that would otherwise be impossible using conventional manufacturing techniques such as Computer Numerical Control (CNC), Core Casting, Investment Casting or Injection Molding. This advantage is allowing designers and engineers to fully exploit the capabilities of modern structural and mechanical simulation and optimization methods. 3D Printing also allow us to experiment using a wide range of materials with different properties and identify which ones perfectly fit for the intended design loads and conditions.

Early additive manufacturing equipment and materials were developed in the 1980s. The Poly-Jet process is different in that a carriage jets photo polymers onto the work space, which are then cured by a UV light. After a thin layer is created, the process repeats itself by jetting additional layers until the part is fully formed.

Stereolithography or "SLA" printing is an early and widely used 3D printing technology. It was invented with the intent of allowing engineers to create prototypes of their designs in a more time effective manner. The term stereolithography was coined in 1984 by Chuck Hull when he filed his patent for the process. Chuck Hull patented stereolithography as a method of creating 3D objects by successively "printing" thin layers of an object using a medium curable by ultraviolet light, starting from the bottom layer to the top layer. Hull's patent described a concentrated beam of ultraviolet light focused onto the surface of a vat filled with a liquid photopolymer. The beam is focused onto the surface of the liquid photopolymer, creating each layer of the desired 3D object by means of crosslinking (generation of intermolecular bonds in polymers). It was invented with the intent of allowing engineers to create prototypes of their designs in a more time effective manner. After the patent was granted in 1986, Hull co-founded the world's first 3D printing company, 3D Systems, to commercialize it.

Selective laser sintering (SLS) came around in the year 1989 and is an additive manufacturing (AM) technique that uses a laser as the power source to sinter powdered material (typically nylon or polyamide), aiming the laser automatically at points in space defined by a 3D model, binding the material together to create a solid structure. It is similar to Selective Laser Melting (SLM); the two are instantiations of the same concept but differ in technical details. Selective laser melting (SLM) uses a comparable concept, but in SLM the material is fully melted rather than sintered, allowing different properties (crystal structure, porosity, and so on).

Finally in 1992 a new patent came out focusing on what was called Fuse Deposition Molding (FDM). FDM uses a thermoplastic filament that is melted down and extruded from a print head. Once extruded into a bead, the material is immediately set in the high temperatures of the machine and layered on a platform. The machine head repeats the extruding and melting, layer by layer, until the part is complete. Fused filament printing is now the most popular process (by number of machines) for hobbyist-grade 3D printing. Other techniques such as photopolymerization and powder sintering may offer better results, but they are much more costly.

6.2.5 Benefits of 3D Printing Prosthetic

3D Imaging and Additive Manufacturing are key enablers to this study. 3D printing is not only allowing us to bring into the world the most audacious designs but is also allowing is to do so faster than ever before, and with the ability to customize any wearable design by combining CAD with 3D imaging techniques from the comfort of a chair and usually miles away from the intended wearer. summarized below are what we think the greatest benefits of applying 3D imaging and 3D printing technologies into prosthetics:

- Faster production time: The time it takes to print a custom prosthetic is greatly reduced when compared with conventional manufacturing methods such as casting. Faster production time means we can deliver more devices in a shorter period of time, taking us a step closer

to our goal of delivering these devices to those unaddressed 38 million amputees around the world.

- Custom fitting comfort: Custom devices means the wearer does not have to worry anymore about the prosthetic being too big or small, or just too uncomfortable. This translates into more satisfied patients who will use the devices to improve their lifestyle and that of their family members.

- Fewer clinic visits: A more efficient, digital production process means fewer trips to the clinic. The process of digital design allows a prosthetitians to do most of the work virtually and without the need of a patient to be in the same room. The patient only needs to be physically present at a location for image data acquisition and for a fitting session at the end of the design and manufacturing process.

- Shorter hospital stays: Patients could be fitted and discharged with non or only one overnight stay. This will greatly reduce the cost for acquiring a prosthetic device which we believe will improve the chances of patients acquiring and wearing their prosthetics.

- safe work environment: The technology we use is safe for technicians and professional doctors to use and operate. Besides from a scanner device and a 3D printer the only tools needed is a computer and a set of software to process, design and manufacture a full wearable prosthetic.

- Develops digital skills: Clinicians will develop expertise and skills in the latest 3D technology.

6.3 Methods

6.3.1 3D Imaging and Modeling

One of the key goals of this study was to allow for the cost-effective 3D modeling of the patient damaged limb through the use of smartphones and photogrammetry techniques. But one question remained unanswered, and it was the accuracy of the 3D model derived from SfM.In order to confirm and quantify the quality and accuracy of the photogrammetry models we also imaged the patient residual limb with a 3D structured light scanner. In addition to this we also scanned the waist and sound leg of the patient which we used later during the component alignment process. This was a big enabler for achieving a fully 3D printable monocoque as we will discuss later. For SfM we selected a Sony a7iii camera (Sony, Japan) as our data acquisition unit and Metashape (Agisoft, Russia) as the photogrammetric processing software. As for Structure Light we picked and used the Omega 3D Scanner (Willow Wood, Ohio) and its companion Omega software package (Willow Wood, Ohio). The OMEGA Scanner 3D has an acquisition frequency of 550,000 measurements/second. The scanned shape generates directly in the OMEGA software so clinicians may immediately see exactly what is captured.

Both of the residual limb scanning process, Figure 6.3-6.4, were straightforward and it was performed as follows:

- The patient was placed in a standing position with a liner covering the residual limb. The liner helped us achieve an even lighting surface for improved imaging as well as capturing the real leg geometry that would be hosted by the socket.
- Making sure a proper distance between the scanner and the residual limb we covered all the regions of interest and collected the necessary data for a 3D point cloud reconstruction.
- Once the data was acquired in the form of point cloud a solid mesh was obtained using the Omega software.

- Finally the solid mesh was exported as an .stl file which can be imported by other CAD software for further processing or modifications.

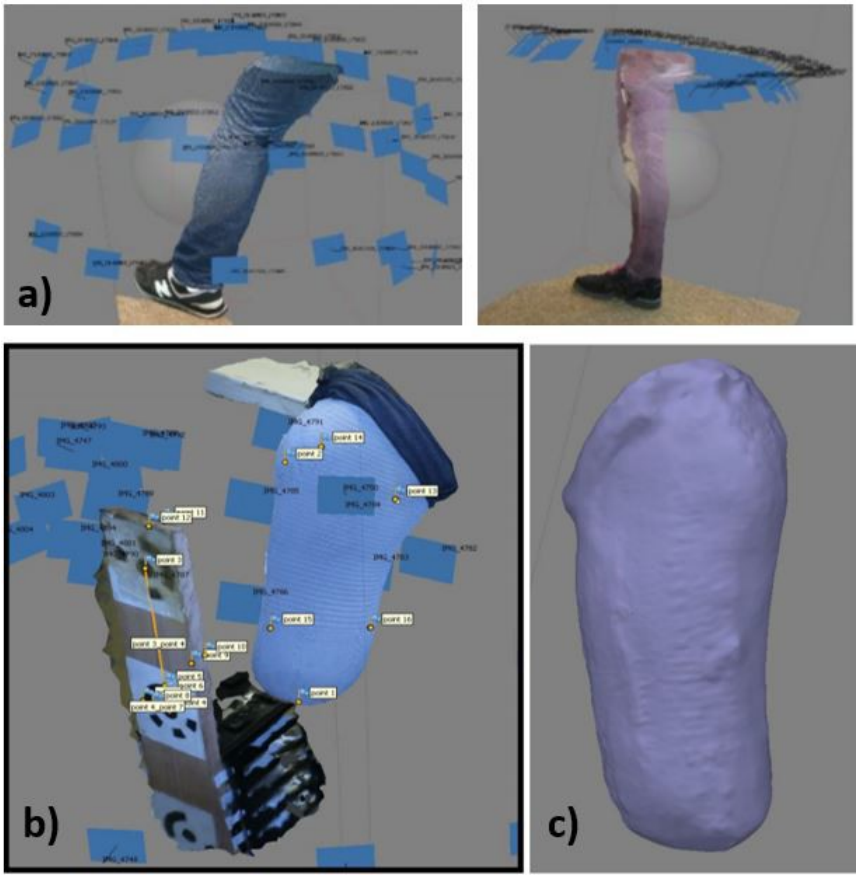

Figure 6.3: Photogrammetry workflow: a) a number of Images were acquired using a standard digital camera or smartphone. b) a series of target markers are placed near the limb in order to generate an accurate scale version of the residual limb. c) a 3D point cloud and a Mesh is generated using a photogrammetry software like Agisoft Methashape.

Another key enabler in the design of the prosthetic leg was the 3D modeling of the healthy leg which served as reference geometry for the sizing and alignment of the three components (Socket, Pylon and food). The sound leg 3D model was generated using Structured Light, then imported into a CAD software Rhinoceros 3D (McNeel, WA) where a mirrored model was generated. The mirrored model was then used to accurately size and align components so a monocoque design could be generated as displayed in figure 6.5.

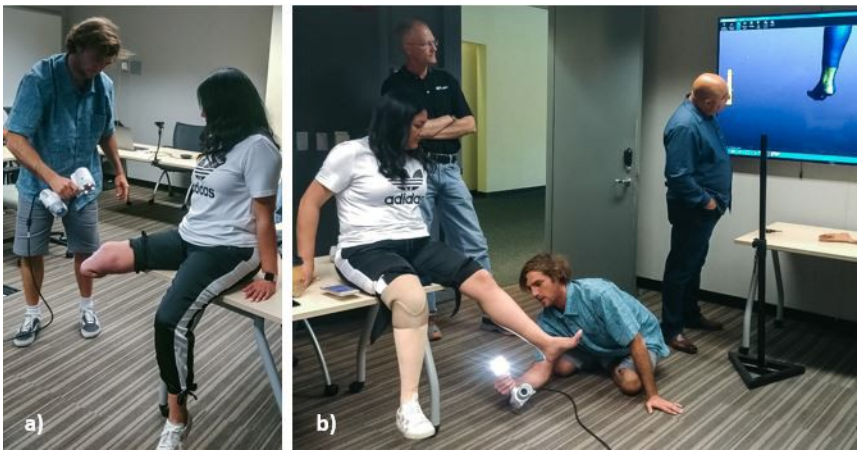

Figure 6.4: Laser Scanning workflow: a) while activating the scanning device the residual limb is scanned by moving the scanner around the region of interest. b) In a similar matter the healthy leg was scanned.

6.3.2 Design

Socket Design:

Process, Modifications, Adjustments and Attachments - A 3D Model of the residual limb was scaled up and then a Boolean Difference, removing one solid from another, between the original and scaled up version was used to create an anatomically identical hollow socket. This socket was then modified using the Omega Software to add and remove materials where areas of different stiffness or support was required in order to properly distribute the pressures and prevent hot spots, figure 6.6. For this case we performed the following operations:

- Cleaned and reduced the volume about 3%.
- Blended evenly to fill and smooth all scar tissue, we would do this if the final fit of the prosthesis was going to be over prosthetic socks.
- In the A-P axis (anterior-posterior) carved about 2 cm wide and 1 cm deep patella tendon bar for weight bearing.
- Reduce the M/L (medical-lateral) proximal above condyles.

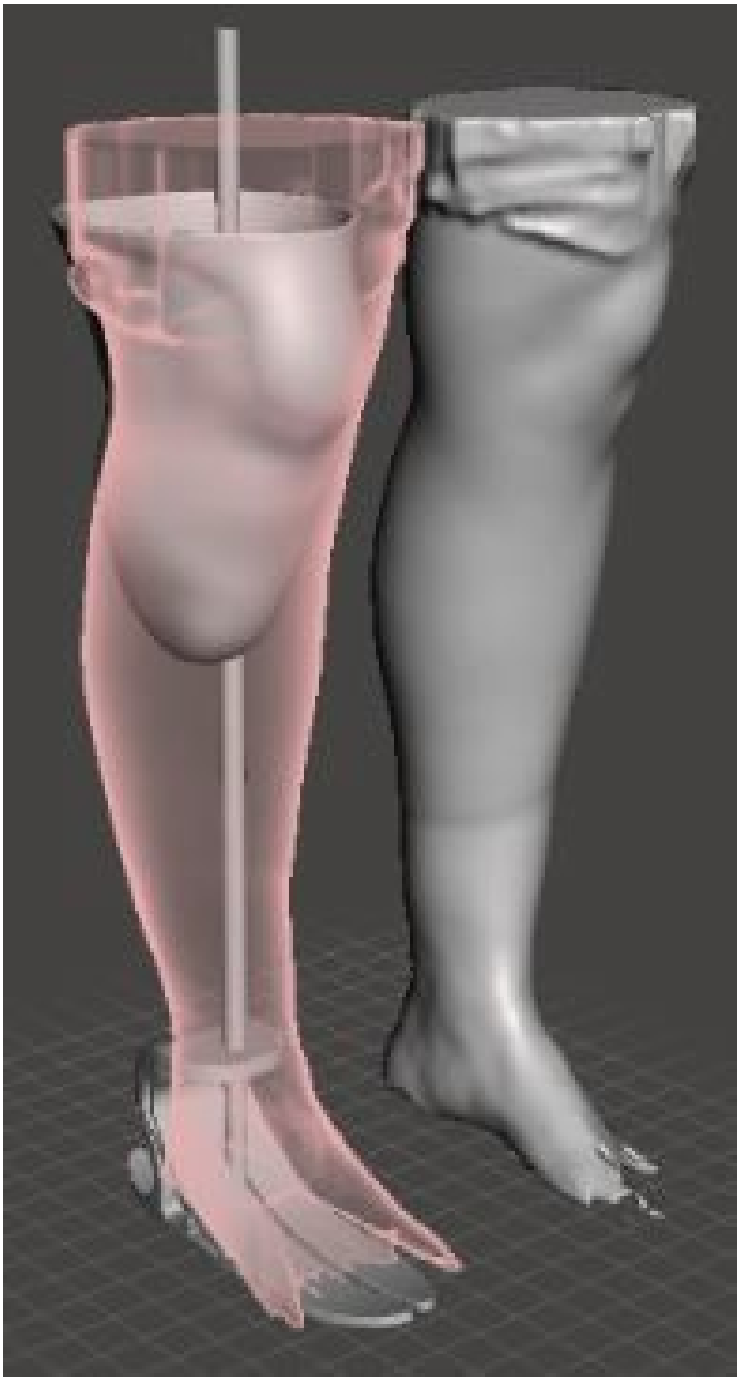

Figure 6.5: Sound Leg Model and Mirrored Leg Combined with Residual Limb, used to size and align components for the generation of a monocoque design.

- Delineated preliminary socket trim lines.
- Now a clear plastic socket can be printed for fitting and total contact testing.

- Build ups adjustments can be made at this point to improve fitting, contact and comfortability.
- We modify the correct socket for a pin connection attachment, and 4 bolt holes at the bottom to allow the attachment of a steel plate that will allow the connection between the socket and the pylon.
- This final socket was then printed and tested by the patient who was very pleased with the performance and comfortability of the 3D printed socket.
- The team was able to lock down a simple procedure to convert a photogrammetry derived model into a functional, anatomically correct custom-made 3D printed socket.

Pylon Design:

Simulations and Topology Optimization - The pylon is located between the knee and the ankle reference planes. In addition, the ISO standard 10328:2006 [ISO06] specifies the maximum torque which the pylon would need to be strong enough to withstand. The pylon is expected to withstand a compressive proof load of 1395 N and a maximum load of 3220 N. Additionally, the pylon is expected to withstand a maximum torque of 50 N-m. For the design of the pylon the starting geometry was extracted from scans of the patient's healthy leg. The basic process was to scan the healthy limb from knee down, refine and mirror the produced model, segment the respective region where the pylon bridges the gap between the foot and socket, and finally perform a shell operation to create a constant wall thickness following that of a Cholla cactus of similar dimensions. This shelled geometry is then run through topology optimization with basic conditions being maximum stiffness and minimum mass. Loading and boundary conditions for the topology optimization study are extracted from the ISO/ASTM standard for transtibial prosthetic devices [citation]. The generation of the new design allowed a perfect model

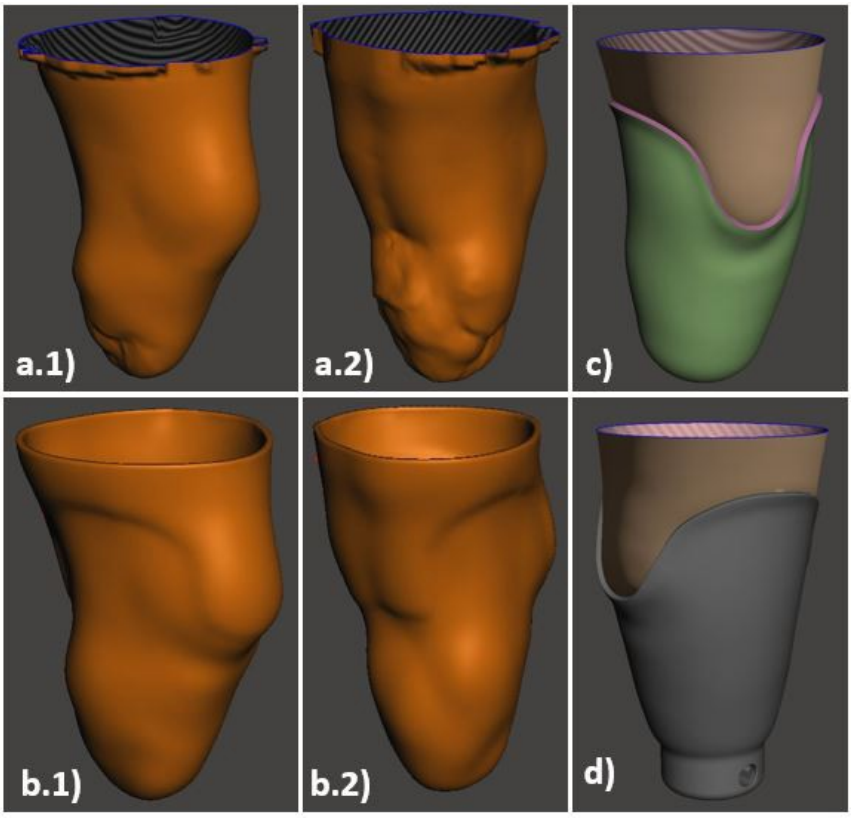

Figure 6.6: Design Process for the generation of a custom fit s ocket: a .1) a.2) anterior and posterior views of the residual limb scanned model which served as a baseline for the generation of the socket. b.1) b.2) anterior and posterior views of the derived leg mold after anatomical modifications were made. c) Resulting socket based on leg mold and added socket trim lines. d) Final socket model with design for lock pin mechanism embedment.

to be used as a linking mechanism between the socket and foot without needs of third-party metallic components. The resulting bio-trust like shape was used to virtually merge the socket, pylon and foot into a monocoque design that can be fully printer in one piece. Final results of the monocoque version of the pylon can be seen in figure 6.7.

Foot Ankle:

Design Iterations - The first steps towards production of a functional foot prosthesis was model acquisition. Once again, plane-cut operations were used to segment the foot section of the mirrored healthy leg scan-model. With the foot isolated, a series of topology optimization

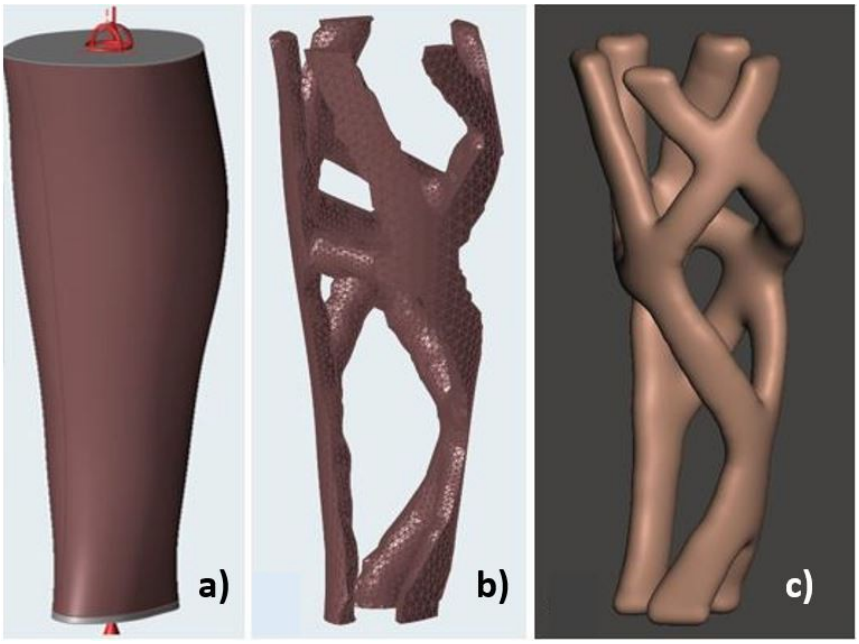

Figure 6.7: Topology Optimization of Pylon Region

studies were performed to reduce mass and maximize stiffness. Throughout topology optimization, simulations were performed to validate the optimized structures. Once an acceptable mesh was produced it was exported as an stl and imported into Fusion 360. Further modification to create attachment points and refine the external profile for matching desired shoes was deemed critical. For this reason, a model was created manually using the mesh as a 3D stencil. This solid part was subsequently modified and iteratively simulated with the same ISO/ASTM standard loading and boundary conditions as the one used for the pylon design [citation]. The modeled geometry was 3D printed and tested but was ultimately limited in its functionality due to the numerous struts as well as requiring a significant amount of time to model each iteration. For these reasons, a simplified model was created, which will be universally viable between patients/users, easily tuned for use-case, activity level, and patient weight/size, aesthetically pleasing, easily simulated, and incorporates functional design elements to passively enable energy recapture and a smooth gait. In order to transition from the complicated, manually modeled, and topology optimized geometry to the simplified model, several key design elements were identified and translated as

highlighted in figure 6.8.

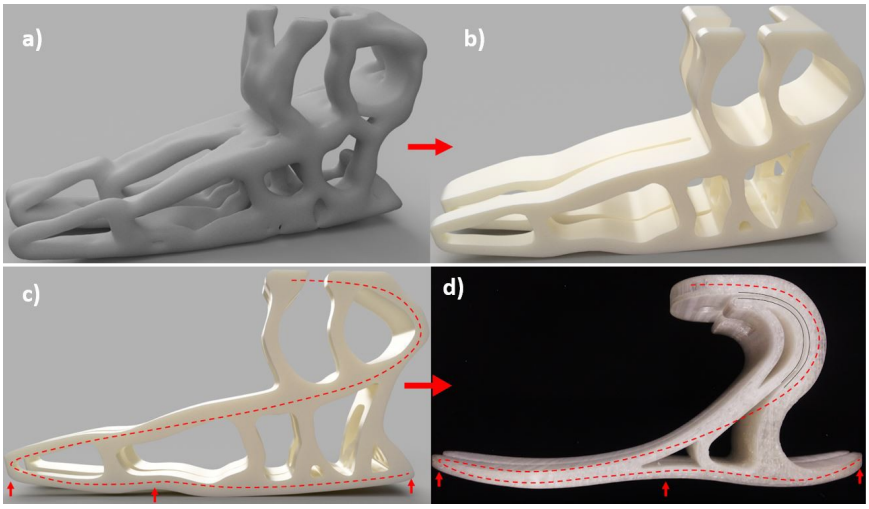

Figure 6.8: a) Initial Topology Optimized foot design using the healthy leg mirrored model as a reference geometry. b) smoother version of the initial topology optimized version. c) Utilizing the topology optimization model, we found insights on how to manually design an optimized foot model. d) Showcasing how insights from topology optimization were utilized to generate a final design model.

Finite Element Analysis of Foot - The below knee prosthesis structural testing standard ISO 10328:2006 [ISO06] gives a comprehensive set of loading conditions that prosthetic devices must satisfy before being certified. The proof force is defined as the set of loading conditions where success is dependent on minimal permanent deformation occurring. The proof force for activity level P5 at heel and forefoot loading conditions for ankle-foot devices and foot units in the static test procedure is 2240N. The foot material is defined as Nylon 6,6. Contact surfaces were defined to avoid surface penetration, as shown by dotted, curved lines in Fig. 1. Forefoot and heel loading was performed as specified by ISO10328 with the top surface of the ankle fixed, A in Fig. One additional loading condition was used to test for proper forward bending resistance at the foot/ankle-pylon connection. The two ground contact points, B in Fig. 1, on the bottom of the foot were fixed and the same proof force of 2240 N was applied in the u-axis, synonymous to the TKA line. 6.9.

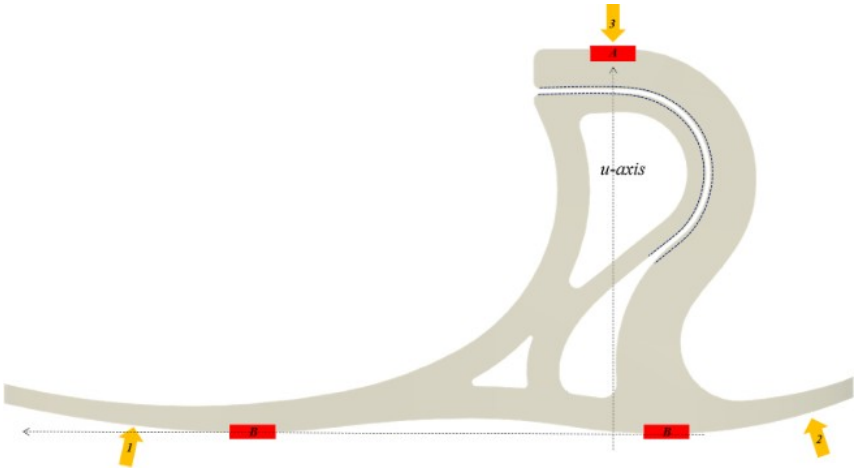

Figure 6.9: Foot unit loading diagram.

Digital Alignment, Integration and Monocoque Design:

Connections and Alignment Components - The first prototype created by the team was a multi component device which had to be connected and aligned using metal third party components. Thanks to the help of our doctor collaborators, Dr. Herb and Dr. Chuy, we were able to get access to medical graded prosthetic components. Figure 6.10 showcases all the different elements required for the full assembly of our first prosthetic leg prototype. First, a custom-made silicone liner (a) with an embedded titanium pin rod (b) had to be ordered and was manufactured by WillowWood, Ohio. The liner helps to improve the fit between the damaged limb and the 3D printed custom socket plus it serves as a cushion and damper which improves comfortability. WillowWood also provided us with a lock pin mechanism that had to be embedded into our 3D printed socket so the liner and the socket can connect securely. The next stage was to connect the pylon to the socket and foot. For this we were provided several modular endoskeletal components also by WillowWood and can be seen in Figure 6.10,e. The first components were a socket attachment plate connected to a titanium 4-hole pyramid adapter that connected to a titanium pylon adapter which further connects with a pipe embedded in the design of the topology optimized pylon. Next, we connected the pylon with the foot also using a titanium 4 hole pyramid

adapter and a titanium pylon adapter. It is important to notice that the pyramid and pylon adapters served not only as structural attachment elements but also as alignment devices that allows the prosthetics to properly align the assembly as required by the patients. The final external component used in this first prototype series was a silicon cover that helps the foot to fit shoes and improve aesthetics when desired. All components were assembled as represented in figure 6.10,f.

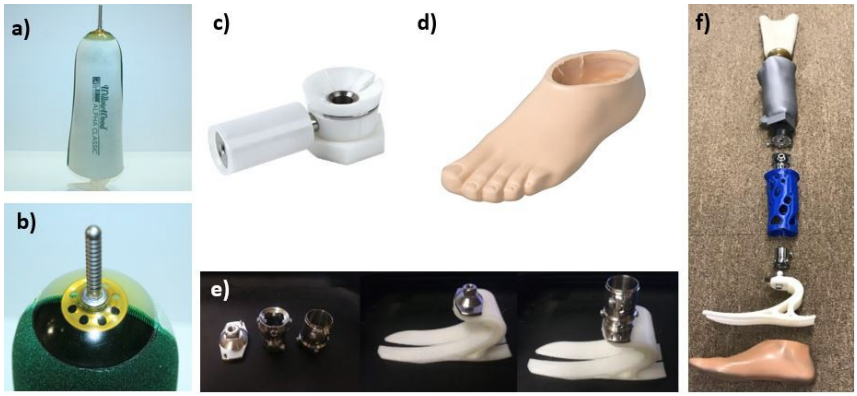

Figure 6.10: Components used as connections in standard designs: a) Custom silicone Liner (WillowWood). b) Titanium pin rod (WillowWood). c) Pin Lock Mechanism (WillowWood). d) Silicon foot cover (WillowWood). e) Modular endoskeletal components (WillowWood). f) assembly of all components.

Digital Alignment and Monocoque Design - The components presented in the previous section are industry standards and almost every professional prosthetics relies on them to fully assemble a prosthetic leg. It is worth noting that although these components are extremely reliable and easy to use they are also extremely costly and not available in all parts of the world. Since the main goal of this study was to create prosthetic legs that can become available to the masses and especially those in developing or poor countries, we continue our design process to find a way to minimize the use of external third-party components. Again, thanks to the use of 3D printing and its ability to manufacture almost any shape you can design we were able to connect all components virtually and generate what we called a monocoque design, figure 6 .11. This new design consisted of the three main elements of a prosthetic leg (socket, pylon and foot) which were aligned and connected using a CAD and mesh editing software such as Meshmixer

(Autodesk, CA). For the alignment we made use of the mirrored healthy leg scan to properly place each component in the right position and angle before virtually connecting them using mesh editing tools. The resulting monocoque design was successfully printed in one go and it only requires one external component, the pin lock mechanism, to be embedded into the socket.

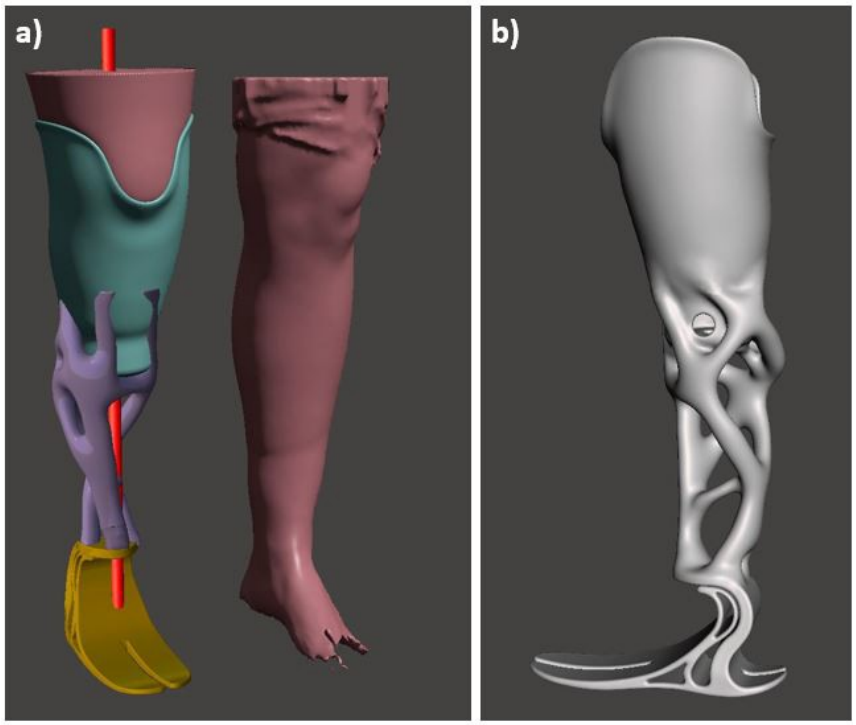

Figure 6.11: a) Using the healthy leg scan and its mirrored model we were able to properly scale and align all components so a ready to use monocoque version could be printed. b) Side view of final monocoque design.

6.3.3 Additive Manufacturing:

In this study we utilized a series of FDM machines such as the 3DP 300 Series Workbench (3D Platform, Illinois) a double nozzle large scale format 3D printer with a print volume of 1000 x 1000 x 700 mm. The selection of FDM as the 3D printing technique was done because of the cost effectiveness of the machines, materials and the process itself. It also offers a broad range of materials to work with ranging from prototyping materials such as PLA to ready to wear

materials like nylon. It is also the most environmentally friendly and can be performed in an office or hospital environment. The 3DP large factor equipment was key in the manufacturing of the monocoque prosthetic since it allowed us to print tall objects in one piece. We also made use of smaller 3D printers such as the LulzBot TAZ 6 for the generation of individual components. Maximum nozzle temperatures between 250-300C enable the use of most available filament types, with the exception of PEEK and PEI.

The large selection of thermoplastic filament available for the FFF process allowed us to select our feedstock material with our specific use-cases in mind. Group one materials for prototyping, alignment, and fit testing, included low-cost materials with high printing performance and lower mechanical properties. Group two materials, for load-testing and end-use parts, were selected primarily for their mechanical properties. The materials selected for group one included PLA, PVA, and PET-G. Lower printing temperatures between 190-240C and small coefficients of thermal expansion reduce bed de-adhesion, delamination of layers, and bulk warping in parts printed with each of these filaments. PVA was rejected because it is hydrophilic, which causes it to absorb water and ruin printing performance. Printing trials between PLA and PET-G concluded PET-G has a higher rate of success for printing overhanging structures, which are often unavoidable in our bio-inspired designs. Group two materials include ABS, PC, and Nylon, which have higher mechanical properties, but require difficult printing conditions. ABS was rejected because it releases Styrene, a toxic chemical, when extruded. PC and Nylon are both hydrophilic and must be dried before printing and sealed in a container with desiccant during printing. Both materials require printing temperatures between 260-280C, build platform temperatures between 80- 100C, and chamber temperatures greater than 40C. PC has a toughness of 60 kJ/m2 (Charpy Impact Method 23C, Notched - ISO 179), elastic modulus of 2350 MPa (ISO 527), strain at failure of 1.2 (ISO 527), and tensile strength of 63 MPa (ISO 527) [[mcp]] at failure of 2.5 (ISO 527), and tensile strength of 60 MPa (ISO 527) [[mcp]]. PET-G has a toughness of 8.1 kJ/m2 (Charpy Impact Method 23C, Notched - ISO 179), elastic modulus of 2020 MPa (ISO

527), strain at failure of 0.23 (ISO 527), and tensile strength of 50 MPa (ISO 527) [[mcp]]. The lower modulus and higher elongation of Nylon made it a suitable candidate for the foot and ankle, which needs to be flexible and have high fatigue resistance for the dynamic gait cycle. While PC had a very high toughness, the socket and pylon require strong and stiff behavior, which made PET-G (with its similar tensile strength and modulus properties) the better candidate due to its much superior printing performance. Further testing of the pylon and socket may identify a need for greater toughness, but for the purposes of this study PET-G and Nylon filament were used to print load-bearing, end-use parts.

After successfully designing both individual elements and monocoque designs the next step was to fabricate them. We utilized additive manufacturing techniques to print full scale models that were used to test the fit, comfort, and mechanical bearing capacity under a controlled load environment as well as active patient loading. The 3D printed not only allowed us to fabricate custom parts on demand in a cost-effective matter, but it also allowed us to quickly turn digital design models into functional prototypes which was a key factor in the iterative design process. The process to 3D prints any model is as follows.

First a 3D CAD model is exported as a closed stl file. The file is then imported into a slicer software, in our case we utilized Simplify3D (Cincinnati, Ohio). In Simplify the model was placed in the desired print bed position, printing parameters such as speed, temperatures and supports were defined. The slicer then generates a g.code file which gives layer by layer information to the 3D printer. The slicer then generates a g.code file which gives layer by layer information to the 3D printer. The g.code was exported into a memory card which was then read by the 3D printer. The memory card was loaded into the printer and the g.code was uploaded. The printer bed and nozzle temperature were set as well as preparing the printing bed with glue to improve adhesion. The printed was started and monitored for any failures during the printing process. Finally, the printed model was then removed from bed and post processed when needed using tools such as sandpaper, pliers and drills.

Using this manufacturing method, we were able to successfully 3D print multiple real scale sockets, pylons, feet and monocoque designs, figure 6.12. Resulting in a reliable, fast, and cost-effective way to manufacture custom prosthetic parts, and a key enabler in our goal to bring reliable custom bionics to those in need.

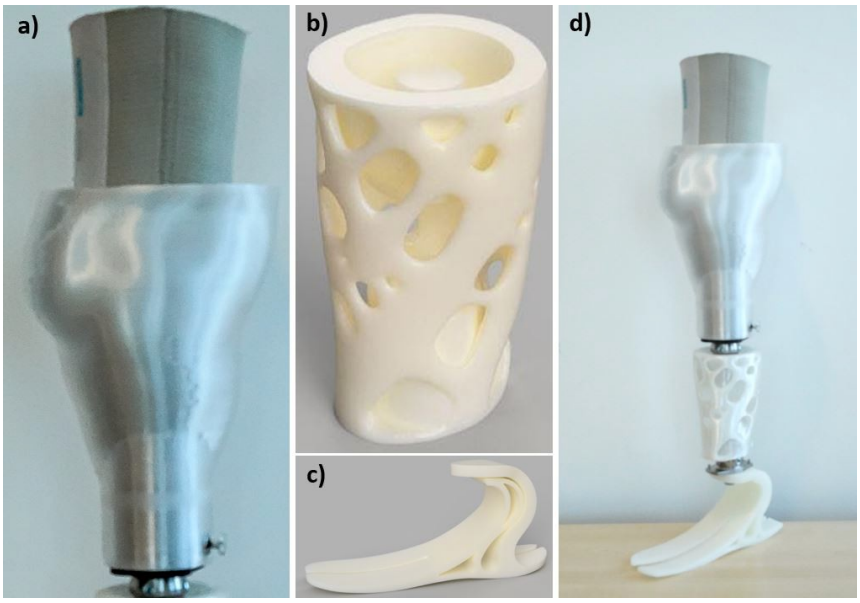

Figure 6.12: Final version of 3D Printed: a) Socket. b) Pylon. c) Foot. d) Fully Assembled Device.

6.4 Results

6.4.1 Imaging

After successfully reconstructing the patient's residual limb morphology with both Photogrammetry and Laser Scanning techniques we compared the two models using a 3D point cloud and mesh processing software such as CloudCompare (CloudCompare, France). In order to compare the accuracy and quality of the photogrammetry scan we imported both models, alignedthem using reference points such as the tip of the limb or the kneecap, calculated surface normal

on both models and performed a cloud-to-cloud distance operation. The results show a maximum local difference of 1.2 mm and a minimum local difference -2.0 mm. The resulting color image, Figure 6.13, represents the difference between the two models in mm and proved to be a good way to guarantee the cost accessible model from photogrammetry is accurate enough so a socket can be derived from it.

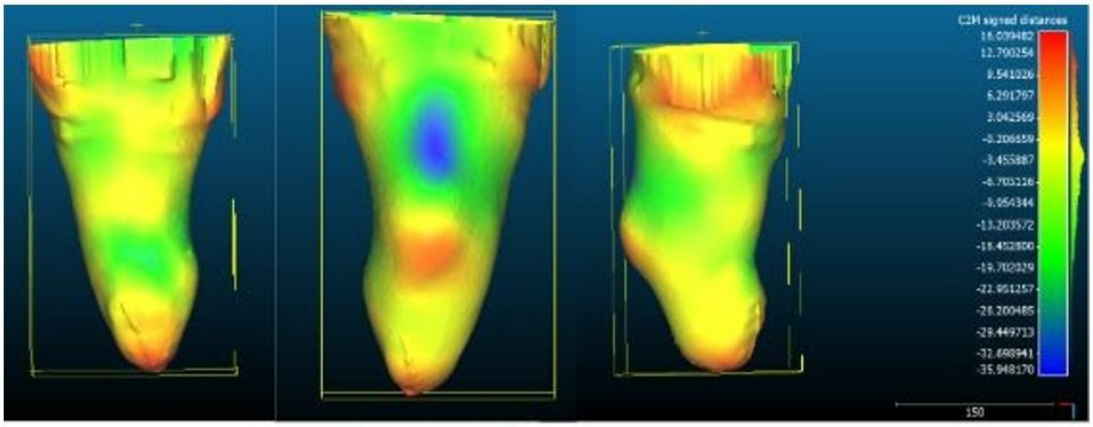

Figure 6.13: using CloudCompare we were able to quantify the difference between the photogrammetry model and the laser scanner model. Distances are displayed as a color map with units in mm.

6.4.2 Pylon

We used Finite Element Analysis (FEA) to validate the safeness of the topology optimized pylon section. We applied the ISO loads of maximum compression (3220 N) and maximum torque (50 N.m) on the top of the model and fixed the bottom surface for translation and rotation. The results, Figure 6.14, shows the Von Mises stress (N/m$\hat{2}$) regions under ISO standard loads. A maximum stress can be found on the frontal-bottom section as well as the back-bottom section, both regions can be seen in red color in figure 6.14. Important to notice that all stress fall below yielding of the Nylon material used in this experiment. When we compare the maximum stress of 16 MPa to the yielding strength of Nylon 6 (Average value: 71.0 MPa) we concluded that our design has a satisfactory factor of safety of 4.4.

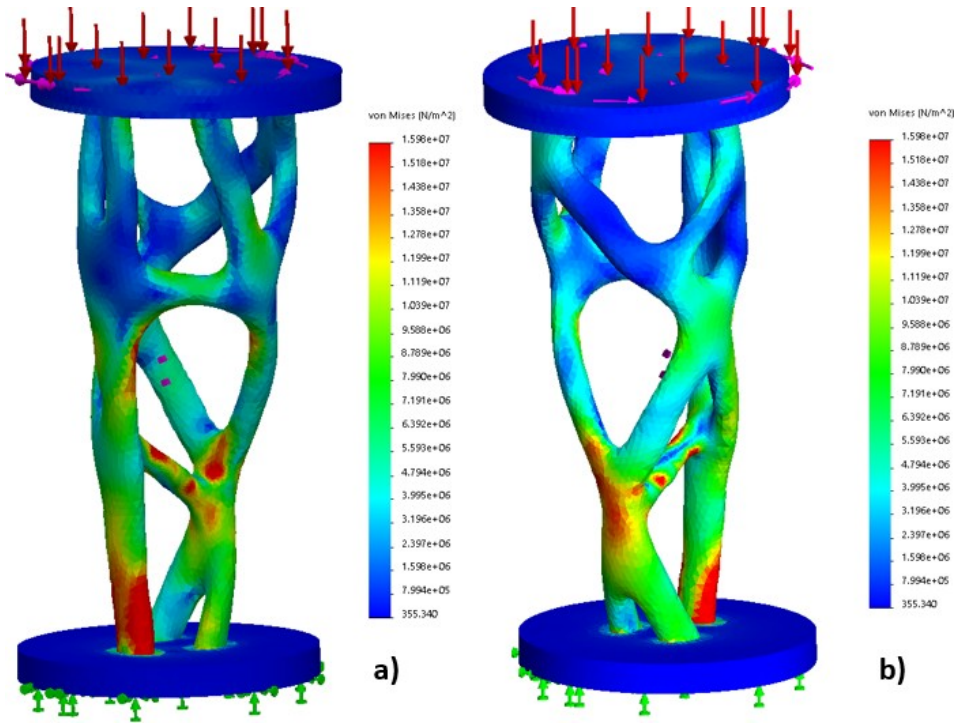

Figure 6.14: Finite Element Analysis of Pylon under ISO standard compressive and torsional loads.

6.4.3 Foot

In this study, the proof force, as defined by the ISO 10328:2006 [ISO06], was analyzed using nonlinear static stress FEA simulations at heel, forefoot, and ankle locations to verify plastic yielding and elastic deformation values stay within set boundaries. In the forefoot loading condition (a), shown in Fig. 6.15, a maximum deflection of 62.08 mm occurs at the toes and the maximum Von Mises stress is 95.61 MPa. In the heel loading condition (b), shown in Fig. 6.15, a maximum deflection of 9.06 mm occurs at the toes and the maximum Von Mises stress is 43.06 MPa. A maximum deflection of 3.21 mm in the negative u-direction occurred at the ankle joint and maximum Von Mises stress of 31.75 was calculated for condition (c) in Fig. 6.15.

Figure 6.15 demonstrates the functional behavior of the LIMBER foot design, with its disconnected surface simple mechanism for ankle flexion. During proof force heel loading, plantar flexion of approximately 3 degrees is achieved. This plantar flexion allows for a smoother

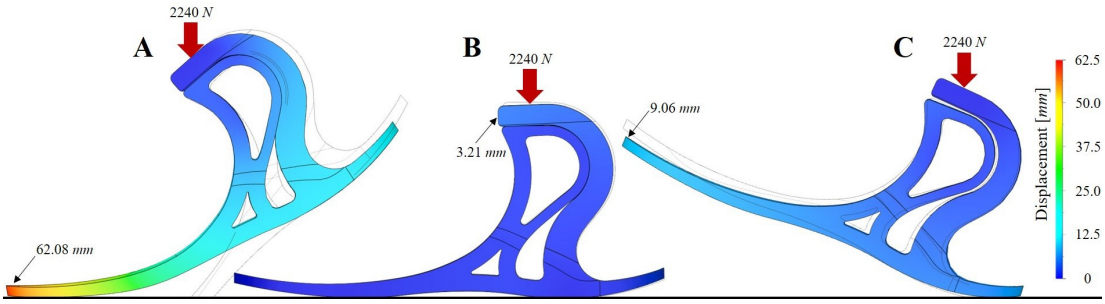

Figure 6.15: Foot unit FEA results showing deformation in (A) forefoot, (B) heel, and (C) u-axis loading conditions.

heel-strike to mid-stance transition and is enabled due to the disconnected-surface foot design. Normal loading along the u-axis resulted in a small deflection that was within acceptable limits for acute hip height misalignment, as validated by Doctor Herb Barrack. The mid-stance to forefoot-liftoff transition is aided by the stored spring energy from the 62.08 mm deflection, resulting in less energy spent by the patient during walking.

6.4.4 Monocoque

One of the challenges of this study was to quantify and validate the advantages of 3D printable transtibial prosthetic monocoques over traditional prosthetic legs. In order to accomplish this we decided to break it down into metrics. The metrics used for this final part of the result section were; Amputee Feedback, Alignment success, weight comparison, cost analysis, and time of design & manufacture.

Socket Comfort

Using digital design enabled the modification of the socket scan for the addition of load bearing regions for the patella tendon as well as developing proper spacing at sensitive areas such as bony protrusions. Using amputee Diana Novitchenko feedback was the best way for us to validate the comfort and fit of the 3D printed socket. "I am amazed at how I can just take

something that did not exist 12 hours ago and just put it on and walk away. The comfort and fit are beyond impressive, the process is so customized that it allows for maximum comfort.". We confirmed that digital design serves as a great tool for customizing and generating 3D sockets that properly fit the patient while providing proper mobility and load bearing functionality.

Alignment TKA Line

A major priority for the design team was to accomplish a well aligned monocoque utilizing digital modeling and additive manufacturing. This is of vital importance because any unseen misalignment could cause bio-mechanical complications to the wearer knees, hips and spine. To validate the alignment of the resulting leg we relied on Doctor Herb Barrack expertise as well as a front and side pictures taken from amputee Diana Novitchenko standing tall wearing a monocoque prosthetic as can be seen in Figure 6.16. For a proper TKA alignment the three points of interest, (Trochanter, Knee and Ankle), have to follow a straight line when viewed fromthe side , Figure 6.16,b.

Cost Analysis

The principal motivation behind this work was the challenge of creating a prosthetic device that could serve the whole world. Expensive prosthetics is the major cause of the accessibility issue that affects 38 million people worldwide. The price of a new prosthetic leg can cost anywhere from $5,000 to $50,000. But even the most expensive prosthetic limbs are built to withstand only three to five years of wear and tear, meaning they will need to be replaced over the course of a lifetime, and they're not a one-time cost [hos]. Normally the total cost of service for a socket will be billed to an insurance company or Medicare at $10,000 for an above-the-knee amputee, and $7,000 for a below-the-knee amputee, on average [Goo16]. A common passive foot in the U.S. costs $1,000 to $10,000 and is made from carbon fiber [Edw18]. Other component costs range from $50 to $500 as is the case for lock mechanisms, foot shells and custom liners.

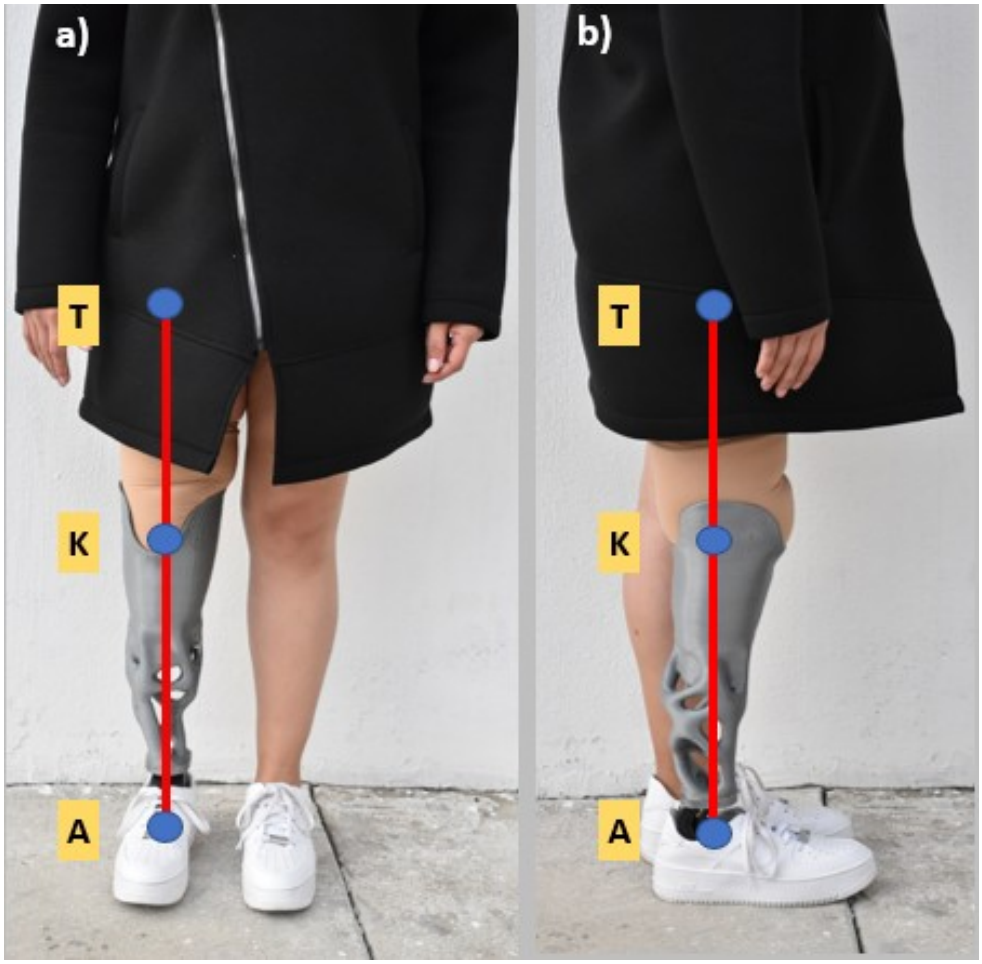

Figure 6.16: Trochanter-knee-ankle (TKA) alignment Line of Diana Novitchenko standing tall wearing a 3D printed Monocoque prosthetic. (a) Front Vide and (b) Side View.

The full cost analysis can be found in the list below. Using this list, we were able to compare the full cost of materials for making a traditional prosthetic versus our fully 3D printer Monocoque prosthetic. It is worth to notice that this comparison was done only using as reference the materials. What we found is that we can reduce up to 95% the cost of making a custom transtibial prosthetic leg.

1. **Traditional Transtibial Prosthetic Leg:**

    - Custom Made Socket: $7,000.00
    - Custom Liner: $500.00

- Titanium Pylon: $150.00
- Ottobock Triton Foot: $2,000.00
- Foot Shell: $150.00
- 4-hole Safety Lock w pin: $200.00
- Stainless Steel 4 Hole Plate: $50.00
- Titanium 4 Hole Male Pyramid: $60.00
- Titanium 4 Hole Female Pyramid: $60.00
- Titanium Tube Clamp (2x): $70.00 each
- **Total Traditional Cost: $10,310.00**

2. **LIMBER 3D Printed Monocoque:**

- Nylon Filament 1Kg (Monocoque): $140.00
- Flexible Resin 1L(Liner): $65.00
- 4-hole Safety Lock w pin: $200.00
- Foot Shell: $150.00
- **Total LIMBER Monocoque Cost: $550.00**

Weight Comparison

In addition to alignment and cost the team compared the weight between the traditional prosthetic and the LIMBER monocoque. For the traditional prosthetic we weighted a fully Assembly leg with its three main components (Socket, pylon and foot) plus all the extra components (Plates and pyramid connectors). The final weight of Diana's traditional prosthetic was 4 pounds.

Figure 6.17: Final version of full-scale LIMBER 3D Printed Prosthesis Monocoque Version.

On the other hand, the weight of the LIMBER Monocoque was 1.8 lbs. This is a 55% weightreduction which can be accounted for extra comfort and ease to walk. A lighter prosthetic means

less energy is required per every step, especially true on those patients with a short remaining limb. A reduced limb length will require more force to produce the moment force needed to lift the leg and generate a step.

Time of Design & Manufacture

The final metric used in the study to quantify the success of the LIMBER monocoque was to derive the time it takes to design and manufacture and compared to a traditional prosthetic. For a traditional prosthetic various steps need to be taken before we can even start creating the final prosthetic. First the CPO needs to manually measure the patients remaining and healthy limbs. These measurements will help the CPO size the components required for the final assembly. Then the CPO needs to make a mold of the residual limb which then is used to generate the load bearing regions and ears of the socket. This mold serves as a base for the lamination of carbon fiber reinforced polymer (CFRP) or other composite materials. Once the resin cures the socket is de-molded, trimmed and surface finished. Next step is to attach the plates and locking mechanisms to the socket and finally assembly all components. This process traditionally takes on average 14 days from start to finish, but it can take up to 20 days. For the Limber Monocoque there are three main steps required to get to a final wearable custom prosthetic monocoque. First is data acquisition with either a laser scanner or camera, this data is processed to generate the 3D model of the residual limb. Then the design of socket and sizing of pylon and foot, and finally 3D printing the monocoque. All together it will take around 16 hours to go from scan to final printed monocoque. Comparing traditional and LIMBER time for design and manufacture we concluded that our method saves 13 days to create a final custom prosthetic. This is an impressive 95%-time reduction. A breakdown of time can be found on the list below.

1. **Traditional Design and Manufacture Time:**
    - Measurements: 1 Day.

- Mold Creation: 3 Days.
- Socket Creation: 6 Days.
- Assembly and Alignment: 4 Days.
- **Total Traditional Time: 14 Days.**

2. **LIMBER Monocoque Design and Manufacture Time:**

- Data Acquisition: 1 Hour.
- Design Time: 3 Hours.
- Printing time: 12 Hours.
- **Total LIMBER Monocoque Time: 16 Hours**

6.5 Conclusion

The 3D printed proof of concept monocoque proved that a prosthetic device manufactured entirely by 3D printing is possible and a feasible option for deployment in developing areas. The workflow, Figure 6.1, developed in this work offers great potential into helping rural communities where high tech, medical imaging devices such as CT scans are not available, or cost prohibited. Thus, allowing the creation of customized prosthetics to those in need of such devices and with limited resources. The work of this paper presented the design and manufacturing of a 3D printed transtibial prosthesis including socket, pylon, foot, and a monocoque design (Figure 6.17). The design of the prosthetic integrated photogrammetry techniques with biomimicry to showcase the ease of manufacturing complex geometries with 3D printing. This report outlined advancements made by a group of students interested in advancing the restoration of human abilities through lower limb prosthetics.

The team was able to quantify the benefits of our workflow using different set of metrics. We found that using our workflow together with 3D printing we can create custom monocoques that satisfy ISO standards, are comfortable and safe to the wearer, it is properly aligned out of the printer, and when compared to traditional prosthetics it saves 95% on cost, it is 55% lighter, and it can be design and manufacture 95% faster.

6.6 Future Work

Regarding future work for the socket design, the team would have fine-tuned the design for a more comfortable fit for the user. Due to the qualitative and subjective nature of the fitting, the resizing of the socket must be iterated for each individual. In addition to improving the fit of the socket, the team would have liked to improve the pylon to socket attachment as well. The ring connection could be improved to add a bevel on the bottom side, allowing the user to not only adjust the rotation about one axis, but all three. The bevel would also improve the print quality and reduce the print time by using less support material. In addition, the cylinder which houses the check valve can be reduced in length, allowing the user to wear pants with ease. General efficiency improvements to the socket design involving fine details would be desired for future work, improving the print time and alongside it, the print quality. With efficiency, the required post-processing for the surface roughness can be reduced or ideally, eliminated.

The project group would have liked to pursue alternative materials, more elegant integration techniques between the components, and more use of topological optimization if time and other resources were unlimited. Recommended future work would be in these areas. This investigation also focused more on the feasibility of a printed design and did not evaluate the cost effectiveness compared to traditionally manufactured prosthetics. If the design issues are resolved and the product is ready for potential release, a full-scale economic analysis should be conducted to determine if this article is actually a low consumer cost prosthetic alternative.

Chapter 6, in part, is in part a reprint of the material as it appears, title "Towards a 3D Printing of a Monocoque Transtibial Prosthesis using a Bio-inspired Design Workflow". as it appears in Rapid Prototyping Journal 2021. De Vivo, Luca; Pelz, Joshua; Barrack, Herb; Kuester, Falko. The dissertation author was the primary investigator and author of this material.

Chapter 7

Project LIMBER: Structural Test of a Custom 3D Printed Unibody Below the Knee Prosthetic Leg Following ISO.

7.1 Abstract

Recent advances in additive manufacturing have led to early adoption by different industry sectors. Some work has been done in efforts to certify components and structures manufactured using additive manufacturing methods. Areas like aerospace and automotive are already using additive manufacturing to optimize designs and budgets. In the medical field, especially in the prosthetic and orthotic field, there is still a lack of understanding of how additive manufacturing can revolutionize this hundreds of year-old art of restoring the human body and its mobility. This work summarizes previous studies and lays the foundations for the necessary procedures and testing needed to certify and validate the use of 3D printing to manufacture prosthetic and orthotic devices via Fused Filament Fabrication.

7.2 Lit Review: Prosthetics and 3D Printing

This section of the paper presents a foundation for the reader on the state of knowledge in a few key topics relevant to this study. Topics such as Additive Manufacturing (AM), Prosthetics, ISO testing methods and standards for certifying prosthetic components and

systems. Section 7.2.1 introduces 3D printing of prosthetic legs and the certification pathway. Section 7.2.2 introduces additive manufacturing methods and more specifically Fused Filament Fabrication (FFF), and finally Section 7.2.3 and 7.3.4 introduces the standards and testing methods described by ISO for the structural testing of prosthetic legs and components.

7.2.1 Intro to 3D Printed Prosthetic Legs and Certification

Earlier works on data-driven design and digital manufacturing have demonstrated the potential to disrupt the way we think about engineering design processes. However, constant modernization in these fields keeps pushing the boundaries on what is possible, and these territories remain relatively uncharted. In the medical sector digital transformation has been seen over the past decade with the introduction of new digital workflows in the dental and orthopedic implant fields. The introduction of digital workflows and additive manufacturing in the prosthetic sector has remained fairly uninvestigated. Some early attempts focused on the replacement of components from traditional prosthetic assemblies. Some of these works have demonstrated the feasibility of using AM to produce certifiable custom prosthetic sockets. Some of the most advanced work in this topic has studied the use of multi-material 3D printing to optimize and generate region compliant sockets that demonstrated improved comfort and functionality. Yet there is still a lot of room for innovation in this field. Our previous work on the design of a monocoque transtibial prosthetic leg, shown in Figure 1, lays the groundwork for this study. The aim of this work is to validate the use of AM, more specifically Fused Filament Fabrication (FFF), to produce a safe and certifiable unibody below the knee prosthetic leg.

Figure 7.1: Introduction to LIMBER's 3D Printed Unibody below the knee prosthetic leg.

7.2.2 Intro to Additive Manufacturing and Fused Filament Fabrication.

Additive manufacturing (AM) is a process where machines automatically fabricate arbitrary shaped parts, pixel by pixel, layer by layer, from almost any material as opposed to subtractive manufacturing techniques. AM has many strategic advantages over traditional manufacturing processes: the production of complex internal and external part geometries that cannot be made in any other way, rapid iteration through design permutations, and the ability to build customized functional parts in small lot sizes to meet end-user specifications. The technology first emerged in 1987 with stereo lithography (SL), and since then has evolved from a limited number of expensive prototypes to widely available, small-scale commodity production tools.

Additive Manufacturing is expected to transform every aspect of our lives, and some people are calling it "the second industrial revolution". There are many different additive

manufacturing processes all with their specific benefits, drawbacks, and application areas. Currently the available AM processes are divided into 7 groups. Material Extrusion, Material Jetting, Binder Jetting, Sheet Lamination, Vat Photo-polymerization, Powder Bed Fusion, and Direct Energy Deposition (Figure: 1.1.)

The materials required for the final product will determine what AM process is used. Polymers (Thermoplastic filament or powder and Photocurable resins) , and metals (filaments and powders) are the most common types of materials used in AM and can be used to produce molds, prototypes and functioning components. Typical polymers used for 3D printing are; ABS, PLA, PC, PETG, Nylon, PEI and PEEK as can be seen in (Figure: 1.2). On the other side we find among the metals that are available for AM; Aluminum, Copper, Bronze, Cobalt, Nickel, Steel, Stainless Steel, and Titanium plus their respective alloys (Figure: 1.3). There are however possibilities for other materials to be used in AM, such as medical and biomedical graded materials, glass, ceramics, advanced fibers, living cells and even food. These materials come in different shapes and sizes, among them we found powders, liquids and filaments.

Additive manufacturing has distinct advantages and disadvantages, and it is up to the designer or engineer to decide if additive manufacturing is the best fit for the project. Some of the main advantages of AM are: variety is free, reduced lead time, manufacturing skills, few constraints, and less waste. On the other hand, sometimes the major disadvantages related to AM are: slow build rates, higher production costs, required post processing, and poor mechanical properties in certain directions.

7.2.3 Intro to 3D Printing Testing, Previous Works, Certifications and Standards.

Our LIMBER monocoque work demonstrated that in the case of custom prosthetic

devices AM also proved to increase build rates by a factor of four, lower production costs in half, and require little to none post processing and alignment. The main question that remains is to prove the mechanical properties of LIMBER 3D printed devices via FFF. This is not only a challenge for LIMBER but for the whole industry. There have been many attempts and there is currently a lot of effort put into the certification of AM in many sectors of our economy. From certifying aircraft tertiary and secondary structures, and jet fuel injection systems, to certifying spinal disk and hip implants. The list goes on and on and the attempts to certify new and old designs manufactured via AM will continue to be a major focus for the scientific and engineering community for the next few decades. An organization that has been recording and laying down the foundations of the standardization efforts for AM is the American Standard for Testing and Materials or best known as ASTM. A summary of the previous work to certify 3D printing processes and materials can be found in table 7.1. There is a lot of data and studies available on AM processes and common materials following ASTM previous works for other manufacturing methods such as injection molding and casting, where the material is expected to be homogenous, or composite lay up methods, where the material behaves more orthotopically. Many of these old standards and testing procedures were demonstrated to be viable when testing 3D printed components. All examples in Table 7.1 have been validated to serve the AM community. It is important to point out that most of the test found in Table7.1 are for the characterization of the material itself and use coupons as test samples, for more complex structures and systems it is recommended to follow specific device category testing and certifications which will be explained in detail in the next section.

Table 7.1: Material Testing Standards for Additive Manufacturing of Polymer Materials.

Type of Load:	Test or Standard	Description
Tensile	ISO 527-2:2012	Plastics Determination of tensile properties
Tensile	ASTM D638 -10	Standard test method for tensile properties of plastics
Torsion	ISO 458-1:1985	Determination of stiffness in torsion of flexible materials part 1: general method
Flexure	OSP 178:2010	Plastics - Determination of flexural properties
Flexure	ASTM D6272 -10	Standards test method for flexural properties of unreinforced and reinforced plastics.
Compression	ASTM D695 - 10	Standard test method for compressive properties of rigid plastics
Compression	ISO 604	Plastics determination of compressive properties
Shear	ISO 15310:1999	Fibre reinforced plastic composites determination of in plane shear modulus by plate twist method.
Creep	ISO 899 - 1 :2003	Plastics determination of creep behavior - tensile creep
Creep	ASTM D2990 - 09	Standard test method for tensile, compressive and flexural creep and creep rupture.
Fatigue	ISO 15850:2014	Determination of tension-tension fatigue crack propagation -- Linear elastic fracture mechanics approach.
Fracture Toughness	ISO 13586:2000	Determination of fracture toughness (GIC and KIC) Linear elastic fracture mechanics approach (LEFM)
Impact	ISO 179-1 and 2:2010	Determination of Charpy impact properties: part 1 and 2

7.2.4 Intro to 3D Printing Testing, Previous Works, Certifications and Standards.

As stated in the previous paragraph for the certification and testing of specific structures, devices or systems there is also previous work that can help guide the certification process of AM devices and systems. There have also been calls by main associations such as the Association of American Orthopedics and Prosthetist that incentivizes the use of AM in the prosthetic field. Also as stated previously in this text there are many Certified Prosthetist and Orthotist (CPO) who currently use AM to produce end products such as 3D printed custom prosthetic sockets and test sockets. The International Standard Organization or ISO also provides the guidelines to test

and certify prosthetic devices. In this standard can be found the support of the organization to test and certify unibody devices. As stated in the ISO 10328:2016 – Structural testing of lower limb prostheses, “For example, such a leg could be a one-piece flexible plastic structure that includes the foot. If the test sample satisfies the requirements of the relevant clauses of this International Standard, then compliance with these clauses can be claimed.”. Is this standard that we decided to follow in our attempts to certify our LIMBER 3D printed monocoque prosthetic leg. The next section explains in more detail the methods and equipment used to test our 3D printed prosthetic devices.

Table 7.2: International Standard Organization test for the certification of prosthetic devices

Type of Test:	Test or Standard	Description
Prosthetic Leg	ISO 10328:2016	Structural testing of lower-limb prostheses — Requirements and test methods
Prosthetic Ankle-Foot	ISO 22675:2016	Testing of ankle-foot devices and foot units — Requirements and test methods

7.3 Methods

This section of the paper explains in more detail the printing methods, and the printing equipment, the multi-parameter optimization of the printing process, the materials, the testing equipment, attachments and tests to be performed. We hope this helps future attempts by other scientists, engineers, and innovators to certify and build confidence in their own devices and this way help millions of people in need of prosthetic and orthotic devices.

7.3.1 Additive Manufacturing Methods

7.3.1.1 Equipment:

In order to 3D print prosthetic components that are safe for the end user we had to turn to engineering materials that could withstand the loads and the wear and tear of the daily

prosthetic use. 3D Printing higher performance polymers that are stronger, more durable and functional requires specific environmental conditions. In order to prevent large amounts of warping, a lower thermal gradient between print part and environment is desired, for this we had to build a 3D printer inside a chamber. This 3D printer had to be designed and engineered so every part used inside the chamber had to have a serviceable temperature of up to 120 C. Over the past year we focused a lot of effort into building the LIMBER Fused Filament Fabrication (FFF) 3D Printer. The printer is a delta design with a printing volume of 400x400x650 mm in order to print long prosthetic legs. The rail system is based on screw linear rails with feedback loop control to prevent slippage. The extruder head was built using a volcano hot end extruder that allow us to print with large nozzles and at temperatures of up to 285 C. The bed can heat up to 150 C, and the chamber temperature is achieved using a heating source and a fan pointing downwards from the sealing of the printing chamber, all monitored and adjusted by a PID controller. All the printer actuators, temperature and motion sensors are controlled using a DUET processor board with a high processing speed which is critical when printing with a delta machine. The board can be access via Bluetooth and Wi-Fi and can be updated with other sensors such as visual and thermal cameras, humidity sensors, etc. This allows us to always control and monitor the printing process and prevent unexpected failures or waste of materials. Having built this printer allow us now to control more parameters with the aim of improving layer adhesion, preventing thermal stress concentrations and warping, and making the printing process a lot faster and enjoyable specially when working with engineering grade materials.

7.3.1.2 Multi-Parameter optimization and Material Selection:

Now that we are able to control more parameters and improve the performance of printing engineering grade materials it is time to select what those parameters will be for any given material. For this study we selected a Nylon alloy infused with finely chopped carbon fiber (CF). This is a material that needs to be printed at 175C to provide enough flowability in the extruder head and during layup. The bed was kept at 110C and the chamber temperature at a constant 70C during printing. Post printing the chamber was cooled down gradually to room

temperature by turning off the heating element of the ceiling and the bed. The layer height was set to 0.6 mm with a nozzle of 1mm in diameter. It was crucially important to dehydrate and prepare the nylon material before printing to eliminate any moist inside the filament and bubbling while printing. The fan speed was kept at a minimal just to ensure heat flow through the chamber with low enough that it was not over cooling the part as this may cause poor layer adhesion and warping. The parts were printed using 100% filament and only with support material at the bottom of the blade and at the gap at the ankle region. The Nylon CF used in this study was provided by Matterhackers, CA. It has a fiber content of 20 % by weight.

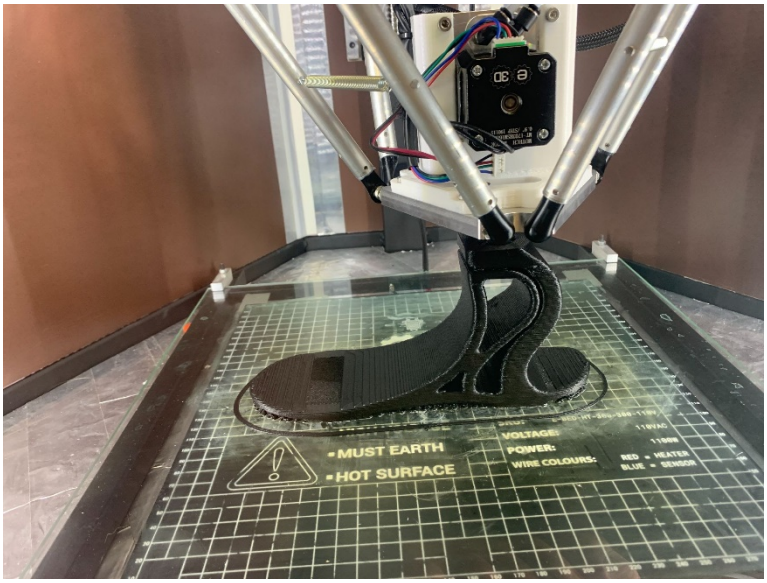

Figure 7.2: LIMBER 3D Printer printing a LIMBER ankle-foot test sample using NylonX (CF Reinforced) from Matterhackers.

7.3.2 Testing Methods: ISO 10328:200

7.3.2.1 Testing Equipment:

The last step of this study is to test and challenge the structural and mechanical response of the 3D printed prosthetic components. We printed a series of ankle-foot devices designed to be attached to the testing rig using a series of bolts at the support end as shown in Figure#. The Instron 3367 device is a displacement-controlled load frame. This means that the crosshead is raised or lowered by turning screws. This machine has a Load Cell which serves as the

measurement transducer for the load applied. The maximum load this cell is designed for 30,000 N. For the test of the ankle-foot devices we machined two slopes as described by the ISO 10328 standard. One slope of 20 deg was designed to test the toe strike and flexion and another slope of 15 deg to test the heel strike.

Figure 7.3: LIMBER ankle-foot mounted on the Instron testing machine ready for toe side static and cyclic testing.

7.3.2.2 Test to Perform – ISO10328:2016

As stated in the ISO 10328:2016 10.2.1.3 For a transtibial (below-knee) prosthesis, a complete structure consists of the ankle unit or ankle attachment and the socket attachment with all parts between. It may also contain parts above the socket attachment, including the socket (see 10.2.1.4), and below the ankle unit or ankle attachment, including the foot unit. 10.2.1.4 The mechanical connection between a socket and the distal shin-socket or knee-socket attachment is a critical region of a prosthetic structure. 10.2.2 For any type of prosthesis, a partial structure is less than a complete structure and may be a single component, such as a knee unit or an ankle-foot device. The end connections shall have mechanical characteristics similar to those of the intended adjacent components. 10.2.3 For any other structure such a leg could be a one-piece flexible plastic structure that includes the foot. If the test sample satisfies the requirements of the

relevant clauses of this International Standard, then compliance with these clauses can be claimed.

The aim of this study is to comply and satisfy the performance requirements described in the ISO 10328:2016. This standard describes the structural testing of lower-limb prostheses and the test methods required to certify a prosthetic leg under the International Standards. ISO 10328:2016 lays down the seven different tests needed to bring a new prosthetic design and manufacturing process to patients safely. This paper will present test results for test numbers 5, 6, and 7 which focus on the certification of the ankle foot device and foot units. This set of tests were selected as our first step in the certification of our designs because it allows us to validate the material selection efficiently while testing the most flexible and prone to failure component of the unibody prosthetic leg. Tests 5 and 6 describe the static proof and ultimate strength tests while test 7 describes the cyclic test. All three tests have two parts, one is the heel side loading and the other is toe side loading. This allows the validation of the two critical loading conditions of walking and running loads which are lift off and landing. Once the material selection and printing processes are optimized future work will focus on the testing of LIMBER unibody prosthetic leg following Test 1, 2, 3, and 4. Tests 1,2 and 3 will test the flexural response of the leg system and test 4 will test the torsional response of the unibody leg.

A **Total of 22 Pieces per material per setting** are needed to fully certify a new 3D printed prosthetic leg following ISO 10328:200. Because the aim of this study is to present results for the latest 3 tests (5,6, and 7) we only needed to 3D print 12 test specimens of the ankle foot test. In addition, a series of testing attachments had to be machined in order to comply with section 17.2.3.1 of ISO 10328. One piece was the upper attachment that connects the Instron rig to the test specimen and the other was the wedges intended to simulate gait loading of the ankle foot. The heel side wedge was prescribed with an angle of 15 degrees from the horizontal plane and the forefoot wedge with an angle of 20 degrees. The longitudinal axis of the foot shall also be turned by 7 degrees to give a toe out position of the ankle-foot device or foot unit.

- **Principal Structural Test: Test Loading Condition I and II**
  - Test 1: Static proof test See 16.2.1.1
  - Test 2: Static ultimate strength test 16.2.2.1
  - Test 3: Cyclic test 16.3.2
- **Separate test in torsion:**
  - Test 4: Static test See
- **Separate test on ankle foot devices and foot units: angle α and angle β,**
  - Test 5: Static Proof test See 17.2.3.1
  - Test 6: Static Ultimate strength test 17.2.4.1
  - Test 7: Cyclic test 17.2.5.1

7.3.2.3 Static Proof, Ultimate strength and Cyclic test of ankle foot devices and foot units:

For the static proof test and the ultimate strength test of the ankle-foot device we designed our foot unit to comply and satisfy the requirements of section 17.2.3, 17.2.4, and 17.2.5. These sections specify the testing procedures, alignment methods and loading conditions needed to comply with this ISO standard. The flowchart for each of these sections can be found in the appendix of this work as well the tables used to follow the loading conditions both for the static and cyclic tests. Some of the most relevant guidance to follow when performing this part of ISO10328 for the testing of our ankle-foot device was the different recommendations and requirements for attachments, as well as loading procedures and boundary conditions. For the attachments two main parts were addressed in this work. The first is the attachment from the ankle-foot device to the Instron Loading arm. This had to replicate the geometry used to connect the ankle-foot with the pylon region. The solution for this was to design an attachment with 4 bolt holes that was blended to the 3D printed ankle-foot model and 3D printed as a single piece. This addition to the model was made to be fitted and secured by the bolts to a steel machined part meant to attach to the Strong Arm with a pin lock.

The second part was to design and manufacture two wedges as our loading platforms. The angle of these wedges was specified by the standard as 20 degrees from the horizontal plane for the toe side test and 15 degrees for the heel side test. The wedges were manufactured using a saw machine and calibrated by a lab technician. The surface of the wedges was made smooth enough to simulate a roller boundary condition allowing the samples to slide as load is increased. Lastly using the Instron testing software we were able to calibrate the Instron machine and set up the 3 different test loading levels for a P5 device. For the proof test a load of 1300N was prescribed, and for the ultimate strength test a load of 6000N was prescribed. And for the cyclic test we also followed table 11 and set up the minimum and maximum test force as 50N and 1330N respectively at a loading rate of 250N/s, and post cyclic loading a final static force of 2240N. The standard recommends a total of 2 million cycles to comply with this test.

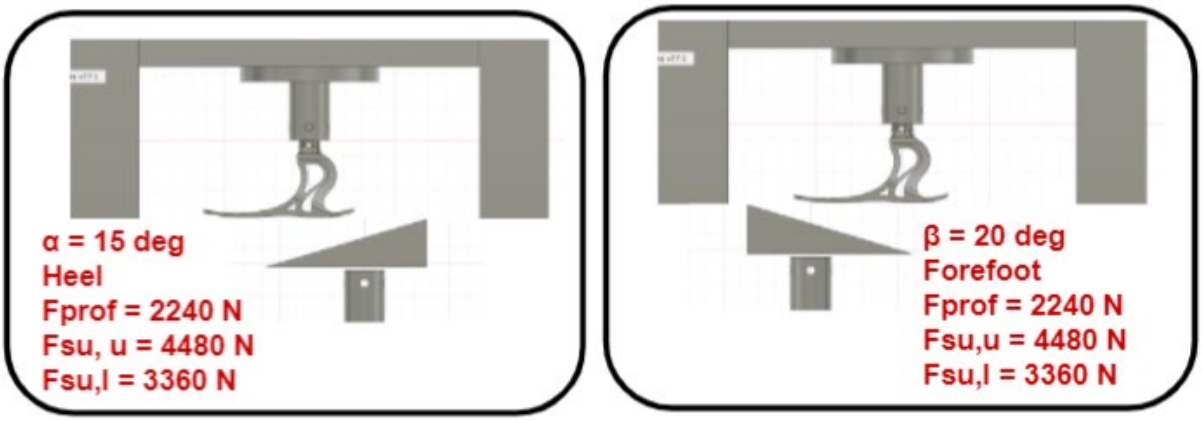

Figure 7.4: Test Loading Level P5 for the Static Proof and Ultimate Test of LIMBER 3D printed ankle-foot

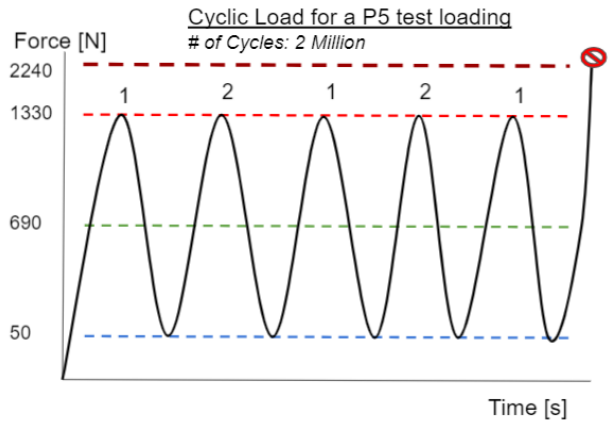

Figure 7.5: Test Loading Level P5 for the Cyclic Test of LIMBER 3D printed ankle-foot.

7.4 Expected Results

7.4.1 Test 5 and 6 of ISO 10328:200: Static Loading

Sections 17.2.3.1 and 17.2.4.1 of the ISO standard lays down the instructions for attaching and aligning the ankle-foot unit to the Testing machine. As explained in the previous section two loading conditions were tested. First a heel side that simulates landing and the following phases of walking, and heel side which simulates final phases of gate and lift of. Two polypropylene machined wedges were used as boundary conditions. The results were obtained after running the Instron machine at 250N/s with a proof target of 2240N and an Ultimate load target of 4480N. As can be seen in Figure 7.6 the deformation of the ankle-foot unit during toe loading behaves elastic all the way past the upper target of 4480N and it only suffers brittle failure after reaching 5800N. Post examination of the failure revealed a shear failure at the upper posterior region of the ankle where the Achilles tendon would normally be. Figure 7.6 and 7.7 shows a series of static and cyclic loads for the toe and heel loading configurations. It can be seen in these figures the ability of our 3D printed CFN ankle/food device to surpass Ultimate Strength P5 levels while sustaining elastic behavior under continuous cyclic loading.

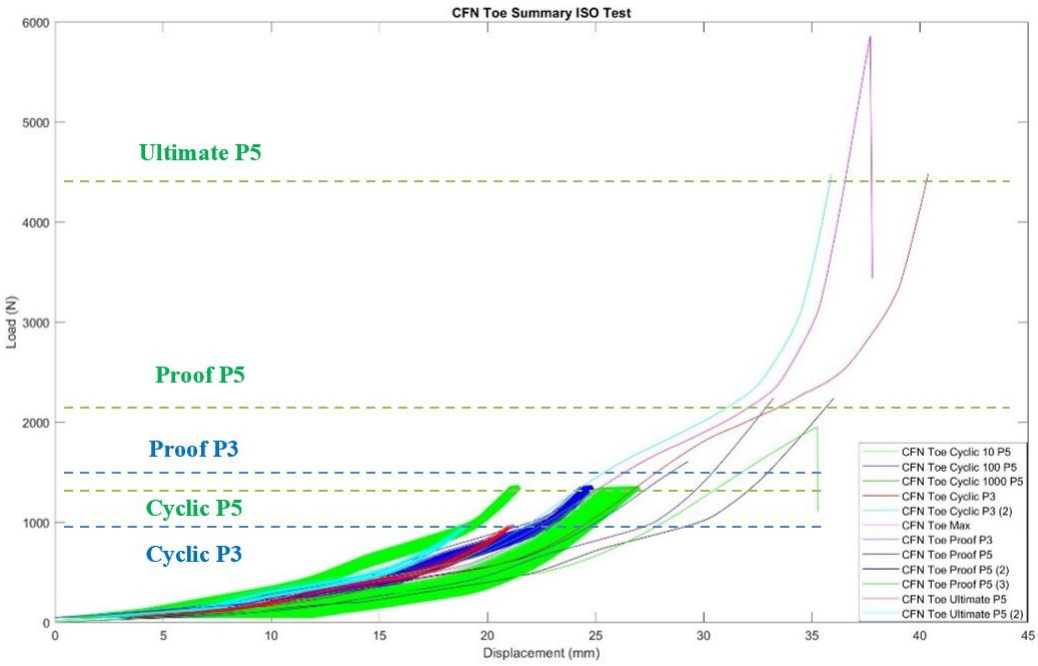

Figure 7.6: Load vs extension curve from Toe CFN static test

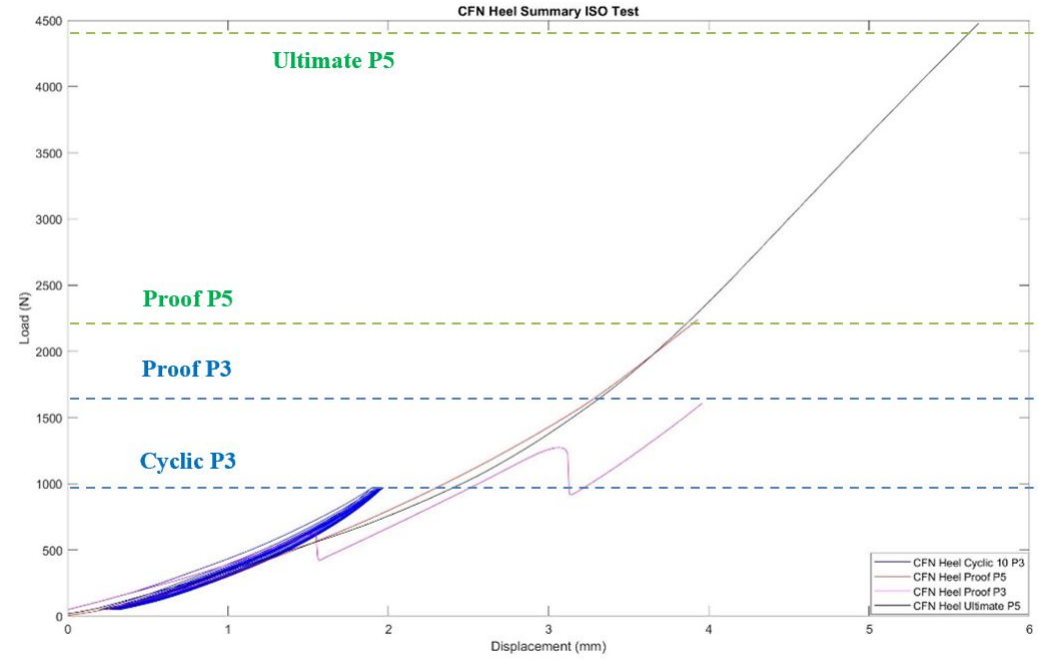

Figure 7.7: Load vs extension curve from Heel CFN static test

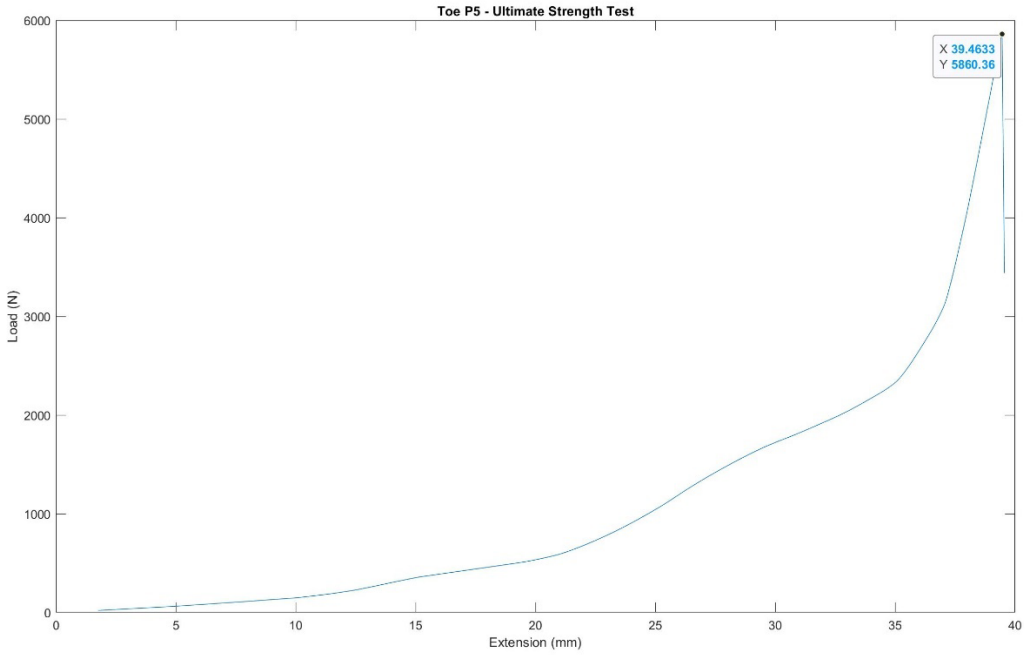

Figure 7.8: Toe CFN Ultimate Strength Failure test of ankle-foot device.

7.4.1 Test 7 of ISO 10328:200: Cyclic Loading

Section 17.2.5.1 of the ISO standard explains in detail how to perform the cyclic test of a prosthetic ankle-foot device. The test prescribes the set of loads and boundary conditions as well as cyclic loading profiles, frequencies and load rates. We were able to follow this test and this way prove the fatigue response of our 3D printed ankle foot device. Figure 7.9 shows the loading progression in the downward direction. It can be seen the flexural response of the blade. Figures 7.10, 7.11, and 7.12 show the hysteresis curve of the cyclic test where it can be seen a settling period of around 20 cycles followed by a stable elastic loading/unloading cycling. The loads used in this test were Lmin = 50N, Lmean = 690N, and Lmax = 1330N for both toe and heel loading. The prescribed cycle number by the ISO is 2 million cycles. This study was able to achieve satisfactory cyclic conditions and results, but work remains to be done to achieve the 2 million prescribed by the standard. Figures 7.10 and 7.11 show the cyclic test performed for both toe and heel loading conditions. Figure 7.10 shows a total of 100 cycles completed successfully

with a loading rate of 2 mm/sec where Figure 7.11 show a total of 10,000 cycles completed successfully with a faster loading rate of 7 mm/sec. Figure 7.12 show a single cycle of loading and unloading where it can be seen little to no plastic deformation.

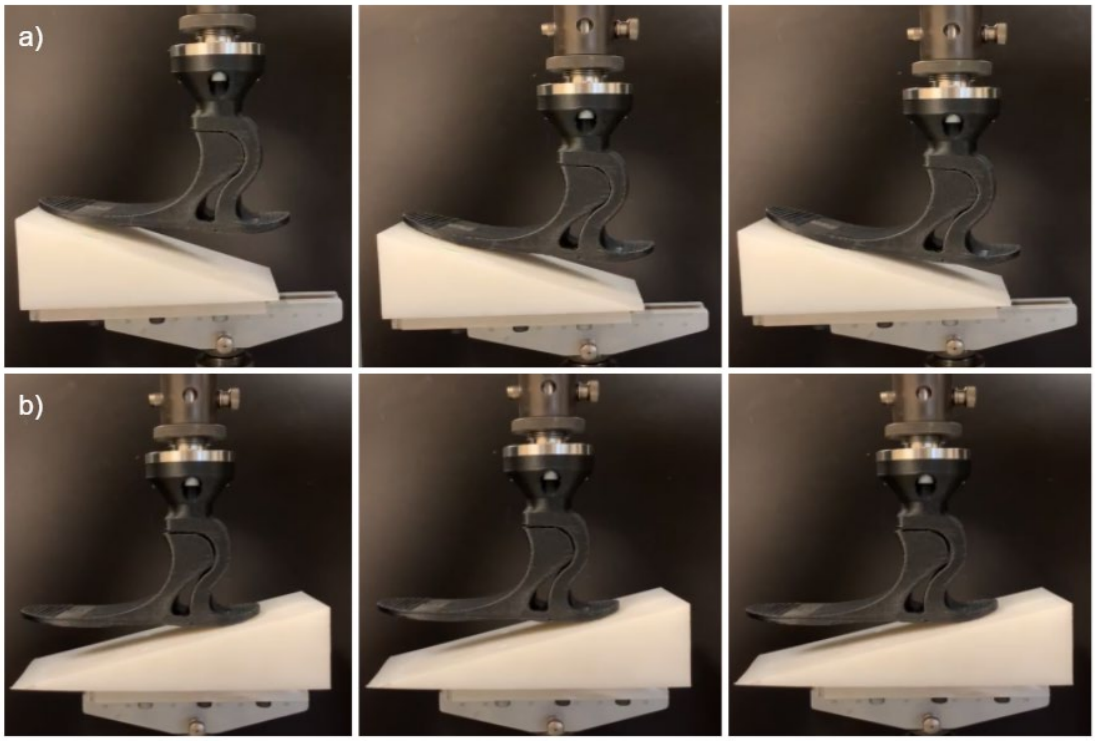

Figure 7.9: Test Loading Level P5 Cyclic Test Loading Progression: a) Toe side and b) Heel side. Lmin = 50N (left), Lmean = 690N (center), and Lmax = 1330N (right)

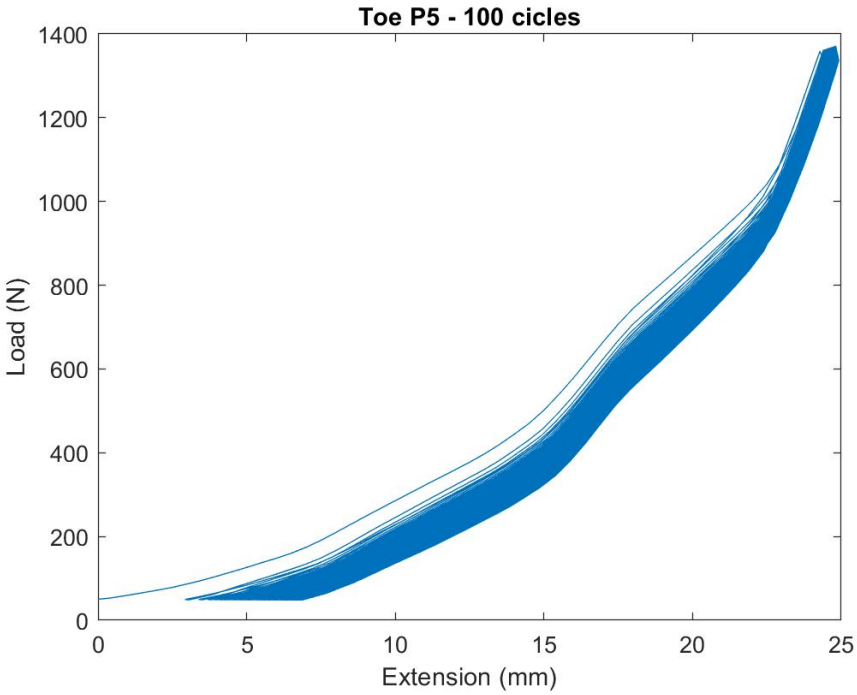

Figure 7.10: Load vs extension from Toe CFN cyclic test

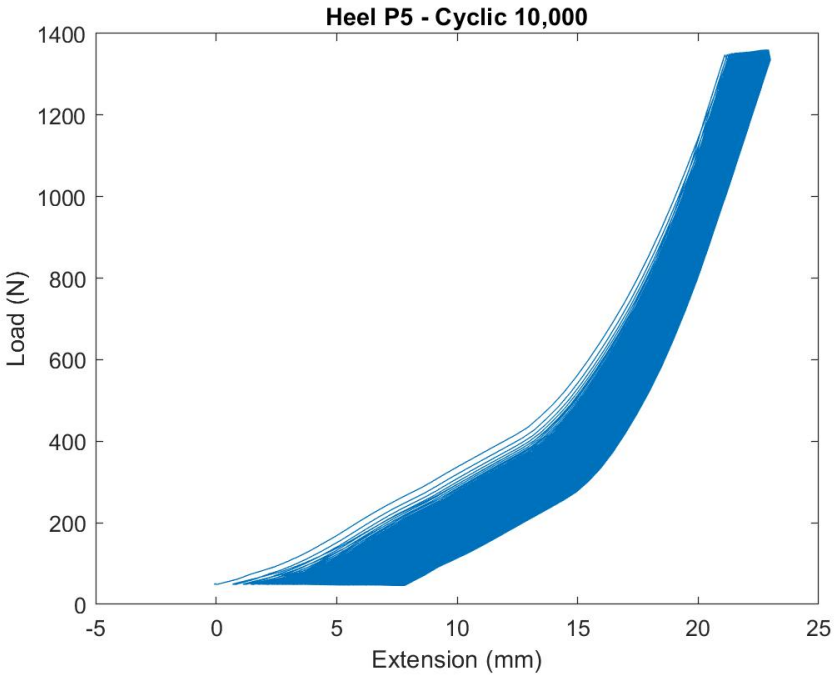

Figure 7.11: Load vs extension from Heel CFN cyclic test

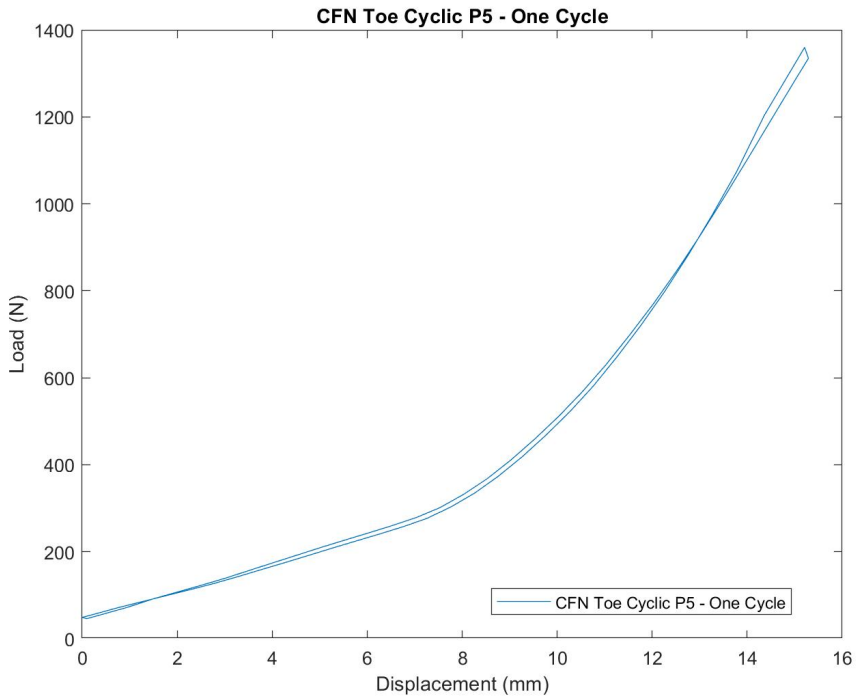

Figure 7.12: Hysteresis Loop: Load vs extension from Toe CFN cyclic test

7.4 Discussion and Conclusions

This paper presents the methods and results of the mechanical testing and certification of a 3D printed ankle-foot prosthetic device. The test samples were manufactured using a heated chamber Fused Filament Fabrication 3D printer and NylonX (CF reinforced) polymer filament. The testing machine was an Instron 3367 and together with the Instron software provided the means to apply loads specified in the ISO10328 standard and retrieve the data needed to analyze the performance of the LIMBER 3D printed ankle-foot. Post analysis of the data we were able to validate our design and manufacturing process and comply with the ISO requirements. The maximum load achieved during static loading on the heel side was 4,500N, and 5,800N for the toe side. A maximum of 10,000 circles were successfully demonstrated under P5 loading conditions. These tests allowed us to build confidence in our 3D printing methods and digital designs and served as an opportunity to select materials and printing parameters for our future

work of certifying a 3D printed unibody below the knee prosthetic leg following this same ISO10328 standard. Future work will experiment with different materials such as Polycarbonates (PC) and Polyamides (PA) or better known as Nylons. We believe finding the right material properties in terms of stiffness and maximum elongation are key for making a comfortable and functional prosthetic leg. We will also explore how to achieve the 2 million cycles prescribed by the ISO standard as well as testing full unibody legs (foot/ankle/pylon/socket) under similar loading conditions. In future mechanical test we will go beyond proving safety and maximum structural capacity, we will also incorporate other indicators such as maximum deflection limits at different load values in order to optimize the functionality and gait of the prosthetic device.

Chapter 7, in part, is in part a reprint of the material as it appears, title "Towards a 3D Printing of a Monocoque Transtibial Prosthesis using a Bio-inspired Design Workflow". as it appears in Rapid Prototyping Journal 2021. De Vivo, Luca; Pelz, Joshua; Barrack, Herb; Kuester, Falko. The dissertation author was the primary investigator and author of this material.

Chapter 8

Concluding Remarks

8.1 Principle Contributions

It was truly and honor and a pleasure to be guided and mentored by true giants. During my PhD studies nature continuously proved to me to be the wisest when it comes to ingenuity, simplicity and functionality. Nature didn't spent billions of year iterating over the design space, something we like to call evolution, in vain. Over the past 3.8 billion of years in our planet something amazing has been taking place. The constant evolution of design to ensure survival is a marvelous thing. It is in this continuous iteration of nature that I found, and find, my inspiration and guidance. I believe nature is something to be preserved and the millions and millions of species that make our flora and fauna should be treated as wise mentors and the most amazing library of knowledge there is on this planet and perhaps the whole universe. During my work I was able to learn from multiple species and gain insights on how to tackle a specific problem from a systems engineering standpoint following natures proven principles and solutions. The first example of this can be found in Chapter 2, 3 and 4 where we designed and developed a highly efficient Prandtl Box-Wing UAV which took inspiration in the way birds curve their wing tips to create efficient winglets in order to minimize drag. Followed Chapter 5, where we gained deep understanding from the Cholla cactus on how to design and create lightweight yet strong and resilient structures. Finally in Chapter 6 and 7 inspired by the Cholla cactus we were able to create a novel workflow for making custom 3D printed unibody prosthetic leg that has the potential to disrupt this market globally and help millions of people in need of a prosthetic leg. Lastly, I would like to remark the exploration in the digital design, 3D scanning and additive manufacturing spaces during my years of study. During all my chapters combining multiple of

these techniques allowed me to think outside of the box when I came to design and innovation. I believe there is still more room to explore in this area of research and I would like to continue expanding on its possibilities.

8.2 Future Work

My Future work will focus on expanding Chapter 6 and 7 as part of a post-doctorate program with professor Falko Kuester and the CHEI lab. We will focus on completing the 2 million cycles prescribed by the ISO standard using a variety of 3D printable polymers. In future mechanical test we will go beyond proving safety and maximum structural capacity, we will incorporate other indicators such as maximum deflection limits at different load values to optimize the functionality and gait of the prosthetic device. We will also explore different printing parameters and settings with our LIMBER 3D printer and will be looking into optimizing printing quality for both structural and functional purposes. We will also be looking into adapting multi-material printing to our designs as well as incorporating a series of sensors and actuators to make our unibody leg a smart leg. The LIMBER smart leg is a prosthetic leg that can monitor patient volumetric fluctuations, temperature and humidity, adapt to these daily changes. It was also designed to monitor the structural health of the prosthetic leg over its serviceable lifespan using a series of non-destructive evaluation techniques such as strain gauges and optic fiber Bragg grating.

Bibliography

[ASG07] Mostafa M. Abdalla, Shahriar Setoodeh, and Zafer GÃijrdal. Design of variable stiffness composite panels for maximum fundamental frequency using lamination parameters. *Composite Structures*, 81(2):283âĂŞ291, 2007.

[Ben09] J.M. Benyus. *Biomimicry: Innovation Inspired by Nature*. HarperCollins e-books, 2009.

[BHB] C. Bregler, A. Hertzmann, and H. Biermann. Recovering non-rigid 3d shape from image streams. *Proceedings IEEE Conference on Computer Vision and Pattern Recognition. CVPR 2000 (Cat. No.PR00662)*.

[Bou84] Robert Boucher. History of solar flight. In *20th joint propulsion conference*, page 1429, 1984.

[BWK15] Christopher J Brampton, K Chauncey Wu, and H Alicia Kim. New optimization method for steered fiber composites using the level set method. *Structural and Multidisciplinary Optimization*, 52(3):493–505, 2015.

[Cav14] Rauno Cavallaro. *Nonlinear Aeroelastic Analysis of Joined-Wing Configurations*. PhD thesis, UC San Diego, 2014.

[CW96] N. J. Colella and G. S. Wenneker. Pathfinder. developing a solar rechargeable aircraft. *IEEE Potentials*, 15(1):18–23, Feb 1996.

[CZ13] Luyun Chen and Yufang Zhang. A study on the application of material selection optimization approach for structural-acoustic optimization. *Materials & Design (1980-2015)*, 52:207–213, 2013.

[DeL16] Denise DeLuca. The power of the biomimicry design spiral, Jun 2016.

[Dev19] Web Development. History of the prosthetic leg: Across the ages, Oct 2019.

[DII16] Stanciu Mariana Domnica, Curtu Ioan, and Tesula Ionut. Structural optimization of composite from wind turbine blades with horizontal axis using finite element analysis. *Procedia Technology*, 22:726–733, 2016.

[DKY89] S.m. Dunn, R.l. Keizer, and J. Yu. Measuring the area and volume of the human body with structured light. *IEEE Transactions on Systems, Man, and Cybernetics*, 19(6):1350âĂŞ1364, 1989.

[DL89] Marc T DiNardo and Paul A Lagace. Buckling and postbuckling of laminated composite plates with ply dropoffs. *AIAA journal*, 27(10):1392–1398, 1989.

[DSTT] F. Dellaert, S.m. Seitz, C.e. Thorpe, and S. Thrun. Structure from motion without correspondence. *Proceedings IEEE Conference on Computer Vision and Pattern Recognition. CVPR 2000 (Cat. No.PR00662)*.

[Edw18] Charlotte Edwards. Low-cost prosthetic foot facilitates natural walking, Jul 2018.

[ESSAJ13] YA El-Shekeil, SM Sapuan, MD Azaman, and M Jawaid. Optimization of blending parameters and fiber size of kenaf-bast-fiber-reinforced the thermoplastic polyurethane composites by taguchi method. *Advances in Materials Science and Engineering*, 2013, 2013.

[FSS94] H Fukunaga, H Sekine, and M Sato. Optimal design of symmetric laminated plates for fundamental frequency. *Journal of sound and vibration*, 171(2):219–229, 1994.

[Gen11] Jason Geng. Structured-light 3d surface imaging: a tutorial. *Advances in Optics and Photonics*, 3(2):128, 2011.

[GMSW10] Wojciech Glinkowski, Jakub Michonski, Robert Sitnik, and Marcin Witkowski. 3d diagnostic system for anatomical structures detection based on a parameterized method of body surface analysis. *Advances in Intelligent and Soft Computing Information Technologies in Biomedicine*, page 153âĂŞ164, 2010.

[GO93] Zafer Gurdal and Reynaldo Olmedo. In-plane response of laminates with spatially varying fiber orientations-variable stiffness concept. *AIAA journal*, 31(4):751–758, 1993.

[Goo16] Lauren Goode. Meet the company building modular prosthetics for amputees, Apr 2016.

[Gri16] J. Griffet. Amputation and prosthesis fitting in paediatric patients. *Orthopaedics and Traumatology: Surgery and Research*, 102(1), 2016.

[GZ16] Hugo Gagnon and David W Zingg. Aerodynamic optimization trade study of a box-wing aircraft configuration. *Journal of Aircraft*, 53(4):971–981, 2016.

[HH05] Jinhua Huang and RT Haftka. Optimization of fiber orientations near a hole for increased load-carrying capacity of composite laminates. *Structural and Multidisciplinary Optimization*, 30(5):335–341, 2005.

[HDT+16] V Ho-Huu, TD Do-Thi, H Dang-Trung, T Vo-Duy, and T Nguyen-Thoi. Optimization of laminated composite plates for maximizing buckling load using improved differential evolution and smoothed finite element method. *Composite Structures*, 146:132–147, 2016.

[HJTA17] Nurhanisah Mohd Hawari, Mohammad Jawaid, Paridah Md Tahir, and Raja Ahmad Azmeer. Case study: survey of patient satisfaction with prosthesis quality and design among below-knee prosthetic leg socket users. *Disability and Rehabilitation: Assistive Technology*, 12(8):868âĂŞ874, Oct 2017.

[HL91] Michael W Hyer and HH Lee. The use of curvilinear fiber format to improve buckling resistance of composite plates with central circular holes. *Composite structures*, 18(3):239–261, 1991.

[Hul12] Chuck Hull. On stereolithography. *Virtual and Physical Prototyping*, 7(3):177–177, 2012.

[IAG10] Samuel T IJsselmuiden, Mostafa M Abdalla, and Zafer Gurdal. Optimiza- tion of variable-stiffness panels for maximum buckling load using lamination parameters. *AIAA journal*, 48(1):134–143, 2010.

[INL+16] Marta Invernizzi, Gabriele Natale, Marinella Levi, Stefano Turri, and Gianmarco Griffini. Uv-assisted 3d printing of glass and carbon fiber-reinforced dual-cure polymer composites. *Materials*, 9(7):583, 2016.

[ISO06] Prosthetics âĂŤ Structural testing of lower-limb prostheses âĂŤ Requirements and test methods. Standard, International Organization for Standardization, Geneva, CH, October 2006.

[KL13] Rubem Matimoto Koide and Marco Antonio Luersen. Maximization of fundamental frequency of laminated composite cylindrical shells by ant colony algorithm. *Journal of Aerospace Technology and Management*, 5(1):75–82, 2013.

[Koe18] Jeffrey H. Koessler. Dynamic soaring kinetic energy reference frames. *AIAA Atmospheric Flight Mechanics Conference*, 2018.

[KS09] Csukru Karakaya and Omer Soykasap. Buckling optimization of laminated composite plates using genetic algorithm and generalized pattern search algorithm. *Structural and Multidisciplinary Optimization*, 39(5):477, 2009.

[KSK09] Kyung-Su and Ji-Hwan Kim. Volume fraction optimization of functionally graded composite panels for stress reduction and critical temperature. *Finite Elements in Analysis and Design*, 45(11):845–851, 2009.

[KTC88] Chen-Ming Kuo, Kiyohisa Takahashi, and Tsu-Wei Chou. Effect of fiber waviness on the nonlinear elastic behavior of flexible composites. *Journal of Composite Materials*, 22(11):1004âĂŞ1025, 1988.

[LAWS18] PaweÅĆ Liberadzki, Marcin Adamczyk, Marcin Witkowski, and Robert Sitnik. Structured-light-based system for shape measurement of the human body in motion. *Sensors*, 18(9):2827, 2018.

[LCB+74] RH Lange, JF Cahill, ES Bradley, RR Eudaily, CM Jenness, and DG Macwilkinson. Feasibility study of the transonic biplane concept for transport aircraft application. 1974.

[LeM16] Robert LeMoyne. Passive transtibial prosthesis and associated prosthetic components. In *Advances for Prosthetic Technology*, pages 59–68. Springer, 2016.

[LeM18] Robert LeMoyne. *Advances for Prosthetic Technology From Historical Perspective to Current Status to Future Application*. Springer Tokyo, 2018.

[Lip11] Hod Lipson. The shape of things to come: frontiers in additive manufacturing. *Frontiers of Engineering*, pages 33–44, 2011.

[Mar] Gerald F. Marshall. Pre-objective polygonal scanning. *Handbook of Optical and Laser Scanning*, page 359âĂŞ392.

[Mat04] C. Mattheck. *Design in nature: learning from the trees*. Springer-Verlag, 2004.

[MDP15] Scott Morton, Ruben D'Sa, and Nikolaos Papanikolopoulos. Solar powered uav: Design and experiments. In *2015 IEEE/RSJ International Conference on Intelligent Robots and Systems (IROS)*, pages 2460–2466. IEEE, 2015.

[Mir72] LR Miranda. Boxplane configuration–conceptual analysis and initial experimental verification. *Lockheed California Co., Rept. LR*, 25180, 1972.

[MK97] Gerhard Claus. Mattheck and Hans Kubler. *Wood - the internal optimization of trees*. Springer, 1997.

[ML89] A. F. Martin and A. W. Leissa. Application of the ritz method to plane elasticity problems for composite sheets with variable fibre spacing. *International Journal for Numerical Methods in Engineering*, 28(8):1813âĂŞ1825, 1989.

[MLL17] Munjed Al Muderis, William Lu, and Jiao Jiao Li. Osseointegrated pros- thetic limb for the treatment of lower limb amputations. *Der Unfallchirurg*, 120(4):306âĂŞ311, Sep 2017.

[MRGM+15] Jairo Alexander Malaver Rojas, Luis Felipe Gonzalez, Nunzio Motta, Tommaso Francesco Villa, Victor Kwesi Etse, and Eduard Puig. Design and flight testing of an integrated solar powered uav and wsn for greenhouse gas monitoring emissions in agricultural farms. In *2015 IEEE/RSJ International Conference on Intelligent Robots and Systems*, volume 1, pages 1–6. IEEE, 2015.

[MSP13] Scott Morton, Luke Scharber, and Nikolaos Papanikolopoulos. Solar powered unmanned aerial vehicle for continuous flight: Conceptual overview and optimization. In *2013 IEEE International Conference on Robotics and Automation*, pages 766–771. IEEE, 2013.

[MUN+16] Ryosuke Matsuzaki, Masahito Ueda, Masaki Namiki, Tae-Kun Jeong, Hirosuke Asahara, Keisuke Horiguchi, Taishi Nakamura, Akira Todoroki, and Yoshiyasu Hirano. Three-dimensional printing of continuous-fiber composites by in-nozzle impregnation. *Scientific reports*, 6:23058, 2016.

[Not08] Andre Noth. Design of solar powered airplanes for continous flight. 2008.

[NSE06] A. North, R. Siegwart, and W. Engel. Autonomous solar uav for sustainable flights. *Advances in Unmanned Aerial Vehicles Intelligent Systems, Control and Automation: Science and Engineering*, page 377âĂŞ405, Sep 2006.

[OMM+16] P. Oettershagen, A. Melzer, T. Mantel, K. Rudin, T. Stastny, B. Wawrzacz, T. Hinzmann, K. Alexis, and R. Siegwart. Perpetual flight with a small solar-powered uav: Flight results, performance analysis and model validation. In *2016 IEEE Aerospace Conference*, pages 1–8, 2016.

[OMM+17] Philipp Oettershagen, Amir Melzer, Thomas Mantel, Konrad Rudin, Thomas Stastny, Bartosz Wawrzacz, Timo Hinzmann, Stefan Leutenegger, Kostas Alexis, and Roland Siegwart. Design of small hand-launched solar-powered uavs: From concept study to a multi-day world endurance record flight. *Journal of Field Robotics*, 34(7):1352–1377, 2017.

[PAOE+14] Gh Pirouzi, NA Abu Osman, A Eshraghi, S Ali, H Gholizadeh, and WAB Wan Abas. Review of the socket design and interface pressure measurement for transtibial prosthesis. *The scientific World journal*, 2014, 2014.

[Pra24] Ludwig Prandtl. Induced drag of multiplanes. 1924.

[RMT70] D Reuschel, C Mattheck, and M Teschner. Determination of optimal fibre arrangement of complex two or three dimensional geometries. *WIT Transactions on The Built Environment*, 31, 1970.

[Run19] Jennifer Runyon. Solar plane breaks two-night flight barrier, Sep 2019.

[SAG06] Shahriar Setoodeh, Mostafa M Abdalla, and Zafer Gurdal. Design of variable–stiffness laminates using lamination parameters. *Composites Part B: Engineering*, 37(4-5):301–309, 2006.

[SB12] MH Sadr and H Ghashochi Bargh. Optimization of laminated composite plates for maximum fundamental frequency using elitist-genetic algorithm and finite strip method. *Journal of Global Optimization*, 54(4):707–728, 2012.

[Sel95] Michael S Selig. *Summary of low speed airfoil data*. SOARTECH publications, 1995.

[SFSA12] Christoph Schmalz, Frank Forster, Anton Schick, and Elli Angelopoulou. An endoscopic 3d scanner based on structured light. *Medical Image Analysis*, 16(5):1063âĂŞ1072, 2012.

[SGW06] Shahriar Setoodeh, Zafer Gurdal, and Layne T Watson. Design of variable-stiffness composite layers using cellular automata. *Computer Methods in Applied Mechanics and Engineering*, 195(9-12):836–851, 2006.

[SH13a] David Moinina Sengeh and Hugh Herr. A variable-impedance prosthetic socket for a transtibial amputee designed from magnetic resonance imaging data. *JPO Journal of Prosthetics and Orthotics*, 25(3):129âĂŞ137, 2013.

[SH13b] David Moinina Sengeh and Hugh Herr. A variable-impedance prosthetic socket for a transtibial amputee designed from magnetic resonance imaging data. *JPO: Journal of Prosthetics and Orthotics*, 25(3):129–137, 2013.

[SP94] C Michael Schuch and Charles H. Pritham. International standards organization terminology: Application to prosthetics and orthotics. *JPO Journal of Prosthetics and Orthotics*, 6(1):29âĂŞ33, 1994.

[SPH08] Christian Schaller, Jochen Penne, and Joachim Hornegger. Time-of-flight sensor for respiratory motion gating. *Medical Physics*, 35(7Part1):3090âĂŞ3093, 2008.

[SS98] Scott R Schall and Tracy C Slemker. Method for fabricating a prosthetic limb socket, October 20 1998. US Patent 5,824,111.

[Str06] Erin Strait. Prosthetics in developing countries. *Prosthetic Resident*, page 3, 2006.

[TKB16] LYL Tse, S Kapila, and K Barton. Contoured 3d printing of fiber reinforced polymers. In *Proceedings of the Solid Freeform Fabrication Symposium: An Additive Manufacturing Conference*, pages 1205–1216, 2016.

[TKVG+14] Halil L Tekinalp, Vlastimil Kunc, Gregorio M Velez-Garcia, Chad E Duty, Lonnie J Love, Amit K Naskar, Craig A Blue, and Soydan Ozcan. Highly oriented carbon fiber–polymer composites via additive manufacturing. *Composites Science and Technology*, 105:144–150, 2014.

[TTM16] Daniel-Alexander Türk, Lukas Triebe, and Mirko Meboldt. Combining additive manufacturing with advanced composites for highly integrated robotic structures. *Procedia CIRP*, 50:402–407, 2016.

[TW07] Philip Treleaven and Jonathan Wells. 3d body scanning and healthcare applications. *Computer*, 40(7):28âĂŞ34, 2007.

[Tyl17] Kenneth Tyler. Method and apparatus for additive mechanical growth of tubular structures, November 7 2017. US Patent 9,808,991.

[uni19] Un report: Nature's dangerous decline 'unprecedented'; species extinction rates 'accelerating' - united nations sustainable development, May 2019.

[Van17] THJ Vaneker. The role of design for additive manufacturing in the successful economical introduction of am. *Procedia Cirp*, 60:181–186, 2017.

[VCKG12] Julien MJF Van Campen, Christos Kassapoglou, and Zafer Gürdal. Generating realistic laminate fiber angle distributions for optimal variable stiffness laminates. *Composites Part B: Engineering*, 43(2):354–360, 2012.

[WG11] Terry Wohlers and Tim Gornet. " history of additive manufacturing," wohlers report: Additive manufacturing and 3d printing state of the industry annual worldwide progress report. 2011.

[WZX15] Feng Wang, Wei Ping Zhao, and Song Xiang. Fiber orientation angles optimization for maximum fundamental frequency of laminated composite plates by the genetic algorithm and meshless method. In *Applied Mechanics and Materials*, volume 709, pages 130–134. Trans Tech Publ, 2015.

[YTU+16] Yusuke Yamanaka, Akira Todoroki, Masahito Ueda, Yoshiyasu Hirano, Ryosuke Matsuzaki, et al. Fiber line optimization in single ply for 3d printed composites. *Open Journal of Composite Materials*, 6(04):121, 2016.

[ZGME+08] Kathryn Ziegler-Graham, Ellen J. Mackenzie, Patti L. Ephraim, Thomas G. Travison, and Ron Brookmeyer. Estimating the prevalence of limb loss in the united states: 2005 to 2050. *Archives of Physical Medicine and Rehabilitation*, 89(3):422âĂŞ429, 2008.